Supplementary Material

How Reliable is the Real Adsorbed Solution Theory (RAST) for Estimating Ternary Mixture Equilibrium in Microporous Host Materials?

Rajamani Krishna* and Jasper M. van Baten

Van 't Hoff Institute for Molecular Sciences
University of Amsterdam
Science Park 904
1098 XH Amsterdam, The Netherlands
email: r.krishna@uva.nl; r.krishna@contact.uva.nl
ORCID 0000-0002-4784-8530

Contents

1 Preamble

The Supporting Information accompanying our article *How Reliable is the Real Adsorbed Solution Theory (RAST) for Estimating Ternary Mixture Equilibrium in Microporous Host Materials?* provides (a) structural details of host zeolites, (b) details of the CBMC simulation methodology including choice of force fields, (b) details of the IAST, and Real Adsorbed Solution Theory (RAST) calculations for mixture adsorption equilibrium, (c) unary isotherm fit parameters, (d) Wilson, NRTL, and Margules parameters fits for thermodynamic non-idealities, (e) plots of CBMC simulation data and comparisons with IAST/RAST estimates.

For ease of reading, the Supplementary Material is written as a stand-alone document. As a consequence, there is some overlap of material with the main manuscript.

2 Structural details of host zeolites

The investigated host materials fall into five broad classes.

1. One-dimensional (1D) channels (Mg_2(dobdc), JBW, Co(BDP)).).
2. One-dimensional channels with side pockets (MOR)
3. Intersecting channels (MFI, ISV)
4. Cages separated by narrow windows (CHA, DDR, ZIF-8, AFX, LTA (all-silica), LTA-4A)
5. Cavities with large windows (FAU (all-silica), NaY (144 Si, 48 Al, 48 Na^+, Si/Al=3), NaX (106 Si, 86 Al, 86 Na^+, Si/Al=1.23))

The crystallographic data are available on the zeolite atlas website of the International Zeolite Association (IZA).[1, 2] Further details on the structure, landscape, pore dimensions of a very wide variety of micro-porous materials are available in the published literature.[3-10] Table S1, and Table S2 provide some salient structural information on CHA, DDR, MOR, LTA-4A and NaX zeolites. See also Figure S1 - Figure S10. Also included are the data for the all-silica versions, LTA (all silica), and FAU (all silica) for which simulations were also undertaken in order to highlight the influence of extra-framework cations on the thermodynamic non-idealiites.

Watch also the presentations titled **Diffusion in LTA-4A and 5A Zeolites, Diffusion in Cage-Type Zeolites, Inter-cage Hopping in DDR Zeolite, Inter-cage Hopping in CHA Zeolite, ZIF-8 Membranes, Visualizing Motion of Guest Molecules in ZIF-8, Diffusion in LTA Zeolite, Diffusion in CHA Zeolite, Diffusion in DDR Zeolite, Diffusion in ZIF-8, Guest Mobility in CuBTC**

on YouTube https://www.youtube.com/@rajamanikrishna250/videos

2.1 List of Tables for Structural details of host zeolites

Table S1. Salient structural information.

Structure	Topology	Fractional pore volume, ϕ	Pore volume/ cm^3/g	Framework density/ kg/m^3
Mg_2(dobdc)	1D hexagonal-shaped channels of 11 Å	0.708	0.782	905
Co(BDP)	10 Å square-shaped 1D channels	0.669	0.927	721.55
JBW	1D channels	0.161	0.086	1873.80
CHA	316 $Å^3$ cages separated by 3.77 Å × 4.23 Å size windows	0.382	0.264	1444
MOR	12-ring (7.0 Å × 6.5 Å) 1D channels, connected to 8-ring (5.7 Å × 2.6 Å) pockets	0.285	0.166	1714.69
DDR	277.8 $Å^3$ cages separated by 3.65 Å × 4.37 Å size windows	0.245	0.139	1760
LTA (all silica)	cages of 743 $Å^3$ volume, separated by 4.11 Å × 4.47 Å 8-ring windows	0.399	0.31	1285.2
LTA-4A	cages of 694 $Å^3$ volume, separated by 4 Å × 4.48 Å 8-ring windows	0.375	0.245	1529.6
AFX	490 $Å^3$ size cages connected to pockets of 98 $Å^3$ in size. Cages are separated by 3.4 Å × 3.9 Å size windows.	0.359	0.246	1463.71
ZIF-8	1168 $Å^3$ cages separated by 3.26 Å size windows	0.476	0.515	924
MFI	10-ring intersecting channels of 5.4 Å – 5.5 Å and 5.4 Å – 5.6 Å size	0.297	0.165	1796
ISV	Intersecting channels of two sizes: 12-ring of 6.1 Å -6.5 Å and 12-ring of 5.9 Å - 6.6 Å	0.426	0.278	1533
FAU (all silica)	786 $Å^3$ cages separated by 7.4 Å size windows	0.439	0.328	1338
NaY	786 $Å^3$ cages separated by 7.4 Å size windows	0.41	0.303	1347
NaX	781 $Å^3$ cages separated by 7.4 Å size windows	0.40	0.280	1421

Table S2. Pore volumes, surface areas, and characteristic (Delaunay) dimensions.

Structure	**Pore volume** / $cm^3\ g^{-1}$	**Surface area** / $m^2\ g^{-1}$	**Delaunay diameter**/ Å
MFI	0.165	487.2	5.16
ISV	0.278	911.4	5.96
FAU (all silica)	0.328	1086	7.4
NaY	0.303	950	7.4
NaX	0.280	950	7.4
CHA	0.264	757.5	3.98
DDR	0.139	350	4.02
AFX	0.246	674.5	3.8
ZIF-8	0.515	1164.7	3.26
LTA-4A	0.245	896	4
Mg_2(dobdc)	0.782	1640.0	10.7
Co(BDP)	0.927	2148.8	10
JBW	0.086	25	3.66
MOR	0.166	417	6.44

2.2 List of Figures for Structural details of host zeolites

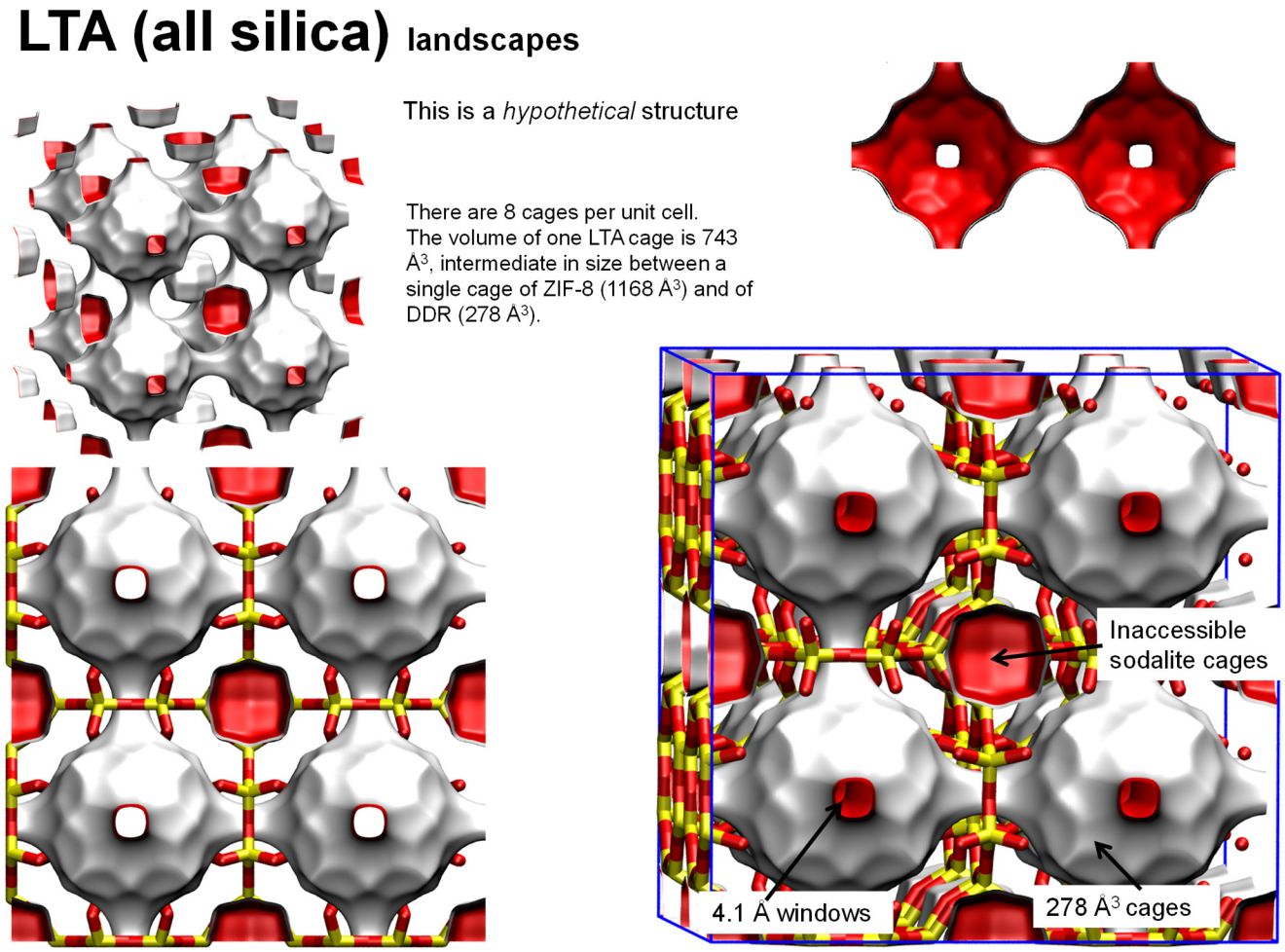

Figure S1. Pore landscape of all-silica LTA zeolite.

LTA (all-silica) window and pore dimensions

8-ring window of LTA

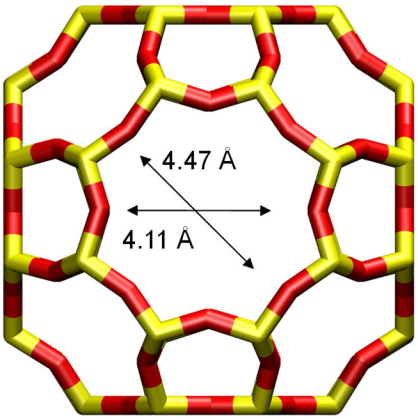

The window dimension calculated using the van der Waals diameter of framework atoms = 2.7 Å is indicated above by the arrows.

This plot of surface area versus pore dimension is determined using a combination of the DeLaunay triangulation method for pore dimension determination, and the procedure of Düren for determination of the surface area.

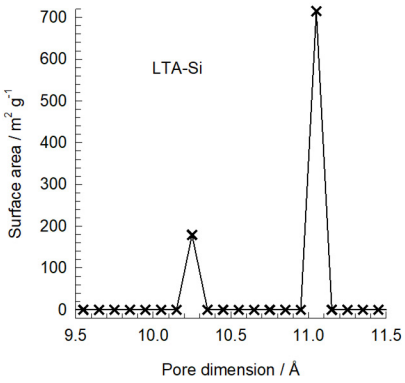

	LTA-Si
a /Å	24.61
b /Å	24.61
c /Å	24.61
Cell volume / Å^3	14905.1
conversion factor for [molec/uc] to [mol per kg Framework]	0.0867
conversion factor for [molec/uc] to [kmol/m^3]	0.2794
ρ [kg/m3]	1285.248
MW unit cell [g/mol(framework)]	11536.28
ϕ, fractional pore volume	0.399
open space / Å^3/uc	5944.4
Pore volume / cm^3/g	0.310
Surface area /m^2/g	896.0
DeLaunay diameter /Å	4.10

Figure S2. Structural details for all-silica LTA zeolite.

LTA-4A

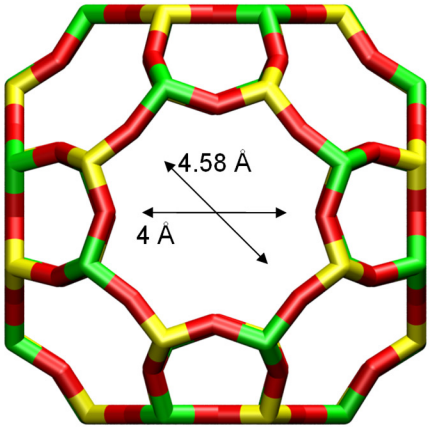

LTA-4A

The window dimension calculated using the van der Waals diameter of framework atoms = 2.7 Å is indicated above by the arrow.

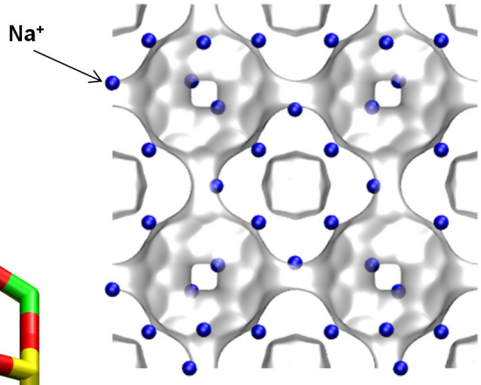

LTA-4A (96 Na+)

	LTA-4A
a /Å	24.555
b /Å	24.555
c /Å	24.555
Cell volume / Å^3	14805.39
conversion factor for [molec/uc] to [mol per kg Framework]	0.0733
conversion factor for [molec/uc] to [kmol/m^3]	0.2991
ρ [kg/m3] (with cations)	1529.55
MW unit cell [g/mol(framework+cations)]	13637.27
ϕ, fractional pore volume	0.375
open space / Å^3/uc	5552.0
Pore volume / cm^3/g	0.245
Surface area /m^2/g	
DeLaunay diameter /Å	4.00

Figure S3. Structural details for LTA-4A zeolite.

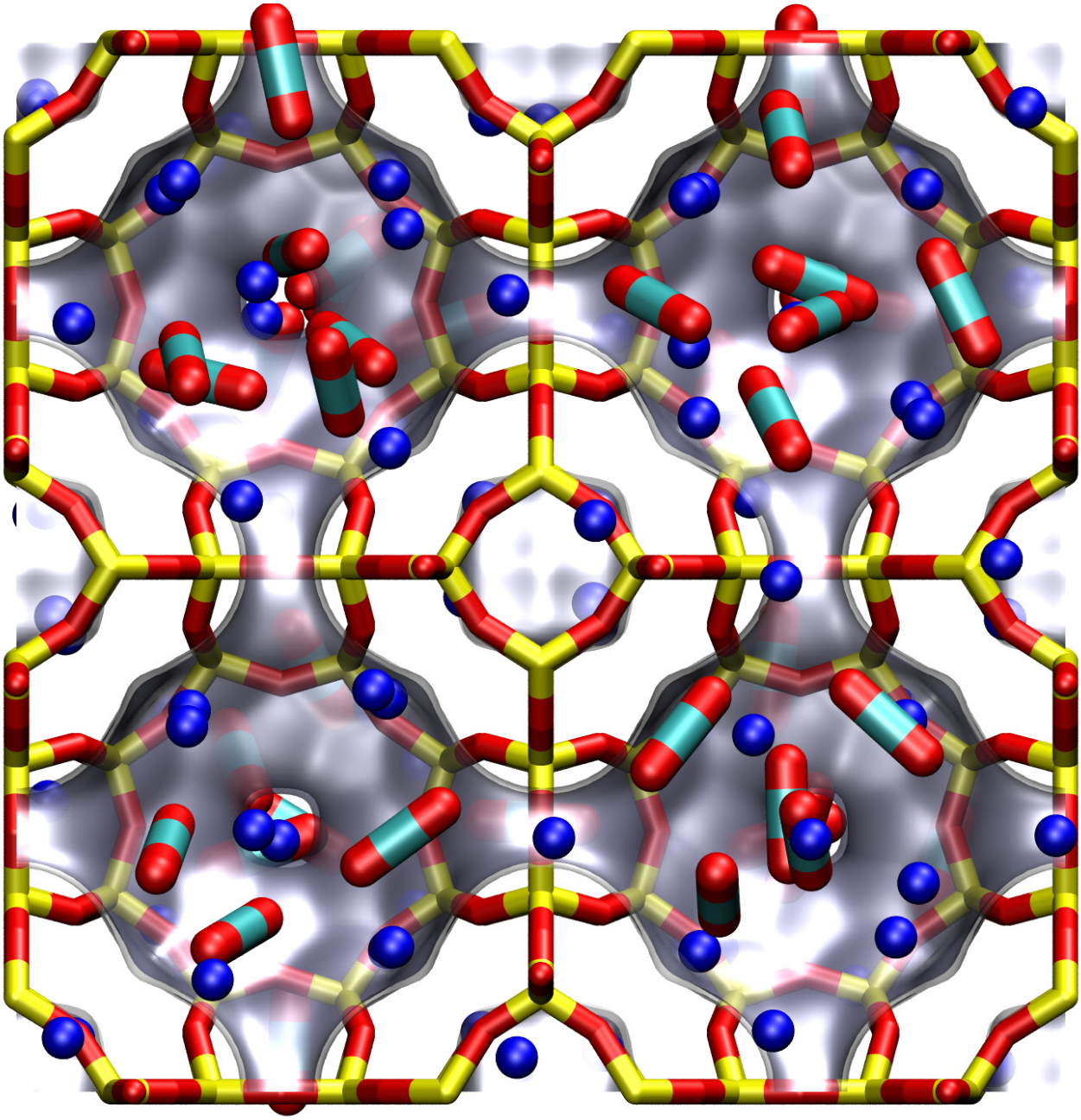

Figure S4. Location of extra-framework cations in LTA-4A zeolite.

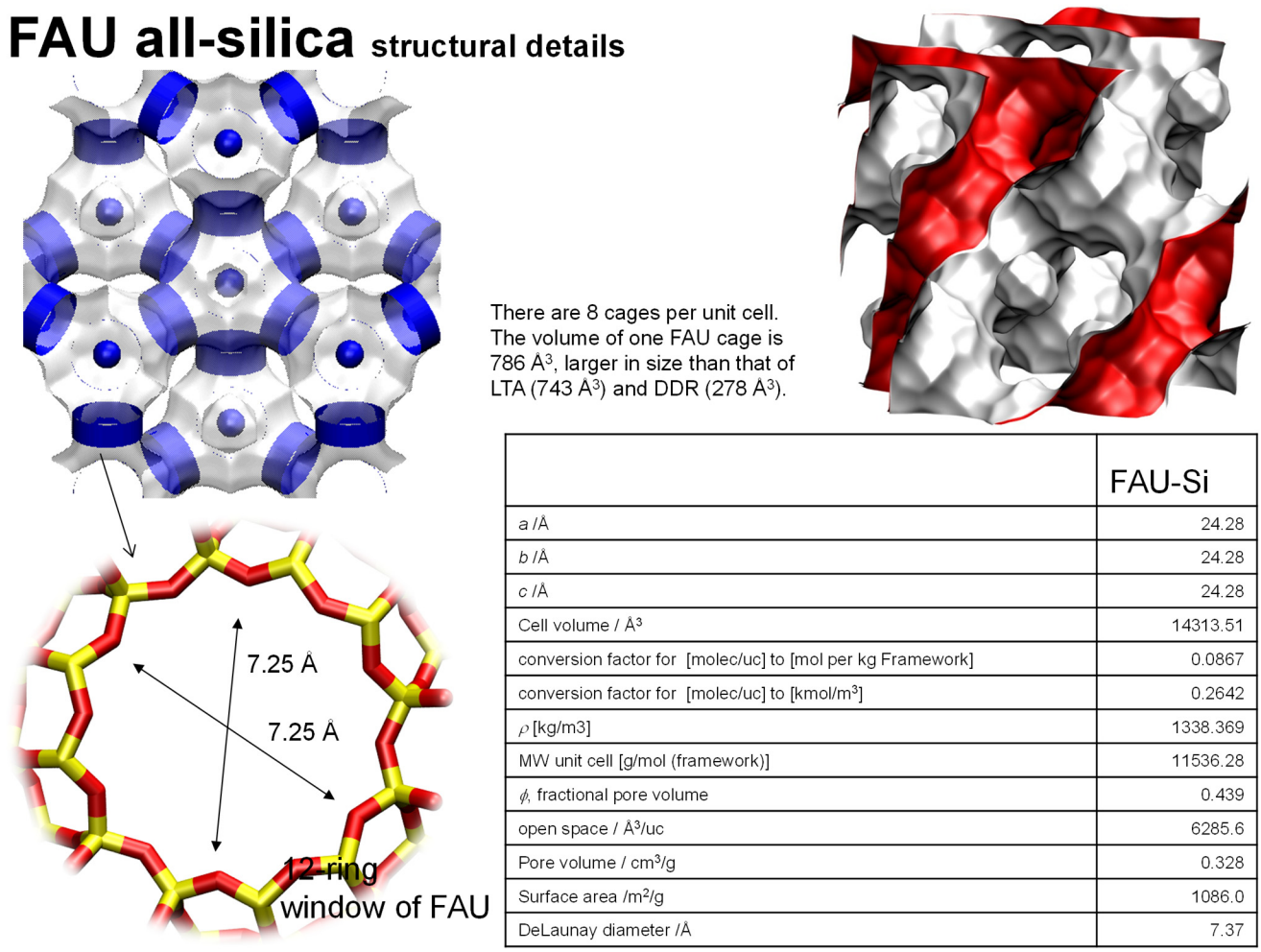

	FAU-Si
a /Å	24.28
b /Å	24.28
c /Å	24.28
Cell volume / Å^3	14313.51
conversion factor for [molec/uc] to [mol per kg Framework]	0.0867
conversion factor for [molec/uc] to [kmol/m^3]	0.2642
ρ [kg/m3]	1338.369
MW unit cell [g/mol (framework)]	11536.28
ϕ, fractional pore volume	0.439
open space / Å^3/uc	6285.6
Pore volume / cm^3/g	0.328
Surface area /m^2/g	1086.0
DeLaunay diameter /Å	7.37

Figure S5. Pore landscape for all-silica FAU zeolite.

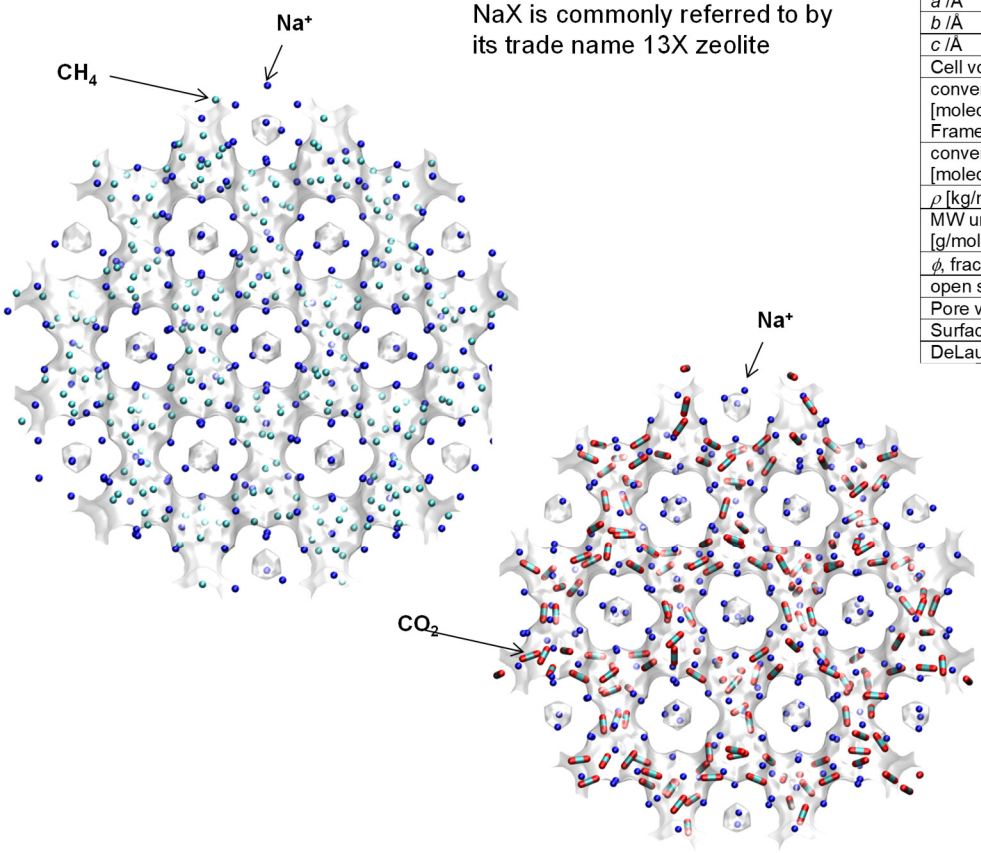

	NaX 86 Na/uc
a /Å	25.028
b /Å	25.028
c /Å	25.028
Cell volume / Å^3	15677.56
conversion factor for [molec/uc] to [mol per kg Framework]	0.0745
conversion factor for [molec/uc] to [kmol/m^3]	0.2658
ρ [kg/m3] (with cations)	1421.277
MW unit cell [g/mol(framework+cations)]	13418.42
ϕ, fractional pore volume	0.399
open space / Å^3/uc	6248.0
Pore volume / cm^3/g	0.280
Surface area /m^2/g	
DeLaunay diameter /Å	7.37

Figure S6. Structural details for NaX zeolite (106 Si, 86 Al, 86 Na^+, Si/Al=1.23).

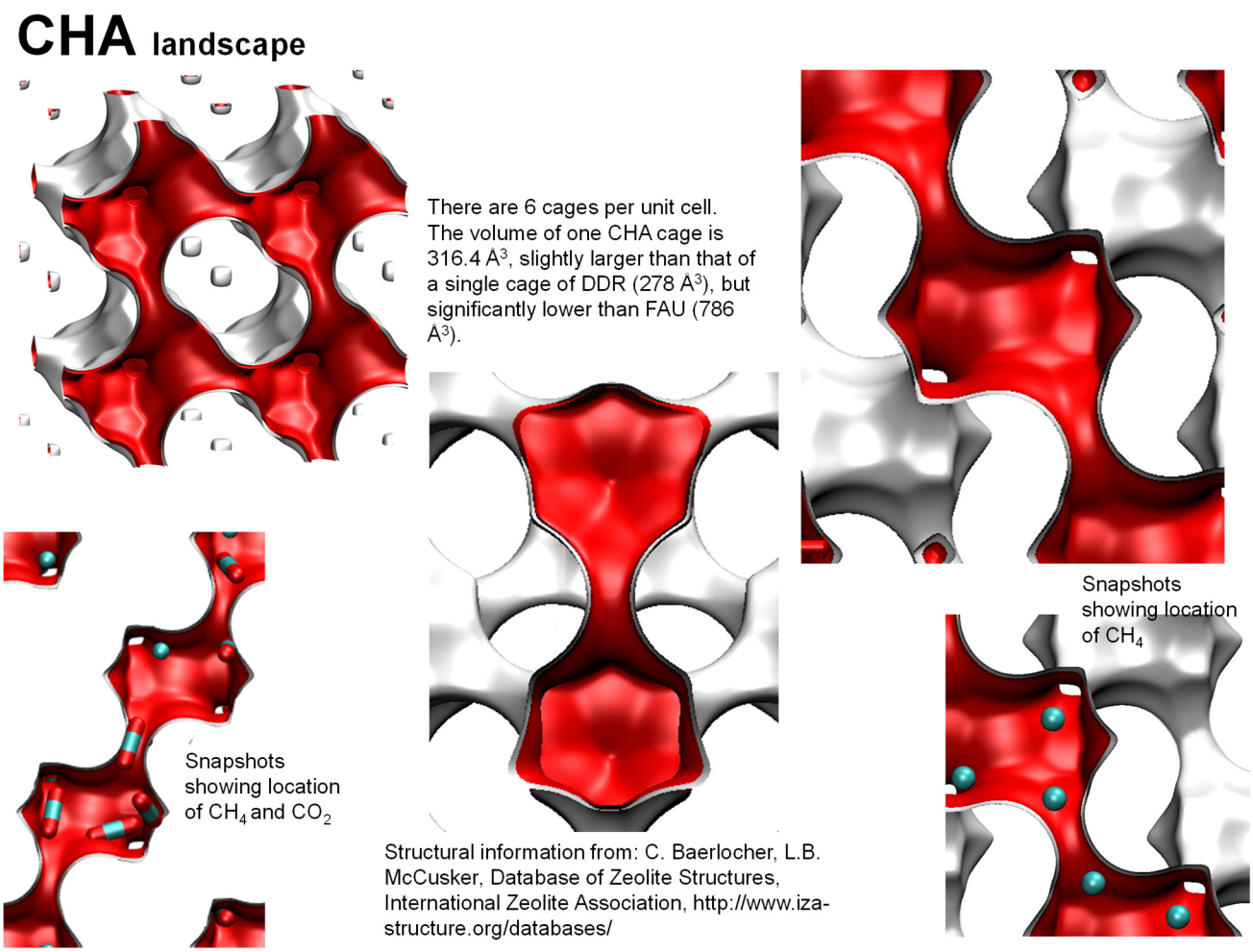

Figure S7. Pore landscape of all-silica CHA zeolite.

CHA window and pore dimensions

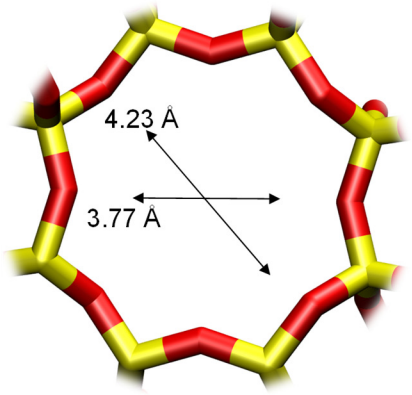

CHA

The window dimensions calculated using the van der Waals diameter of framework atoms = 2.7 Å are indicated above by the arrows.

	CHA
a /Å	15.075
b /Å	23.907
c /Å	13.803
Cell volume / Å^3	4974.574
conversion factor for [molec/uc] to [mol per kg Framework]	0.2312
conversion factor for [molec/uc] to [kmol/m^3]	0.8747
ρ [kg/m3]	1444.1
MW unit cell [g/mol(framework)]	4326.106
ϕ, fractional pore volume	0.382
open space / Å^3/uc	1898.4
Pore volume / cm^3/g	0.264
Surface area /m^2/g	758.0
DeLaunay diameter /Å	3.77

Figure S8. Structural details for CHA zeolite.

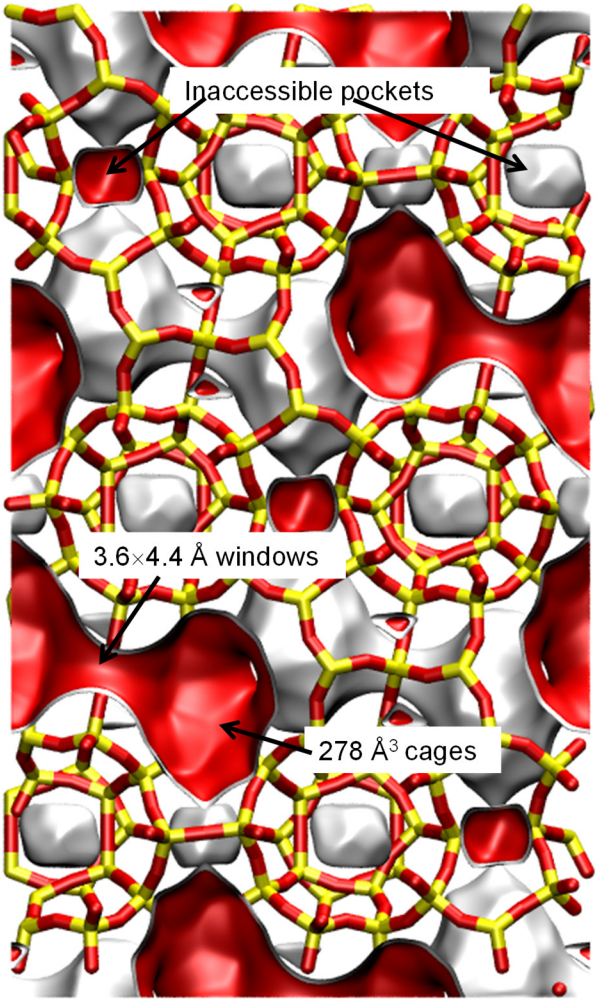

DDR landscape

To convert from molecules per unit cell to mol kg^{-1}, multiply by 0.06936.
The pore volume is 0.182 cm^3/g.

There are 12 cages per unit cell. The volume of one DDR cage is 278 Å^3, significantly smaller than that of a single cage of FAU (786 Å^3), or ZIF-8 (1168 Å^3).

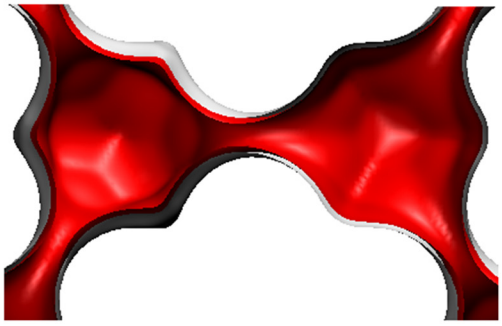

Structural information from: C. Baerlocher, L.B. McCusker, Database of Zeolite Structures, International Zeolite Association, http://www.iza-structure.org/databases/

Figure S9. Pore landscape of all-silica DDR zeolite.

DDR window and pore dimensions

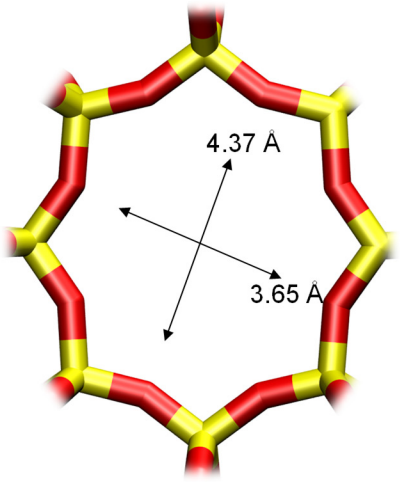

DDR

The window dimensions calculated using the van der Waals diameter of framework atoms = 2.7 Å are indicated above by the arrows.

	DDR
a /Å	24.006
b /Å	13.86
c /Å	40.892
Cell volume / Å^3	13605.72
conversion factor for [molec/uc] to [mol per kg Framework]	0.0693
conversion factor for [molec/uc] to [kmol/m^3]	0.4981
ρ [kg/m3]	1759.991
MW unit cell [g/mol(framework)]	14420.35
ϕ, fractional pore volume	0.245
open space / Å^3/uc	3333.5
Pore volume / cm^3/g	0.139
Surface area /m^2/g	350.0
DeLaunay diameter /Å	3.65

Figure S10. Structural details for DDR zeolite.

3 Configurational-Bias Monte Carlo Simulation Methodology

The simulation methodologies and the force field information used are the same as detailed in the Supplementary Materials accompanying our earlier publications.[3, 5, 9, 11-18] A short summary is provided hereunder.

3.1 Zeolites (all silica)

CH_4 molecules are described with a united atom model, in which each molecule is treated as a single interaction center.[19] The interaction between adsorbed molecules is described with Lennard-Jones terms; see Figure S11. The Lennard-Jones parameters for CH_4-zeolite interactions are taken from Dubbeldam et al.[20]. For simulations with linear alkanes with two or more C atoms, the beads in the chain are connected by harmonic bonding potentials. A harmonic cosine bending potential models the bond bending between three neighboring beads, a Ryckaert-Bellemans potential controls the torsion angle. The beads in a chain separated by more than three bonds interact with each other through a Lennard-Jones potential; see schematic in Figure S11. The force fields of Dubbeldam et al.[20] was used for the variety of potentials.

CO_2 molecules are taken linear and rigid with bond length C–O of 1.16 Å according to the 3LJ3CB.EPM2 model developed by Harris and Young.[21] CO_2 was represented by a 3-site charged Lennard-Jones model as described by Garcia-Sánchez et al.[22] We use the 2LJ3CB.MSKM model for N_2 dumbbell molecules with a rigid interatomic bond of 1.098Å. [23, 24] The partial charges of N_2 and CO_2 are distributed around each molecule to reproduce experimental quadrupole moment.

The force field for H_2 corresponds to that given by Kumar et al.[25] In implementing this force field, quantum effects for H_2 have been ignored because the work of Kumar et al.[25] has shown that quantum effects are of negligible importance for temperatures above 200 K; all our simulations were performed at 300 K. The Lennard-Jones parameters for CO_2-zeolite and N_2-zeolite are those of Makrodimitris et al.[24]; see also García-Pérez et al.[26] and García-Sanchez et al.[22]

The Lennard-Jones potentials are shifted and cut at 12 Å.

For simulations of adsorption of guest molecules water, methanol, and ethanol, the force field implementation follows earlier publications.[27-30] Water is modeled using the Tip5pEw potential.[31] The alcohols are described with the TraPPE force field.[32] Intramolecular potentials are included to describe the flexibility of alcohols, while the water molecules are kept rigid. The bond lengths are fixed for all molecules. Bond bending potentials are considered for methanol and ethanol, and a torsion potential is used for ethanol.[32] The force field parameters are summarized in Table S4.

[2]The zeolite frameworks were considered to be rigid in all the simulation results reported in the article.

All simulations are performed in the grand canonical ensemble; the chemical potentials of each component in the bulk fluid phase equal that of the corresponding guest adsorbate within the microporous framework. In our simulations, the partial fugacities in the bulk fluid mixture as specified; this fixes the values of the chemical potentials.

Following Kiselev and co-workers,[33] the zeolite is modeled as a rigid crystal. The interactions of the guest (pseudo) atoms with the host zeolite atoms aredominated by the dispersive interactions with the oxygen atoms, these interactions are described with a Lennard-Jones potential; see Table S3.

ZIF-8 is also modelled as a rigid structure. The Lennard-Jones potentials for the framework atoms of ZIF-8 were taken from the combined works of Mayo et al.[34], Yang and Zhong [35], and Jorgensen et al.[36] as was reported in the computational study of Zhou et al.[37] The framework charges of ZIF-8 were estimated using the group-contribution procedure based on quantum mechanical calculations described in the recent paper by Xu and Zhong.[38] Table S5 provides a summary of the force fields for ZIF-8 framework atoms.

The Lorentz-Berthelot mixing rules were applied for calculating the Lennard-Jones parameters describing guest-host interactions

$$\sigma_{guest-host} = \frac{\left(\sigma_{guest} + \sigma_{host}\right)}{2}$$
$$\frac{\varepsilon_{guest-host}}{k_B} = \sqrt{\frac{\varepsilon_{guest}}{k_B} \times \frac{\varepsilon_{host}}{k_B}} \qquad \text{(S1)}$$

The Lennard-Jones potentials are shifted and cut at 12 Å. Periodic boundary conditions were employed. The Configurational-Bias Monte Carlo (CBMC) simulation technique used is identical to that used by Kuhn et al.,[30] and is described in detail by Frenkel and Smit.[39]

The following cation-exchanged structures were investigated

NaX (106 Si, 86 Al, 86 Na^+, Si/Al=1.23)

LTA-4A (96 Si, 96 Al, 96 Na^+, Si/Al=1)

The presence of cations reduces the accessible pore volume. The location of the cations are pictured in Figure S3, Figure S4, and Figure S6.

The force field information for the simulations with cations are taken from García-Sanchez et al.[22] In the MC simulations, the cations were allowed to move within the framework and both Lennard-Jones and Coulombic interactions are taken into consideration.

In the CBMC simulations both Lennard-Jones and Coulombic interactions are taken into consideration; see schematic sketch in Figure S12.

3.2 CBMC code

All simulations reported in this work were carried out using an in-house BIGMAC code, originally developed by T.J.H. Vlugt. This code was modified to handle rigid molecular structures and charges. The calculation of the accessible pore volume using the Widom insertion of He probe atoms is implemented within the BIGMAC code.

All CBMC simulations reported in this work were conducted at a temperature T = 300 K.

3.3 List of Tables for Configurational-Bias Monte Carlo Simulation Methodology

Table S3. Lennard-Jones parameters for host atoms in all-silica zeolites.

(pseudo-) atom	σ / Å	ε/k_B / K	charge
Si			2.05
O	3	93.53	-1.025

Table S4. Lennard-Jones parameters for guest pseudo-atoms. as provided in Table 1 of Kuhn et al.[30] The water model has two off-center charges that are labeled M in the Table. The name "alcohol" refers to both methanol and ethanol molecules.

Molecule	(pseudo-) atom	σ / Å	ε/k_B / K	charge
water	O	3.097	89.516	0
water	H	0	0	0.241
water	M	0	0	-0.241
methanol	CH3	3.75	98	0.265
ethanol	CH3	3.75	98	0
ethanol	CH2	3.95	46	0.265
alcohol	O	3.02	93	-0.7
alcohol	H	0	0	0.435

Table S5. The Lennard-Jones potentials for the host framework atoms of ZIF-8 were taken from the combined works of Mayo et al.[34] Yang and Zhong,[35] and Jorgensen et al.[36] as was reported in the computational study of Zhou et al.[37] The framework charges of ZIF-8 were estimated using the group-contribution procedure based on quantum mechanical calculations described by Xu and Zhong.[38]

(pseudo-) atom	σ / Å	ε/k_B / K	charge
Zn	4.54	27.59	0.749
N	3.25	85.29	-0.387
Ca	2.25	25.08	0.698
Cb	3.55	35.12	-0.0093
Cc	3.5	20.03	0.0117
Ha	2.5	15.05	-0.139
Hb	3.19	7.53	0.0627

See Cartoon below for further explanation:

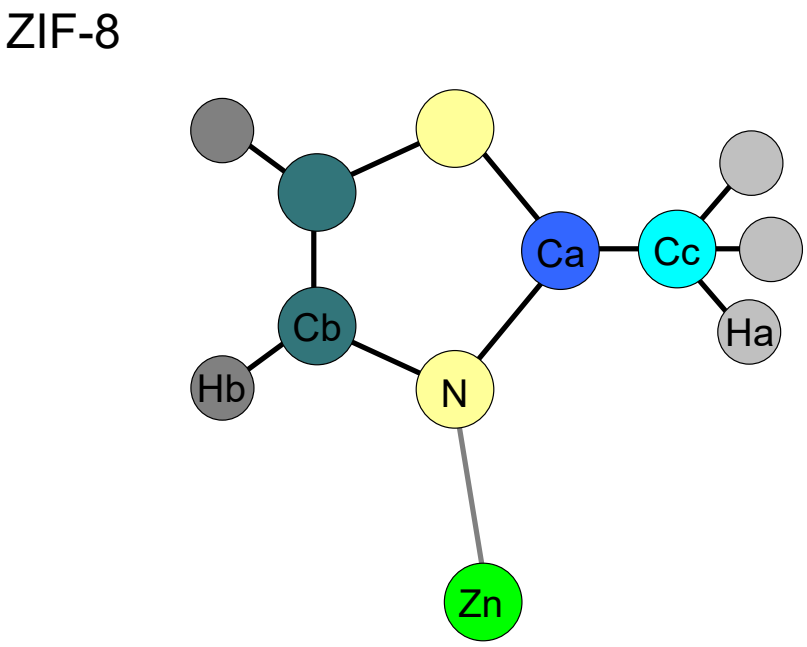

3.4 List of Figures for Configurational-Bias Monte Carlo Simulation Methodology

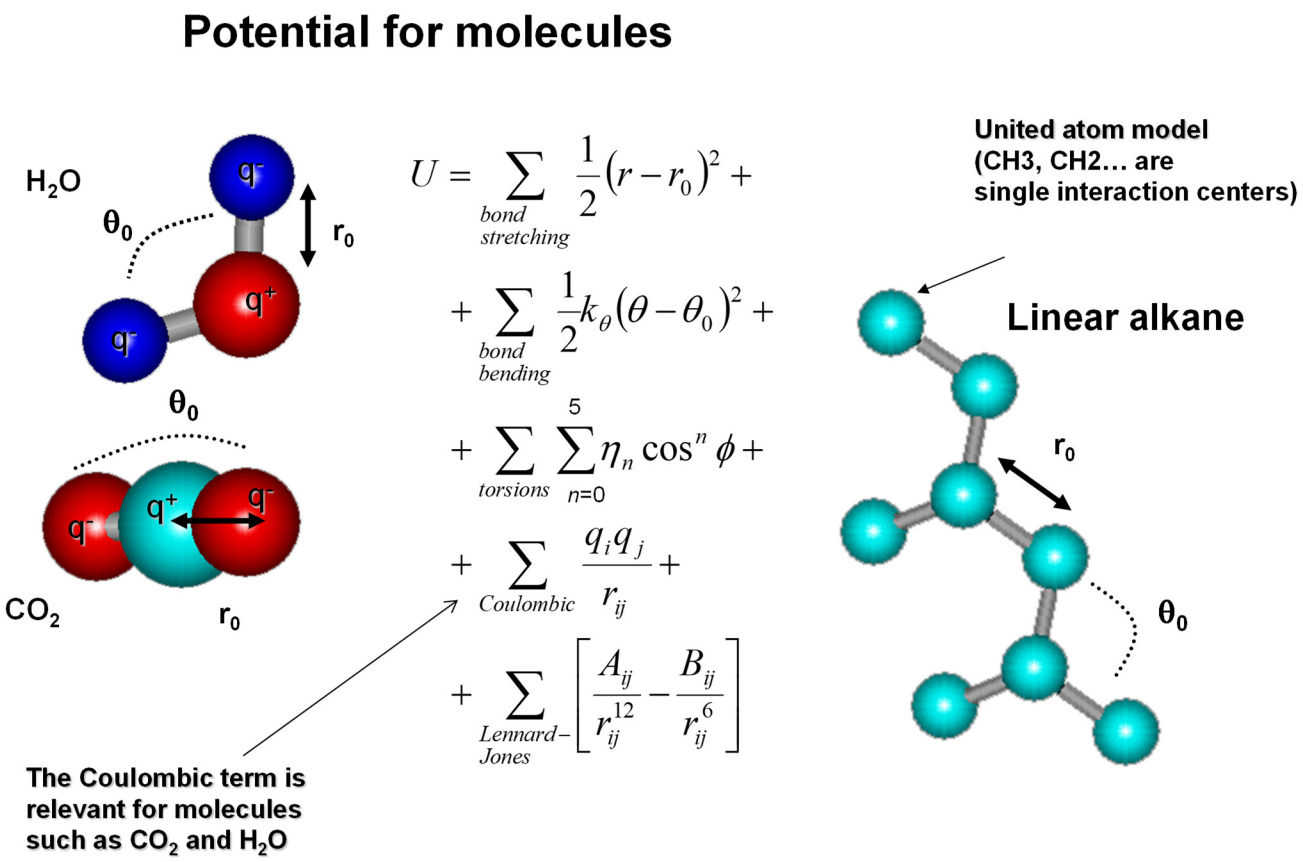

Figure S11. Potential for molecules.

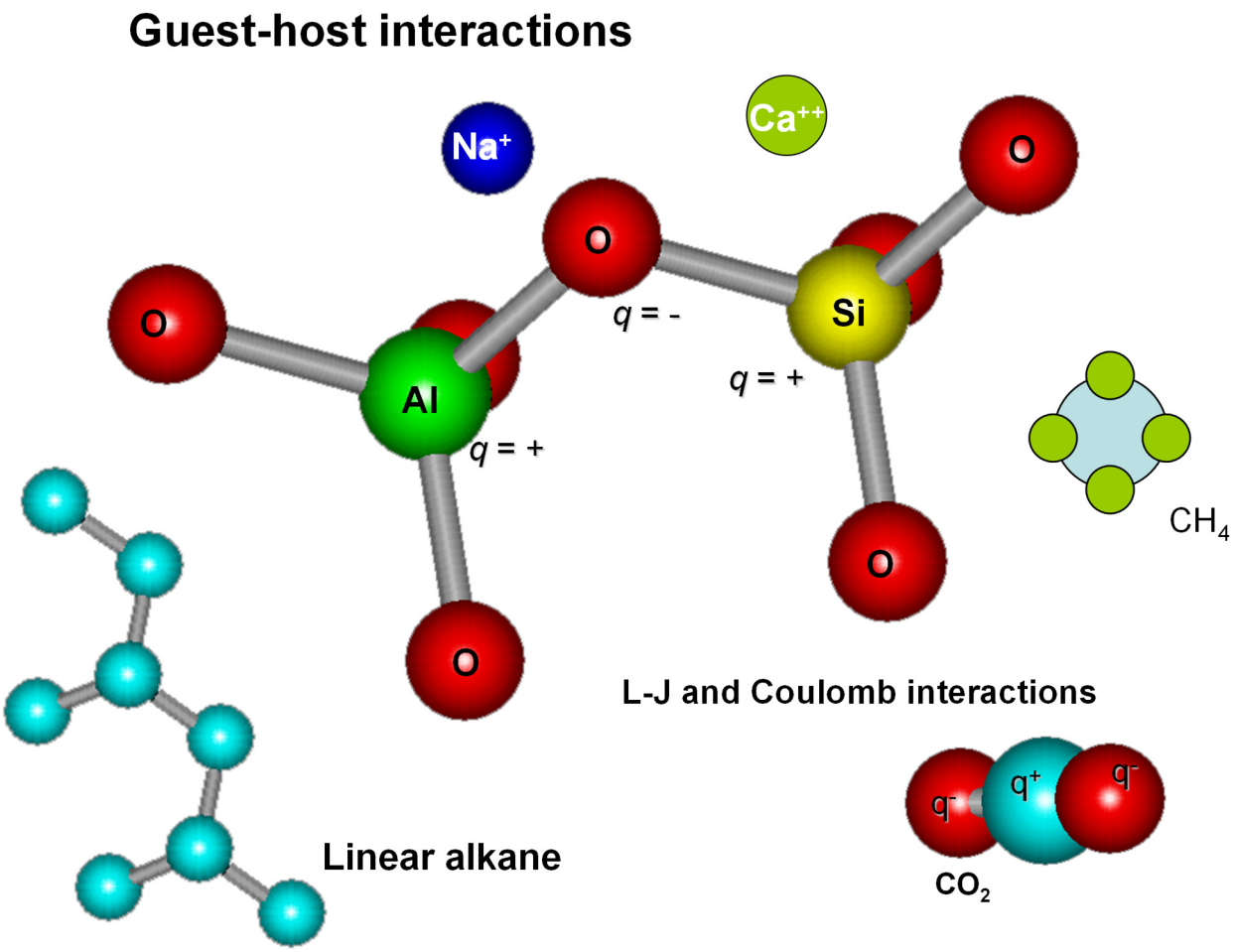

Figure S12. Guest-host interactions.

4 The Ideal Adsorbed Solution Theory

We provide a brief outline of the Ideal Adsorbed Solution Theory for calculation of mixture adsorption equilibrium.

4.1 Gibbsian thermodynamics of mixture adsorption

The Gibbs adsorption equation[40] in differential form is

$$Ad\pi = \sum_{i=1}^{n} q_i d\mu_i \tag{S2}$$

The quantity A is the surface area per kg of framework, with units of m^2 per kg of the framework of the crystalline material; q_i is the molar loading of component i in the adsorbed phase with units moles per kg of framework; μ_i is the molar chemical potential of component i. The spreading pressure π has the same units as surface tension, i.e. N m^{-1}.

The chemical potential of any component in the adsorbed phase, μ_i, equals that in the bulk fluid phase. If the partial fugacities in the bulk fluid phase are f_i, we have

$$d\mu_i = RTd\ln f_i \tag{S3}$$

where R is the gas constant (= 8.314 J mol^{-1} K^{-1}).

Briefly, the basic equation of Ideal Adsorbed Solution Theory (IAST) theory of Myers and Prausnitz[41] is the analogue of Raoult's law for vapor-liquid equilibrium, i.e.

$$. f_i = P_i^0 x_i; \quad i = 1, 2, ...n . \tag{S4}$$

where x_i is the mole fraction in the adsorbed phase

$$x_i = \frac{q_i}{q_1 + q_2 + ...q_n} \tag{S5}$$

and P_i^0 is the pressure for sorption of every component i, which yields the same spreading pressure, π for each of the pure components, as that for the mixture:

$$\frac{\pi A}{RT} \equiv \Phi = \int_0^{P_1^0} \frac{q_1^0(f)}{f} df = \int_0^{P_2^0} \frac{q_2^0(f)}{f} df = \int_0^{P_3^0} \frac{q_3^0(f)}{f} df = ... \tag{S6}$$

where . $q_i^0(f)$. is the *pure* component adsorption isotherm. The units of $\Phi \equiv \frac{\pi A}{RT}$, also called the surface potential, [42-46] are mol kg^{-1}.

The unary isotherm may be described by say the 1-site Langmuir isotherm

$$q^0(f) = q_{sat} \frac{bf}{1+bf}; \quad \theta = \frac{bf}{1+bf} \tag{S7}$$

where we define the fractional *occupancy* of the adsorbate molecules, $\theta = q^0(f)/q_{sat}$. The superscript 0 is used to emphasize that $q^0(f)$ relates the *pure component* loading to the bulk fluid fugacity. For unary isotherms described by the dual-site Langmuir-Freundlich (DSLF) model

$$q^0(f) = q_{A,sat} \frac{b_A f^{\nu A}}{1+b_A f^{\nu A}} + q_{B,sat} \frac{b_B f^{\nu B}}{1+b_B f^{\nu B}} \tag{S8}$$

each of the integrals in eq (S6) can be evaluated analytically. The integration yields for component *i*,

$$\begin{aligned} \Phi \equiv \frac{\pi A}{RT} &= \int_{f=0}^{P_i^0} \frac{q_i^0(f)}{f} df = \frac{q_{A,sat}}{\nu_A} \ln\left(1+b_A\left(P_i^0\right)^{\nu_A}\right) + \frac{q_{B,sat}}{\nu_B} \ln\left(1+b_B\left(P_i^0\right)^{\nu_B}\right); \\ \Phi \equiv \frac{\pi A}{RT} &= \int_{f=0}^{P_i^0} \frac{q_i^0(f)}{f} df = \frac{q_{A,sat}}{\nu_A} \ln\left(1+b_A\left(\frac{f_i}{x_i}\right)^{\nu_A}\right) + \frac{q_{B,sat}}{\nu_B} \ln\left(1+b_B\left(\frac{f_i}{x_i}\right)^{\nu_B}\right) \end{aligned} \tag{S9}$$

The right hand side of eq (S9) is a function of P_i^0 . For multicomponent mixture adsorption, each of the equalities on the right hand side of Eq (S6) must be satisfied. These constraints may be solved using a suitable equation solver, to yield the set of values of , P_2^0 , P_3^0 ,.. P_n^0 , each of which satisfy eq (S6). The corresponding values of the integrals using these as upper limits of integration must yield the same value of Φ for each component; this ensures that the obtained solution is the correct one.

In the IAST, the adsorbed phase mole fractions x_i are then determined from

$$x_i = \frac{f_i}{P_i^0}; \quad i = 1, 2, ...n \tag{S10}$$

The applicability of eqs (S4) and (S10) mandates that all of the adsorption sites within the microporous material are equally accessible to each of the guest molecules, implying a homogeneous distribution of guest adsorbates within the pore landscape, with no preferential locations of any guest species. The circumstances in which this mandate is not fulfilled are highlighted in recent works.[44, 45, 47, 48]

A further key assumption of the IAST is that the adsorption enthalpies and surface areas of the adsorbed molecules do not change upon mixing.[15] If the total mixture loading is q_t, the area covered by the adsorbed mixture is $\frac{A}{q_t}$ with units of m^2 (mol mixture)$^{-1}$. Therefore, the assumption of no surface area change due to mixture adsorption translates as $\frac{A}{q_t} = \frac{Ax_1}{q_1^0\left(P_1^0\right)} + \frac{Ax_2}{q_2^0\left(P_2^0\right)} + \cdots \frac{Ax_n}{q_n^0\left(P_n^0\right)}$; the total mixture loading is q_t is calculated from

$$q_t = q_1 + q_2 ... + q_n = \frac{1}{\frac{x_1}{q_1^0(P_1^0)} + \frac{x_2}{q_2^0(P_2^0)} + ... + \frac{x_n}{q_n^0(P_n^0)}} \tag{S11}$$

in which $q_1^0(P_1^0)$, $q_2^0(P_2^0)$,… $q_n^0(P_n^0)$ are determined from the unary isotherm fits, using the sorption pressures for each component P_1^0, P_2^0, P_3^0,.. P_n^0 that are available from the solutions to equations Eqs (S6), and (S9).

The occurrence of molecular clustering and hydrogen bonding should be expected to applicability of eq (S11) because the surface area occupied by a molecular cluster is different from that of each of the un-clustered guest molecules in the adsorbed phase; see published literature for details.[27, 46, 48]

The entire set of eqs (S4) to (S11) need to be solved numerically to obtain the loadings, q_i of the individual components in the mixture.

In a number of publications on CO_2 capture from mixtures containing N_2, CH_4, C_2H_4, C_2H_6, C_3H_8, and H_2O using cation-exchanged zeolites,[15, 18, 44, 45, 47, 49-53] the IAST has been shown to fail due to non-compliance with one or more of the afore-mentioned tenets.

For further explanation on the numerical techniques for solving the IAST, fitting of isotherms, the tenets of the IAST, the concept of the surface potential, watch the presentations titled **The IAST for Mixture Adsorption Equilibrium, Dependence of Adsorption Selectivity on Mixture Composition, Adsorption Selectivity vs Total Pressure, Significance of the Spreading Pressure Concept, Hydrogen Bonding Influences on Adsorption, Langmuir Model for Binary Mixture Adsorption, Reversals in Adsorption Selectivity, Competitive CO_2/H_2O Mixture Adsorption in CALF-20** on YouTube https://www.youtube.com/@rajamanikrishna250/videos

4.2 Selectivity for mixture adsorption

For *n*-component mixture adsorption, the selectivity of guest constituent *i* with respect to another guest constituent *j*, in that mixture, $S_{ads,ij}$, is defined by

$$S_{ads,ij} = \frac{q_i/q_j}{f_i/f_j} = \frac{x_i/f_i}{x_j/f_j} \tag{S12}$$

where q_i, q_j are the molar loadings of the constituents *i* and *j*, in the adsorbed phase in equilibrium with a bulk fluid phase mixture with partial fugacities f_i, f_j, and mole fractions $y_i = f_i/f_t$; $f_t = \left(\sum_{k=1}^{n} f_k\right)$. In view of eqs (S10), and (S11), we may re-write eq (S12) as the ratio of the sorption pressures

$$S_{ads,ij} = \frac{P_j^0}{P_i^0} \tag{S13}$$

Applying the restriction specified by eq (S6), it follows that $S_{ads,ij}$ is uniquely determined by the surface potential Φ. It is important to note that eq (S13) is valid irrespective of the total number of components in the mixture. Put another way, the presence of component 3 in the ternary mixture has no influence of the adsorption selectivity $S_{ads,12} = \frac{P_2^0}{P_1^0}$ for the 1-2 pair, except insofar as the presence of component 3 alters the value of the surface potential Φ for the 1-2-3 mixture. Therefore, for an ideal adsorbed phase

mixture, the presence of additional guest constituents, say species 3, 4, 5, do not influence the selectivity of the 1-2 pair.

4.3 The IAST model for 1-site Langmuir isotherms

The IAST procedure will be applied for binary mixture adsorption in which the unary isotherms are described by the 1-site Langmuir model in which the saturation capacities of components 1 and 2 are identical to each other, i.e. $q_{1,sat} = q_{2,sat} = q_{sat}$:

$$q_i^0\left(f\right) = q_{sat}\frac{b_i f}{1+b_i f} \tag{S14}$$

For unary adsorption, the surface potential for a 1-site Langmuir isotherm can be calculated analytically

$$\Phi \equiv \frac{\pi A}{RT} = q_{sat}\ln\left(1+bP^0\right) \tag{S15}$$

The objective is to determine the molar loadings, q_1, and q_2, in the adsorbed phase. Performing the integration of eq (S6) results in an expression relating the sorption pressures P_i^0 of the two species

$$\begin{aligned}&\Phi \equiv \frac{\pi A}{RT} = q_{sat}\ln\left(1+b_1P_1^0\right) = q_{sat}\ln\left(1+b_2P_2^0\right)\\ &b_1P_1^0 = b_2P_2^0 = \exp\left(\frac{\pi A}{q_{sat}RT}\right)-1\end{aligned} \tag{S16}$$

The adsorbed phase mole fractions of component 1, and component 2 are given by eq (S10)

$$x_1 = \frac{f_1}{P_1^0};\quad x_2 = 1-x_1 = \frac{f_2}{P_2^0} \tag{S17}$$

Combining eqs (S16), and (S17):

$$\exp\left(\frac{\pi A}{q_{sat}RT}\right)-1 = b_1\frac{f_1}{x_1} = b_2\frac{f_2}{1-x_1} \tag{S18}$$

The adsorbed phase mole fractions can be determined

$$\frac{x_1}{x_2} = \frac{q_1}{q_2} = \frac{b_1f_1}{b_2f_2};\quad x_1 = \frac{q_1}{q_t} = \frac{b_1f_1}{b_1f_1+b_2f_2};\quad x_2 = \frac{q_2}{q_t} = \frac{b_2f_2}{b_1f_1+b_2f_2} \tag{S19}$$

Once x_1, and $x_2 = 1-x_1$ are determined, the sorption pressures can be calculated:

$$P_1^0 = \frac{f_1}{x_1}; \quad P_2^0 = \frac{f_2}{x_2} = \frac{f_2}{1-x_1} \tag{S20}$$

From eqs (S16), and (S20) we get

$$\begin{aligned} b_i P_1^0 &= \frac{b_1 f_1}{x_1} = b_2 P_2^0 = \frac{b_2 f_2}{x_2} = b_1 f_1 + b_2 f_2 \\ 1 + b_i P_1^0 &= 1 + b_2 P_2^0 = 1 + b_1 f_1 + b_2 f_2 \end{aligned} \tag{S21}$$

Combining eqs (S16), and (S21) we obtain the following explicit expression for the surface potential

$$\Phi = q_{sat} \ln\left(1 + b_1 f_1 + b_2 f_2\right) \tag{S22}$$

The total amount adsorbed, $q_t = q_1 + q_2$ can be calculated from Eq (S11)

$$q_t = q_1 + q_2 = q_{sat} \frac{b_1 P_1^0}{1 + b_1 P_1^0} = q_{sat} \frac{b_2 P_2^0}{1 + b_2 P_2^0} = q_{sat} \frac{b_1 f_1 + b_2 f_2}{1 + b_1 f_1 + b_2 f_2} \tag{S23}$$

Combining eqs (S19), and (S23) we obtain the following explicit expressions for the component loadings, and fractional occupancies

$$\theta_1 = \frac{q_1}{q_{sat}} = \frac{b_1 f_1}{1 + b_1 f_1 + b_2 f_2}; \quad \theta_2 = \frac{q_2}{q_{sat}} = \frac{b_2 f_2}{1 + b_1 f_1 + b_2 f_2} \tag{S24}$$

Eq (S24) is commonly referred to as the mixed-gas Langmuir model.

From eqs (S16), (S23), and (S24) we derive the following expression for the total occupancy of the mixture

$$\theta = \theta_1 + \theta_2 = \frac{q_t}{q_{sat}} = 1 - \exp\left(-\frac{\Phi}{q_{sat}}\right) = \frac{b_1 f_1 + b_2 f_2}{1 + b_1 f_1 + b_2 f_2} \tag{S25}$$

For *unary* adsorption of component *i*, say, $f_i = P_i^0$, the occupancy of component 1 is

$$\theta_i = 1 - \exp\left(-\frac{\Phi}{q_{i,sat}}\right) = \frac{b_i f_i}{1 + b_i f_i}; \quad \text{unary adsorption of species i} \tag{S26}$$

From eqs (S25), and (S26) we may also conclude the *occupancy* may be considered to be the appropriate *proxy* for the spreading pressure. The conclusion that we draw from the foregoing analysis is that the equalities of spreading pressures for unary adsorption of component 1, unary adsorption of component 2, and binary 1-2 mixture adsorption also implies the corresponding equalities of the corresponding

occupancies for unary adsorption of component 1, unary adsorption of component 2, and binary 1-2 mixture adsorption.

For *n*-component mixtures, eq (S22) may be generalized to

$$\Phi = q_{sat} \ln\left(1+\sum_{i=1}^{n} b_i f_i\right) \tag{S27}$$

4.4 Generalized expression for fractional occupancy

From knowledge of the surface potential, Φ, the fractional occupancy for *n*-component mixture adsorption is then calculated using

$$\theta = 1-\exp\left(-\frac{\pi A}{q_{sat,mix} RT}\right) = 1-\exp\left(-\frac{\Phi}{q_{sat,mix}}\right) \tag{S28}$$

For an *n*-component mixture, the saturation capacity $q_{sat,mix}$ is calculated from the saturation capacities of the constituent guests

$$q_{sat,mix} = \frac{1}{\frac{x_1}{q_{1,sat}}+\frac{x_2}{q_{2,sat}}+...\frac{x_n}{q_{n,sat}}}; \quad q_{i,sat} = q_{i,A,sat} + q_{i,B,sat}; \quad i = 1,2...n \tag{S29}$$

where

$$x_i = \frac{q_i}{q_1+q_2+...q_n}; \quad i = 1,2,...n \tag{S30}$$

are the mole fractions in the adsorbed mixture. The fundamental justification of Eq (S29) is provided by invoking eq (S11).

For binary mixtures, eq (S29) simplifies to yield $q_{sat,mix} = \frac{1}{\frac{x_1}{q_{1,sat}}+\frac{x_2}{q_{2,sat}}}$.

It is also to be noted that eq (15) of our earlier publication[54] has a typographical error in the calculation of $q_{sat,mix}$; the correct form is given by eq (S29).

As an example, let consider the adsorption of water(1)/ethanol(2) mixtures in CHA zeolite at 300 K. The Dual-site Langmuir-Freundlich isotherm fit parameters are specified in Table S7. The saturation

capacity of water (1) $q_{1,sat} = q_{1,A,sat} + q_{1,B,sat}$ =16.8 + 4.6 = 21.4 mol kg^{-1}. The saturation capacity of ethanol (2) $q_{2,sat} = q_{2,A,sat} + q_{2,B,sat}$ =2.5 + 2.9 = 5.4 mol kg^{-1}. The saturation capacity of the mixture for adsorbed phase compositions, $x_1 = x_2 = 0.5$ is $q_{sat,mix} = \dfrac{1}{\dfrac{x_1}{q_{1,sat}} + \dfrac{x_2}{q_{2,sat}}}$ = 8.62 mol kg^{-1}.

For binary CO_2(1)/CH_4(2) mixture adsorption in CHA, DDR, MFI, and all-silica FAU zeolite at 300 K, the pore occupancies for each host, calculated using eq (S28) are below as function of the corresponding surface potential Φ.

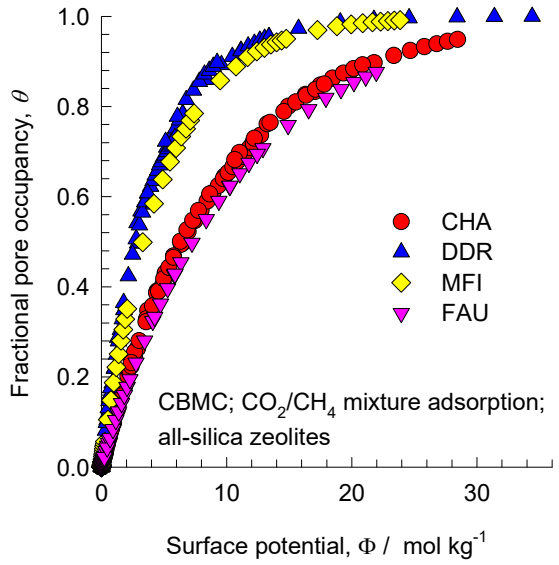

We note that for all four hosts, the pore occupancy $\theta \to 1$ as $\Phi >> 30$ mol kg^{-1}.

5 The Real Adsorbed Solution Theory (RAST)

To quantify non-ideality effects in mixture adsorption, we introduce activity coefficients γ_i into eq (S4) as [15, 41, 48]

$$f_i = P_i^0 x_i \gamma_i \tag{S31}$$

Following the approaches of Myers, Talu, and Siperstein[42, 43, 55] we model the excess Gibbs free energy for n-component mixtures adsorption as follows

$$G^{ex}/RT = \sum_{i=1}^{n} x_i \ln(\gamma_i) \tag{S32}$$

For calculation of the total mixture loading $q_t = q_1 + q_2$ we need to replace eq (S11) by

$$\frac{1}{q_t} = \frac{x_1}{q_1^0(P_1^0)} + \frac{x_2}{q_2^0(P_2^0)} + \left(\frac{1}{q_t}\right)^{ex} \tag{S33}$$

The excess reciprocal loading for the mixture can be related to the partial derivative of the Gibbs free energy with respect to the surface potential at constant composition

$$\left(\frac{1}{q_t}\right)^{ex} = \left.\frac{\partial\left(G^{ex}/RT\right)}{\partial\Phi}\right|_{T,x} \tag{S34}$$

Models such as those of Margules, Wilson, and NRTL may be used for quantifying the dependence of the activity coefficients on the composition of the adsorbed mixture and the pore occupancy θ.

5.1 Margules model for activity coefficients

The Margules model for activity coefficients in binary liquid mixtures needs to be modified to include the influence of the pore occupancy on the activity coefficients

$$\begin{aligned} \ln(\gamma_1) &= x_2^2\left(A_{12} + 2\left(A_{21} - A_{12}\right)x_1\right)\theta \\ \ln(\gamma_2) &= x_1^2\left(A_{21} + 2\left(A_{12} - A_{21}\right)x_2\right)\theta \end{aligned} \tag{S35}$$

The introduction of the multiplier θ will ensure that the activity coefficients tend to unity at vanishingly small pore occupancies $\gamma_i \to 1; \quad \theta \to 0$. In view of eq (S28)

$$\begin{aligned} \ln(\gamma_1) &= x_2^2\left(A_{12} + 2\left(A_{21} - A_{12}\right)x_1\right)\left(1 - \exp\left(-\frac{\Phi}{q_{sat,mix}}\right)\right) \\ \ln(\gamma_2) &= x_1^2\left(A_{21} + 2\left(A_{12} - A_{21}\right)x_2\right)\left(1 - \exp\left(-\frac{\Phi}{q_{sat,mix}}\right)\right) \end{aligned} \tag{S36}$$

where the saturation capacity of the mixture $q_{sat,mix}$ is calculated using eq (S29):

$$q_{sat,mix} = \frac{1}{\frac{x_1}{q_{1,sat}} + \frac{x_2}{q_{2,sat}}}; \quad q_{i,sat} = q_{i,A,sat} + q_{i,B,sat}; \quad i = 1,2.$$

From eq (S28), we note that the expression for the fractional pore occupancy is $\theta = 1 - \exp\left(-\frac{\Phi}{q_{sat,mix}}\right)$.

We should therefore expect that the factor *C* may well be identified with the inverse of the saturation capacity of the binary mixture $q_{sat,mix} = \frac{1}{\frac{x_1}{q_{1,sat}} + \frac{x_2}{q_{2,sat}}}$. One approach is to estimate C by assuming

$C = \frac{x_1}{q_{1,sat}} + \frac{x_2}{q_{2,sat}}$, assuming, say, $x_1 = x_2 = 0.5$.

The Margules model we use in the RAST calculations is

$$\begin{aligned} \ln(\gamma_1) &= x_2^2\left(A_{12} + 2\left(A_{21} - A_{12}\right)x_1\right)\left(1 - \exp\left(-C\Phi\right)\right) \\ \ln(\gamma_2) &= x_1^2\left(A_{21} + 2\left(A_{12} - A_{21}\right)x_2\right)\left(1 - \exp\left(-C\Phi\right)\right) \end{aligned} \tag{S37}$$

In eq (S37) *C* is a constant with the units kg mol^{-1}. The introduction of $\left(1 - \exp\left(-C\Phi\right)\right)$ imparts the correct limiting behaviors $\Phi \to 0; \quad \theta \to 0; \quad \gamma_i \to 1$ for the activity coefficients in the Henry regime, $f_t \to 0; \quad \Phi \to 0$, as the pore occupancy tends to vanishingly small values. As pore saturation conditions are approached, this correction factor tends to unity: $\left(1 - \exp\left(-C\Phi\right)\right) \to 1$. The Margules coefficients A_{12}, A_{21} may assume either positive or negative values. The choice of $A_{12} = A_{21} = 0$ in eq (S37), yields

unity values for the activity coefficients. We note, in passing, that this correction factor $\left(1-\exp\left(-C\Phi\right)\right)$ is often ignored in the RAST implementations in some published works.[56-59]

Krishna and van Baten[17] have established the need for inclusion of the correction factor $\left(1-\exp\left(-C\Phi\right)\right)$ in the RAST modelling of CO_2/H_2O mixture adsorption in CALF-20. Watch the presentations titled **Thermodynamic Non-Idealities for Mixture Adsorption in CALF-20** on YouTube https://www.youtube.com/@rajamanikrishna250/videos

For calculation of the total mixture loading $q_t = q_1 + q_2$ we need to replace eq (S11) by

$$\frac{1}{q_t} = \frac{x_1}{q_1^0(P_1^0)} + \frac{x_2}{q_2^0(P_2^0)} + x_1 x_2 \left[A_{12}x_2 + A_{21}x_1\right] C\exp\left(-C\Phi\right) \tag{S38}$$

5.2 Wilson model for activity coefficients

The Wilson model for activity coefficients are given for binary mixtures by

$$\begin{aligned}
\ln(\gamma_1) &= \left(1-\ln(x_1\Lambda_{11}+x_2\Lambda_{12}) - \frac{x_1\Lambda_{11}}{x_1\Lambda_{11}+x_2\Lambda_{12}} - \frac{x_2\Lambda_{21}}{x_2+x_1\Lambda_{21}}\right)\left(1-\exp\left(-C\Phi\right)\right) \\
\ln(\gamma_2) &= \left(1-\ln(x_1\Lambda_{21}+x_2\Lambda_{22}) - \frac{x_1\Lambda_{12}}{x_1\Lambda_{11}+x_2\Lambda_{12}} - \frac{x_2\Lambda_{22}}{x_1\Lambda_{21}+x_2\Lambda_{22}}\right)\left(1-\exp\left(-C\Phi\right)\right)
\end{aligned} \tag{S39}$$

In eq (S39), $\Lambda_{11} \equiv 1$; $\Lambda_{22} \equiv 1$, and C is a constant with the units kg mol^{-1}. The choice of $\Lambda_{12} = \Lambda_{21} = 1$ in eq (S39), yields unity values for the activity coefficients.

The excess reciprocal loading for the mixture can be related to the partial derivative of the Gibbs free energy with respect to the surface potential at constant composition

$$\left(\frac{1}{q_t}\right)^{ex} = \left.\frac{\partial\left(G^{ex}/RT\right)}{\partial\Phi}\right|_{T,x} = \left[-x_1\ln(x_1+x_2\Lambda_{12}) - x_2\ln\left(x_2+x_1\Lambda_{21}\right)\right] C\exp\left(-C\Phi\right) \tag{S40}$$

For calculation of the total mixture loading we need to replace Eq (S11) by

$$\frac{1}{q_t} = \frac{x_1}{q_1^0(P_1^0)} + \frac{x_2}{q_2^0(P_2^0)} + \left[-x_1\ln(x_1+x_2\Lambda_{12}) - x_2\ln\left(x_2+x_1\Lambda_{21}\right)\right] C\exp\left(-C\Phi\right) \tag{S41}$$

The parameters C; Λ_{12}; Λ_{21} are fitted to match the experimental or CBMC data on mixture adsorption.

The extension of eq (S39) to multicomponent mixtures is

$$\ln(\gamma_i) = \left(1 - \ln\left(\sum_{j=1}^{n} x_j \Lambda_{ij} \right) - \sum_{k=1}^{n} x_k \frac{\Lambda_{ki}}{\sum_{l=1}^{n} x_l \Lambda_{kl}} \right) \left(1 - \exp\left(-C\Phi\right)\right); \quad \Lambda_{ii} \equiv 1; \qquad i = 1, 2, ...n \tag{S42}$$

Our approach for ternary mixtures is to estimate C as $C = \frac{x_1}{q_{1,sat}} + \frac{x_2}{q_{2,sat}} + \frac{x_3}{q_{3,sat}}$, assuming, $x_1 = x_2 = x_3 = 1/3$.

5.3 NRTL model for activity coefficients in binary mixtures

The NRTL model for activity coefficients are given for binary mixtures by

$$\begin{aligned} \ln(\gamma_1) &= x_2^2 \left(\tau_{21} \left(\frac{G_{21}}{x_1 + x_2 G_{21}} \right)^2 + \frac{\tau_{12} G_{12}}{\left(x_2 + x_1 G_{12}\right)^2} \right) \left(1 - \exp\left(-C\Phi\right)\right) \\ \ln(\gamma_2) &= x_1^2 \left(\tau_{12} \left(\frac{G_{12}}{x_2 + x_1 G_{12}} \right)^2 + \frac{\tau_{21} G_{21}}{\left(x_1 + x_2 G_{21}\right)^2} \right) \left(1 - \exp\left(-C\Phi\right)\right) \\ G_{12} &= \exp\left(-\alpha_{12}\tau_{12}\right); \quad G_{21} = \exp\left(-\alpha_{21}\tau_{21}\right); \quad \alpha_{12} = \alpha_{21} \end{aligned} \tag{S43}$$

In eq (S43) C is a constant with the units kg mol^{-1}. The choice of $\tau_{12} = \tau_{21} = 0$ in eq (S43), yields unity values for the activity coefficients.

The extension of eq (S43) to n-component mixtures is

$$\ln(\gamma_i) = \left[\frac{\sum_{j=1}^{n} x_j \tau_{ji} G_{ji}}{\sum_{k=1}^{n} x_k G_{ki}} + \sum_{j=1}^{n} \frac{x_j G_{ij}}{\sum_{k=1}^{n} x_k G_{kj}} \left(\tau_{ij} - \frac{\sum_{l=1}^{n} x_l \tau_{lj} G_{lj}}{\sum_{k=1}^{n} x_k G_{kj}} \right) \right] \left(1 - \exp\left(-C\Phi\right)\right) \tag{S44}$$

$$G_{ij} = \exp\left(-\alpha_{ij}\tau_{ij}\right); \quad \alpha_{ij} = \alpha_{ji}; \quad \tau_{ii} = 0; \quad G_{ii} = 1$$

Our approach for ternary mixtures is to estimate C as $C = \frac{x_1}{q_{1,sat}} + \frac{x_2}{q_{2,sat}} + \frac{x_3}{q_{3,sat}}$, assuming, $x_1 = x_2 = x_3 = 1/3$.

For further details of the RAST calculations and the need for inclusion of the $\left(1-\exp\left(-C\Phi\right)\right)$ correction factor watch the presentations titled **Dependence of Adsorption Selectivity on Mixture Composition, Hydrogen Bonding Influences on Adsorption, How Reliable is the IAST?, The Real Adsorbed Solution Theory, Co-operative Mixture Adsorption in Zeolites & MOFs, Azeotropic Adsorption, What is Azeotropic Adsorption, Water/Alcohol Azeotropic Adsorption, Segregation and Congregation Effects in CO_2 capture, Thermodynamic Non-Idealities for Mixture Adsorption in CALF-20** on YouTube https://www.youtube.com/@rajamanikrishna250/videos

With the introduction of activity coefficients, the expression for the adsorption selectivity for the *i*-*j* pair in an *n*-component mixture is

$$S_{ads,ij} = \frac{q_i/q_j}{f_i/f_j} = \frac{x_i/x_j}{f_i/f_j} = \frac{P_j^0\gamma_j}{P_i^0\gamma_i} \tag{S45}$$

Since the activity coefficients are composition dependent, the adsorption selectivity is also composition dependent, and S_{ads} is not uniquely related to the surface potential, Φ.

6 CBMC simulation campaigns

A comprehensive campaign of CBMC simulations for adsorption of ternary $CO_2/CH_4/N_2$, $CO_2/CH_4/C_3H_8$, $CO_2/CH_4/H_2$, and water/methanol/ethanol mixtures in NaX, LTA-4A, CHA, and DDR zeolites. In these ternary mixture the bulk fluid phase composition held constant at constant composition. Also, CBMC simulations of the constituent binary mixtures were conducted. Two different campaigns were conducted.

Campaign A. The bulk fluid phase composition held constant at a fixed composition $y_1 = 1 - y_2$, and the bulk fluid phase fugacity $f_t = f_1 + f_2$ was varied over a wide range from the Henry regime of adsorption, $\Phi \to 0$, to pore saturation conditions, typically $\Phi > 30$.

Campaign B. The bulk fluid phase fugacity $f_t = f_1 + f_2$ was held at a constant value of 10 kPa, and the bulk fluid phase mixture composition y_1 was varied $0 < y_1 < 1$.

Each CBMC simulation data point, with specified partial fugacities in the bulk fluid phase, f_1, f_2, yields the component loadings, $q_{1,CBMC}; q_{2,CBMC}$, and the total mixture loading $q_{t,CBMC} = q_{1,CBMC} + q_{2,CBMC}$.

For each guest/host combination, CBMC simulations of the unary isotherms of the constituent guest molecules were also carried out.

For each CBMC mixture simulation campaign (Campaign A, or Campaign B), the mole fractions of the adsorbed phase, $x_1 = \frac{q_{1,CBMC}}{q_{t,CBMC}}; x_2 = \frac{q_{2,CBMC}}{q_{t,CBMC}}; q_{t,CBMC} = q_{1,CBMC} + q_{2,CBMC}$ are determined. The sorption pressures P_1^0, P_2^0, each of which satisfying eq (S6), can be determined from using the unary isotherm fits for each of the components in the binary mixture.

The activity coefficients of the two components $\gamma_{1,CBMC}; \gamma_{2,CBMC}$ are determined from eq (S31):

$$\gamma_{1,CBMC} = \frac{f_1}{P_1^0 x_{1,CBMC}}; \gamma_{2,CBMC} = \frac{f_2}{P_2^0 x_{2,CBMC}} \tag{S46}$$

The activity coefficients of the two components $\gamma_{1,CBMC}; \gamma_{2,CBMC}$, determined using eq (S46) are subject to a degree of scatter that is inherent in the CBMC mixture simulation data.

For each mixture/host combination, the set of three Wilson parameters $C; \quad \Lambda_{12}; \quad \Lambda_{21}$ that yield the minimum value for the objective function calculated as the sum of the mean-squared deviations between the CBMC simulated component loadings, and those predicted using RAST

$$\text{Objective Function} = \sum \left[\left(q_{1,CBMC} - q_{1,RAST} \right)^2 + \left(q_{2,CBMC} - q_{2,RAST} \right)^2 \right] \tag{S47}$$

The $C; \quad \Lambda_{12}; \quad \Lambda_{21}$ were determined using the Excel solver function.

An analogous procedure is employed to determine NRTL and Margules parameters.

7 Mixture adsorption in all-silica CHA zeolite

CHA zeolite consists of cages of volume 316 $Å^3$, separated by 3.8 Å × 4.2 Å 8-ring windows; the pore landscape and structural details are provided in Figure S7, and Figure S8. SAPO-34 has the same structural topology of CHA zeolite.

7.1 CO_2/CH_4 mixture adsorption in all-silica CHA zeolite

A key assumption of the IAST is that the composition of the adsorbed phase is homogeneously and uniformly distributed within zeolite or metal-organic frameworks. Preferential location of molecules at certain locations within the crystalline, causes segregated adsorption and deviations from the assumption of homogeneous distribution. For separation of CO_2 from gaseous mixtures with CH_4, cage-type zeolites such as CHA, DDR, LTA, and ERI are of practical interest; these materials consist of cages separated by narrow windows, in the 3.3 – 4.5 Å range. For adsorption of CO_2/CH_4 mixtures, CBMC simulations[60] show that the window regions of cage-type zeolites has a significantly higher proportion of CO_2 than within the cages; see computational snapshots in Figure S13 for CHA zeolite.

To demonstrate non-ideality effects in mixture adsorption, three different sets of CBMC campaigns were conducted.

Three different campaigns were carried out for CBMC simulations of CO_2/CH_4 mixture adsorption in CHA zeolite at 300 K. In campaign A, the mole fraction of CO_2(1) in the bulk gas phase is held constant (at two different values $y_1 = 0.15$, and $y_1 = 0.5$) and the bulk gas phase fugacity $f_t = f_1 + f_2$ was varied. In campaign B, the mole fraction of CO_2(1) in the bulk gas phase, y_1 was varied from 0 to 1, keeping the bulk gas phase mixture fugacity $f_t = f_1 + f_2$ constant at a value of 1 MPa. The CBMC results of these campaigns are presented in Figure S14.

Figure S14c,e compares CBMC data on adsorption selectivity, $S_{ads} = \frac{q_1/q_2}{f_1/f_2}$, compared with IAST estimates indicated by the dashed lines. We note that IAST severely overestimates S_{ads} for all campaigns. The IAST anticipates S_{ads} depends only on the surface potential Φ; this expectation is not fulfilled for any campaign. In Figure S14c, the CBMC simulated values of the adsorption selectivity S_{ads} are plotted as function of the surface potential Φ. At values of $\Phi > 10$ mol kg^{-1}, corresponding to a pore occupancy $\theta > 0.7$, the IAST significantly overestimates S_{ads}.

The continuous solid lines in Figure S14b,c,d,e,f,g,h,i are the RAST calculations using fitted Wilson parameters as specified in Table S6. For the Wilson fits, we calculate the parameter C using $C = \frac{1}{\frac{x_1}{q_{1,sat}} + \frac{x_2}{q_{2,sat}}}$; $q_{i,sat} = q_{i,A,sat} + q_{i,B,sat}$; $i = 1,2$, with the arbitrary assumption that $x_1 = x_2 = 0.5$.

Figure S14f,g,i plot the activity coefficients of the guest components in the adsorbed phase as function of (g) mole fraction of CO_2(1) in the adsorbed phase for campaign B, x_1, and (f, i) the surface potential Φ for campaigns A. For campaign B, we note the limiting behaviors $x_i \to 1$; $\gamma_i \to 1$. For campaigns A we note that the activity coefficients are also dependent the surface potential Φ with the limiting characteristic $\Phi \to 0$; $\gamma_1 \to 1$; $\gamma_2 \to 1$. The introduction of $\left(1 - \exp\left(-C\Phi\right)\right)$ in the Wilson model, eq (S39), imparts the correct limiting behaviors $\Phi \to 0$; $\theta \to 0$; $\gamma_i \to 1$ for the activity coefficients in the Henry regime, $f_t \to 0$; $\Phi \to 0$, as the pore occupancy tends to vanishingly small values. As pore saturation conditions are approached, this correction factor tends to unity: $\left(1 - \exp\left(-C\Phi\right)\right) \to 1$.

The CBMC data in Figure S14 lead us to conclude that the activity coefficients are functions of both Φ and x_1. In Figure S15a the CBMC data for the excess Gibbs free energy $G^{ex}/RT = x_1 \ln\left(\gamma_1\right) + x_2 \ln\left(\gamma_2\right)$ for the aforementioned CBMC campaigns, along with an additional CBMC campaign A (with $y_1 = 0.2$), are plotted in 3D space as function of Φ and x_1. The entire CBMC

data set resides on a 3D surface mesh determined from the fitted Wilson parameters in Table S6; see Figure S15.

In Figure S15b the CBMC data on the CO_2/CH_4 adsorption selectivity are plotted in 3D space as function of the surface potential Φ and the mole fraction of CO_2 in the bulk gas phase, y_1. The entire CBMC data set resides on a 3D surface mesh determined from the fitted Wilson parameters in Table S6. Figure S15b confirms that the adsorption selectivity is not uniquely determined by the surface potential, Φ, but is additionally dependent on the bulk phase mixture composition.

7.2 CO_2/N_2 and CO_2/H_2 mixture adsorption in all-silica CHA zeolite

Figure S16a,b presents the CBMC data for adsorption selectivity of CO_2/N_2 and CO_2/H_2 mixtures in CHA zeolite, both for Campaigns A with fixed values of the bulk gas mixture compositions, y_1. The IAST selectivities are not in perfect agreement with the CBMC data. Thermodynamic non-ideality effects, quantified with fitted Wilson parameters in Table S6, allow better agreement with the CBMC data on S_{ads}.

Figure S16c,d presents the CBMC data for adsorption selectivity of CO_2/N_2 and CO_2/H_2 mixtures in CHA zeolite as 3D plots as function of the surface potential Φ and the mole fraction of CO_2 in the bulk gas phase, y_1. The entire CBMC data set resides on a 3D surface mesh determined from the fitted Wilson parameters in Table S6.

7.3 CH_4/N_2 and CH_4/H_2 mixture adsorption in all-silica CHA zeolite

Figure S17a,b present CBMC data for component loadings for (a) CH_4/N_2 and (b) CH_4/H_2 mixtures in CHA zeolite, both for Campaign A with $y_1 = 0.5$. The dashed lines are IAST estimates; the unary isotherm parameters are specified in Table S6. The IAST estimates are in reasonable agreement with IAST estimates, indicating that non-ideality effects are of minor importance.

7.4 $CO_2/CH_4/N_2$ mixture adsorption in CHA zeolite

CBMC simulations were carried out for ternary 20/40/40 $CO_2/CH_4/N_2$ mixtures in CHA at 300 K for a range of total fugacities, $f_t = f_1 + f_2 + f_3$. In Figure S18a,b,c the component loadings from CBMC are compared with IAST and RAST estimates. The Wilson parameters for the binary pairs $\Lambda_{12}, \Lambda_{21}, \Lambda_{13}, \Lambda_{31}, \Lambda_{23}, \Lambda_{32}$ are taken to the same as for the corresponding binary pairs as listed in Table S6. Since the binary CH_4/N_2 mixtures behave ideally (cf. Figure S17a), we assert $\Lambda_{23} = 1; \Lambda_{32} = 1$. Our approach for ternary mixtures is to estimate C as $C = \frac{x_1}{q_{1,sat}} + \frac{x_2}{q_{2,sat}} + \frac{x_3}{q_{3,sat}}$, assuming, $x_1 = x_2 = x_3 = 1/3$. The RAST estimates are in good agreement with the ternary CBMC data. Figure S18d plots the activity coefficients $\gamma_1, \gamma_2, \gamma_3$ as function of the surface potential Φ. There is good agreement between the CBMC data on $\gamma_1, \gamma_2, \gamma_3$ with RAST calculations.

In Figure S19 the excess Gibbs free energy $G^{ex}/RT = \sum_{i=1}^{n} x_i \ln(\gamma_i)$ determined from CBMC data for 20/40/40 $CO_2/CH_4/N_2$ mixtures in CHA are plotted in 3D space as function of Φ and x_1. The continuous solid line represents the ternary RAST Wilson calculations. The agreement is good, validating the ternary RAST Wilson model.

7.5 $CO_2/CH_4/H_2$ mixture adsorption in CHA zeolite

CBMC simulations were carried out for ternary 10/20/70 $CO_2/CH_4/H_2$ mixtures in CHA at 300 K for a range of total fugacities, f_t. In Figure S20a,b,c the component loadings from CBMC are compared with IAST and RAST estimates. The Wilson parameters for the binary pairs $\Lambda_{12}, \Lambda_{21}, \Lambda_{13}, \Lambda_{31}, \Lambda_{23}, \Lambda_{32}$ are taken to be the same as for the corresponding binary pairs as listed in Table S6. Since the binary CH_4/H_2 mixtures behave ideally (cf. Figure S17b), we assert $\Lambda_{23} = 1; \Lambda_{32} = 1$. Our approach for ternary mixtures is to estimate C as $C = \frac{x_1}{q_{1,sat}} + \frac{x_2}{q_{2,sat}} + \frac{x_3}{q_{3,sat}}$, assuming, $x_1 = x_2 = x_3 = 1/3$. The RAST estimates are in good

agreement with the ternary CBMC data. Figure S20d plots the activity coefficients as function of the surface potential.

In Figure S21 the excess Gibbs free energy $G^{ex}/RT = \sum_{i=1}^{n} x_i \ln(\gamma_i)$ determined from CBMC data for 10/20/70 $CO_2/CH_4/H_2$ mixtures in CHA at 300 K are plotted in 3D space as function of Φ and x_1. The continuous solid line represents the ternary RAST Wilson calculations. The agreement is good, validating the ternary RAST Wilson model.

7.6 Water/methanol/ethanol mixture adsorption in CHA zeolite

For adsorption of water(1)/ethanol(2) mixtures in CHA zeolite at 300 K, three different CBMC simulations were carried out: Campaign A (with $y_1 = 0.5$, and $y_1 = 0.05$, vary f_t), and campaign B, the mole fraction of water(1) in the bulk fluid phase, y_1 was varied from 0 to 1, keeping the bulk fluid phase mixture fugacity $f_t = f_1 + f_2$ constant at a value of 10 kPa. The CBMC data on component loadings, adsorption selectivities, and activity coefficients are presented in Figure S22. The dashed lines are the IAST estimates. The failure of the IAST to match the CBMC data presented in Figure S22 is a consequence of hydrogen bonding between guest molecules in water/alcohol mixtures. [15, 18, 47, 48, 60] One of the mandates of the IAST is violated because of the formation of water/alcohol clusters.[15, 46, 48]

In order to demonstrate the occurrence of hydrogen bonding in water/methanol, and water/ethanol mixtures CBMC simulation data on the spatial locations of the guest molecules were sampled to determine the O···H distances of various pairs of molecules. By sampling a total of 10^6 simulation steps, the radial distribution functions (RDF) of O···H distances were determined for water-water, water-alcohol, and alcohol-alcohol pairs.

Figure S23a shows the RDF of O…H distances for molecular pairs of water(1)/methanol(2) mixture adsorption in CHA zeolite at 300 K. The partial fugacities of components 1 and 2 are f_1= 2.5 kPa, f_2= 7.5 kPa. We note the first peaks in the RDFs occur at a distance less than 2 Å, that is characteristic of hydrogen bonding.[27, 61] The heights of the first peaks are a direct reflection of the degree of hydrogen bonding

between the molecular pairs. We may conclude, therefore that for water/methanol mixtures the degree of H-bonding between water-methanol pairs is significantly larger, by about an order of magnitude, than for water-water, and methanol-methanol pairs. Analogous set of conclusions can be drawn for water/ethanol mixtures, for which the RDF data are presented in Figure S23b, i.e. the degree of H-bonding between water-ethanol pairs is larger than for water-water, and ethanol-ethanol pairs. For comparison purposes, the RDF data for adsorption of methanol/ethanol mixtures are shown in Figure S23c. The magnitude of the first peaks for methanol-ethanol, methanol-methanol, ethanol-ethanol pairs are significantly lower than the water-alcohol peaks in Figure S23a,b. Therefore, the H-bonding effects should be expected to be of less importance for methanol/ethanol mixture adsorption in CHA than for water/methanol and water/ethanol mixtures.

A visual appreciation of hydrogen bonding is gleaned from the snapshots in Figure S24 for mixture adsorption in CHA.

The continuous solid lines in Figure S22 are the RAST calculations with fitted NRTL parameters specified in Table S7.

The CBMC data in Figure S22f,g,i lead us to conclude that the activity coefficients are functions of both Φ and x_1. In Figure S25a, the CBMC data for the excess Gibbs free energy $G^{ex}/RT = x_1 \ln(\gamma_1) + x_2 \ln(\gamma_2)$ for the aforementioned CBMC campaigns for water/ethanol mixtures are plotted in 3D space as function of surface potential Φ and mole fraction of water in the adsorbed phase mixture, x_1. The entire CBMC data set on G^{ex}/RT resides on a 3D surface mesh determined from the fitted NRTL parameters specified in Table S7.

In Figure S25b, the CBMC data for the water/ethanol adsorption selectivity for water/ethanol mixtures are plotted in 3D space as function of surface potential Φ and mole fraction of water in the bulk fluid phase mixture. y_1. The entire CBMC data set on S_{ads} resides on a 3D surface mesh determined from the fitted NRTL parameters specified in Table S7. Figure S25b confirms that the adsorption selectivity is not

uniquely determined by the surface potential, Φ, but is additionally dependent on the bulk phase mixture composition.

Analogously, in Figure S26a, the CBMC data for the excess Gibbs free energy $\frac{G^{ex}}{RT} = x_1 \ln(\gamma_1) + x_2 \ln(\gamma_2)$ for the three different CBMC campaigns for water/methanol mixtures are plotted in 3D space as function of Φ and mole fraction of water in the adsorbed phase mixture, x_1. The The entire CBMC data set resides on a 3D surface mesh determined from the fitted NRTL parameters specified in Table S7.

In Figure S26b, the CBMC data for the water/methanol adsorption selectivity for water/methanol mixtures are plotted in 3D space as function of surface potential Φ and mole fraction of water in the bulk fluid phase mixture. y_1. The entire CBMC data set on S_{ads} resides on a 3D surface mesh determined from the fitted NRTL parameters specified in Table S7. Figure S26b confirms that the adsorption selectivity is not uniquely determined by the surface potential, Φ, but is additionally dependent on the bulk phase mixture composition.

In Figure S27a the CBMC data for the excess Gibbs free energy $G^{ex}/RT = x_1 \ln(\gamma_1) + x_2 \ln(\gamma_2)$ for CBMC campaign for methanol/ethanol mixtures in CHA are plotted in 3D space as function of the surface potential Φ and mole fraction of water in the adsorbed phase mixture, x_1. The entire CBMC data set resides on a 3D surface mesh determined from the fitted NRTL parameters specified in Table S7.

In Figure S27b, the CBMC data for the methanol/ethanol adsorption selectivity for methanol/ethanol mixtures are plotted in 3D space as function of surface potential Φ and mole fraction of methanol in the bulk fluid phase mixture. y_1. The entire CBMC data set on S_{ads} resides on a 3D surface mesh determined from the fitted NRTL parameters specified in Table S7. Figure S27b confirms that the adsorption selectivity is not uniquely determined by the surface potential, Φ, but is additionally dependent on the bulk phase mixture composition.

Figure S28a,b,c presents CBMC simulations of component loadings, q_i, for equimolar $f_1 = f_2 = f_3$ water(1)/methanol(2)/ethanol(3) mixture adsorption in CHA zeolite with varying total fugacity $f_t = f_1 + f_2 + f_3$, plotted as a function of the surface potential Φ. The component activity coefficients are plotted in Figure S28d. The dashed lines in Figure S28 are IAST estimates; the continuous solid lines are RAST calculations The continuous solid lines in Figure S28 are RAST calculations using eq (S44). In these calculations the NRTL parameters $\tau_{12}, \tau_{21}, \alpha_{12}, \tau_{13}, \tau_{31}, \alpha_{13}, \tau_{23}, \tau_{32}, \alpha_{23}$ are taken to the same as for the corresponding binary pairs as listed in Table S7. Our approach for ternary mixtures is to estimate *C* as $C = \frac{x_1}{q_{1,sat}} + \frac{x_2}{q_{2,sat}} + \frac{x_3}{q_{3,sat}}$, assuming, $x_1 = x_2 = x_3 = 1/3$. The RAST calculations are in reasonable agreement with CBMC data.

In Figure S29 the excess Gibbs free energy $G^{ex}/RT = \sum_{i=1}^{n} x_i \ln(\gamma_i)$ determined from CBMC data for equimolar $f_1 = f_2 = f_3$ water(1)/methanol(2)/ethanol(3) mixture adsorption in CHA zeolite are plotted in 3D space as function of Φ and x_1. The continuous solid line represents the ternary RAST NRTL calculations. The agreement is good, validating the ternary RAST NRTL model.

7.7 List of Tables for Mixture adsorption in all-silica CHA zeolite

Table S6. Dual-site Langmuir-Freundlich parameters for guest molecules in CHA (all-silica) at 300 K.

	Site A			Site B		
	$\frac{q_{A,sat}}{\text{mol kg}^{-1}}$	$\frac{b_A}{\text{Pa}^{-\nu_A}}$	ν_A	$\frac{q_{B,sat}}{\text{mol kg}^{-1}}$	$\frac{b_B}{\text{Pa}^{-\nu_B}}$	ν_B
CO_2	6.8	2.446E-06	1.06	2.8	5.181E-06	0.7
CH_4	2.7	1.313E-06	1.02	5.5	2.703E-07	0.84
N_2	5.1	1.019E-07	0.88	2.9	4.013E-07	1
H_2	14.563	2.58E-08	0.73	15.719	1.57E-08	1

Fitted Wilson non-ideality parameters for mixture adsorption in CHA at 300 K.

	C / kg mol^{-1}	Λ_{12}	Λ_{12}
CO_2/CH_4	0.113	3.300	0.111
CO_2/N_2	0.115	2.509	0.169
CO_2/H_2	0.069	1.965	0.281
$CO_2/CH_4//N_2$	0.117	$\Lambda_{12}, \Lambda_{21}, \Lambda_{13}, \Lambda_{31}, \Lambda_{23}, \Lambda_{32}$ as above	
$CO_2/CH_4/H_2$	0.0864	$\Lambda_{12}, \Lambda_{21}, \Lambda_{13}, \Lambda_{31}, \Lambda_{23}, \Lambda_{32}$ as above	

Table S7. Dual-site Langmuir-Freundlich parameters for pure component water, methanol, and ethanol in CHA zeolite at 300 K. The fit parameters are based on the CBMC simulations of pure component isotherms presented in earlier works.[48, 62]

	Site A			Site B		
	$\frac{q_{A,sat}}{\text{mol kg}^{-1}}$	$\frac{b_A}{\text{Pa}^{-\nu_A}}$	ν_A	$\frac{q_{B,sat}}{\text{mol kg}^{-1}}$	$\frac{b_B}{\text{Pa}^{-\nu_B}}$	ν_B
water	16.8	3.031E-54	15.6	4.6	2.218E-05	1
methanol	3.7	4.281E-11	3.37	3.7	4.545E-04	1
ethanol	2.5	8.578E-06	1.07	2.9	3.505E-03	1.1

Fitted NRTL non-ideality parameters for binary mixture adsorption at 300 K in CHA zeolite.

	C / kg mol^{-1}	τ_{12}	τ_{21}	α
water/methanol	0.091	-3.529	0.970	0.586
water/ethanol	0.116	-3.674	-0.878	0.275
methanol/ethanol	0.017	-1.314	-2.333	0.010
water/methanol/ethanol	0.122	$\tau_{12},\tau_{21},\alpha_{12},\tau_{13},\tau_{31},\alpha_{13},\tau_{23},\tau_{32},\alpha_{23}$ as above		

7.8 List of Figures for Mixture adsorption in all-silica CHA zeolite

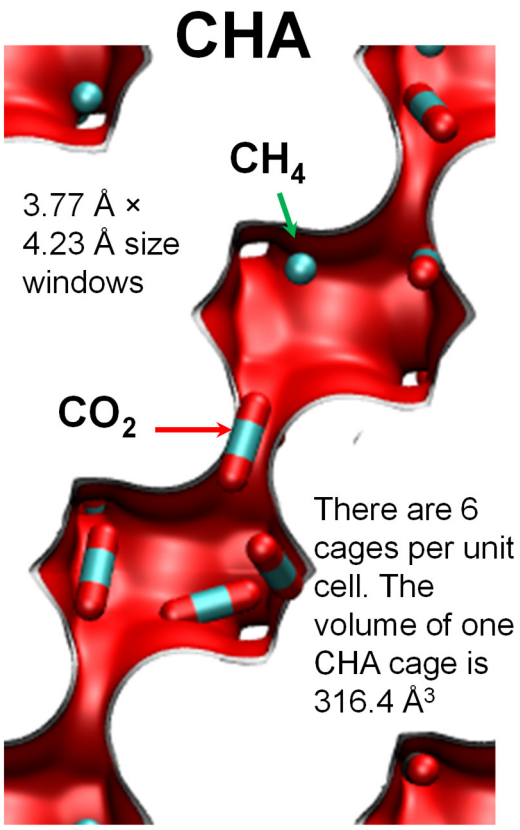

Figure S13. Computational snapshots for CO_2(1)/CH_4(2) mixture adsorption in CHA zeolite at 300 K.

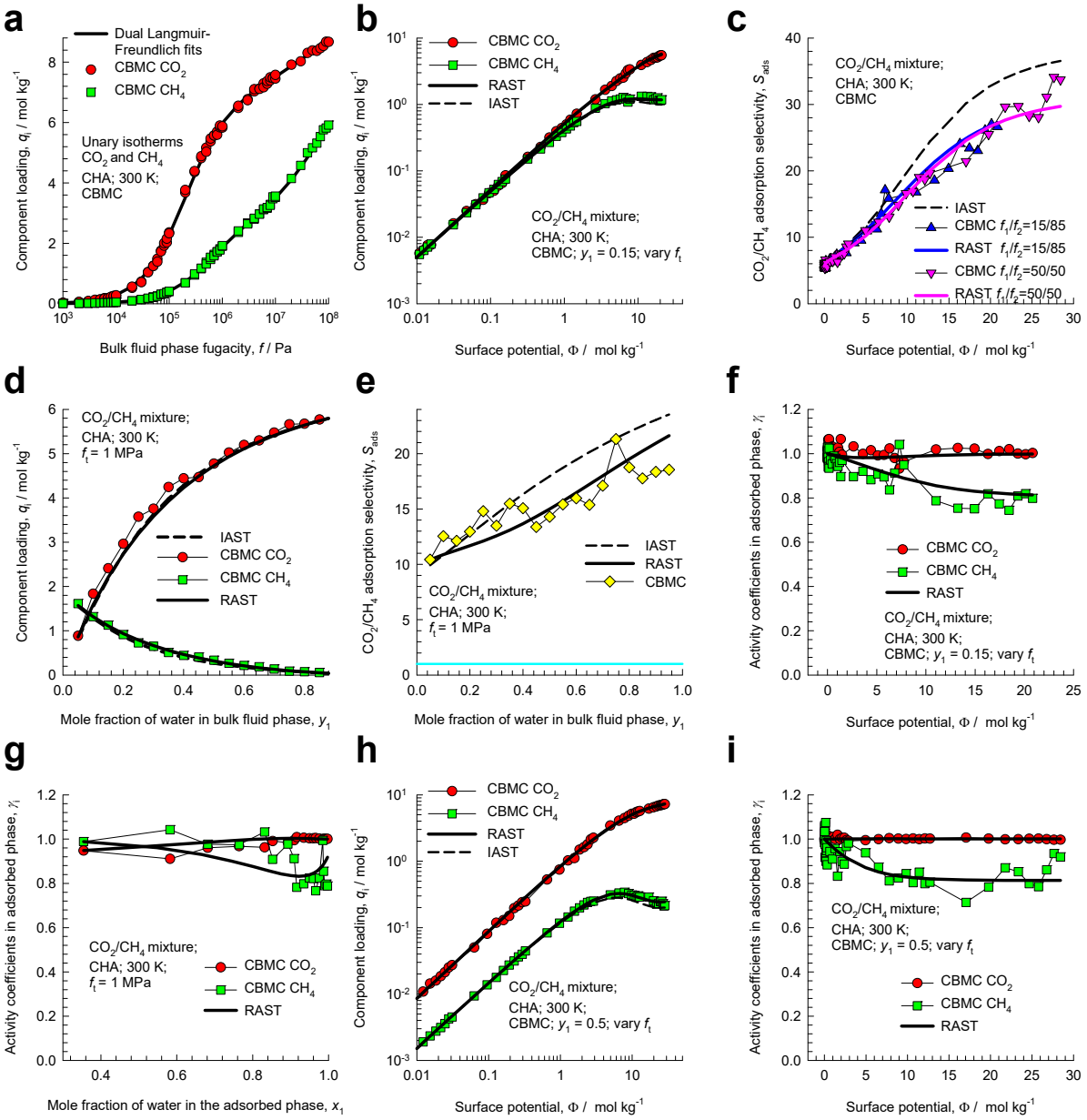

Figure S14. CBMC simulation data and analysis for three different campaigns CO_2(1)/CH_4(2) mixture adsorption in CHA zeolite at 300 K. (a) Unary isotherms and fits. (b, d, h) Component loadings in mixture compared with IAST/RAST estimates. (c, e) CBMC data for CO_2(1)/CH_4(2) adsorption selectivity compared with IAST and RAST estimates. (f, g, i) Activity coefficients from CBMC compared with RAST model calculations. The unary isotherm data fits and Wilson parameters are provided in Table S6.

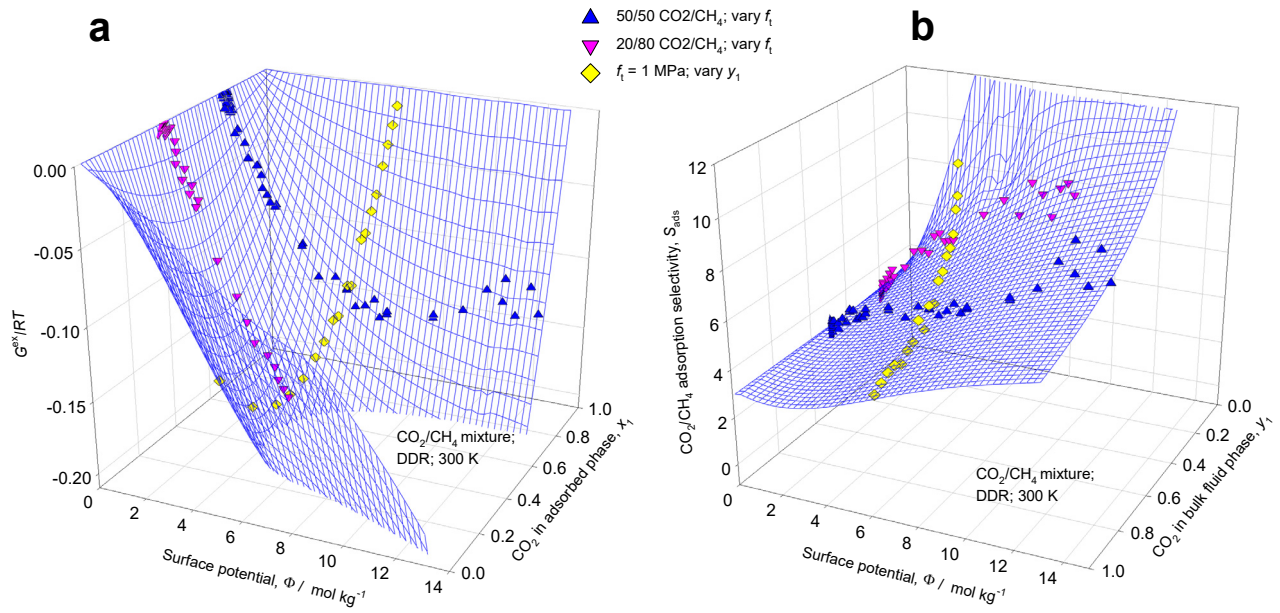

Figure S15. 3D plots of CBMC data on (a) excess Gibbs free energy $G^{ex}/RT = x_1 \ln(\gamma_1) + x_2 \ln(\gamma_2)$ and (b) $CO_2(1)/CH_4(2)$ adsorption selectivity for $CO_2(1)/CH_4(2)$ mixture adsorption in CHA zeolite at 300 K. The 3D mesh is constructed using the Wilson parameters provided in Table S6.

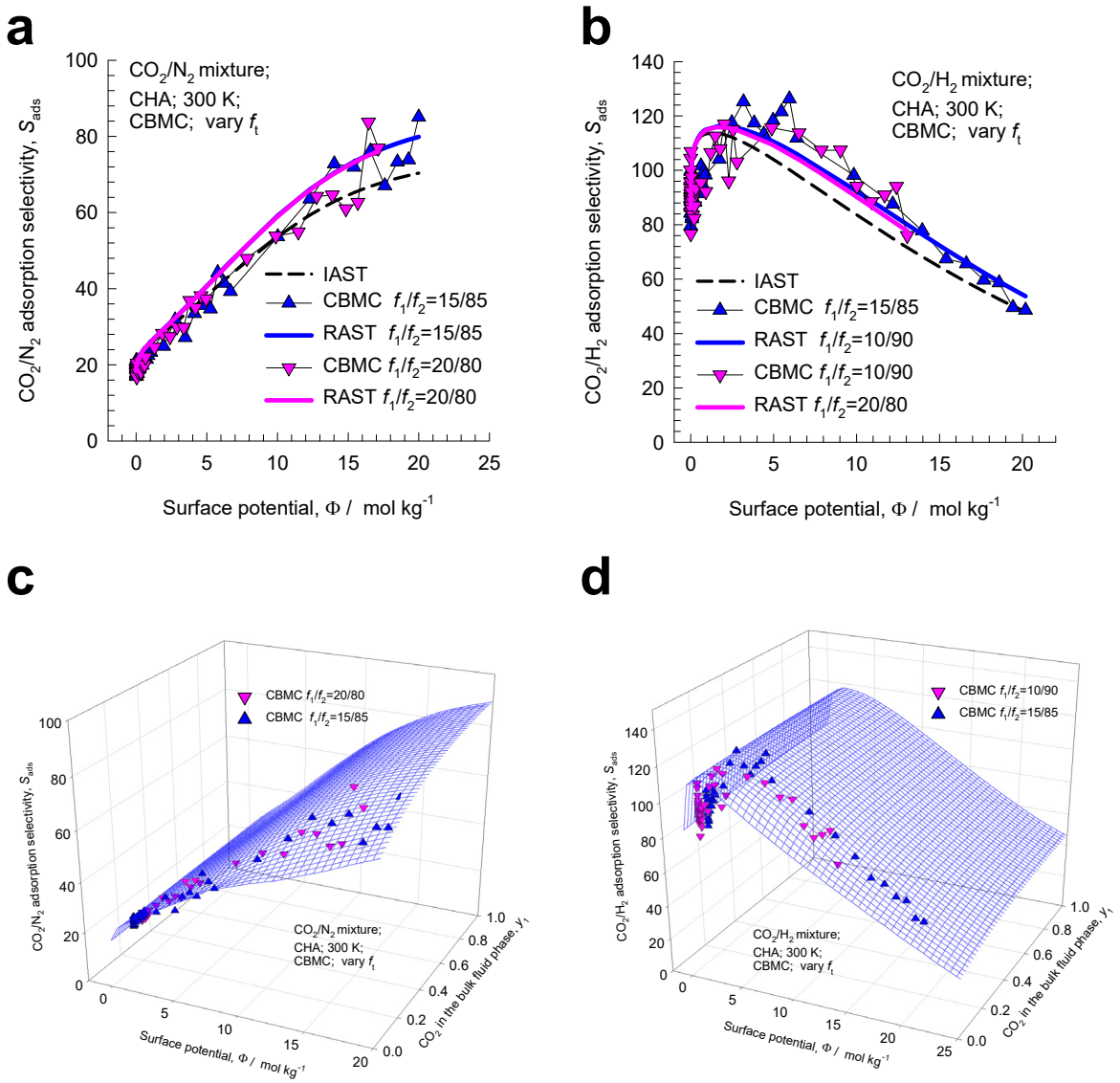

Figure S16, CBMC data for adsorption selectivity of (a, c) CO_2/N_2 and (b, d) CO_2/H_2 mixtures in CHA zeolite, both for Campaign A with fixed values of the bulk phase mixture compositions. The dashed lines are IAST estimates; the continuous solid lines are RAST calculations with fitted Wilson parameters specified in Table S6. (c, d) Adsorption selectivities are plotted in 3D space as function of the surface potential Φ and the mole fraction of CO_2 in the bulk gas phase, y_1. The 3D mesh is constructed using the Wilson parameters provided in Table S6.

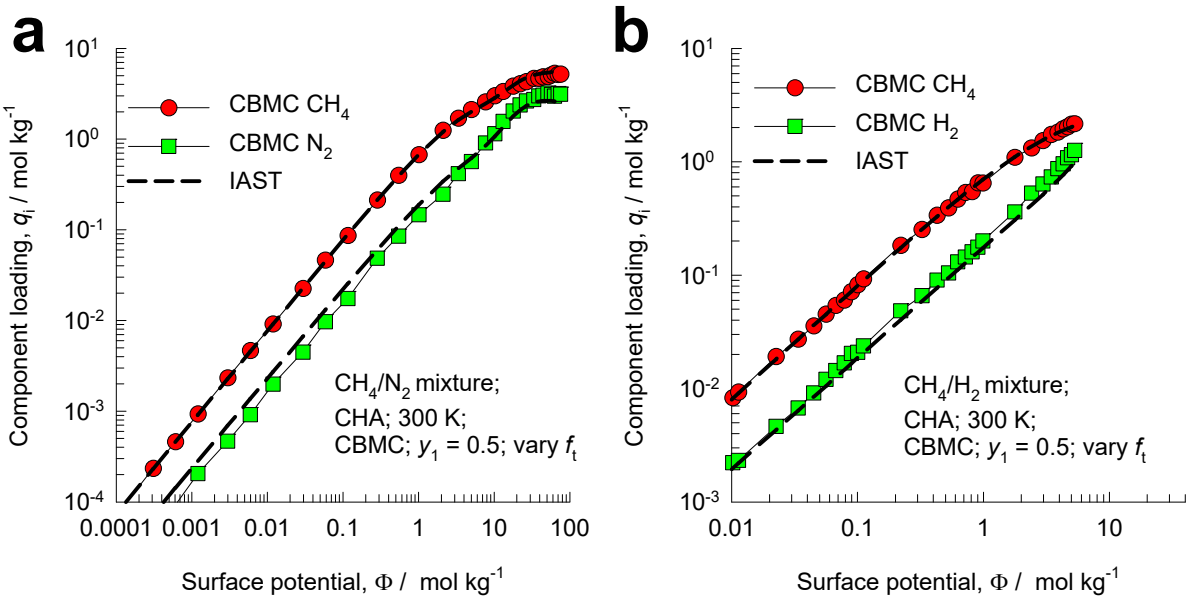

Figure S17, CBMC data for component loadings for (a) CH_4/N_2 and (b) CH_4/H_2 mixtures in CHA zeolite, both for Campaign A with y_1 = 0.5. The dashed lines are IAST estimates; the unary isotherm parameters are specified in Table S6.

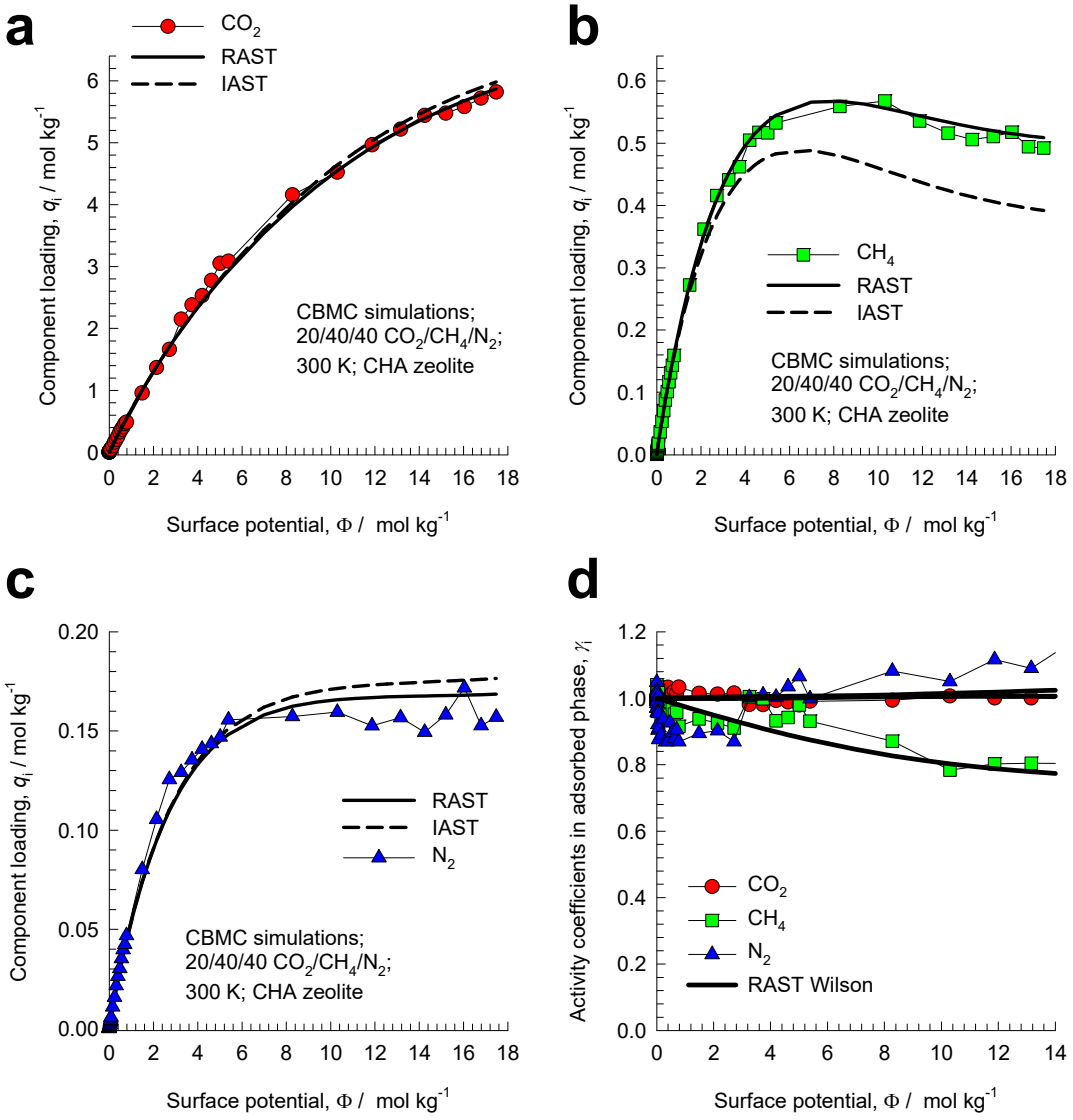

Figure S18. CBMC simulations (indicated by symbols) for 20/40/40 CO_2(1)/CH_4(2)/N_2(3) mixtures in CHA zeolite at 300 K. (a, b, c) Component loadings from CBMC are compared with IAST and RAST estimates. (d) Activity coefficients as function of the surface potential. The Wilson parameters for the binary pairs are provided in Table S6.

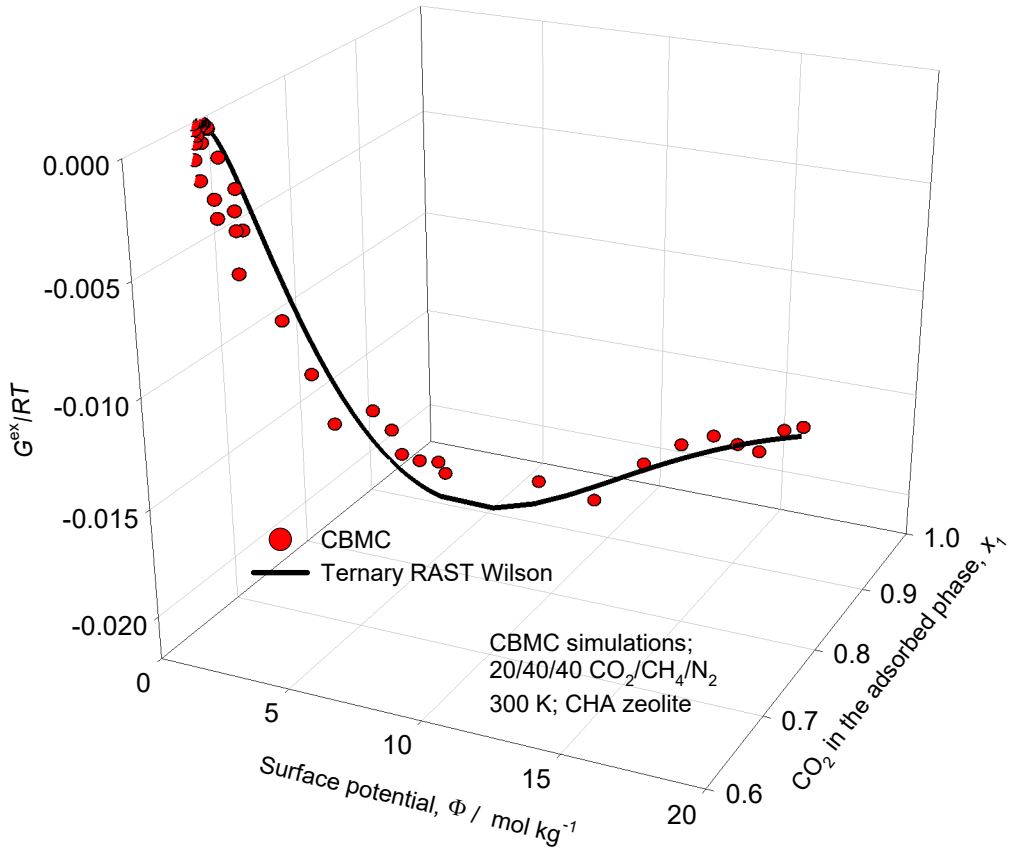

Figure S19. 3D plot of CBMC data on excess Gibbs free energy $G^{ex}/RT = \sum_{i=1}^{n} x_i \ln(\gamma_i)$ for 20/40/40 $CO_2(1)/CH_4(2)/N_2(3)$ mixtures in CHA zeolite at 300 K. Comparison is made with the estimates of the ternary Wilson RAST model. The Wilson parameters for the binary pairs are as provided in Table S6.

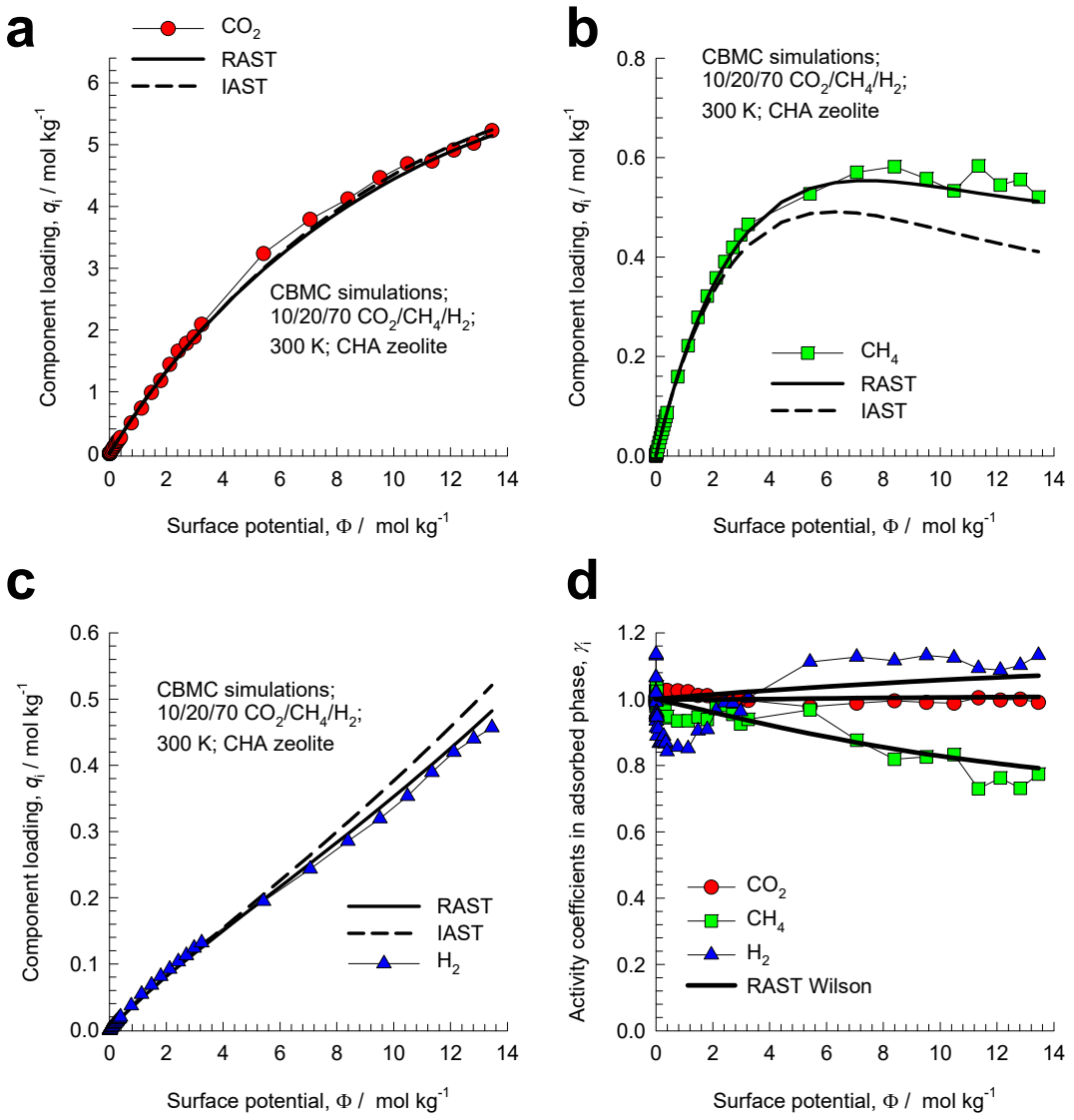

Figure S20. CBMC simulations (indicated by symbols) for 10/20/70 CO_2(1)/CH_4(2)/H_2(3) mixtures in CHA zeolite at 300 K. (a, b, c) Component loadings from CBMC are compared with IAST and RAST estimates. (d) Activity coefficients as function of the surface potential. The Wilson parameters for the binary pairs are as provided in Table S6.

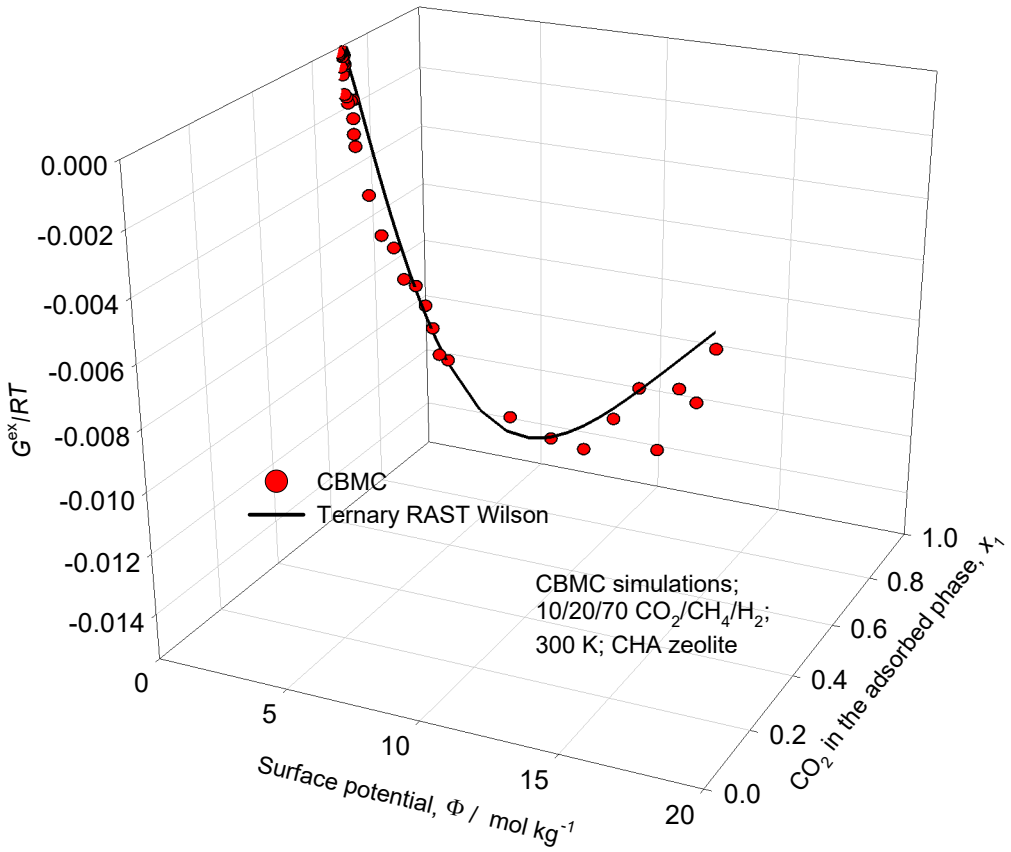

Figure S21. 3D plot of CBMC data on excess Gibbs free energy $G^{ex}/RT = \sum_{i=1}^{n} x_i \ln(\gamma_i)$ for 10/20/70 $CO_2(1)//CH_4(2)/H_2(3)$ mixtures in CHA zeolite at 300 K. Comparison is made with the estimates of the ternary Wilson RAST model. The Wilson parameters for the binary pairs are as provided in Table S6.

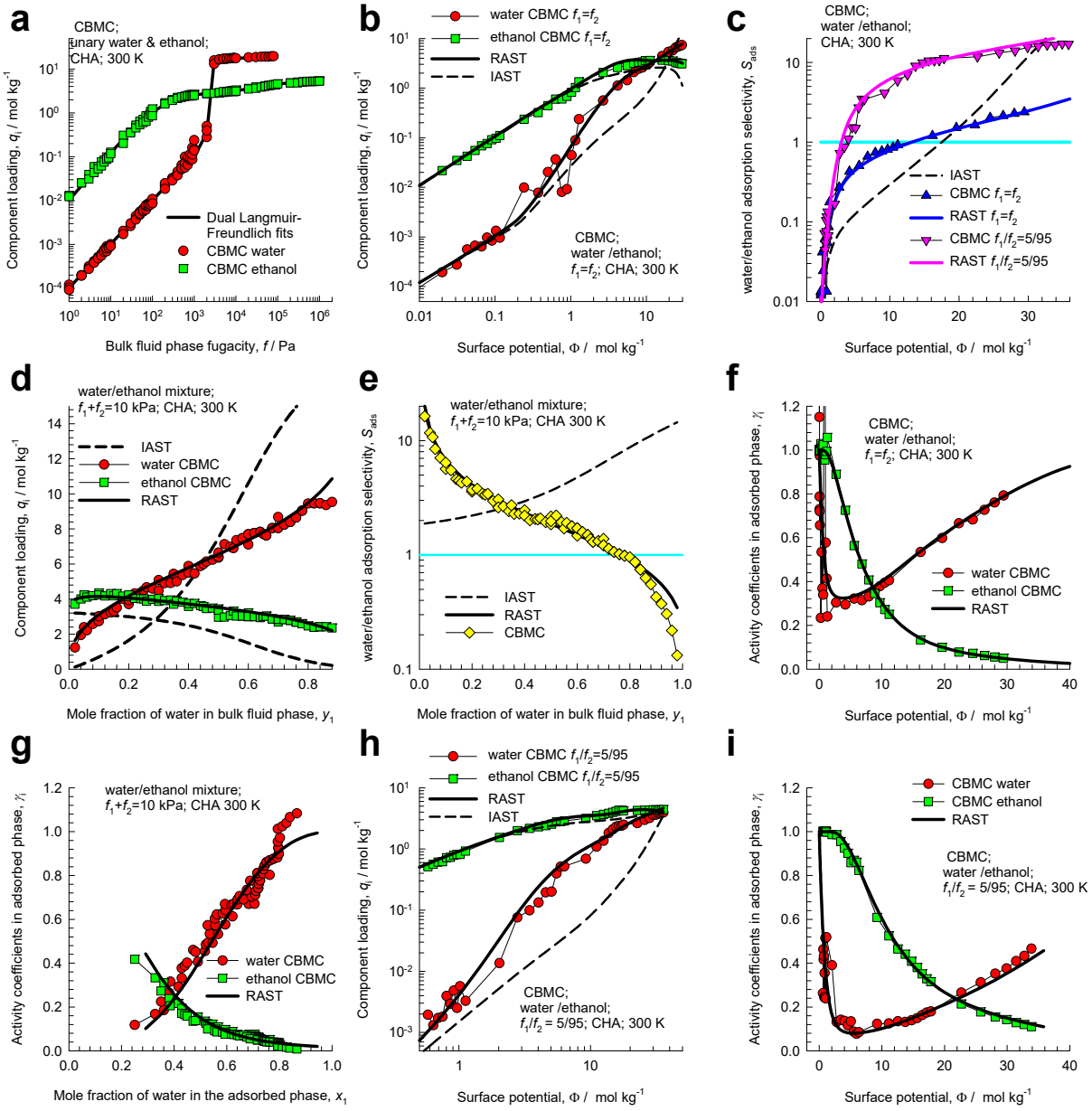

Figure S22. CBMC simulation data on component loadings, selectivities, and activity coefficients for Campaigns A (y_1= 0.5 and y_1= 0.05) and Campaign B (f_t= 10 kPa) for water(1)/ethanol(2) mixtures in CHA zeolite at 300 K The CBMC data are compared with RAST calculations using fitted NRTL parameters provided in Table S7. The dashed lines are IAST calculations.

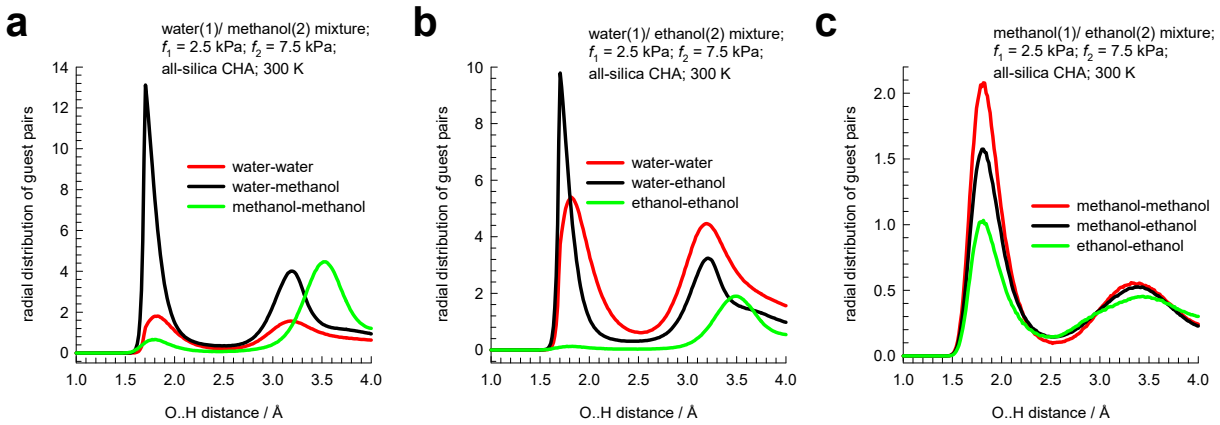

Figure S23. RDF of O···H distances for molecular pairs of (a) water(1)/methanol(2), (b) water(1)/ethanol(2), and (c) methanol(1)/ethanol(2) mixture adsorption in CHA zeolite at 300 K. For all three sets of mixtures, the partial fugacities of components 1 and 2 are f_1= 2.5 kPa, f_2= 7.5 kPa. The *y*-axes are normalized in the same manner and, therefore, the magnitudes of the first peaks is a direct reflection of the degree of hydrogen bonding between the molecular pairs.

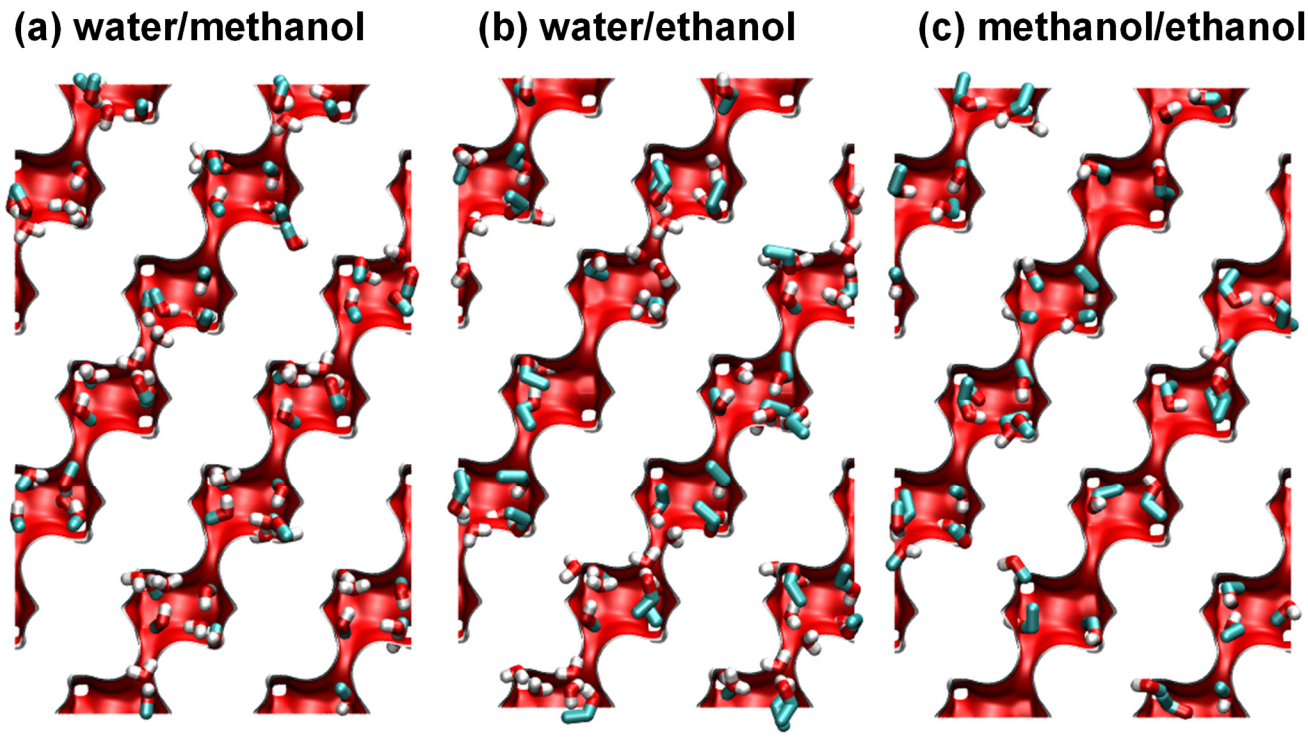

Figure S24. Snapshots showing location and conformations of guest molecules for adsorption of (a) water(1)/methanol(2), (b) water(1)/ethanol(2), and (c) methanol(1)/ethanol(2) mixture adsorption in CHA zeolite at 300 K. The partial fugacities of components 1 and 2 are f_1= 2.5 kPa, f_2= 7.5 kPa.

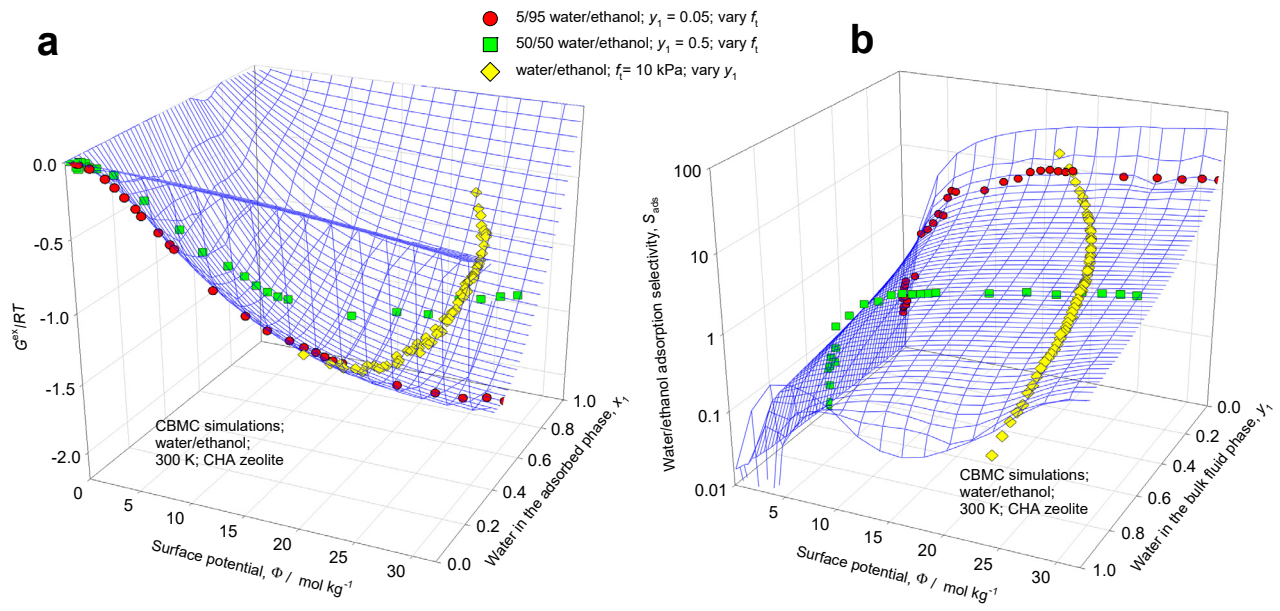

Figure S25. 3D plots of CBMC data for three different campaigns on (a) excess Gibbs free energy $G^{ex}/RT = x_1 \ln(\gamma_1) + x_2 \ln(\gamma_2)$, and (b) adsorption selectivity for water(1)/ethanol(2) mixture adsorption in CHA zeolite at 300 K. The 3D mesh is constructed using the NRTL parameters provided in Table S7.

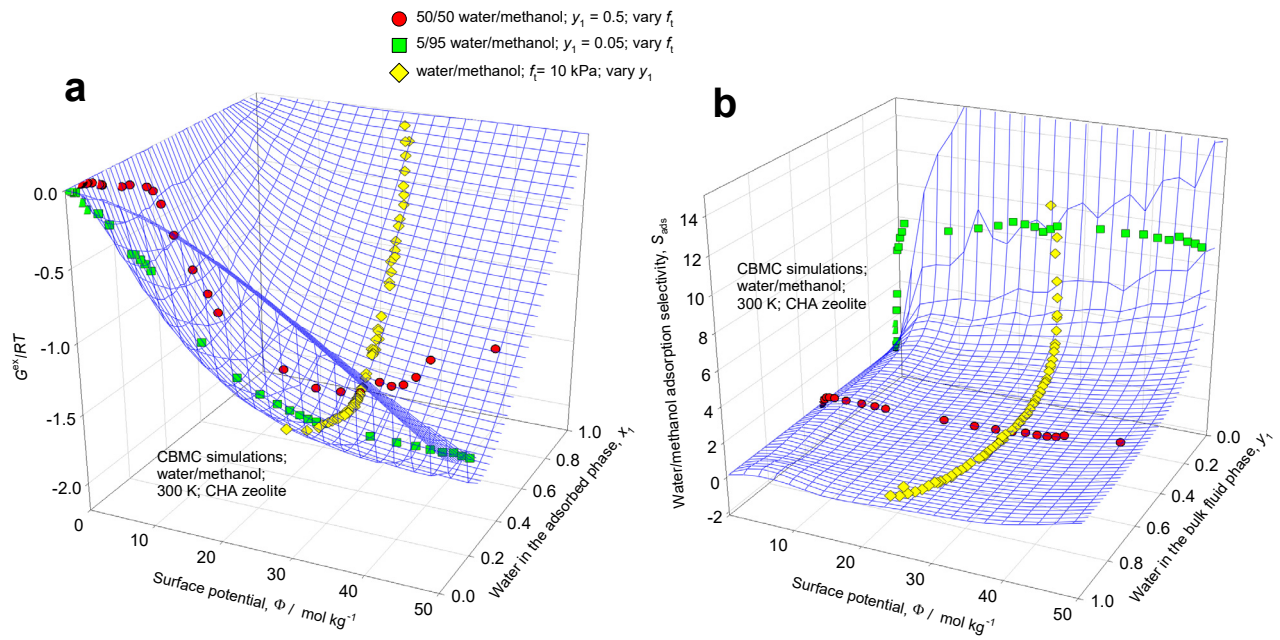

Figure S26. 3D plots of CBMC data for three different campaigns on excess Gibbs free energy $G^{ex}/RT = x_1 \ln(\gamma_1) + x_2 \ln(\gamma_2)$, and (b) adsorption selectivity for water(1)/methanol(2) mixture adsorption in CHA zeolite at 300 K. The 3D mesh is constructed using the NRTL parameters provided in Table S7.

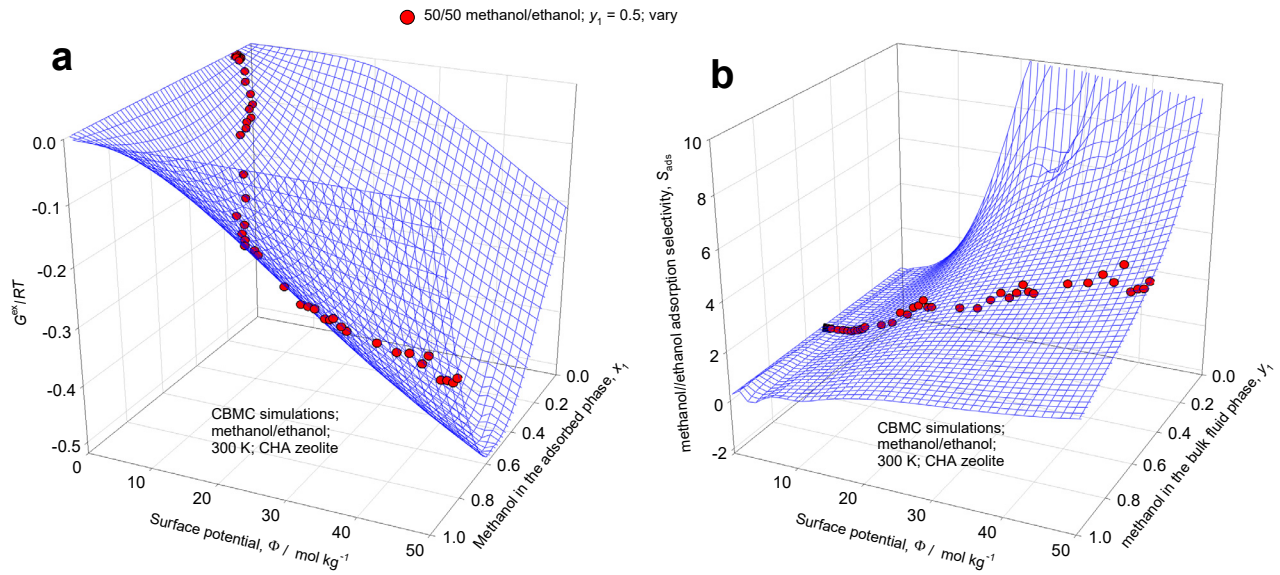

Figure S27. 3D plots of CBMC data on (a) excess Gibbs free energy $G^{ex}/RT = x_1 \ln(\gamma_1) + x_2 \ln(\gamma_2)$, and (b) adsorption selectivity for methanol(1)/ethanol(2) mixture adsorption in CHA zeolite at 300 K. The 3D mesh is constructed using the NRTL parameters provided in Table S7.

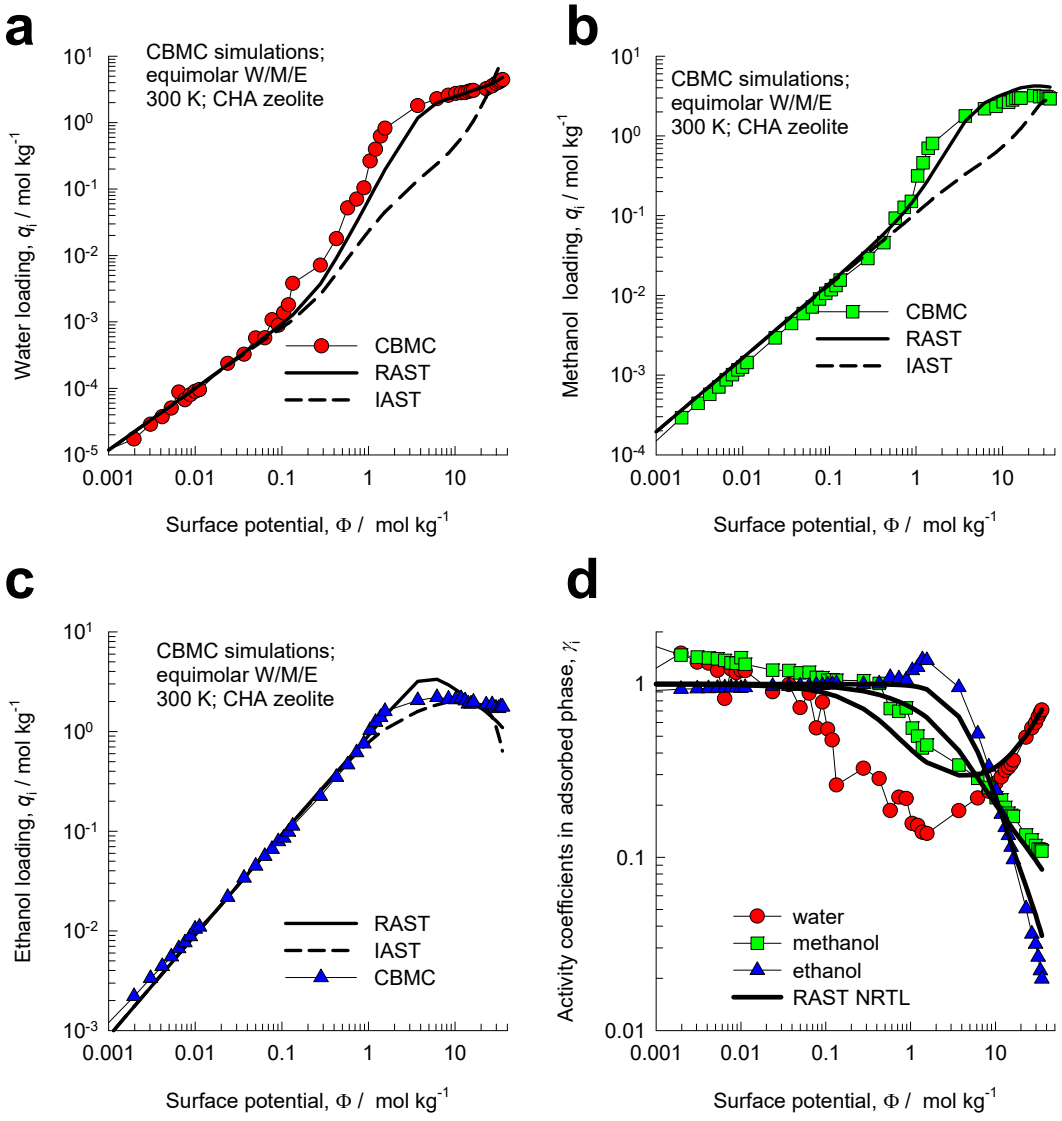

Figure S28. CBMC simulations (indicated by symbols) for equimolar $(f_1 = f_2 = f_3)$ water(1)/methanol(2)/ethanol(3) mixtures in CHA zeolite at 300 K. (a, b, c) Component loadings from CBMC are compared with IAST and RAST estimates. (d) Activity coefficients as function of the surface potential. The NRTL parameters are provided in Table S7.

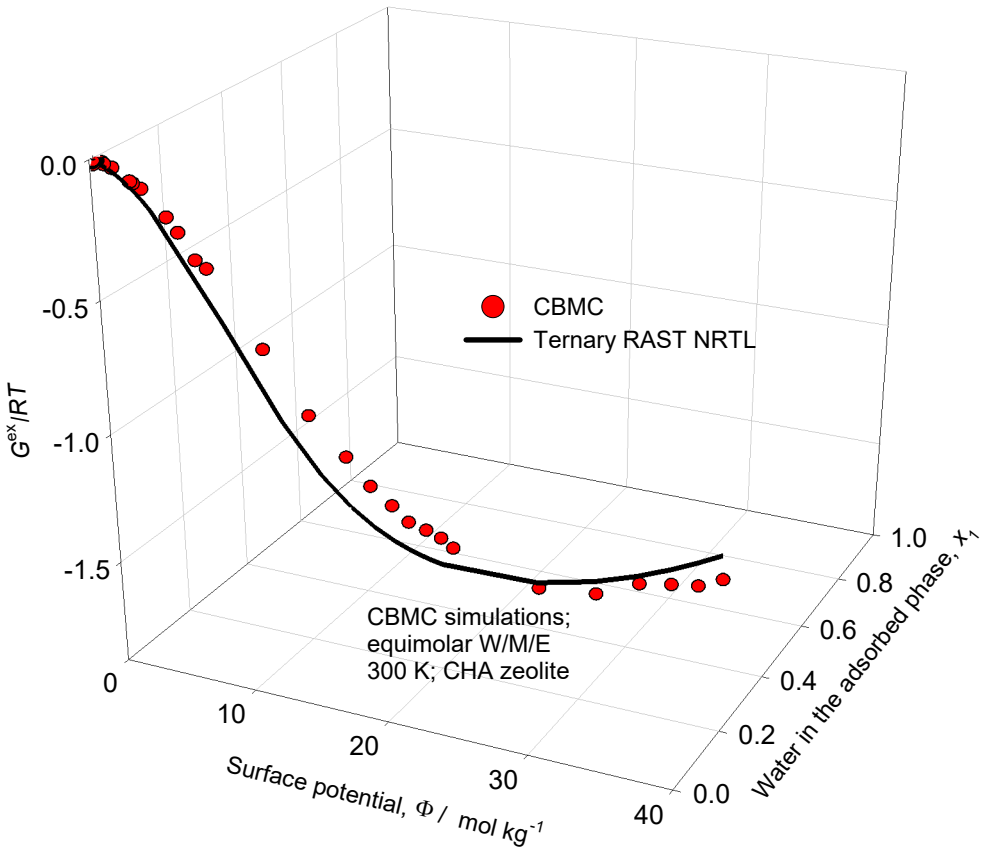

Figure S29. 3D plot of CBMC data on excess Gibbs free energy $G^{ex}/RT = \sum_{i=1}^{n} x_i \ln(\gamma_i)$ for equimolar $(f_1 = f_2 = f_3)$ water(1)/methanol(2)/ethanol(3) mixtures in CHA zeolite at 300 K. Comparison is made with the estimates of the ternary NRTL RAST model. The NRTL parameters for the binary pairs are as provided in Table S7.

8 Mixture adsorption in all-silica DDR zeolite

DDR consists of cages of 277.8 $Å^3$ volume, separated by 3.65 Å × 4.37 Å 8-ring windows; the pore landscapes and structural details are provided in Figure S9, and Figure S10.

8.1 CO_2/CH_4 mixture adsorption in all-silica DDR zeolite

A key assumption of the IAST is that the composition of the adsorbed phase is homogeneously and uniformly distributed within zeolite or metal-organic frameworks. Preferential location of molecules at certain locations within the crystalline, causes segregated adsorption and deviations from the assumption of homogeneous distribution. For separation of CO_2 from gaseous mixtures with CH_4, cage-type zeolites such as CHA, DDR, LTA, and ERI are of practical interest; these materials consist of cages separated by narrow windows, in the 3.3 – 4.5 Å range. For adsorption of CO_2/CH_4 mixtures, CBMC simulations[60] show that the window regions of cage-type zeolites has a significantly higher proportion of CO_2 than within the cages; see computational snapshots in Figure S30 for DDR. Due to the segregated nature of mixture adsorption, the IAST is unable to predict the mixture loadings accurately. Due to preferential location of CO_2 in the window regions the CH_4 molecules experience a less severe competition from CO_2.

To demonstrate non-ideality effects in mixture adsorption, three different sets of CBMC campaigns were conducted.

Three different campaigns were carried out for CBMC simulations of CO_2/CH_4 mixture adsorption in CHA zeolite at 300 K. In campaign A, the mole fraction of CO_2(1) in the bulk gas phase is held constant (at two different values $y_1 = 0.20$, and $y_1 = 0.5$) and the bulk gas phase fugacity $f_t = f_1 + f_2$ was varied. In campaign B, the mole fraction of CO_2(1) in the bulk gas phase, y_1 was varied from 0 to 1, keeping the bulk gas phase mixture fugacity $f_t = f_1 + f_2$ constant at a value of 1 MPa. The CBMC results of these campaigns are presented in Figure S31.

Figure S31c,e compares CBMC data on adsorption selectivity, $S_{ads} = \frac{q_1/q_2}{f_1/f_2}$, compared with IAST estimates indicated by the dashed lines. Broadly speaking, we note that IAST overestimates S_{ads}. The IAST anticipates S_{ads} depends only on the surface potential Φ; this expectation is not fulfilled for any campaigns A. In Figure S31c, the CBMC simulated values of the adsorption selectivity S_{ads} are plotted as function of the surface potential Φ. Except in the limit $\Phi \to 0;\ \theta \to 0;\ \gamma_i \to 1$, the IAST significantly overestimates S_{ads}.

The continuous solid lines in Figure S31b,c,d,e,f,g,h,i are the RAST calculations using fitted Wilson parameters as specified in in Table S8. For the Wilson fits, we calculate the parameter C using $C = \frac{1}{\frac{x_1}{q_{1,sat}} + \frac{x_2}{q_{2,sat}}};\quad q_{i,sat} = q_{i,A,sat} + q_{i,B,sat};\quad i = 1,2$, with the arbitrary assumption that $x_1 = x_2 = 0.5$.

Figure S31f,g,i plot the activity coefficients of the guest components in the adsorbed phase as function of (g) mole fraction of CO_2(1) in the adsorbed phase for campaign B, x_1, and (f, i) the surface potential Φ for campaigns A. For campaign B, we note the limiting behaviors $x_i \to 1;\ \gamma_i \to 1$. For campaigns A we note that the activity coefficients are also dependent the surface potential Φ with the limiting characteristic $\Phi \to 0;\ \gamma_1 \to 1;\ \gamma_2 \to 1$. The introduction of $\left(1 - \exp\left(-C\Phi\right)\right)$ in the Wilson model, eq (S39), imparts the correct limiting behaviors $\Phi \to 0;\ \theta \to 0;\ \gamma_i \to 1$ for the activity coefficients in the Henry regime, , as the pore occupancy tends to vanishingly small values. As pore saturation conditions are approached, this correction factor tends to unity: $\left(1 - \exp\left(-C\Phi\right)\right) \to 1$.

The CBMC data in Figure S31 lead us to conclude that the activity coefficients are functions of both Φ and x_1. In Figure S32a the CBMC data for the excess Gibbs free energy $G^{ex}/RT = x_1 \ln\left(\gamma_1\right) + x_2 \ln\left(\gamma_2\right)$ for the aforementioned CBMC campaigns are plotted in 3D space as

function of Φ and x_1. The entire CBMC data set resides on a 3D surface mesh determined from the fitted Wilson parameters in Table S8.

In Figure S32b the CBMC data on the CO_2/CH_4 adsorption selectivity are plotted in 3D space as function of the surface potential Φ and the mole fraction of CO_2 in the bulk gas phase, y_1. The entire CBMC data set resides on a 3D surface mesh determined from the fitted Wilson parameters in Table S8. Figure S32b confirms that the adsorption selectivity is not uniquely determined by the surface potential, Φ, but is additionally dependent on the bulk phase mixture composition.

8.2 CO_2/N_2 and CO_2/H_2 mixture adsorption in DDR zeolite

Figure S33a,b presents the CBMC data for adsorption selectivity of CO_2/N_2 and CO_2/H_2 mixtures in DDR zeolite, , both for Campaigns A with fixed values of the bulk gas mixture compositions, y_1. The IAST selectivities are not in perfect agreement with the CBMC data. Thermodynamic non-ideality effects, quantified with fitted Wilson parameters in Table S8, allow better agreement with the CBMC data on S_{ads}.

8.3 CH_4/N_2 and CH_4/H_2 mixture adsorption in all-silica DDR zeolite

Figure S34a,b present CBMC data for component loadings for (a) CH_4/N_2 and (b) CH_4/H_2 mixtures in DDR zeolite, both for Campaign A with $y_1 = 0.2$. The dashed lines are IAST estimates; the unary isotherm parameters are specified in Table S8. The Φ IAST estimates are in good agreement with IAST estimates, indicating that non-ideality effects are of negligible importance.

8.4 $CO_2/CH_4/N_2$ mixture adsorption in DDR zeolite

CBMC simulations were carried out for ternary 20/40/40 $CO_2/CH_4/N_2$ mixtures in DDR at 300 K for a range of total fugacities, f_t. In Figure S35a,b,c the component loadings from CBMC are compared with IAST and RAST estimates. The Wilson parameters for the binary pairs $\Lambda_{12}, \Lambda_{21}, \Lambda_{13}, \Lambda_{31}, \Lambda_{23}, \Lambda_{32}$ are taken to the same as for the corresponding binary pairs as listed in Table S6. Since the binary CH_4/N_2

mixtures behave ideally (cf. Figure S34a), we assert $\Lambda_{23}=1;\Lambda_{32}=1$. Our approach for ternary mixtures is to estimate C as $C=\frac{x_1}{q_{1,sat}}+\frac{x_2}{q_{2,sat}}+\frac{x_3}{q_{3,sat}}$, assuming, $x_1=x_2=x_3=1/3$. The RAST estimates are in good agreement with the ternary CBMC data. Figure S35d plots the activity coefficients as function of the surface potential.

In Figure S36 the excess Gibbs free energy $G^{ex}/RT=\sum_{i=1}^{n}x_i\ln(\gamma_i)$ determined from CBMC data for 20/40/40 $CO_2/CH_4/N_2$ mixtures in DDR are plotted in 3D space as function of Φ and x_1. The continuous solid line represents the ternary RAST Wilson calculations. The agreement is good, validating the ternary RAST Wilson model.

8.5 $CO_2/CH_4/H_2$ mixture adsorption in DDR zeolite

CBMC simulations were carried out for ternary 10/20/70 $CO_2/CH_4/H_2$ mixtures in DDR at 300 K for a range of total fugacities, f_t. In Figure S37a,b,c the component loadings from CBMC are compared with IAST and RAST estimates. The Wilson parameters for the binary pairs $\Lambda_{12},\Lambda_{21},\Lambda_{13},\Lambda_{31},\Lambda_{23},\Lambda_{32}$ are taken to the same as for the corresponding binary pairs as listed in Table S6. Since the binary CH_4/H_2 mixtures behave ideally (cf. Figure S34b), we assert $\Lambda_{23}=1;\Lambda_{32}=1$. Our approach for ternary mixtures is to estimate C as $C=\frac{x_1}{q_{1,sat}}+\frac{x_2}{q_{2,sat}}+\frac{x_3}{q_{3,sat}}$, assuming, $x_1=x_2=x_3=1/3$. The RAST estimates are in good agreement with the ternary CBMC data. Figure S37d plots the activity coefficients as function of the surface potential.

In Figure S38 the excess Gibbs free energy $G^{ex}/RT=\sum_{i=1}^{n}x_i\ln(\gamma_i)$ determined from CBMC data for 10/20/70 $CO_2/CH_4/H_2$ mixtures in DDR at 300 K are plotted in 3D space as function of and x_1. The continuous solid line represents the ternary RAST Wilson calculations. The agreement is good, validating the ternary RAST Wilson model.

8.6 Water/methanol/ethanol mixture adsorption in DDR zeolite

For adsorption of water(1)/ethanol(2) mixtures in DDR zeolite at 300 K, three different CBMC simulations were carried out: Campaign A (with $y_1 = 0.5$, and $y_1 = 0.05$, vary f_t), and campaign B, the mole fraction of water(1) in the bulk fluid phase, y_1 was varied from 0 to 1, keeping the bulk fluid phase mixture fugacity $f_t = f_1 + f_2$ constant at a value of 10 kPa. The CBMC data on component loadings, adsorption selectivities, and activity coefficients are presented in Figure S39. The dashed lines are the IAST estimates. The failure of the IAST to match the CBMC data presented in Figure S39 is a consequence of hydrogen bonding between guest molecules in water/alcohol mixtures. [15, 18, 47, 48, 60] One of the mandates of the IAST is violated because of the formation of water/alcohol clusters.[15, 46, 48] The continuous solid lines are the RAST calculations with fitted NRTL parameters specified in Table S9.

In order to demonstrate the occurrence of hydrogen bonding in water/methanol, and water/ethanol mixtures CBMC simulation data on the spatial locations of the guest molecules were sampled to determine the O···H distances of various pairs of molecules. By sampling a total of 10^6 simulation steps, the radial distribution functions (RDF) of O···H distances were determined for water-water, water-alcohol, and alcohol-alcohol pairs.

Figure S40 shows the RDF of O···H distances for molecular pairs of water(1)/ethanol(2) mixture adsorption in DDR zeolite at 300 K. The H-bonding between water/ethanol pairs is much stronger than for water/water and ethanol/ethanol pairs; these conclusions are in line with those for CHA zeolite.

A visual appreciation of hydrogen bonding is gleaned from the snapshots in Figure S41 for mixture adsorption in DDR.

The CBMC data in Figure S39 lead us to conclude that the activity coefficients are functions of both Φ and x_1. In Figure S42a, the CBMC data for the excess Gibbs free energy $G^{ex}/RT = x_1 \ln(\gamma_1) + x_2 \ln(\gamma_2)$ for the aforementioned CBMC campaigns for water/ethanol mixtures are plotted in 3D space as function of Φ and x_1. The entire CBMC data set resides on a 3D surface mesh determined from the fitted NRTL parameters specified in Table S9.

In Figure S42b, the CBMC data for the water/ethanol adsorption selectivity for water/ethanol mixtures are plotted in 3D space as function of surface potential Φ and mole fraction of water in the bulk fluid phase mixture. y_1. The entire CBMC data set on S_{ads} resides on a 3D surface mesh determined from the fitted NRTL parameters specified in Table S9. Figure S42b confirms that the adsorption selectivity is not uniquely determined by the surface potential, Φ, but is additionally dependent on the bulk phase mixture composition.

Analogously, in Figure S43a, the CBMC data for the excess Gibbs free energy $G^{ex}/RT = x_1 \ln(\gamma_1) + x_2 \ln(\gamma_2)$ for the three different CBMC campaigns for water/methanol mixtures are plotted in 3D space as function of Φ and x_1. The entire CBMC data set resides on a 3D surface mesh determined from the fitted NRTL parameters specified in Table S9. In Figure S43b, the CBMC data for the water/methanol adsorption selectivity for water/ethanol mixtures are plotted in 3D space as function of surface potential Φ and mole fraction of water in the bulk fluid phase mixture. y_1. The entire CBMC data set on S_{ads} resides on a 3D surface mesh determined from the fitted NRTL parameters specified in Table S9. Figure S43b confirms that the adsorption selectivity is not uniquely determined by the surface potential, Φ, but is additionally dependent on the bulk phase mixture composition.

In Figure S44a, the CBMC data for the excess Gibbs free energy $G^{ex}/RT = x_1 \ln(\gamma_1) + x_2 \ln(\gamma_2)$ for CBMC campaign for methanol/ethanol mixtures in DDR are plotted in 3D space as function of the surface potential Φ and adsorbed phase mole fraction x_1. The entire CBMC data set resides on a 3D surface mesh determined from the fitted NRTL parameters specified in Table S9. In Figure S44b, the CBMC data for the methanol/ethanol adsorption selectivity are plotted in 3D space as function of surface potential Φ and mole fraction of water in the bulk fluid phase mixture. y_1. The entire CBMC data set on S_{ads} resides on a 3D surface mesh determined from the fitted NRTL parameters specified in Table S9. Figure S44b confirms that the adsorption selectivity is not uniquely determined by the surface potential, Φ, but is additionally dependent on the bulk phase mixture composition.

Figure S45a,b,c presents CBMC simulations of component loadings, q_i, for equimolar $f_1 = f_2 = f_3$ water(1)/methanol(2)/ethanol(3) mixture adsorption in DDR zeolite with varying total fugacity $f_t = f_1 + f_2 + f_3$, plotted as a function of the surface potential Φ. The component activity coefficients are plotted in Figure S45d. The dashed lines in Figure S45 are IAST estimates; the continuous solid lines are RAST calculations The continuous solid lines in Figure S45 are RAST calculations using eq (S44). In these calculations the NRTL parameters $\tau_{12}, \tau_{21}, \alpha_{12}, \tau_{13}, \tau_{31}, \alpha_{13}, \tau_{23}, \tau_{32}, \alpha_{23}$ are taken to the same as for the corresponding binary pairs as listed in Table S9. Our approach for ternary mixtures is to estimate *C* as $C = \frac{x_1}{q_{1,sat}} + \frac{x_2}{q_{2,sat}} + \frac{x_3}{q_{3,sat}}$, assuming, $x_1 = x_2 = x_3 = 1/3$. The RAST calculations are in reasonable agreement with CBMC data.

In Figure S46 the excess Gibbs free energy $G^{ex}/RT = \sum_{i=1}^{n} x_i \ln(\gamma_i)$ determined from CBMC data for equimolar $f_1 = f_2 = f_3$ water(1)/methanol(2)/ethanol(3) mixture adsorption in DDR zeolite are plotted in 3D space as function of Φ and x_1. The continuous solid line represents the ternary RAST NRTL calculations. The agreement is good, validating the ternary RAST NRTL model.

8.7 List of Tables for Mixture adsorption in all-silica DDR zeolite

Table S8. Dual-site Langmuir-Freundlich parameters for guest molecules in DDR (all-silica) at 300 K.

	Site A			Site B		
	$\frac{q_{A,sat}}{\text{mol kg}^{-1}}$	$\frac{b_A}{\text{Pa}^{-\nu_A}}$	ν_A	$\frac{q_{B,sat}}{\text{mol kg}^{-1}}$	$\frac{b_B}{\text{Pa}^{-\nu_B}}$	ν_B
CO_2	1.5	1.010E-06	0.79	3	6.076E-06	1
CH_4	1.4	4.035E-06	1	1.95	1.814E-06	0.75
N_2	1.25	9.887E-07	1	1.55	5.549E-08	1
H_2	5	5.028E-08	1	12	2.442E-09	1

Fitted Wilson non-ideality parameters for mixture adsorption in DDR at 300 K.

	C / kg mol^{-1}	Λ_{12}	Λ_{12}
CO_2/CH_4	0.113	3.300	0.111
CO_2/N_2	0.115	2.509	0.169
CO_2/H_2	0.069	1.965	0.281
$CO_2/CH_4//N_2$	0.117	$\Lambda_{12}, \Lambda_{21}, \Lambda_{13}, \Lambda_{31}, \Lambda_{23}, \Lambda_{32}$ as above	
$CO_2/CH_4/H_2$	0.0864	$\Lambda_{12}, \Lambda_{21}, \Lambda_{13}, \Lambda_{31}, \Lambda_{23}, \Lambda_{32}$ as above	

Table S9. Dual-site Langmuir-Freundlich parameters for pure component water, methanol, and ethanol at 300 K in all-silica DDR zeolite. The fit parameters are based on the CBMC simulations of pure component isotherms presented in earlier works.[27, 48]

	Site A			Site B		
	$\frac{q_{A,sat}}{\text{mol kg}^{-1}}$	$\frac{b_A}{\text{Pa}^{-\nu_A}}$	ν_A	$\frac{q_{B,sat}}{\text{mol kg}^{-1}}$	$\frac{b_B}{\text{Pa}^{-\nu_B}}$	ν_B
water	6.45	2.776E-17	4.3	2.4	1.300E-05	1.06
methanol	1.7	1.186E-04	1.3	1.7	6.055E-04	0.78
ethanol	1.6	9.962E-03	0.88	1.2	9.160E-05	0.66

Fitted NRTL non-ideality parameters for binary mixture adsorption at 300 K in DDR zeolite.

	C / kg mol^{-1}	τ_{12}	τ_{21}	α
water/methanol	8.261	-3.207	1.528	0.055
water/ethanol	0.235	-2.749	-0.913	0.250
methanol/ethanol	0.326	1.216	-2.336	0.092
water/methanol/ethanol	0.255	$\tau_{12},\tau_{21},\alpha_{12},\tau_{13},\tau_{31},\alpha_{13},\tau_{23},\tau_{32},\alpha_{23}$ as above		

8.8 List of Figures for Mixture adsorption in all-silica DDR zeolite

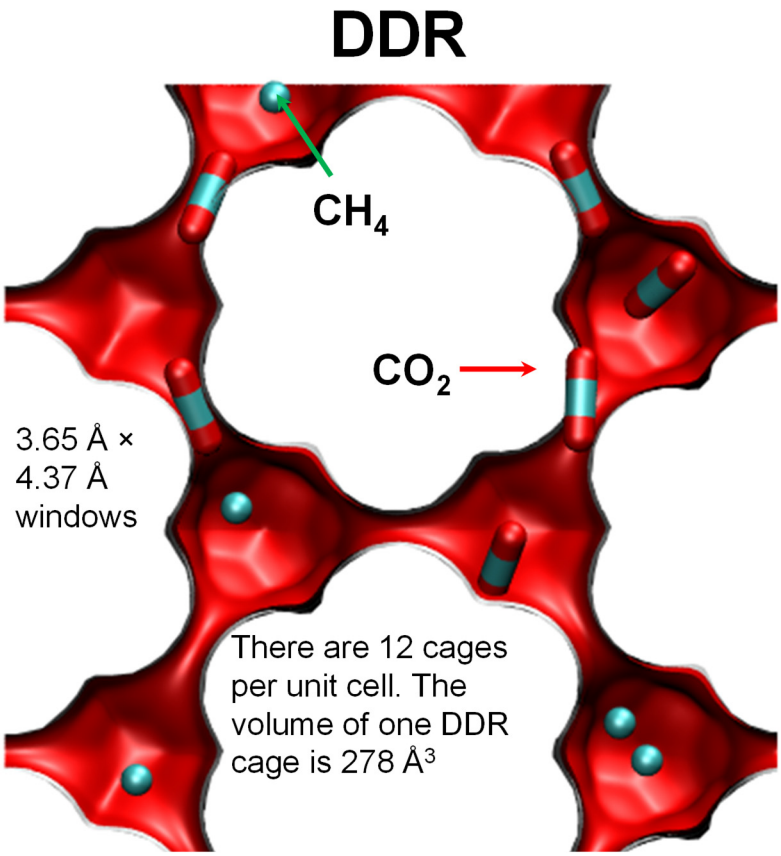

Figure S30. Computational snapshots for CO_2(1)/CH_4(2) mixture adsorption in DDR zeolite at 300 K.

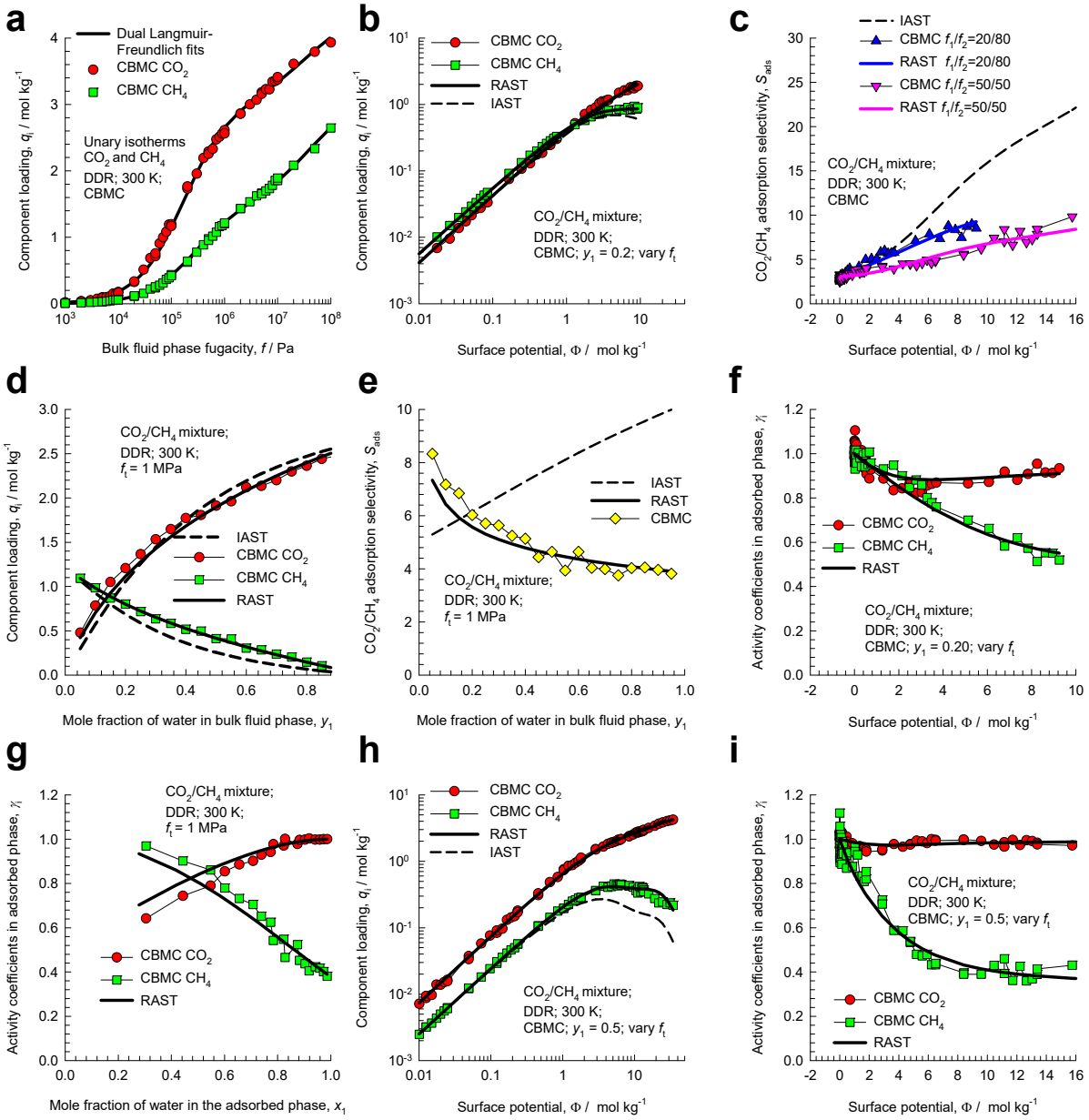

Figure S31. CBMC simulation data and analysis for three different campaigns CO_2(1)/CH_4(2) mixture adsorption in DDR zeolite at 300 K. (a) Unary isotherms and fits. (b, d, h) Component loadings in mixture compared with IAST/RAST estimates. (c, e) CBMC data for CO_2(1)/CH_4(2) adsorption selectivity compared with IAST and RAST estimates. (f, g, i) Activity coefficients from CBMC compared with RAST model calculations. The unary isotherm data fits and Wilson parameters are provided in Table S8.

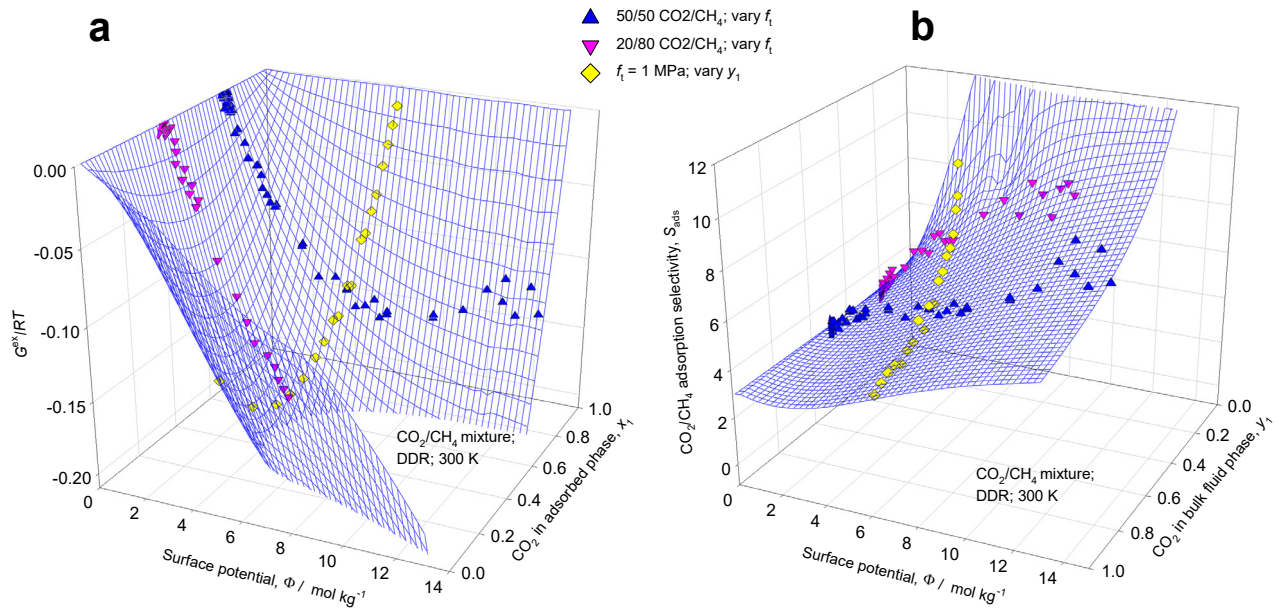

Figure S32. 3D plots of CBMC data on (a) excess Gibbs free energy $G^{ex}/RT = x_1 \ln(\gamma_1) + x_2 \ln(\gamma_2)$ and (b) $CO_2(1)/CH_4(2)$ adsorption selectivity for $CO_2(1)/CH_4(2)$ mixture adsorption in DDR zeolite at 300 K. The 3D mesh is constructed using the Wilson parameters provided in Table S8.

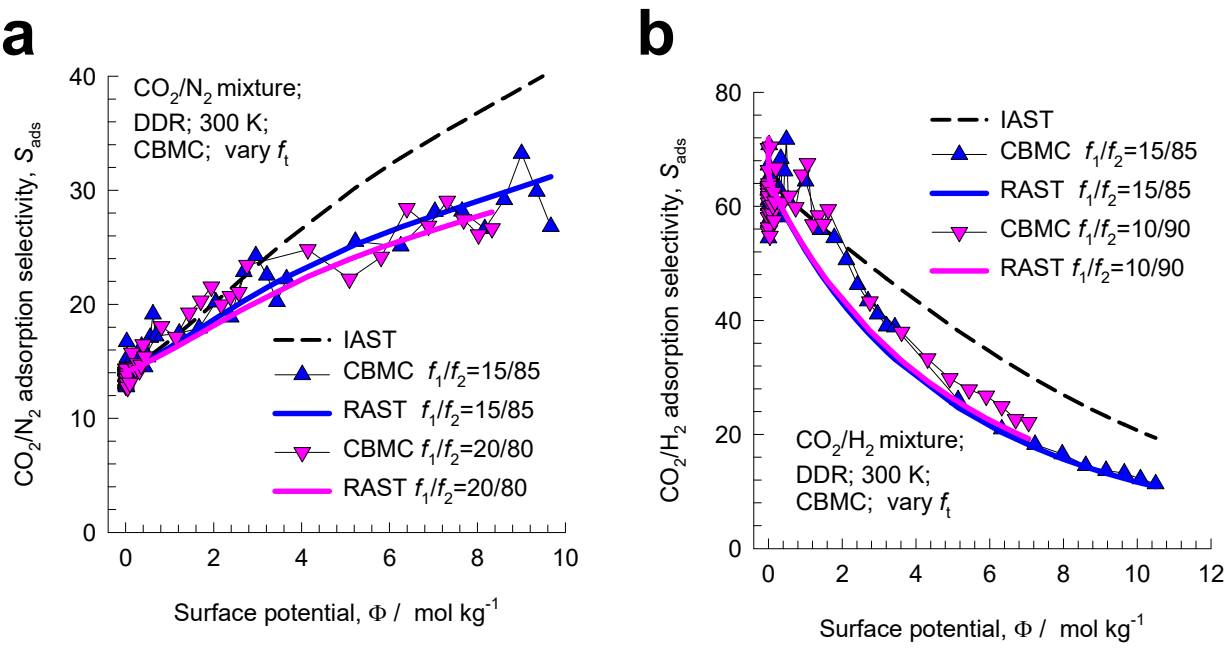

Figure S33. CBMC data for adsorption selectivity of (a) CO_2/N_2 and (b) CO_2/H_2 mixtures in DDR zeolite, both for Campaign A with fixed values of the bulk phase mixture compositions, The dashed lines are IAST estimates; the continuous solid lines are RAST calculations with fitted Wilson parameters specified in Table S8.

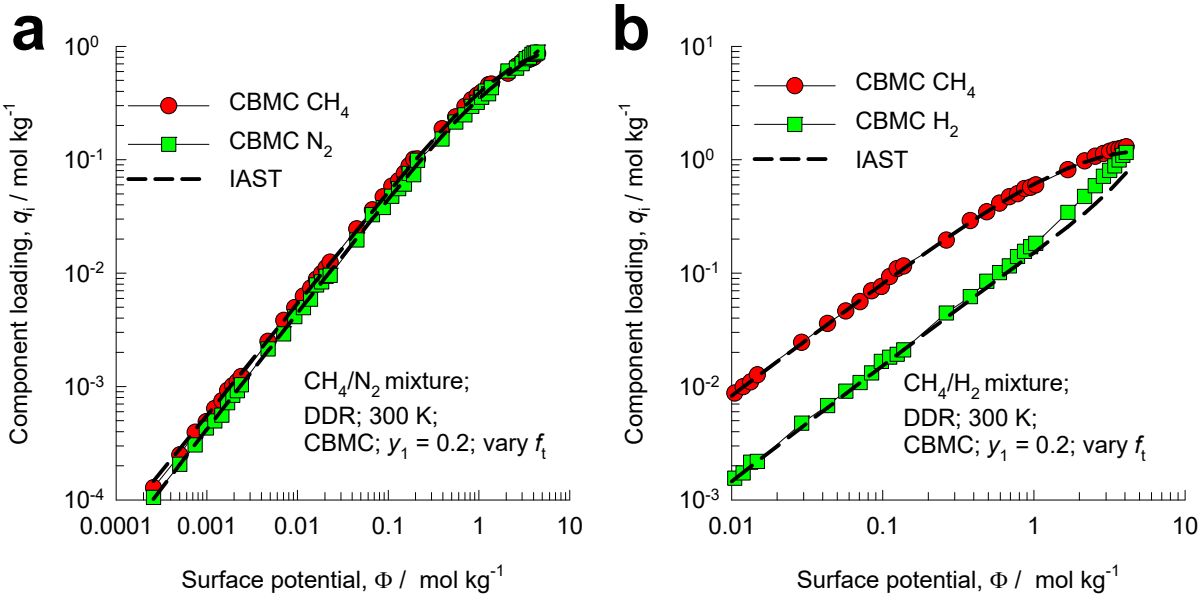

Figure S34. CBMC data for component loadings for (a) CH_4/N_2 and (b) CH_4/H_2 mixtures in DDR zeolite, both for Campaign A with $y_1 = 0.2$. The dashed lines are IAST estimates; the unary isotherm parameters are specified in Table S8.

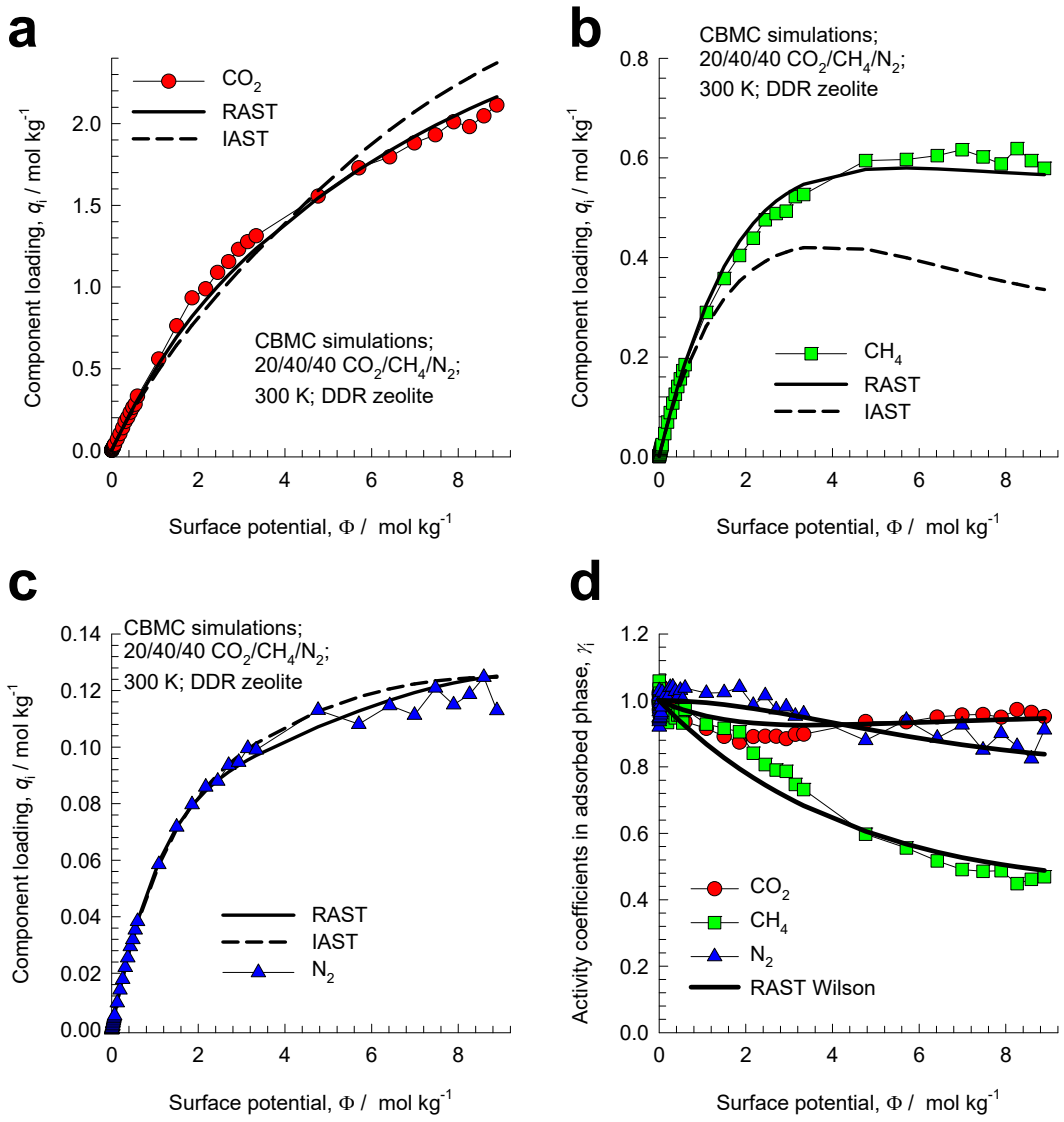

Figure S35. CBMC simulations (indicated by symbols) for 20/40/40 CO_2(1)//CH_4(2)/N_2(3) mixtures in DDR zeolite at 300 K. (a, b, c) Component loadings from CBMC are compared with IAST and RAST estimates. (d) Activity coefficients as function of the surface potential. The Wilson parameters for the binary pairs are provided in Table S8.

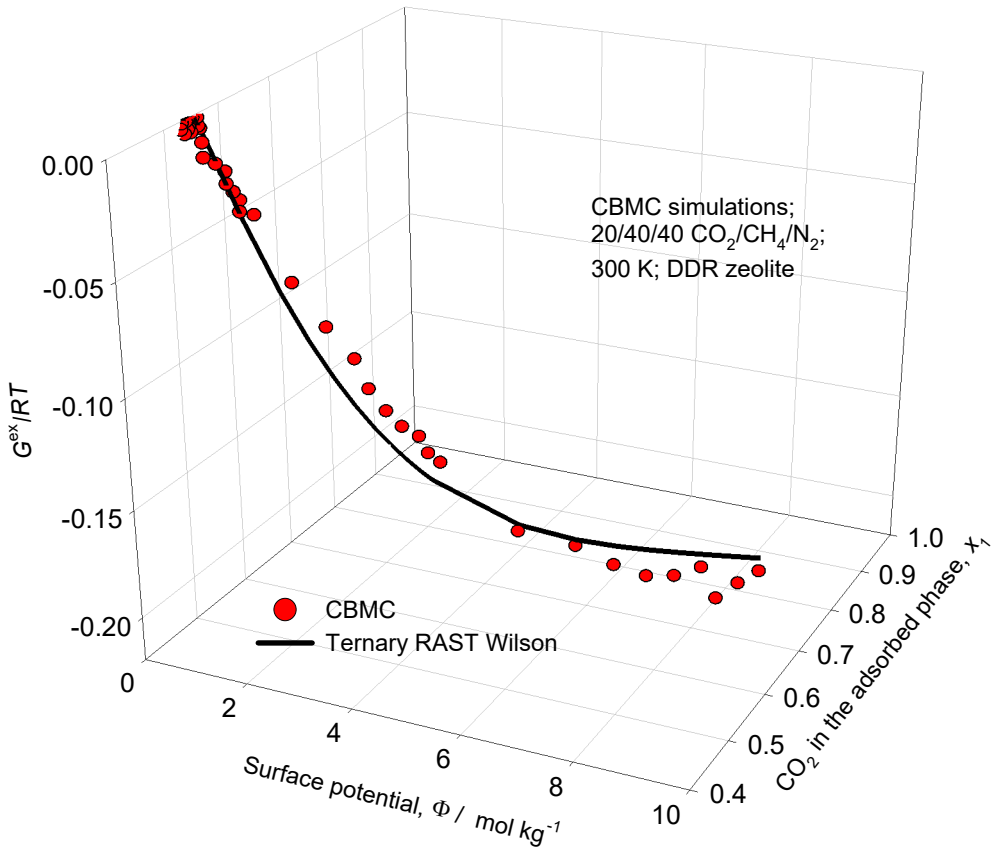

Figure S36. 3D plot of CBMC data on excess Gibbs free energy $G^{ex}/RT = \sum_{i=1}^{n} x_i \ln(\gamma_i)$ for 20/40/40 $CO_2(1)//CH_4(2)/N_2(3)$ mixtures in DDR zeolite at 300 K. Comparison is made with the estimates of the ternary Wilson RAST model. The Wilson parameters for the binary pairs are provided in Table S8.

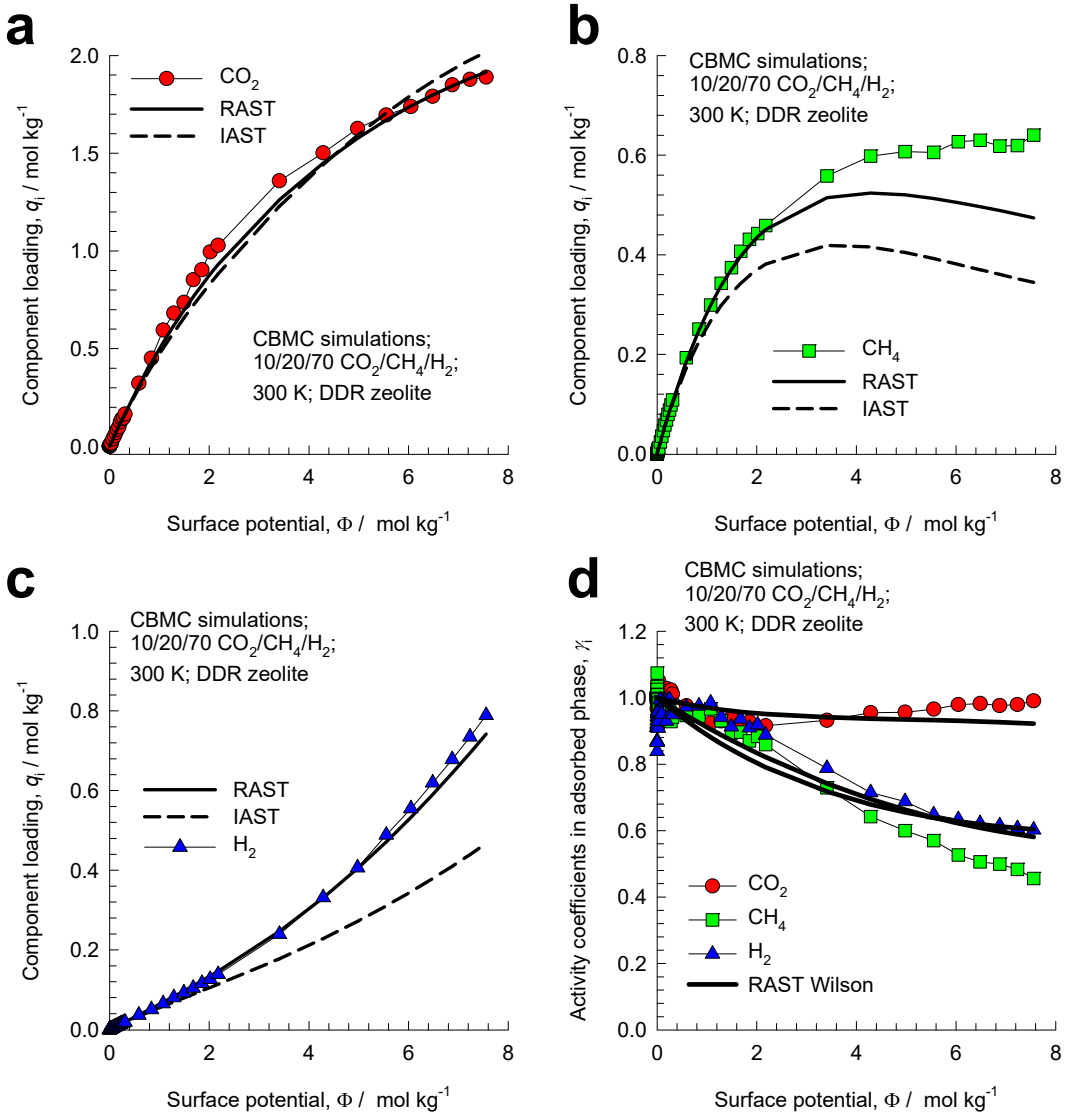

Figure S37. CBMC simulations (indicated by symbols) for 10/20/70 CO_2(1)//CH_4(2)/H_2(3) mixtures in DDR zeolite at 300 K. (a, b, c) Component loadings from CBMC are compared with IAST and RAST estimates. (d) Activity coefficients as function of the surface potential. The Wilson parameters for the binary pairs are provided in Table S8.

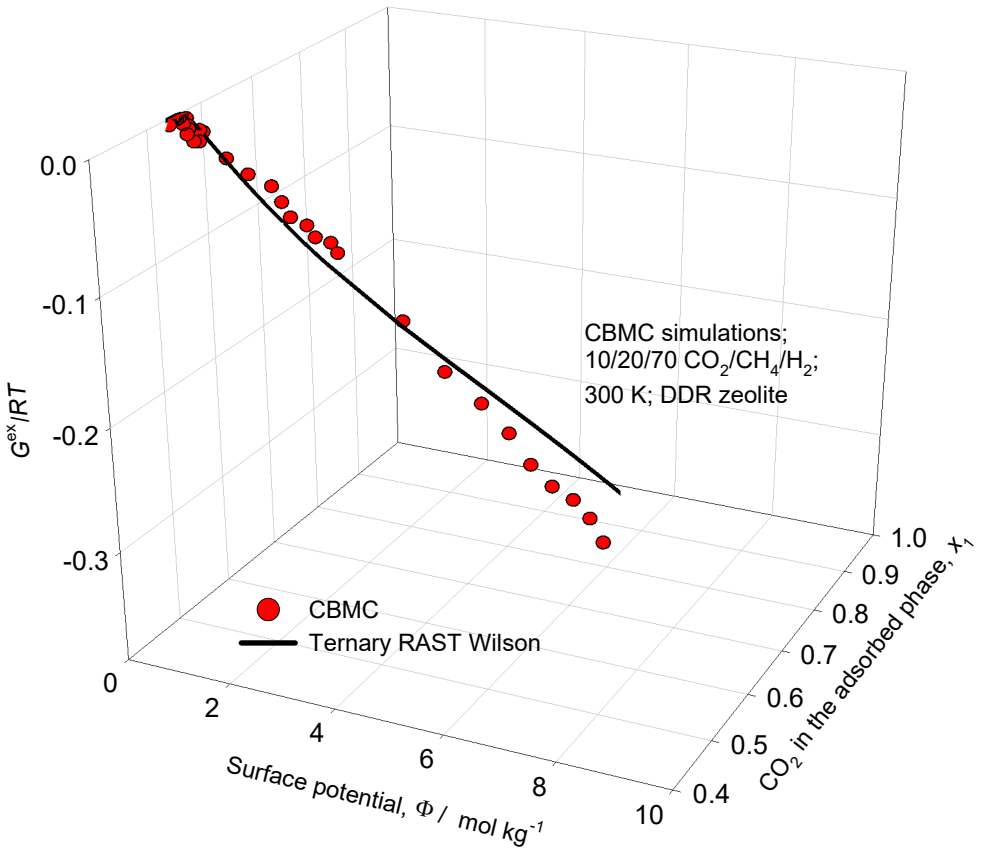

Figure S38. 3D plot of CBMC data on excess Gibbs free energy $G^{ex}/RT = \sum_{i=1}^{n} x_i \ln(\gamma_i)$ for 10/20/70 $CO_2(1)//CH_4(2)/H_2(3)$ mixtures in DDR zeolite at 300 K. Comparison is made with the estimates of the ternary Wilson RAST model. The Wilson parameters for the binary pairs are provided in Table S8.

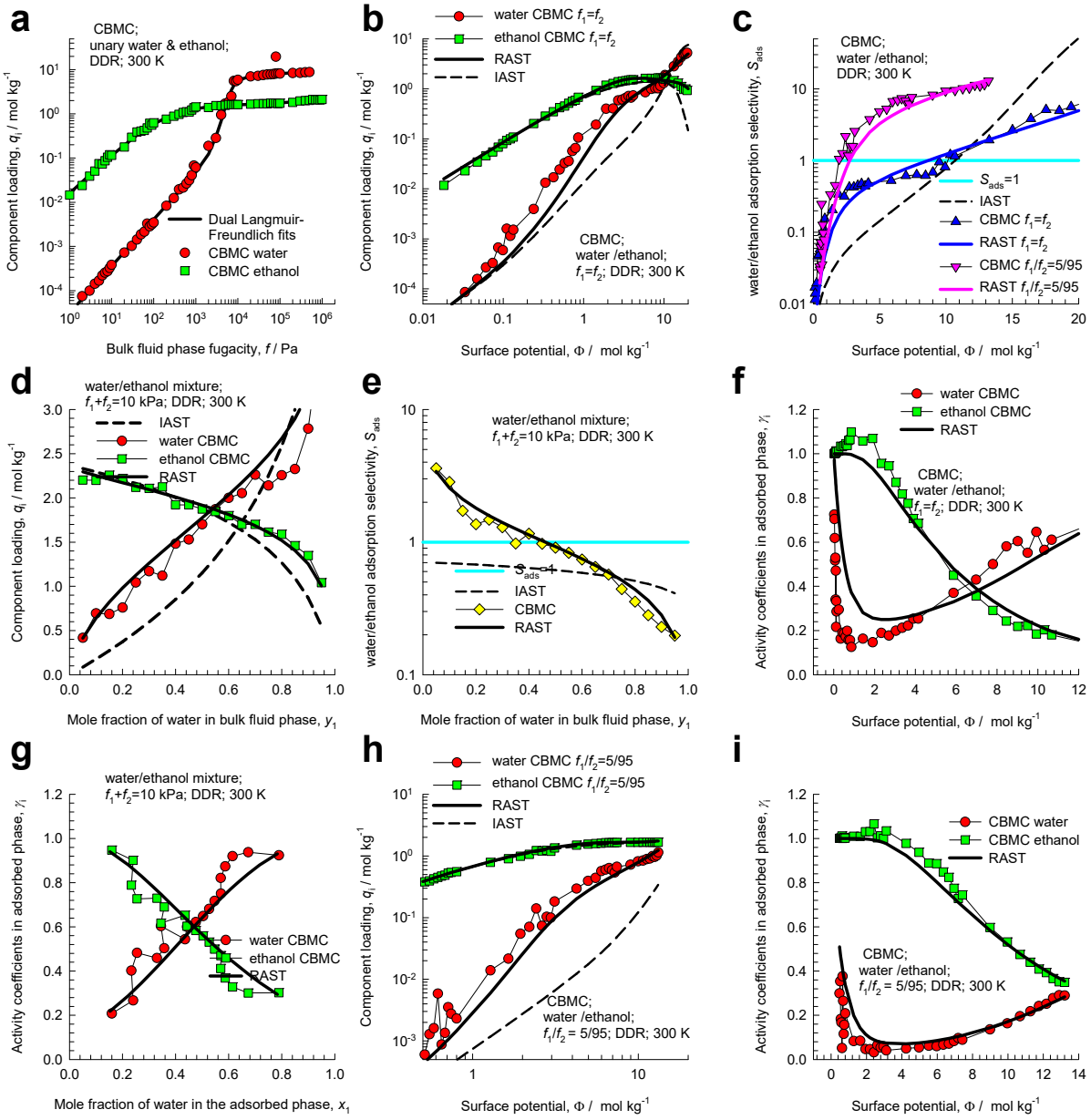

Figure S39. CBMC simulation data on component loadings, selectivities, and activity coefficients for Campaigns A (y_1= 0.5 and y_1= 0.05) and Campaign B (f_t= 10 kPa) for water(1)/ethanol(2) mixtures in DDR zeolite at 300 K The CBMC data are compared with RAST calculations using fitted NRTL parameters provided in Table S9. The dashed lines are IAST calculations.

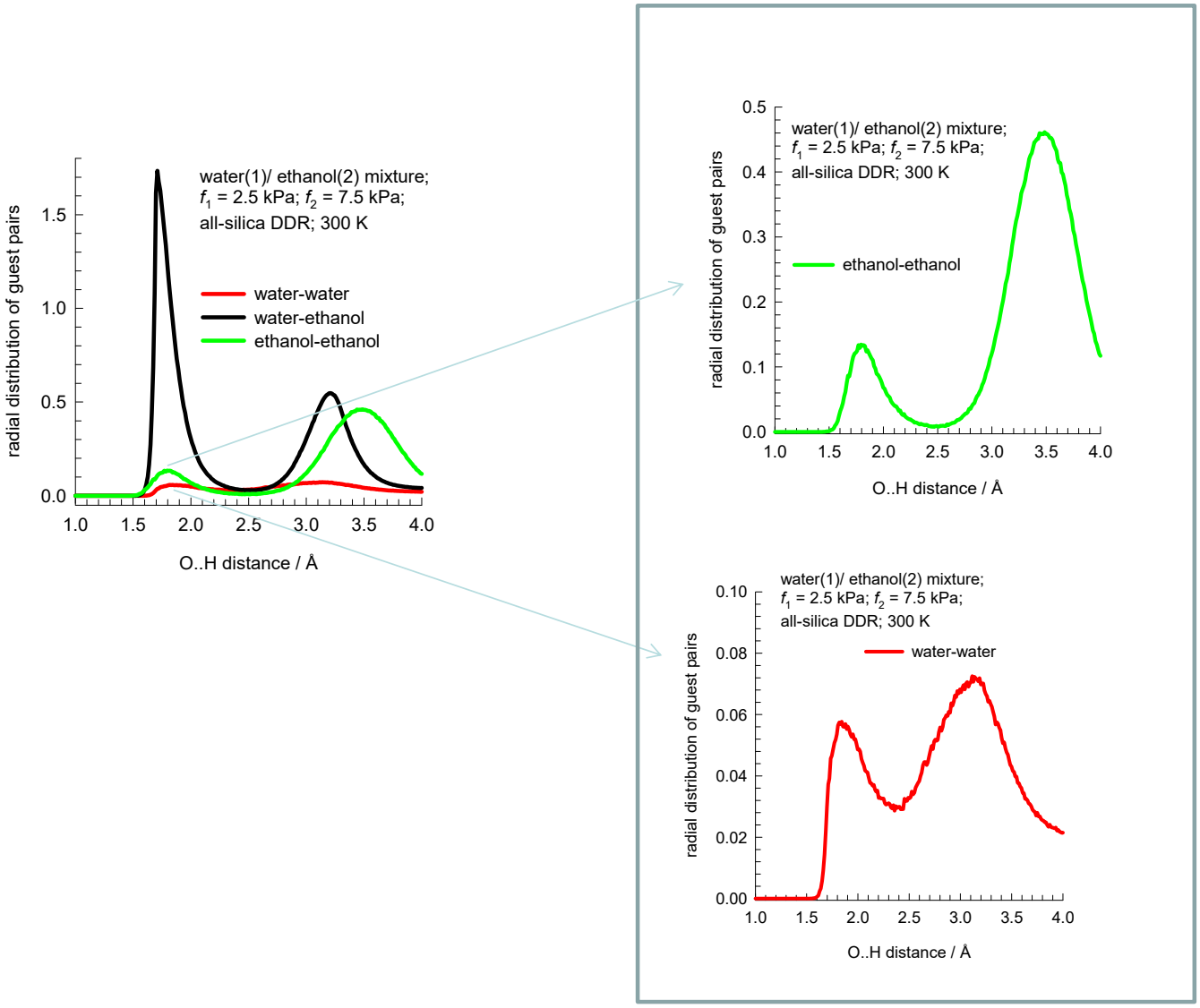

Figure S40. RDF of O···H distances for molecular pairs of water(1)/ethanol(2) mixture adsorption in DDR zeolite at 300 K. The partial fugacities of components 1 and 2 are f_1= 2.5 kPa, f_2= 7.5 kPa.

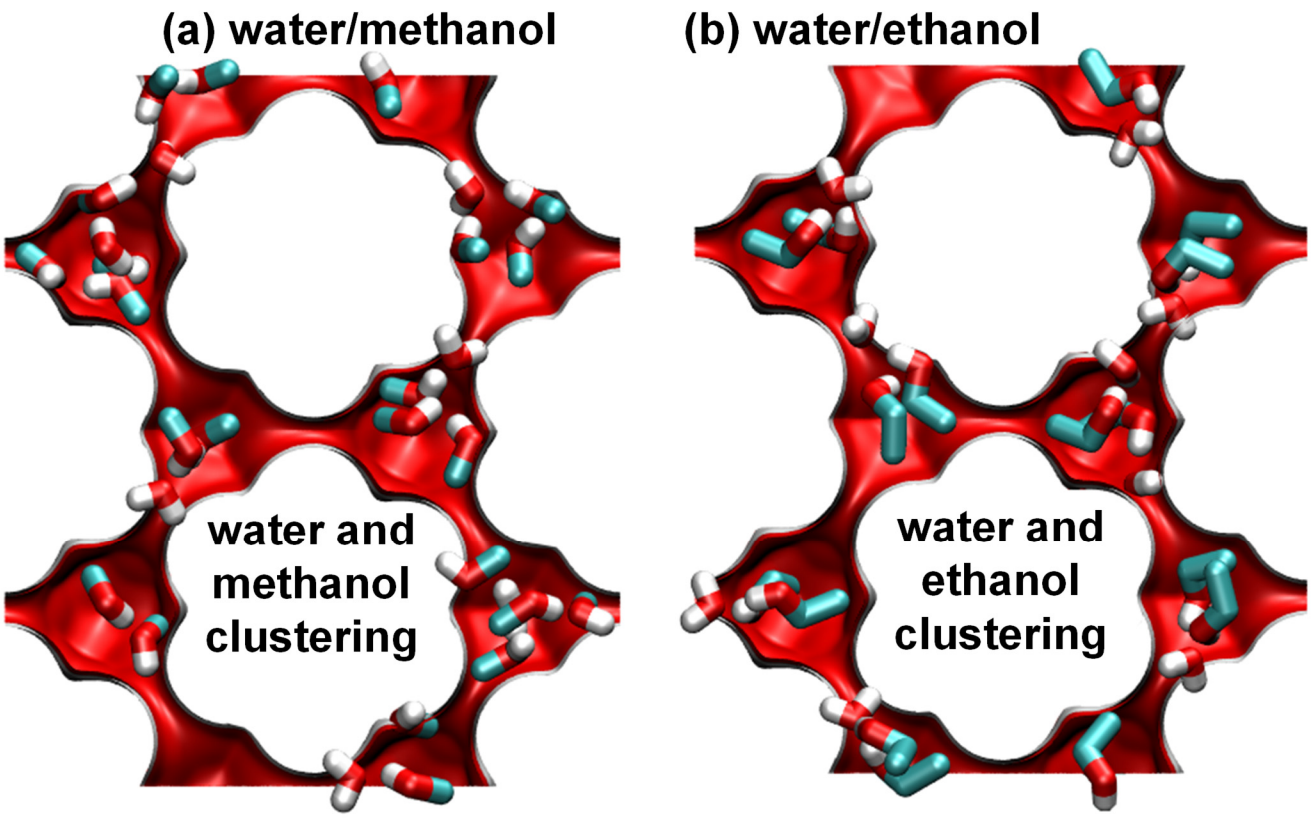

Figure S41. Snapshots showing location and conformations of guest molecules for adsorption of (a) water(1)/methanol(2), and (b) water(1)/ethanol(2) mixture adsorption in DDR zeolite at 300 K. The partial fugacities of components 1 and 2 are f_1= 2.5 kPa, f_2= 7.5 kPa.

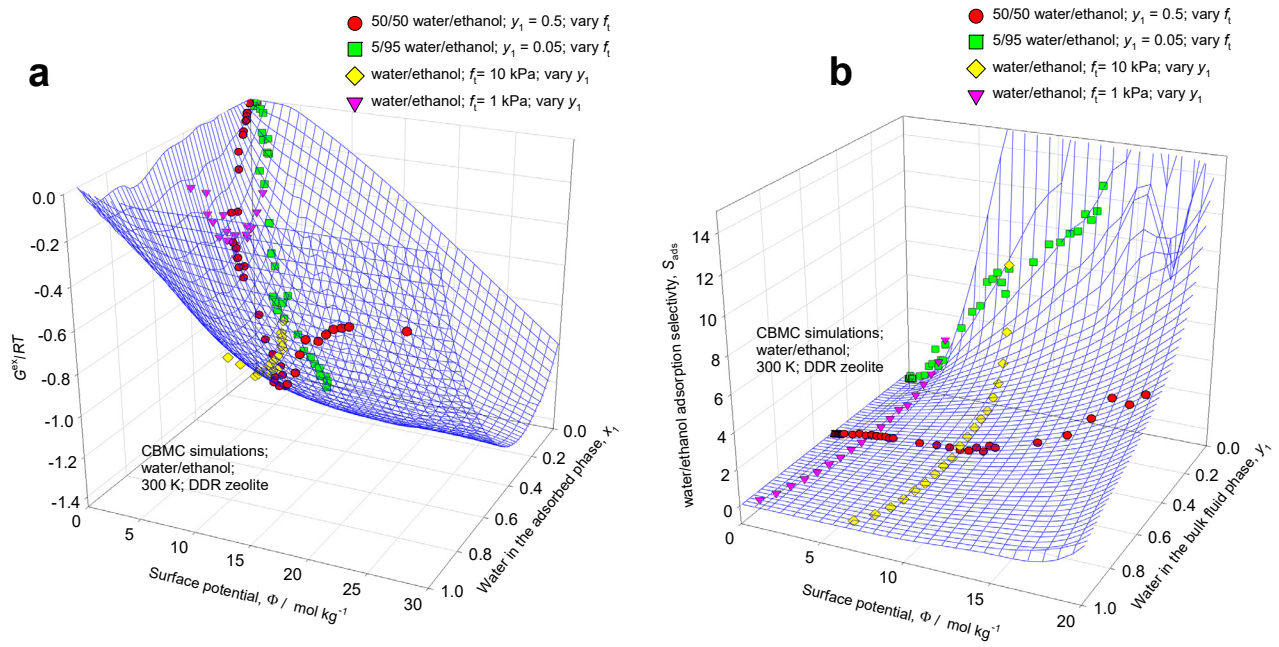

Figure S42. 3D plots of CBMC data for three different campaigns on (a) excess Gibbs free energy $G^{ex}/RT = x_1 \ln(\gamma_1) + x_2 \ln(\gamma_2)$, and (b) adsorption selectivity for water(1)/ethanol(2) mixture adsorption in DDR zeolite at 300 K. The 3D mesh is constructed using the NRTL parameters provided in Table S9.

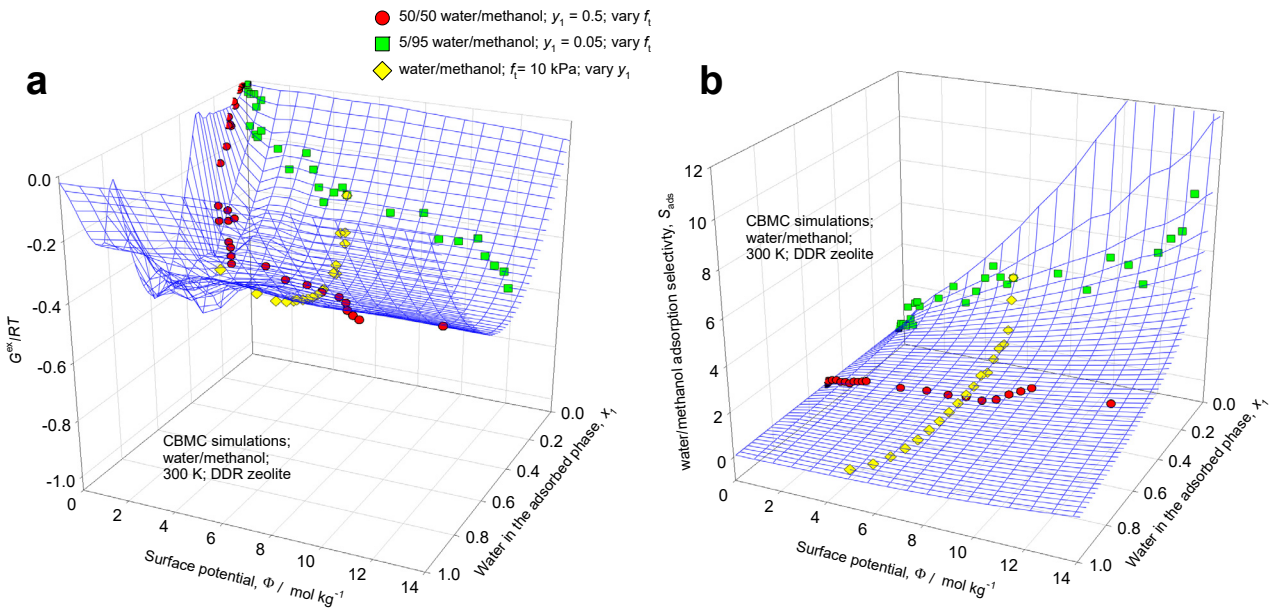

Figure S43. 3D plots of CBMC data for three different campaigns on excess Gibbs free energy $G^{ex}/RT = x_1 \ln(\gamma_1) + x_2 \ln(\gamma_2)$ for water(1)/methanol(2) mixture adsorption in DDR zeolite at 300 K. The 3D mesh is constructed using the NRTL parameters provided in Table S9.

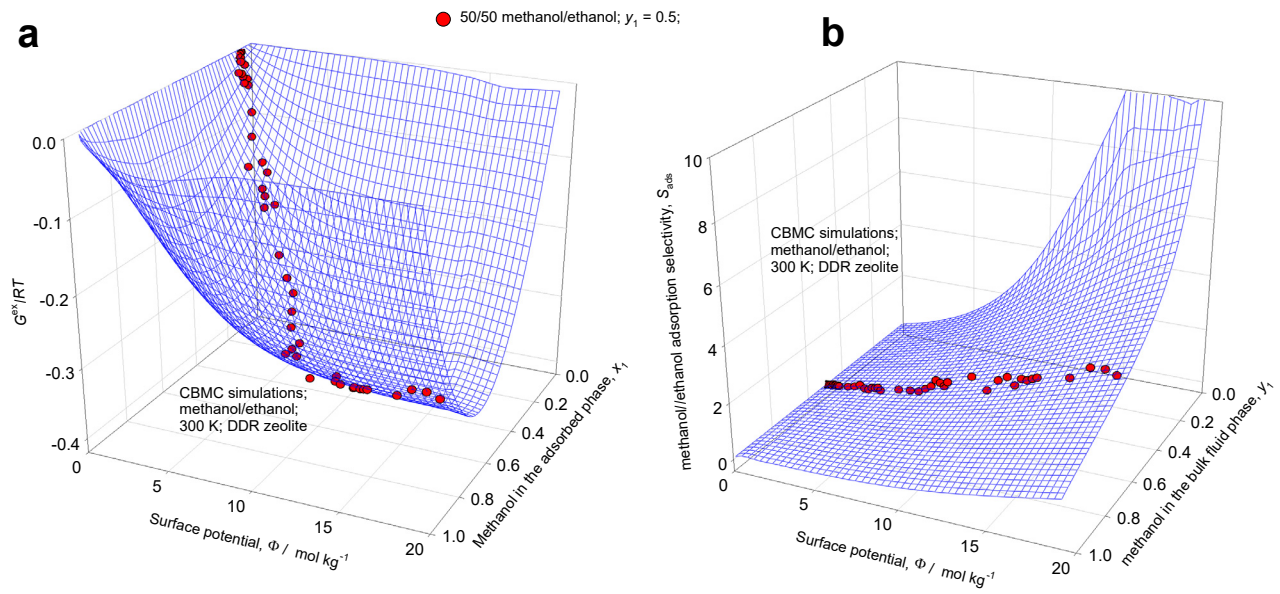

Figure S44. 3D plots of CBMC data on (a) excess Gibbs free energy $G^{ex}/RT = x_1 \ln(\gamma_1) + x_2 \ln(\gamma_2)$ and (b) adsorption selectivity for methanol(1)/ethanol(2) mixture adsorption in DDR zeolite at 300 K. The 3D mesh is constructed using the NRTL parameters provided in Table S9.

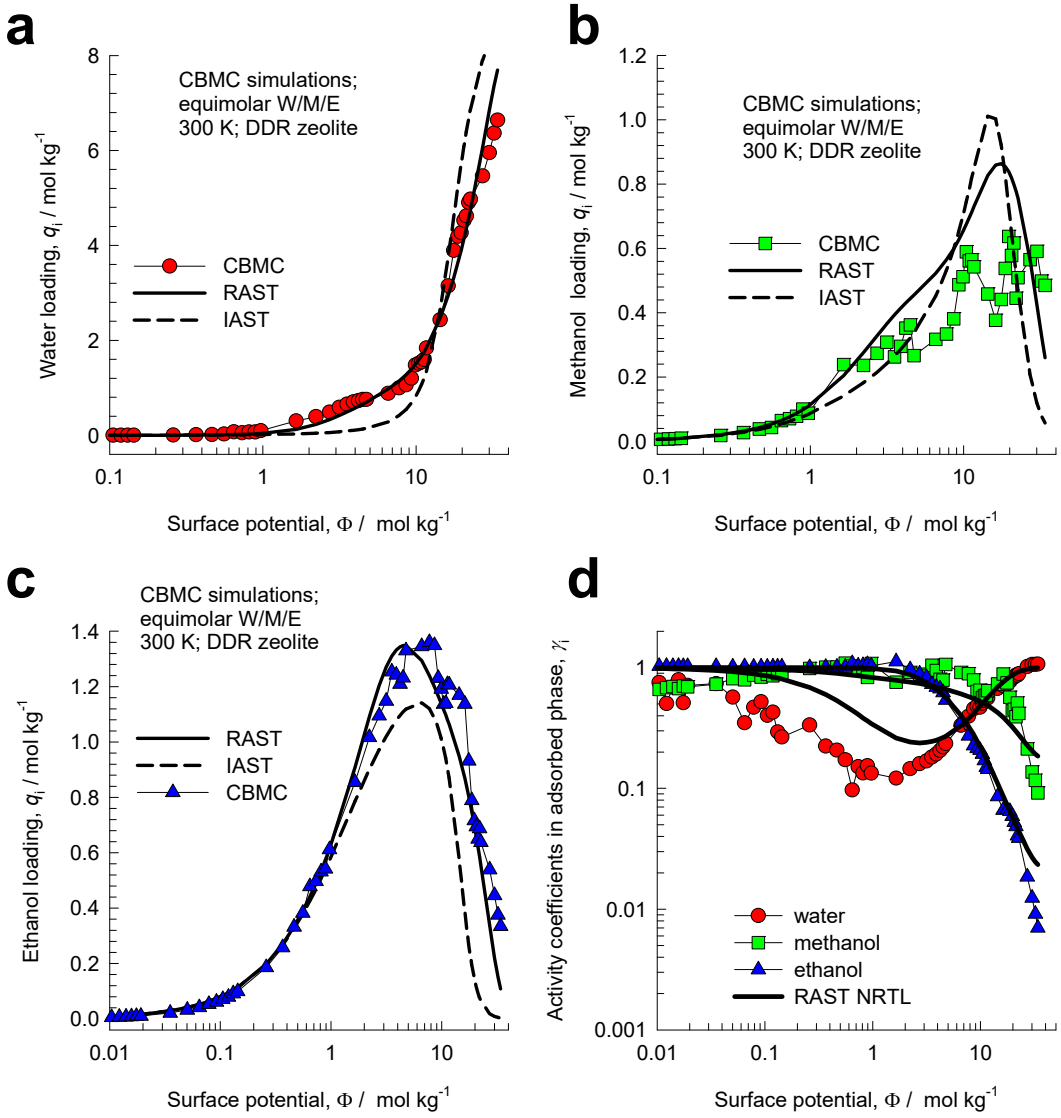

Figure S45. CBMC simulations (indicated by symbols) for equimolar 1/1/1 water(1)/methanol(2)/ethanol(3) mixtures in DDR zeolite at 300 K. (a, b, c) Component loadings from CBMC are compared with IAST and RAST estimates. (d) Activity coefficients as function of the surface potential. The NRTL parameters are provided in Table S9.

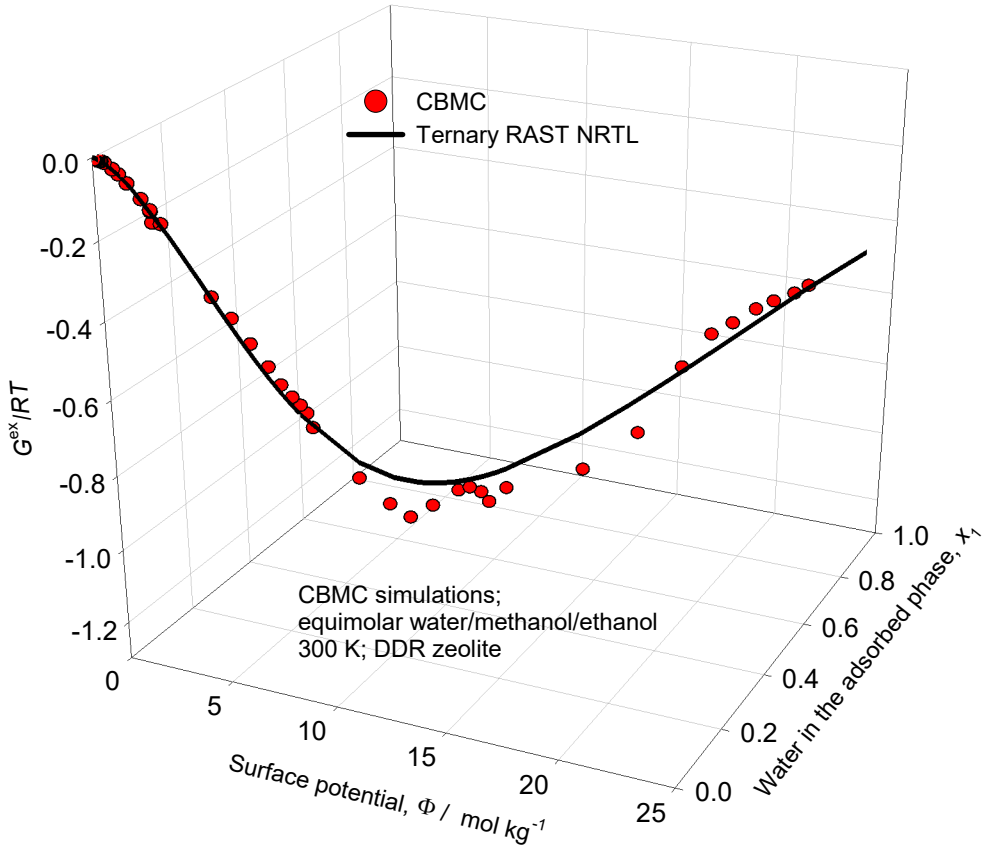

Figure S46. 3D plot of CBMC data on excess Gibbs free energy $G^{ex}/RT = \sum_{i=1}^{n} x_i \ln(\gamma_i)$ for equimolar 1/1/1 water(1)/methanol(2)/ethanol(3) mixtures in DDR zeolite at 300 K. Comparison is made with the estimates of the ternary NRTL RAST model. The NRTL parameters for the binary pairs are as provided in Table S9.

9 Mixture adsorption in FAU and NaX zeolites

Figure S5 presents the structural details of FAU (all-silica) zeolite. It has cages of 786 Å^3 volume, separated by 7.4 Å 12-ring windows. Figure S6 show the structural details of NaX (= 86 Na^+/uc = 13X) zeolite. Per unit cell of NaX zeolite we have 106 Si, 86 Al, 86 Na^+ with Si/Al=1.23. This material is also commonly referred to by its trade name: 13X zeolite.

9.1 CO_2/CH_4 mixture adsorption in NaX zeolite

Three different campaigns were carried out for CBMC simulations of $CO_2(1)/CH_4(2)$ mixture adsorption in NaX zeolite at 300 K. In campaign A, the mole fraction of $CO_2(1)$ in the bulk gas phase is held constant (at two different values $y_1 = 0.05$, and $y_1 = 0.5$) and the bulk gas phase fugacity $f_t = f_1 + f_2$ was varied. In campaign B, the mole fraction of $CO_2(1)$ in the bulk gas phase, y_1 was varied from 0 to 1, keeping the bulk gas phase mixture fugacity $f_t = f_1 + f_2$ constant at a value of 100 kPa. The CBMC results of these campaigns are presented in Figure S47.

Figure S47a,b compares CBMC data on adsorption selectivity, $S_{ads} = \frac{q_1/q_2}{f_1/f_2}$, compared with IAST estimates indicated by the dashed lines. We note that IAST severely overestimates S_{ads} for all campaigns. The IAST anticipates S_{ads} to be independent of bulk gas mixture composition, $y_1 = \frac{f_1}{f_1 + f_2}$, and depends only on the surface potential Φ; this expectation is not fulfilled for any campaign.

The continuous solid lines in Figure S47 are the RAST calculations using fitted Wilson parameters as specified in Table S10. For the Wilson fits, we calculate the parameter C using $C = \frac{1}{\frac{x_1}{q_{1,sat}} + \frac{x_2}{q_{2,sat}}}$; $q_{i,sat} = q_{i,A,sat} + q_{i,B,sat}$; $i = 1, 2$, with the arbitrary assumption that $x_1 = x_2 = 0.5$.

Figure S47c,d,e plot the activity coefficients of the guest components in the adsorbed phase as function of (c) mole fraction of CO_2(1) in the adsorbed phase for campaign B, , and (d, e) the surface potential Φ for campaigns A. For campaign B, we note the limiting behaviors $x_i \to 1; \quad \gamma_i \to 1$. For campaigns A we note that the activity coefficients are also dependent the surface potential Φ with the limiting characteristic $\Phi \to 0; \quad \gamma_1 \to 1; \quad \gamma_2 \to 1$. The introduction of $\left(1-\exp\left(-C\Phi\right)\right)$ in the Wilson model, eq (S39), imparts the correct limiting behaviors $\Phi \to 0; \quad \theta \to 0; \quad \gamma_i \to 1$ for the activity coefficients in the Henry regime, $f_t \to 0; \quad \Phi \to 0$, as the pore occupancy tends to vanishingly small values. As pore saturation conditions are approached, this correction factor tends to unity: $\left(1-\exp\left(-C\Phi\right)\right) \to 1$.

The CBMC data in Figure S47c,d,e lead us to conclude that the activity coefficients are functions of both Φ and x_1. In Figure S48 the CBMC data for the excess Gibbs free energy $G^{ex}/RT = x_1 \ln\left(\gamma_1\right) + x_2 \ln\left(\gamma_2\right)$ for the aforementioned campaigns, along with an additional CBMC campaign A (with y_1 = 0.1, and y_1 = 0.2) are plotted in 3D space as function of Φ and x_1. The entire CBMC data set resides on a 3D surface mesh determined from the fitted Wilson parameters in Table S10; see Figure S48b.

The failure of the IAST witnessed in Figure S47 is traceable to the non-uniform distribution of the guest molecules CO_2, and CH_4 within the cages of NaX zeolite. To demonstrate this, the CBMC simulation data on the spatial locations of the guest molecules were sampled to determine the inter-molecular distances. By sampling a total of 10^5 simulation steps, the radial distribution of the separation distances between the molecular pairs CO_2-CO_2, CO_2-Na^+, CO_2-CH_4, and CH_4-CH_4 were determined. The samples were taken up to a radial distance of 12 Å, but the *x*-axis has been truncated at 8 Å because only the first peaks are of interest in the discussions to follow. The plotted RDF data has been normalized such that the area under each of the curves is identical to one another (and equals 1000). Figure S49a presents the RDF data for a total fugacity f_t = 1 MPa and y_1=0.01. If we compare the first peaks, it is noteworthy that the CO_2-CO_2, and CO_2-Na^+ pairs are close together, indicating that the major proportion

of CO_2 congregates around the cations. A further point to note is that the CO_2-CH_4 separation distance is significantly higher than the CO_2-CO_2 and CH_4-CH_4 separation distances. This implies that the CH_4 molecules face a less severe competitive adsorption with CO_2 than is anticipated by the IAST.

A visual appreciation of the congregation effects can be gained from the snapshot presented in Figure S50.

The primary reason for the congregation of CO_2 molecules is the presence of cations. In order to demonstrate this, we also carried out CBMC simulations for adsorption of CO_2/CH_4 mixtures in all-silica zeolite at a total fugacity f_t = 500 kPa and y_1=0.2 at 300 K. The RDF data on the distances between the molecular pairs CO_2-CO_2, CO_2-CH_4, and CH_4-CH_4 are shown in Figure S49b. We note that the peaks occur at practically the same intermolecular distances. This indicates that there are no congregation effects and that the guest molecules are homogeneously distributed within the pore landscape. Such a homogeneous distribution of guest molecules fulfils the requirement of the IAST theory. Consequently, we should expect the IAST to provide a good quantitative description of CO_2/CH_4 mixture adsorption in all-silica zeolite.

To confirm this expectation, Figure S51a compares the CBMC simulated values of the adsorption selectivity for 50/50 CO_2/CH_4, 20/80 CO_2/CH_4, 15/85 CO_2/N_2, 20/80 CO_2/N_2, and 20/40/40 CO_2/CH_4/N_2 mixtures in all-silica FAU with the corresponding IAST calculations. The CO_2/CH_4, and CO_2/N_2 selectivities are uniquely determined by the surface potential , irrespective of the composition of the bulk fluid phase mixture and the preΦsence of the third component. The IAST estimations are in good agreement with the CBMC simulated values of S_{ads}.

In sharp contrast, the IAST calculations severely over-predict the adsorption selectivity for equimolar CO_2/CH_4 mixtures in NaX zeolite because the actual competition faced by CH_4 is less severe due to congregation effects; see Figure S51b. Also shown in Figure S51b are the CBMC data for CO_2/CH_4 mixture adsorption in NaY zeolite (138 Si, 54 Al, 54 Na^+, Si/Al=2.56); the IAST estimates are also in excess of the CBMC data, but the departures are less than that experienced with NaX.

Figure S51c presents a different way to demonstrate that the of CO_2/CH_4 selectivity for ideal mixtures is dependent only on the surface potential Φ and not the bulk gas phase composition, y_1, Figure S51b is a 3D plot the of $CO_2(1)/CH_4(2)$ selectivity as a function of Φ and y_1, The CBMC data for 50/50 CO_2/CH_4, 20/80 CO_2/CH_4, 20/40/40 $CO_2/CH_4/N_2$, and 33.333/33.333/33.333 $CO_2/CH_4/N_2$ mixtures reside on a 3D mesh created by IAST calculations. The 3D plot confirms the unique S_{ads} vs Φ dependence.

9.2 CO_2/C_3H_8 mixture adsorption in NaX zeolite

Two different campaigns were carried out for CBMC simulations of $CO_2(1)/C_3H_8(2)$ mixture adsorption in NaX zeolite at 300 K. In campaign A, the mole fraction of $CO_2(1)$ in the bulk gas phase is held constant (at two different values, $y_1 = 0.25$, and $y_1 = 0.5$), and the bulk gas phase fugacity $f_t = f_1 + f_2$ was varied. In campaign A, the mole fraction of $CO_2(1)$ in the bulk gas phase, y_1 was varied from 0 to 1, keeping the bulk gas phase mixture fugacity $f_t = f_1 + f_2$ constant at a value of 1 MPa. The CBMC results of these campaigns are presented in Figure S52,

Figure S52a,b compares CBMC data on adsorption selectivity, $S_{ads} = \frac{q_1/q_2}{f_1/f_2}$, compared with IAST estimates indicated by the dashed lines. We note that IAST overestimates S_{ads} for all campaigns. The IAST anticipates S_{ads} to be independent of bulk gas mixture composition, $y_1 = \frac{f_1}{f_1 + f_2}$, and depends only on the surface potential Φ; this expectation is not fulfilled for any campaign.

The continuous solid lines in Figure S52 are the RAST calculations using fitted Wilson parameters as specified in Table S10. For the Wilson fits, we calculate the parameter C using $C = \frac{1}{\frac{x_1}{q_{1,sat}} + \frac{x_2}{q_{2,sat}}}$; $q_{i,sat} = q_{i,A,sat} + q_{i,B,sat}$; $i = 1, 2$, with the arbitrary assumption that $x_1 = x_2 = 0.5$.

Figure S52c,d,e plot the activity coefficients of the guest components in the adsorbed phase as function of (c) mole fraction of $CO_2(1)$ in the adsorbed phase for campaign B, x_1, and (d, e) the surface potential

Φ for campaign A. For campaign B, we note the limiting behaviors $x_i \to 1; \quad \gamma_i \to 1$. For campaign A we note that the activity coefficients are also dependent the surface potential Φ with the limiting characteristic $\Phi \to 0; \quad \gamma_1 \to 1; \quad \gamma_2 \to 1$. The introduction of $\left(1-\exp\left(-C\Phi\right)\right)$ in the Wilson model, eq (S39), imparts the correct limiting behaviors $\Phi \to 0; \quad \theta \to 0; \quad \gamma_i \to 1$ for the activity coefficients in the Henry regime, $f_t \to 0; \quad \Phi \to 0$, as the pore occupancy tends to vanishingly small values. As pore saturation conditions are approached, this correction factor tends to unity: $\left(1-\exp\left(-C\Phi\right)\right) \to 1$.

Particularly remarkable are the results in which the total bulk fluid phase fugacity is maintained at f_t = 50 kPa; see Figure S53. We note that as the mole fraction of CO_2 in the bulk gas phase, y_1, is increased, the CBMC data shows selectivity reversal at $y_1 > 0.8$, in agreement with the experimental findings of Costa et al.[63] This selectivity reversal in disfavor of CO_2 is not anticipated by the IAST.

The CBMC data in Figure S52, and Figure S53 lead us to conclude that the activity coefficients are functions of both Φ and x_1. In Figure S54a, the CBMC data for the excess Gibbs free energy $G^{ex}/RT = x_1 \ln\left(\gamma_1\right) + x_2 \ln\left(\gamma_2\right)$ are plotted in 3D space as function of Φ and x_1. The entire CBMC data set resides on a 3D surface mesh determined from the fitted Wilson parameters; see Figure S54b.

Figure S54c presents a 3D plot of the $CO_2(1)/C_3H_8(2)$ adsorption selectivity as function of the surface potential Φ and mole fraction of CO_2 in the bulk gas phase, y_1. The entire CBMC data set resides on a 3D surface mesh determined from the fitted Wilson parameters in Table S10. Figure S54c confirms that the adsorption selectivity is not uniquely determined by the surface potential, Φ, but is additionally dependent on the bulk phase mixture composition.

The failure of the IAST to provide quantitatively accurate estimates of component loadings, and adsorption selectivities is attributable to the inhomogeneous distribution of adsorbates in the pore space of NaX zeolite, caused by strong binding of CO_2 with the extra-framework cations. The inhomogeneous distribution is clearly visualized by the computational snapshot in Figure S55 for f_1 = 0.5 MPa, and f_2 = 0.5 MPa. We note that the bottom cage contains only CO_2, and there is no C_3H_8 present in that cage. One

of the key assumptions of the IAST is that the distribution of adsorbates within the pore space is homogenous.

To quantify the inhomogeneous distribution of adsorbates, the CBMC simulation data on the spatial locations of the guest molecules were sampled to determine the inter-molecular distances. By sampling a total of 10^7 simulation steps, the radial distribution of the separation distances between the molecular pairs CO_2-CO_2, CO_2-Na^+, CO_2-C_3H_8, and C_3H_8-C_3H_8 were determined. Figure S56 presents the RDF data for a total fugacity f_t = 1 MPa and y_1=0.5. The samples were taken up to a radial distance of 12 Å, but the *x*-axis has been truncated at 8 Å because only the first peaks are of interest in the discussions to follow. The plotted RDF data has been normalized such that the area under each of the curves is identical to one another. If we compare the first peaks, it is noteworthy that the CO_2-CO_2, and CO_2-Na^+ pairs are close together, indicating that the major proportion of CO_2 congregates around the cations. A further point to note is that the CO_2-C_3H_8 separation distance is significantly higher than the CO_2-CO_2 and CO_2-Na^+ separation distances. This implies that the C_3H_8 molecules face a less severe competitive adsorption with CO_2 than is anticipated by the IAST.

For the mixture of alkanes, there are no segregation effects to be expected in NaX zeolites, and the IAST estimates are in good agreement with CBMC simulation data; see Figure S57a,b for adsorption selectivity S_{ads} for (a) 50/50 C_3H_8(1)/CH_4(2), and (b) 50/50 C_2H_6(1)/CH_4(2) mixture adsorption in NaX zeolite at 300 K, plotted as function of the surface potential Φ. The IAST estimates are in good agreement with CBMC simulation data.

Figure S57c,d present CBMC data on adsorption selectivity S_{ads} for (c) 50/50 CH_4(1)/N_2(2), 25/75 CH_4(1)/N_2(2), and (d) 50/50 CH_4(1)/H_2(2) mixture adsorption in NaX zeolite at 300 K, plotted as function of the surface potential Φ. The IAST estimates are in good agreement with CBMC simulation data confirming that these mixtures also conform with thermodynamic ideality.

9.3 $CO_2/CH_4/C_3H_8$ mixture adsorption in NaX

CBMC simulations were carried out for 10/70/20 $CO_2/CH_4/C_3H_8$ mixtures in NaX at 300 K for a range of total fugacities, f_t. In Figure S58 the excess Gibbs free energy $G^{ex}/RT = \sum_{i=1}^{n} x_i \ln(\gamma_i)$ determined from CBMC data are plotted in 3D space as function of Φ and x_1. The continuous solid line represents the ternary RAST Wilson calculations. The Wilson parameters for the binary pairs $\Lambda_{12}, \Lambda_{21}, \Lambda_{13}, \Lambda_{31}, \Lambda_{23}, \Lambda_{32}$ are taken to the same as for the corresponding binary pairs as listed in Table S10. Noteworthily, $\Lambda_{23} = 1, \Lambda_{32} = 1$ because the CH_4/C_3H_8 mixtures behave ideally (cf. Figure S57a). Our approach for ternary mixtures is to estimate C as $C = \frac{x_1}{q_{1,sat}} + \frac{x_2}{q_{2,sat}} + \frac{x_3}{q_{3,sat}}$, assuming, $x_1 = x_2 = x_3 = 1/3$. The RAST estimates are in reasonable agreement with the ternary CBMC data set.

9.4 CO_2/N_2 mixture adsorption in NaX zeolite; CBMC simulations

Figure S59a presents CBMC simulations of unary isotherm data of CO_2, and N_2 in NaX (106 Si, 86 Al, 86 Na^+ with Si/Al=1.23) zeolite at 300 K. Figure S59b presents the CBMC simulation data (indicated by symbols) of component loadings, q_i, of CO_2, and N_2 for adsorption of CO_2/N_2 mixtures in NaX zeolite at 300K and total fugacity f_t = 100 kPa, as function of the mole fraction of CO_2 in the bulk gas phase, y_1. The dashed lines in Figure S59b are the IAST estimations. The IAST estimations of the component loadings for N_2 are not in good agreement with the CBMC mixture simulations.

Figure S59c plots the CBMC data on the CO_2/N_2 adsorption selectivity as function of the mole fraction of CO_2 in the bulk gas phase. The IAST severely overestimates the adsorption selectivity.

The failure of the IAST is traceable to the non-uniform distribution of the guest molecules CO_2, and N_2 within the cages of NaX zeolite. To demonstrate this, the CBMC simulation data on the spatial locations of the guest molecules were sampled to determine the inter-molecular distances. By sampling a total of 10^6 simulation steps, the radial distribution function (RDF) were determined for CO_2-CO_2, CO_2-Na^+, and CO_2-N_2 separation distances. Figure S60a presents the RDF data for a total fugacity f_t = 100 kPa and

y_1=0.05. The samples were taken up to a radial distance of 12 Å, but the *x*-axis has been truncated at 8 Å because only the first peaks are of interest in the discussions to follow. The plotted RDF data has been normalized such that the area under each of the curves is identical to one another (and equals 1000). If we compare the first peaks, it is noteworthy that the CO_2-CO_2, and CO_2-Na^+ pairs are close together; indicating that the major proportion of CO_2 congregates around the cations. A further point to note is that the CO_2-N_2 separation distance is significantly higher than the CO_2-CO_2 separation distance. This implies that the N_2 molecules face a less severe competitive adsorption with CO_2 than is anticipated by the IAST.

The primary reason for the congregation of CO_2 molecules is the presence of cations. In order to demonstrate this we also carried out CBMC simulations for adsorption of CO_2/N_2 mixtures in all-silica zeolite at a total fugacity f_t = 500 kPa and y_1=0.25 at 300 K. The RDF data on the distances between the molecular pairs CO_2-CO_2, CO_2-N_2, and N_2-N_2 are shown in Figure S60b. We note that the peaks occur at practically the same intermolecular distances. This indicates that there are no congregation effects and that the guest molecules are homogeneously distributed within the pore landscape. Such a homogeneous distribution of guest molecules fulfils the requirement of the IAST theory. Consequently, we should expect the IAST to provide a good quantitative description of CO_2/N_2 mixture adsorption in all-silica zeolite. To confirm this expectation, Figure S61a compares the CBMC simulated values of the adsorption selectivity for equimolar CO_2/N_2 mixtures in all-silica FAU with the corresponding IAST calculations using the CBMC simulated unary isotherm fits in Table S11. There is perfect agreement the two data sets. In sharp contrast, the IAST calculations severely over-predict the adsorption selectivity for equimolar CO_2/N_2 mixtures in NaX zeolite because the actual competition faced by N_2 is less severe due to congregation effects.

9.5 CO_2/CH_4/N_2 mixture adsorption in NaX

CBMC simulations were carried out for ternary 20/40/40 CO_2/CH_4/N_2, and 5/25/70 CO_2/CH_4/N_2 mixtures in NaX at 300 K for a range of total fugacities, f_t. In Figure S62 the excess Gibbs free energy $G^{ex}/RT = \sum_{i=1}^{n} x_i \ln(\gamma_i)$ determined from CBMC data are plotted in 3D space as function of Φ and x_1.

The continuous solid line represents the ternary RAST Wilson calculations. The Wilson parameters for the binary pairs $\Lambda_{12}, \Lambda_{21}, \Lambda_{13}, \Lambda_{31}, \Lambda_{23}, \Lambda_{32}$ are taken to the same as for the corresponding binary pairs as listed in Table S10. Noteworthily, $\Lambda_{23} = 1, \Lambda_{32} = 1$ because the CH_4/N_2 mixtures behave ideally (cf. Figure S57c). Our approach for ternary mixtures is to estimate C as $C = \frac{x_1}{q_{1,sat}} + \frac{x_2}{q_{2,sat}} + \frac{x_3}{q_{3,sat}}$, assuming, $x_1 = x_2 = x_3 = 1/3$. The RAST estimates are in reasonable agreement with the two ternary CBMC data sets.

9.6 Water/alcohol mixture adsorption in FAU (all silica) zeolite

Figure S63a,b presents RDF of O···H distances for molecular pairs of water(1)/methanol(2) (total loading = 72 molecules per unit cell), water(1)/ethanol(2) (total loading = 56 molecules per unit cell) mixture adsorption in FAU zeolite at 300 K; these mixture are equimolar in the adsorbed phase.[27] The degree of molecular clustering due to hydrogen bonding can be characterized by the magnitudes of the first peaks.[27, 61] The RDF data for water/methanol, and water/ethanol mixtures in FAU (all silica) were determined for a range of adsorbed phase compositions.[27] Collecting the data on the magnitude of the first peaks for water-alcohol mixtures in FAU, Figure S63c,d presents plots of the first-peak heights as function of the mole fraction of the alcohol. We observe that molecular clustering effects are higher for water-alcohol pairs, as compared to water-water, and alcohol-alcohol pairs.

Due to molecular clustering, we should anticipate that water/methanol and water/ethanol mixture adsorption in FAU (all silica) zeolite will be subject to significant deviations from the estimations of the IAST.

For adsorption of water(1)/methanol(2) mixtures in FAU (all silica) zeolite at 300 K, three different CBMC simulations were carried out: Campaign A (with y_1 = 0.5, vary f_t), and campaign B, the mole fraction of water(1) in the bulk fluid phase, y_1 was varied from 0 to 1, keeping the bulk fluid phase mixture fugacity $f_t = f_1 + f_2$ constant at values of 1 kPa, and 10 kPa. The CBMC data on component loadings, adsorption selectivities, and activity coefficients are presented in Figure S64.

The dashed lines are the IAST estimates. The failure of the IAST to match the CBMC data presented in is a consequence of hydrogen bonding between guest molecules in water/alcohol mixtures. [15, 18, 47, 48, 60] One of the mandates of the IAST is violated because of the formation of water/alcohol clusters.[15, 46, 48]

The continuous solid lines in Figure S64 are the RAST calculations with fitted Margules parameters specified in Table S12.

The CBMC data in Figure S64f,g leads us to conclude that the activity coefficients are functions of both the surface potential Φ and mole fraction of water in the adsorbed phase mixture, x_1. In Figure S65a the CBMC data for the excess Gibbs free energy $G^{ex}/RT = x_1 \ln(\gamma_1) + x_2 \ln(\gamma_2)$ for the three CBMC campaigns for water/methanol mixtures are plotted in 3D space as function of Φ and x_1. The entire CBMC data set resides on a 3D surface mesh determined from the fitted Margules parameters specified in Table S12.

In Figure S64b, the CBMC data for the water/methanol adsorption selectivity for water/methanol mixtures are plotted in 3D space as function of surface potential Φ and mole fraction of water in the bulk fluid phase mixture, y_1. The entire CBMC data set on S_{ads} resides on a 3D surface mesh determined from the fitted Margules parameters specified in Table S12. Figure S64b confirms that the adsorption selectivity is not uniquely determined by the surface potential, Φ, but is additionally dependent on the bulk phase mixture composition.

For adsorption of water(1)/ethanol(2) mixtures in FAU (all silica) zeolite at 300 K, two different CBMC simulations were carried out: Campaign A (with $y_1 = 0.5$, vary f_t), and campaign B, the mole fraction of water(1) in the bulk fluid phase, y_1 was varied from 0 to 1, keeping the bulk fluid phase mixture fugacity $f_t = f_1 + f_2$ constant at a value of 10 kPa. The CBMC data on component loadings, adsorption selectivities, and activity coefficients are presented in Figure S66. The continuous solid lines in Figure S66 are the RAST calculations with fitted Margules parameters specified in Table S12.

The CBMC data in Figure S66f,g leads us to conclude that the activity coefficients are functions of both the surface potential Φ and mole fraction of water in the adsorbed phase mixture, x_1. In Figure S67a the

CBMC data for the excess Gibbs free energy $G^{ex}/RT = x_1 \ln(\gamma_1) + x_2 \ln(\gamma_2)$ for the three CBMC campaigns for water/methanol mixtures are plotted in 3D space as function of Φ and x_1. The entire CBMC data set resides on a 3D surface mesh determined from the fitted Margules parameters specified in Table S12.

In Figure S67b, the CBMC data for the water/methanol adsorption selectivity for water/methanol mixtures are plotted in 3D space as function of surface potential Φ and mole fraction of water in the bulk fluid phase mixture, y_1. The entire CBMC data set on S_{ads} resides on a 3D surface mesh determined from the fitted Margules parameters specified in Table S12. Figure S67b confirms that the adsorption selectivity is not uniquely determined by the surface potential, Φ, but is additionally dependent on the bulk phase mixture composition.

Figure S68a,b presents CBMC data for two different CBMC campaigns for adsorption of water(1)/2-propanol(2) mixtures in FAU (all silica) zeolite at 300 K: Campaign A (with y_1 = 0.5, vary f_t), and campaign B, the mole fraction of water(1) in the bulk fluid phase, y_1 was varied from 0 to 1, keeping the bulk fluid phase mixture fugacity $f_t = f_1 + f_2$ constant at a value of 10 kPa. Figure S68a compares the CBMC data for the excess Gibbs free energy $G^{ex}/RT = x_1 \ln(\gamma_1) + x_2 \ln(\gamma_2)$ with the IAST estimates of $G^{ex}/RT = 0$. Clearly, thermodynamic non-idealities are in play for water(1)/2-propanol(2) mixture adsorption, as the CBMC data show that G^{ex}/RT is significantly negative.

Figure S68b compares the CBMC data on the adsorption selectivity, S_{ads}, with the IAST determined 3D mesh. The CBMC data shows that the selectivities from CBMC are significantly higher than the IAST estimates.

9.7 List of Tables for Mixture adsorption in FAU and NaX zeolites

Table S10. Dual-site Langmuir-Freundlich parameters for pure components CO_2, CH_4, N_2, and C_3H_8 at 300 K in NaX zeolite containing 86 Na^+/uc with Si/Al=1.23. The fit parameters are based on the CBMC simulations of pure component isotherms.

	Site A			Site B		
	$\frac{q_{A,sat}}{\text{mol kg}^{-1}}$	$\frac{b_A}{\text{Pa}^{-\nu_A}}$	ν_A	$\frac{q_{B,sat}}{\text{mol kg}^{-1}}$	$\frac{b_B}{\text{Pa}^{-\nu_B}}$	ν_B
CO_2	2.1	2.300E-04	0.67	4.4	4.136E-04	1
CH_4	5.5	2.187E-06	1	2.2	1.338E-08	1
N_2	9.8	1.030E-09	1	4.2	1.231E-07	1
C_3H_8	2.2	1.195E-04	1.46	1.6	1.151E-03	0.66

Fitted Wilson non-ideality parameters for mixture adsorption in NaX at 300 K.

	C / kg mol^{-1}	Λ_{12}	Λ_{12}
CO_2/C_3H_8	0.209	2.789	0.781
CO_2/CH_4	0.142	0.000	5.715
CO_2/N_2	0.113	4.303	0.027
$CO_2/CH_4//N_2$	0.118	$\Lambda_{12}, \Lambda_{21}, \Lambda_{13}, \Lambda_{31}, \Lambda_{23}, \Lambda_{32}$ as above	
$CO_2/CH_4/C_3H_8$	0.182	$\Lambda_{12}, \Lambda_{21}, \Lambda_{13}, \Lambda_{31}, \Lambda_{23}, \Lambda_{32}$ as above	

Table S11. Dual-site Langmuir-Freundlich parameters for pure components CO_2, CH_4, H_2, and N_2 at 300K in all-silica FAU. The fit parameters are based on the CBMC simulations of pure component isotherms presented in earlier works.[11, 64, 65]

	Site A			Site B		
	$\frac{q_{A,sat}}{\text{mol kg}^{-1}}$	$\frac{b_A}{\text{Pa}^{-\nu_A}}$	ν_A	$\frac{q_{B,sat}}{\text{mol kg}^{-1}}$	$\frac{b_B}{\text{Pa}^{-\nu_B}}$	ν_B
CO_2	2.4	2.52×10^{-14}	2.4	6.7	6.74×10^{-7}	1
CH_4	4	7×10^{-9}	0.86	6.5	2.75×10^{-7}	1
H_2	6.9	3.506E-08	1	16.7	3.848E-09	1
N_2	5.2	1.55×10^{-9}	1	5.8	1.32×10^{-7}	1

Table S12. Dual-site Langmuir-Freundlich parameters for adsorption of water, methanol, ethanol, and 2-propanol at 300 K in all-silica FAU zeolite. The fit parameters are based on the CBMC simulations of pure component isotherms presented in earlier works. [27, 46, 48]

Adsorbate	Site A			Site B		
	$\frac{q_{A,sat}}{\text{mol kg}^{-1}}$	$\frac{b_A}{\text{Pa}^{-\nu_A}}$	ν_A	$\frac{q_{B,sat}}{\text{mol kg}^{-1}}$	$\frac{b_B}{\text{Pa}^{-\nu_B}}$	ν_B
water	15.4	1.850E-121	32.6	7.4	3.555E-05	1
methanol	3.4	6.362E-16	4.6	5.8	1.679E-04	1
ethanol	2.5	3.189E-13	4.9	2.9	1.000E-03	1.05
2-propanol	1.5	3.906E-06	2.45	2.8	1.951E-03	1

Fitted Margules non-ideality parameters for binary mixture adsorption in all-silica FAU at 300 K. The fits are based on combining CBMC Campaigns A and B for each mixture.

	C / kg mol^{-1}	A_{12}	A_{21}
water/methanol	0.164	-1.131	-2.372
water/ethanol	0.178	-1.102	-1.766

9.8 List of Figures for Mixture adsorption in FAU and NaX zeolites

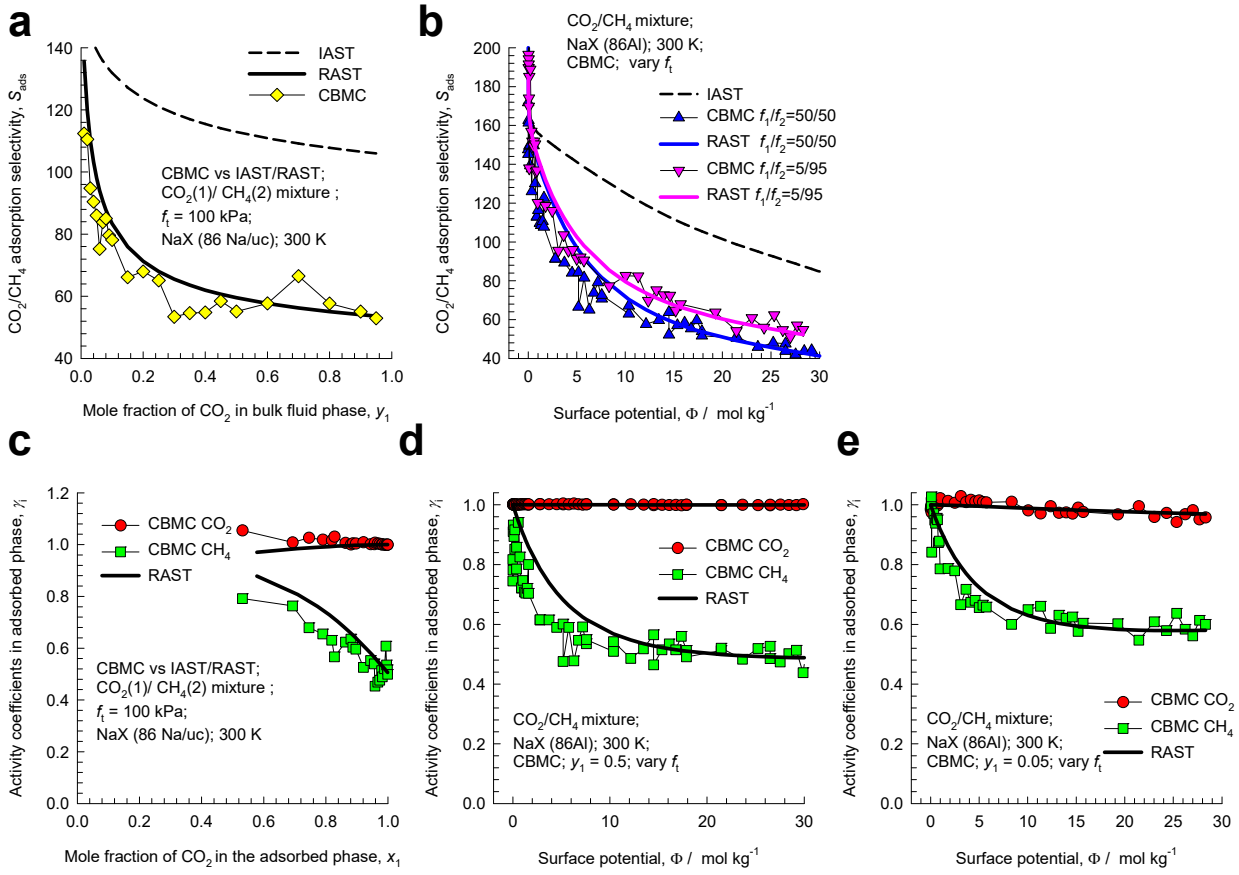

Figure S47. CBMC simulations data for $CO_2(1)/CH_4(2)$ mixture adsorption in NaX zeolite at 300 K. (a, b) CBMC data on adsorption selectivity compared with IAST (dashed lines) and RAST estimates (continuous solid lines). (c, d, e) CBMC data on activity coefficients in the adsorbed phase compared with RAST Wilson fits. The unary isotherm fit parameters and Wilson parameters are provided in Table S10.

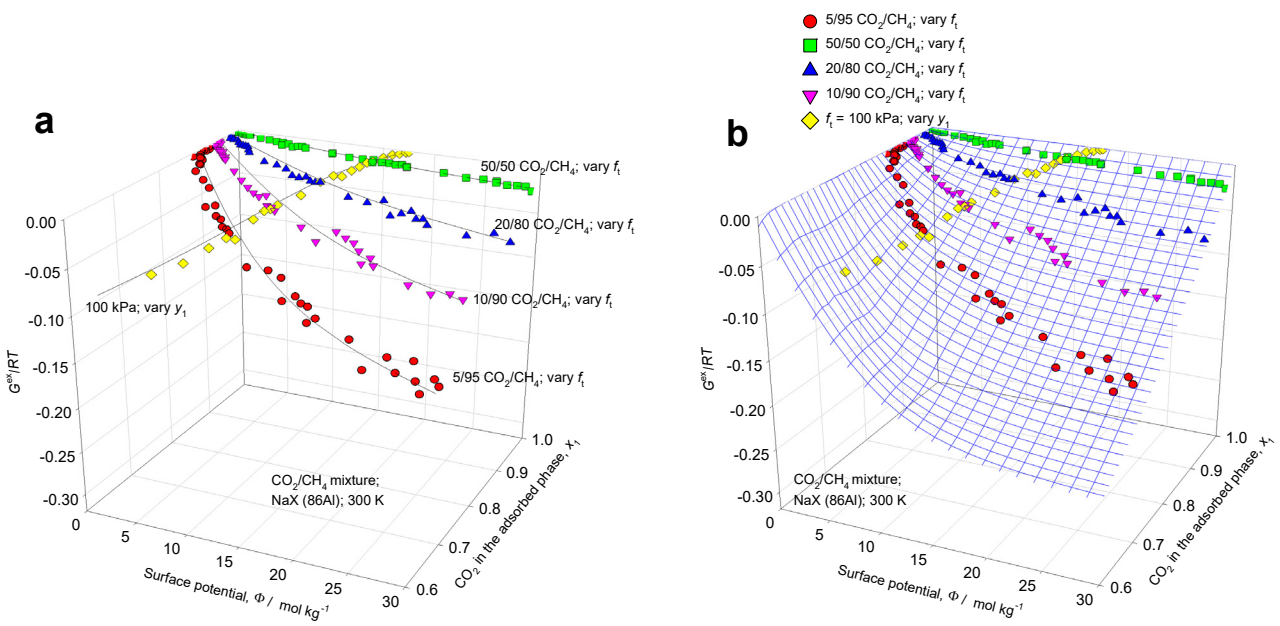

Figure S48. 3D plots of CBMC data on excess Gibbs free energy $G^{ex}/RT = x_1 \ln(\gamma_1) + x_2 \ln(\gamma_2)$ for $CO_2(1)/CH_4(2)$ mixture adsorption in NaX zeolite at 300 K, plotted as function of the surface potential, Φ, and the mole fraction of CO_2 in the adsorbed phase mixture, x_1. The 3D mesh is constructed using the Wilson parameters provided in Table S10.

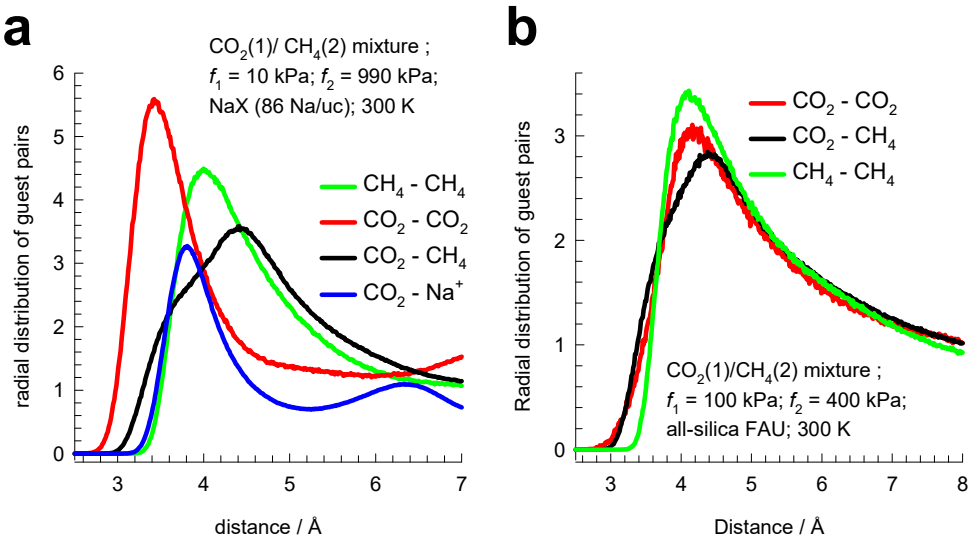

Figure S49. (a) Radial distribution of guest pairs determined from CBMC simulations for adsorption of CO_2/CH_4 mixtures in NaX zeolite at 300 K and total fugacity f_t = 1 MPa, and y_1=0.01. (b) Radial distribution of guest pairs determined from CBMC simulations for adsorption of CO_2/CH_4 mixtures in all-silica FAU zeolite at 300 K and total fugacity f_t = 500 kPa, and y_1=0.2.

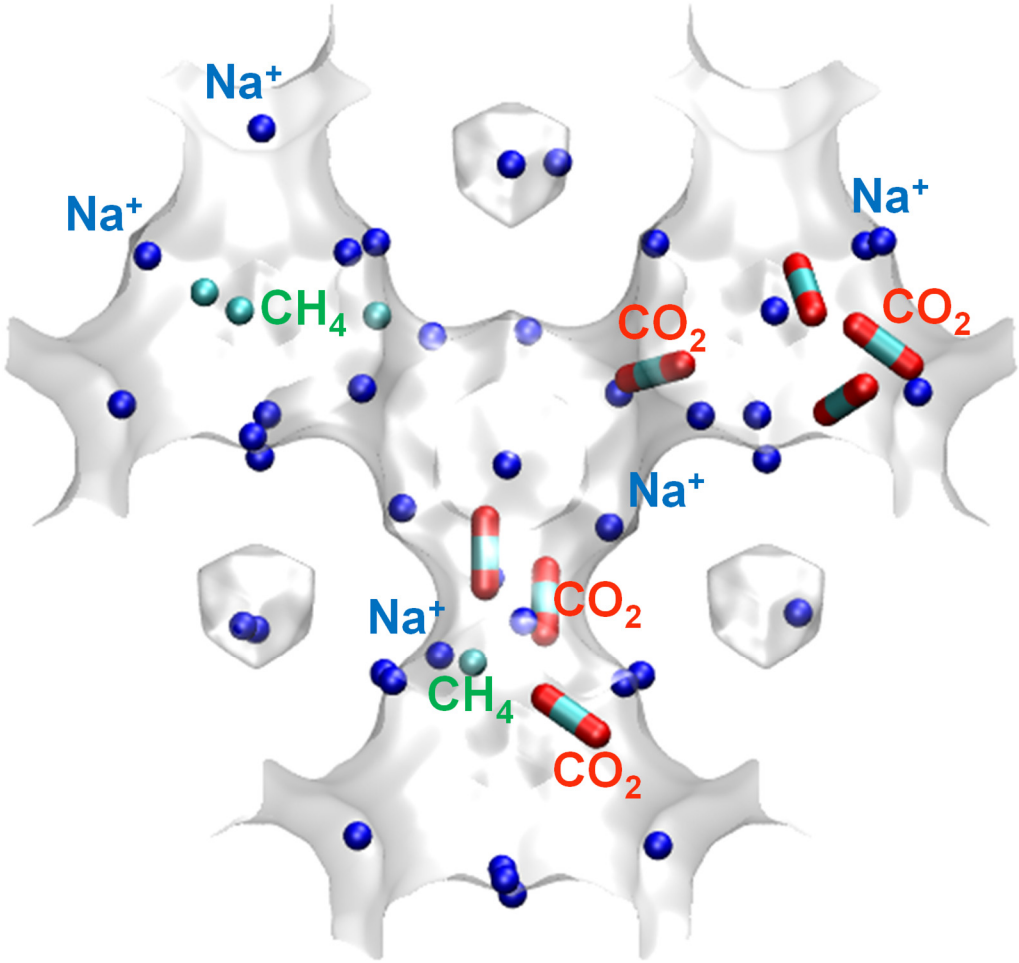

Figure S50. Snapshot showing the location of CO_2, CH_4, and Na+ cations within the pore landscape of NaX (106 Si, 86 Al, 86 Na^+, Si/Al=1.23) zeolite at 300 K and total fugacity f_t = 100 kPa, and y_1=0.02.

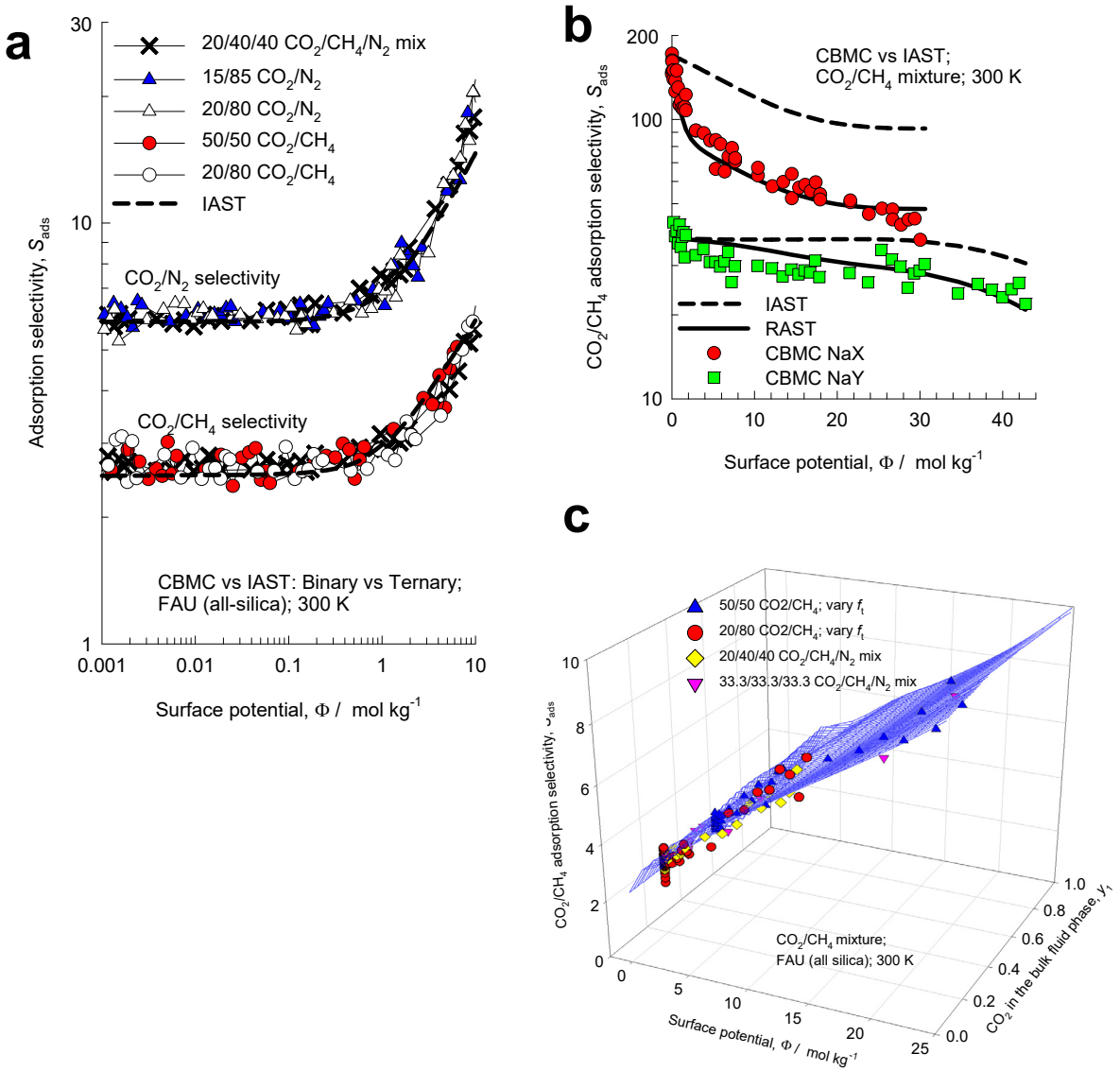

Figure S51. (a) CBMC data for adsorption selectivity of 50/50 CO_2/CH_4, 20/80 CO_2/CH_4, 15/85 CO_2/N_2, 20/80 CO_2/N_2, and 20/40/40 $CO_2/CH_4/N_2$ mixtures in all-silica FAU. (b) Comparison CO_2/CH_4 adsorption selectivities determined from CBMC simulations for NaY (138 Si, 54 Al, 54 Na^+, Si/Al=2.56), and NaX (106 Si, 86 Al, 86 Na^+, Si/Al=1.23) zeolites for at 300 K. The *x*-axes represent the surface potential Φ. The continuous solid and dashed lines are the RAST, and IAST estimations, respectively. (c) 3D plot of CBMC data on S_{ads} for $CO_2(1)/CH_4(2)$ mixture adsorption in all-silica FAU at 300 K, plotted as function of the surface potential, Φ, and the mole fraction of CO_2 in the bulk gas phase mixture, y_1. The 3D mesh is constructed using the IAST.

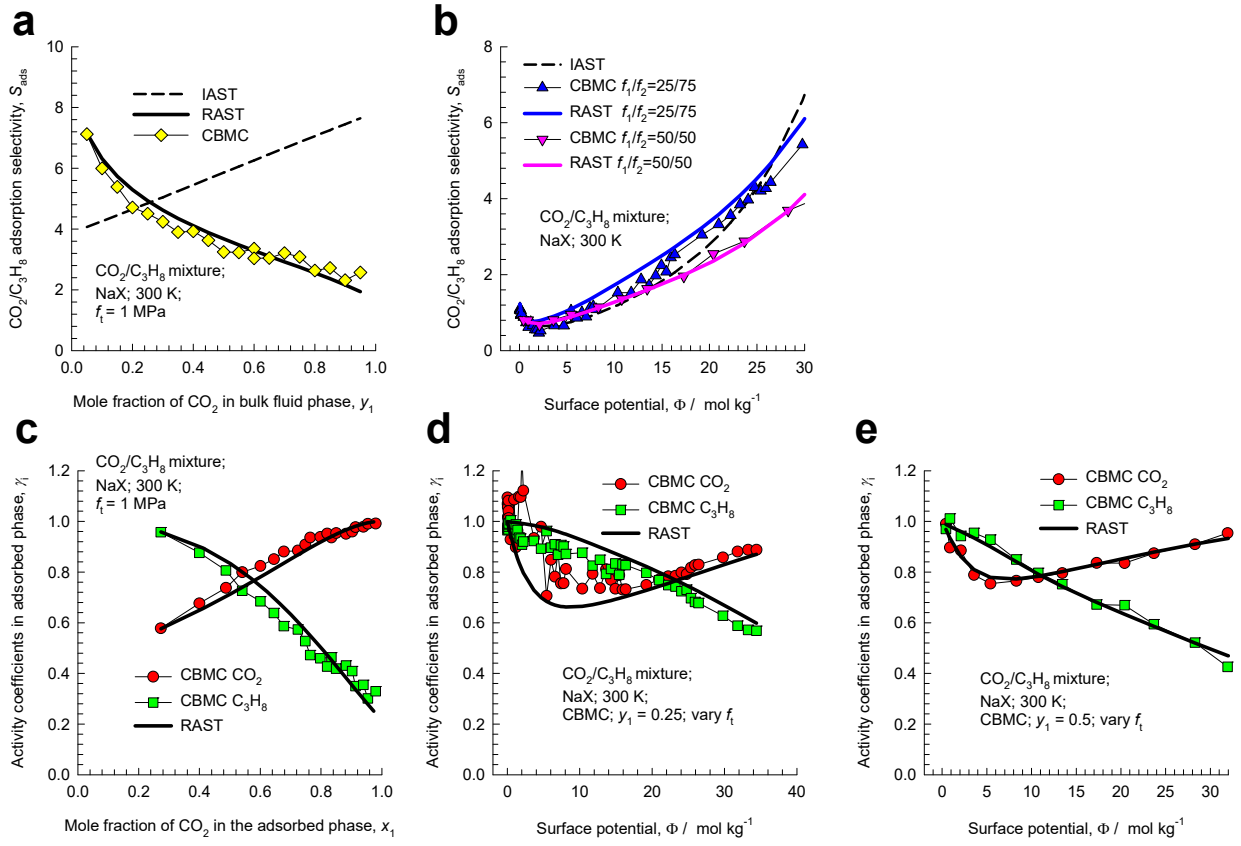

Figure S52. CBMC simulations data for CO_2(1)/C_3H_8(2) mixture adsorption in NaX zeolite at 300 K. (a, b) CBMC data on adsorption selectivity compared with IAST (dashed lines) and RAST estimates (continuous solid lines). (c, d, e) CBMC data on activity coefficients in the adsorbed phase compared with RAST Wilson fits. The unary isotherm fit parameters and Wilson parameters are provided in Table S10.

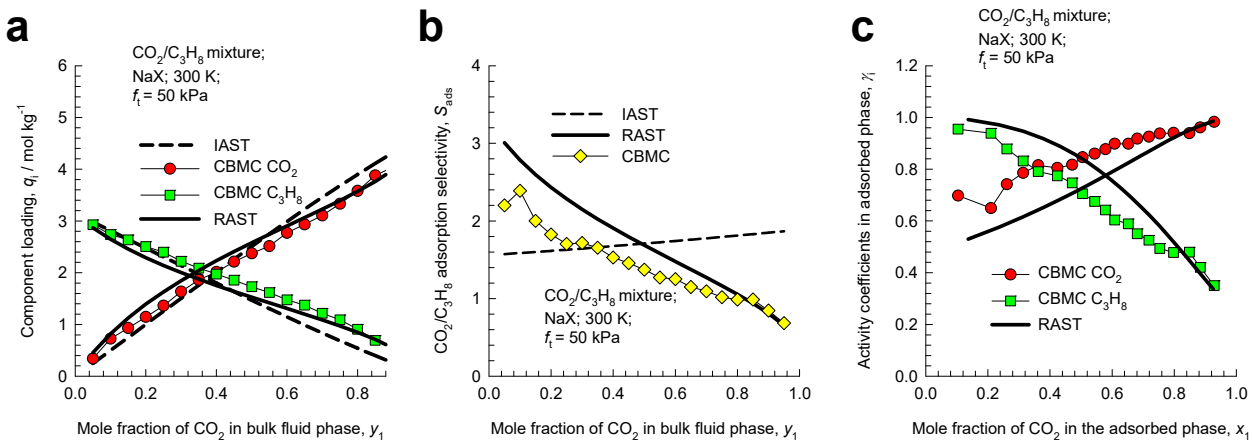

Figure S53. CBMC simulation data and analysis for with f_t = 50 kPa for CO_2(1)/C_3H_8(2) mixture adsorption in NaX zeolite at 300 K. CBMC data for (a) component loadings and (b) CO_2(1)/ C_3H_8(2) adsorption selectivity compared with IAST and RAST estimates. (c) Activity coefficients from CBMC compared with RAST model calculations. The unary isotherm fit parameters and Wilson parameters are provided in Table S10.

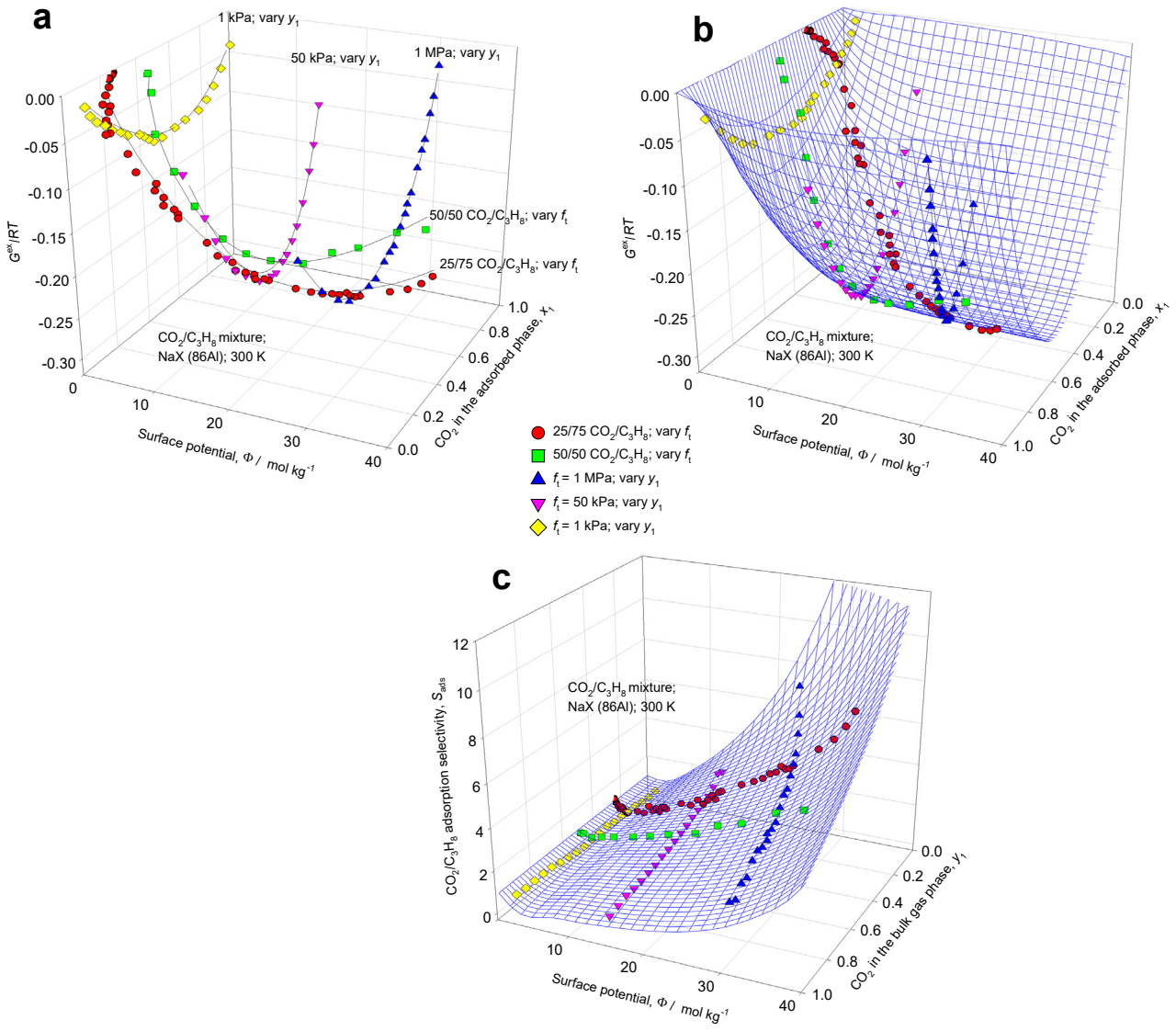

Figure S54. (a, b) 3D plots of CBMC data on excess Gibbs free energy $G^{ex}/RT = x_1 \ln(\gamma_1) + x_2 \ln(\gamma_2)$ for $CO_2(1)/C_3H_8(2)$ mixture adsorption in NaX zeolite at 300 K. (c) 3D plot of the $CO_2(1)/C_3H_8(2)$ adsorption selectivity as function of the surface potential Φ and mole fraction of CO_2 in the bulk gas phase, y_1. The 3D mesh is constructed using the Wilson parameters provided in Table S10.

CO_2/C_3H_8 mixture adsorption in NaX (=13X) zeolite;
Snapshot for f_{CO2} = 500 kPa; f_{C3H8} = 500 kPa

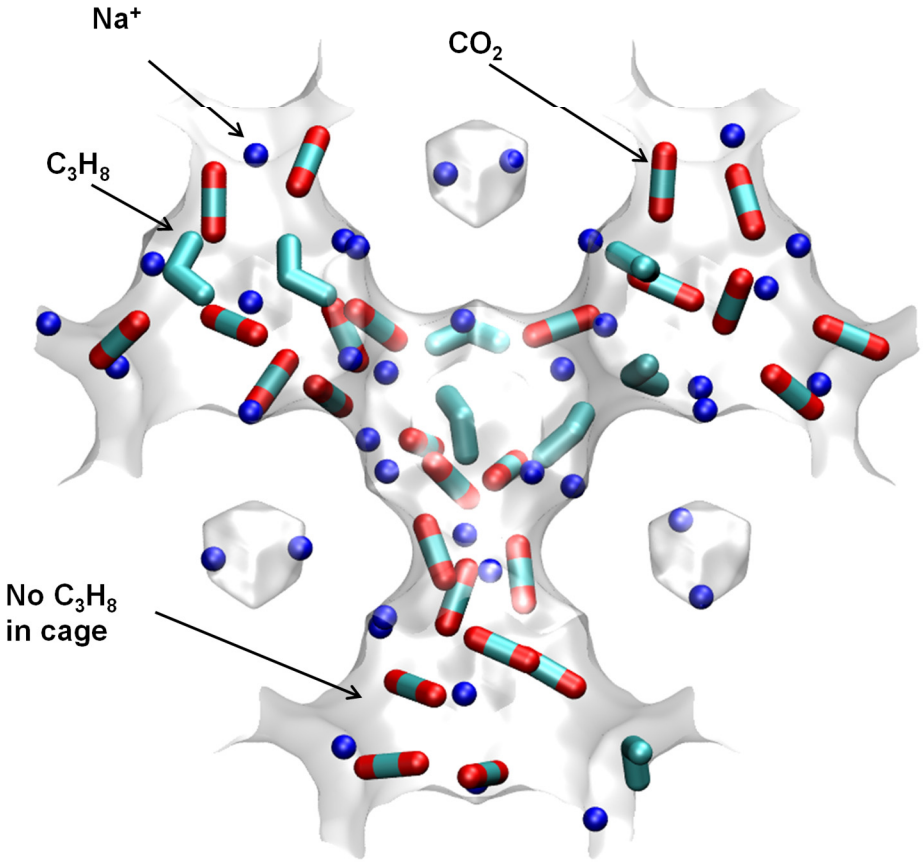

Figure S55. Computational snapshots showing the location of CO_2, and C_3H_8 within the cages of NaX zeolite at 300 K and total fugacity f_t = 1 MPa. The component partial fugacities are f_1 = 0.5 MPa, and f_2 = 0.5 MPa.

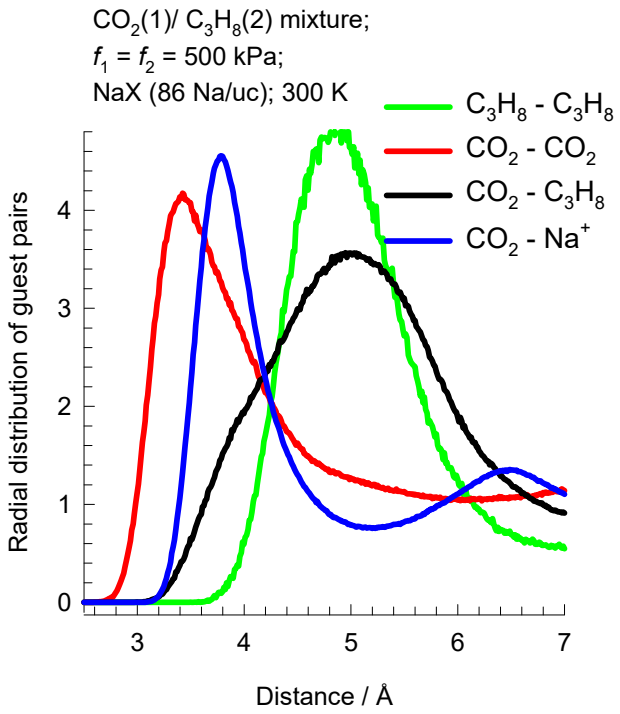

Figure S56. Radial distribution of guest pairs determined from CBMC simulations for adsorption of CO_2/C_3H_8 mixtures in NaX zeolite at 300 K and total fugacity f_t = 1 MPa, and y_1=0.5.

.

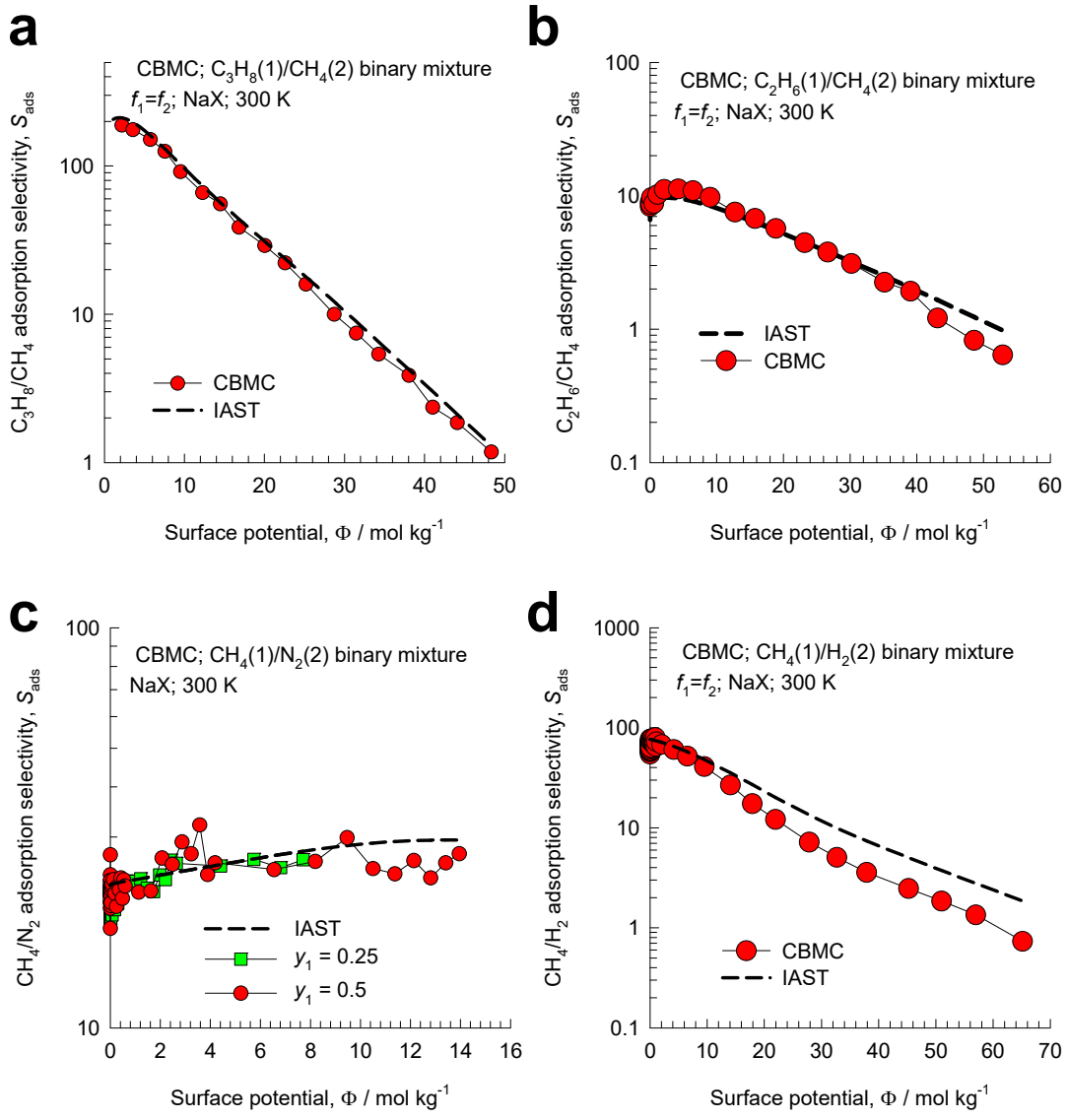

Figure S57. Adsorption selectivity S_{ads} for (a) 50/50 $C_3H_8(1)/CH_4(2)$, (b) 50/50 $C_2H_6(1)/CH_4(2)$, (c) 50/50 $CH_4(1)/N_2(2)$, 25/75 $CH_4(1)/N_2(2)$, and (d) 50/50 $CH_4(1)/H_2(2)$ mixture adsorption in NaX zeolite at 300 K, plotted as function of the surface potential Φ. The CBMC simulated values (indicated by symbols) are compared with IAST estimates (indicated by the dashed lines).

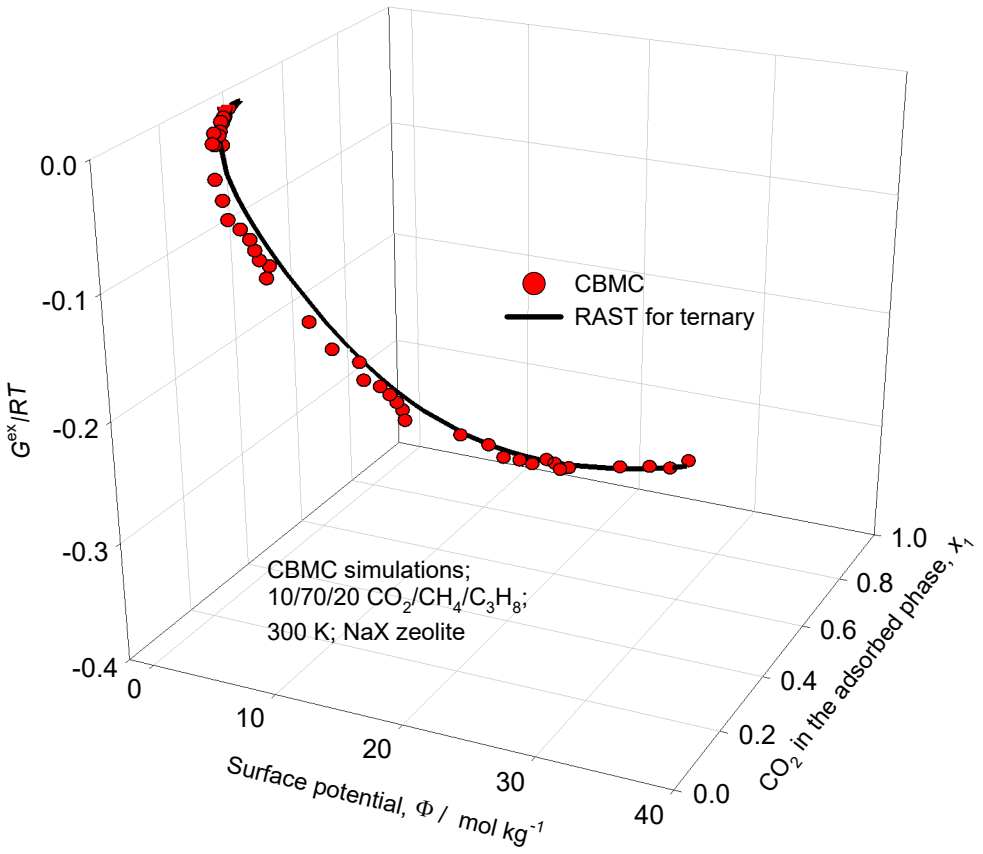

Figure S58. 3D plot of CBMC data on excess Gibbs free energy $G^{ex}/RT = \sum_{i=1}^{n} x_i \ln(\gamma_i)$ for 10/70/20 $CO_2(1)//CH_4(2)/C_3H_8(3)$ mixtures in NaX zeolite at 300 K. Comparison is made of CBMC data with the estimates of the ternary Wilson RAST model. The unary isotherm fit parameters and Wilson parameters are provided in Table S10.

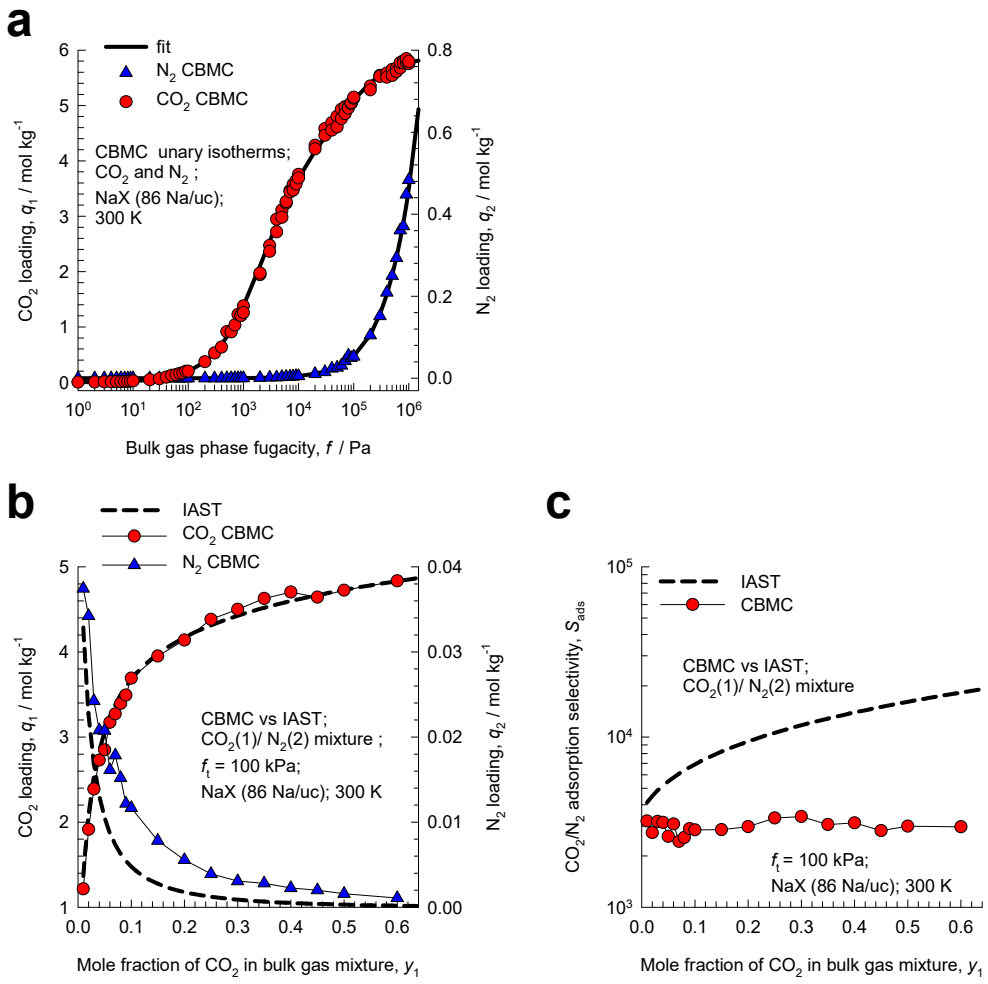

Figure S59. (a) CBMC simulations of unary isotherm data of CO_2, and N_2 in NaX zeolite at 300 K. (b) CBMC simulation data (indicated by symbols) of for component loadings, q_i, of CO_2, and N_2 for adsorption of CO_2/N_2 mixtures in NaX zeolite at 300 K and total fugacity f_t = 100 kPa, as function of the mole fraction of CO_2 in the bulk gas phase, y_1. (c) CO_2/N_2 adsorption selectivity as function of the mole fraction of CO_2 in the bulk gas phase. The dashed lines in (b), and (c) are the IAST estimations.

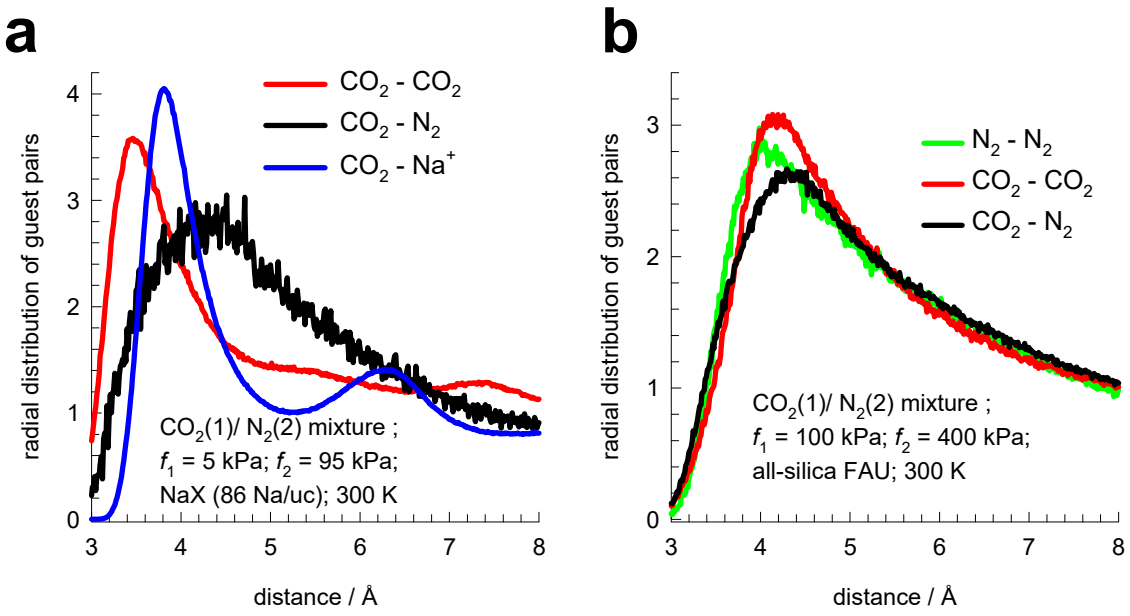

Figure S60. (a) Radial distribution of guest pairs determined from CBMC simulations for adsorption of CO_2/N_2 mixtures in NaX zeolite at 300 K and total fugacity f_t = 100 kPa, and y_1=0.05. (b) Radial distribution of guest pairs determined from CBMC simulations for adsorption of CO_2/N_2 mixtures in all-silica FAU zeolite at 300 K and total fugacity f_t = 500 kPa, and y_1=0.25.

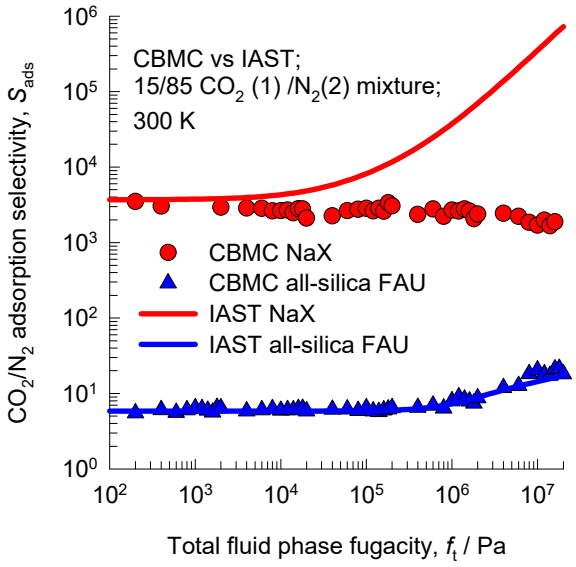

Figure S61. Comparison of CBMC simulated values of CO_2/N_2 adsorption selectivities determined from CBMC simulations for all-silica FAU (192 Si, 0 Al, 0 Na^+, Si/Al=∞), and NaX (106 Si, 86 Al, 86 Na^+, Si/Al=1.23) zeolites for equimolar mixtures at 300 K with IAST estimations.

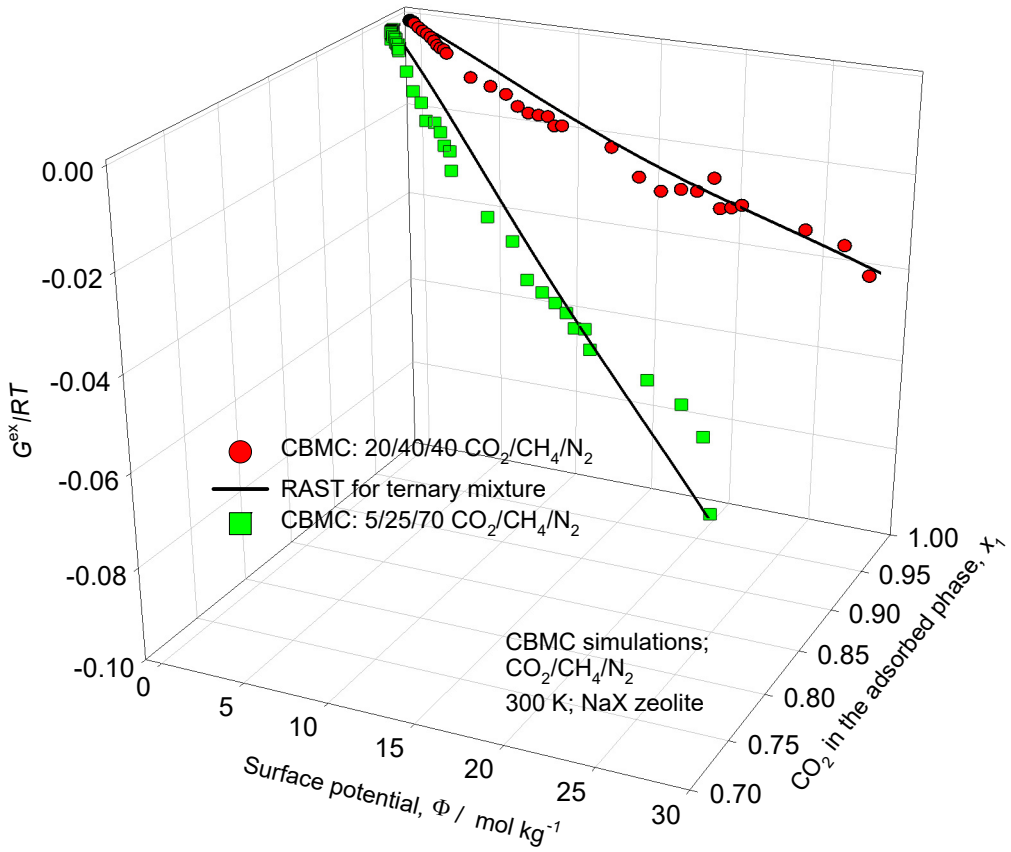

Figure S62. 3D plot of CBMC data on excess Gibbs free energy $G^{ex}/RT = \sum_{i=1}^{n} x_i \ln(\gamma_i)$ for ternary 20/40/40 $CO_2/CH_4/N_2$, and 5/25/70 $CO_2/CH_4/N_2$ mixtures in NaX at 300 K for a range of total fugacities, f_t. Comparison is made of CBMC data with the estimates of the ternary Wilson RAST model. The unary isotherm fit parameters and Wilson parameters are provided in Table S10.

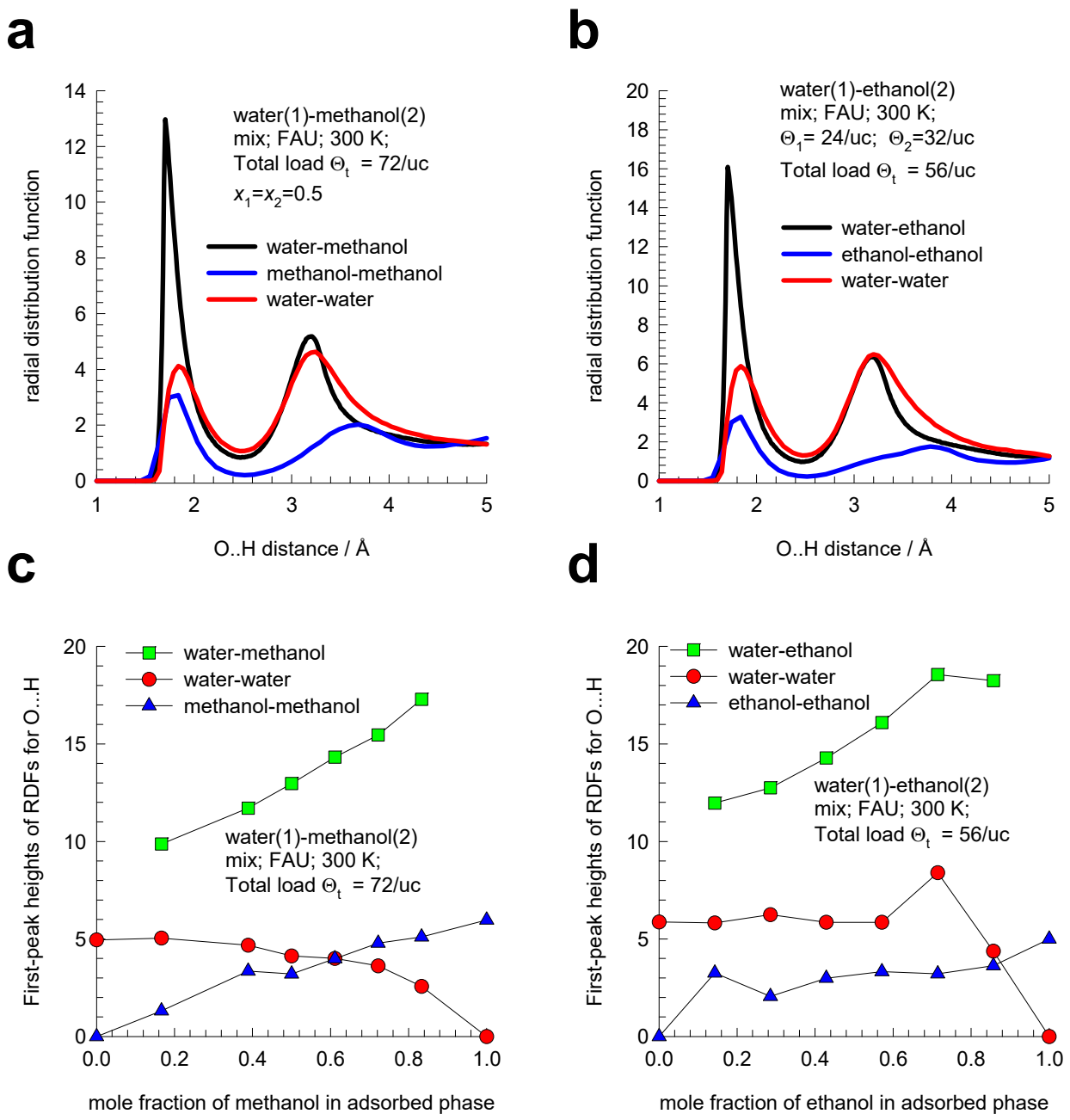

Figure S63. (a, b) RDF of O···H distances for molecular pairs of water(1)/methanol(2) (total loading = 72 molecules per unit cell), water(1)/ethanol(2) (total loading = 56 molecules per unit cell) mixture adsorption in FAU zeolite at 300 K; these mixture are equimolar in the adsorbed phase. (c, d) Plots of the first-peak heights of the RDFs, from data such as those presented in (a, b) for varying compositions in the adsorbed phase.

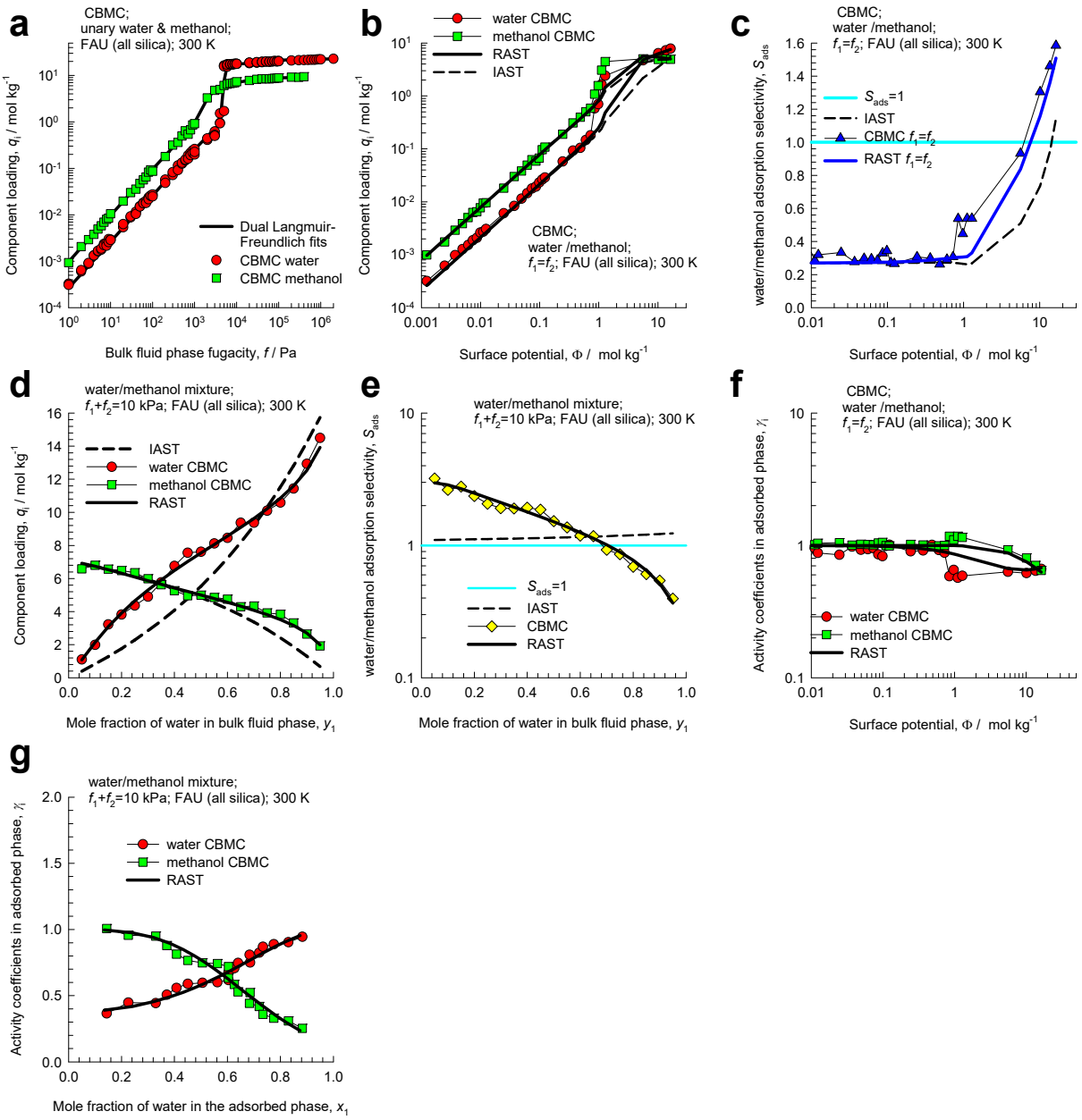

Figure S64. CBMC simulation data and analysis for Campaign A (y_1= 0.5) and for Campaign B (f_t = 10 kPa) for water(1)/methanol(2) mixture adsorption in FAU (all-silica) zeolite at 300 K. (a) Unary isotherms and fits. (b, d) Component loadings in mixture compared with IAST/RAST estimates. (c, e) CBMC data for water(1)/methanol(2) adsorption selectivity compared with IAST and RAST estimates. (f, g) Activity coefficients from CBMC compared with RAST model calculations. The unary isotherm fit parameters and Margules parameters are provided in Table S12.

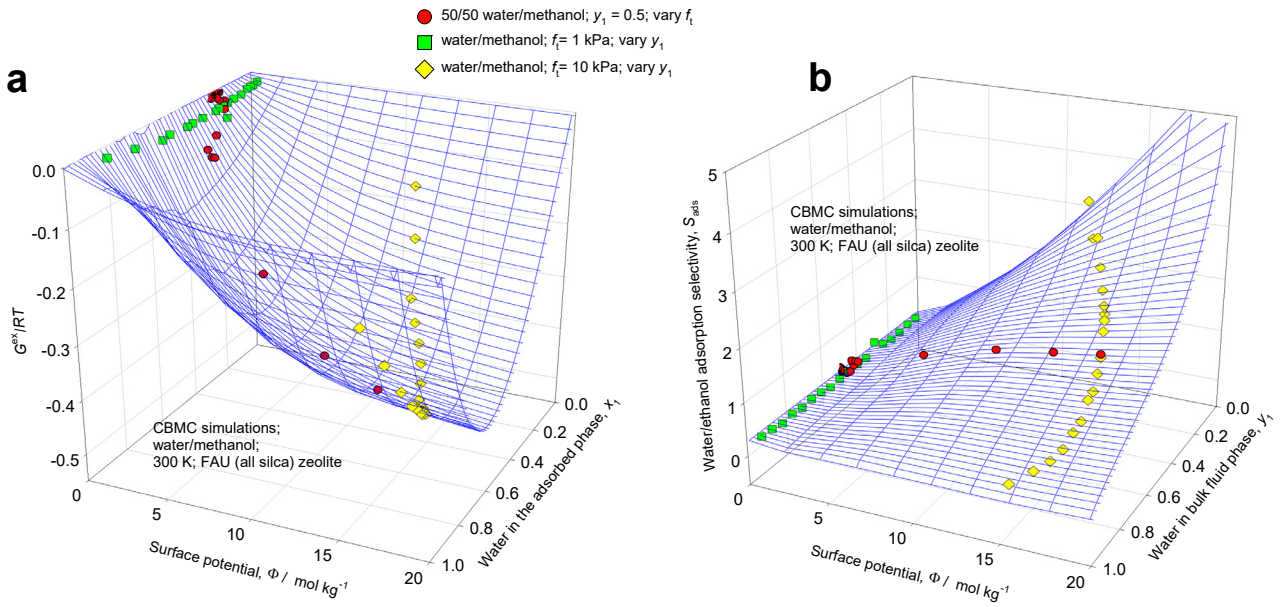

Figure S65. 3D plots of CBMC data for three different CBMC campaigns on (a) excess Gibbs free energy $G^{ex}/RT = x_1 \ln(\gamma_1) + x_2 \ln(\gamma_2)$, and (b) adsorption selectivity for water(1)/methanol(2) mixture adsorption in FAU (all-silica) zeolite at 300 K. The 3D mesh is constructed using the Margules parameters provided in Table S12.

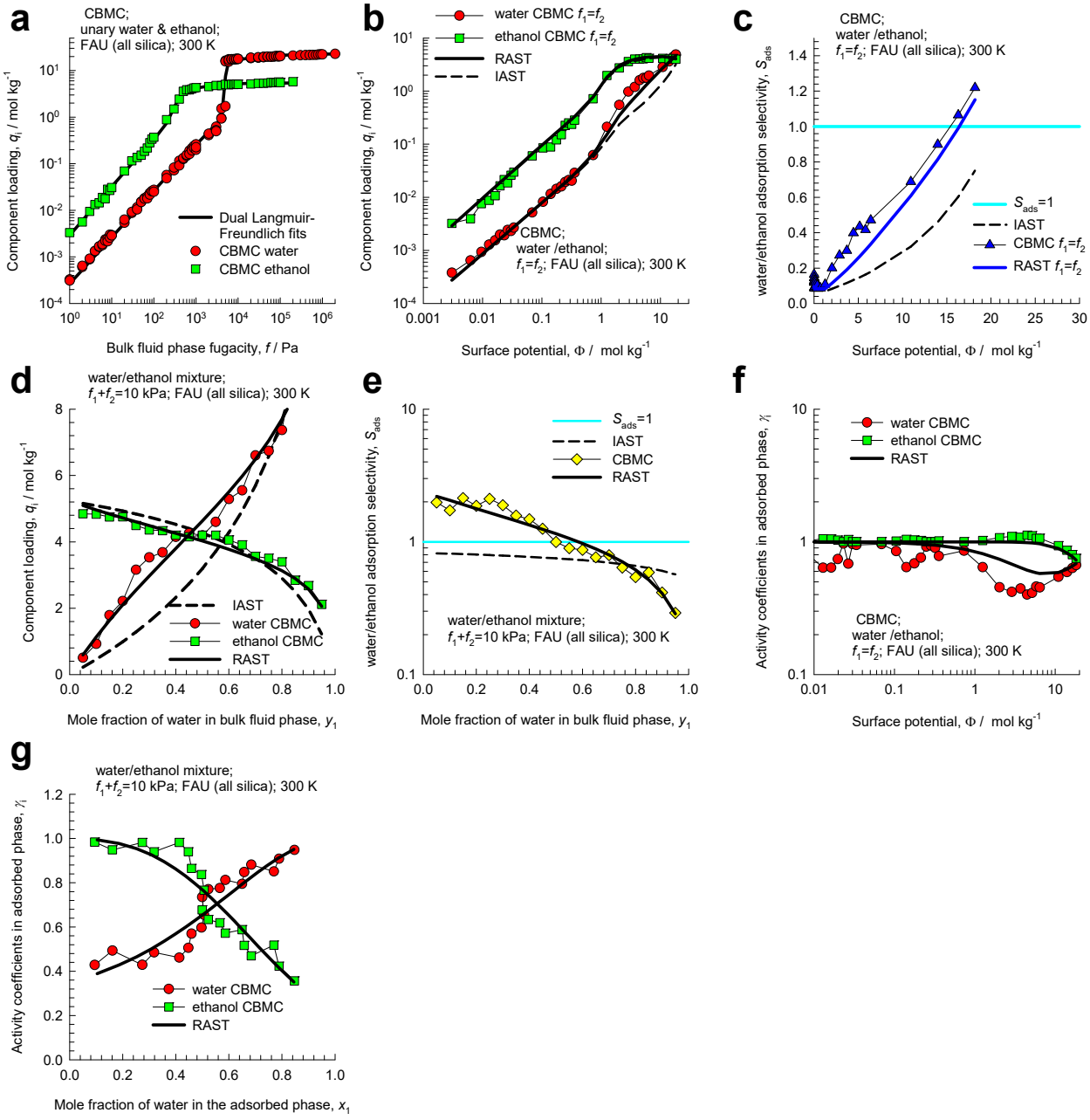

Figure S66. CBMC simulation data and analysis for Campaign A (y_1= 0.5) and for Campaign B (f_t = 10 kPa) for water(1)/ethanol(2) mixture adsorption in FAU (all-silica) zeolite at 300 K. (a) Unary isotherms and fits. (b, d) Component loadings in mixture compared with IAST/RAST estimates. (c, e) CBMC data for water(1)/ethanol(2) adsorption selectivity compared with IAST and RAST estimates. (f, g) Activity coefficients from CBMC compared with RAST model calculations. The unary isotherm fit parameters and Margules parameters are provided in Table S12.

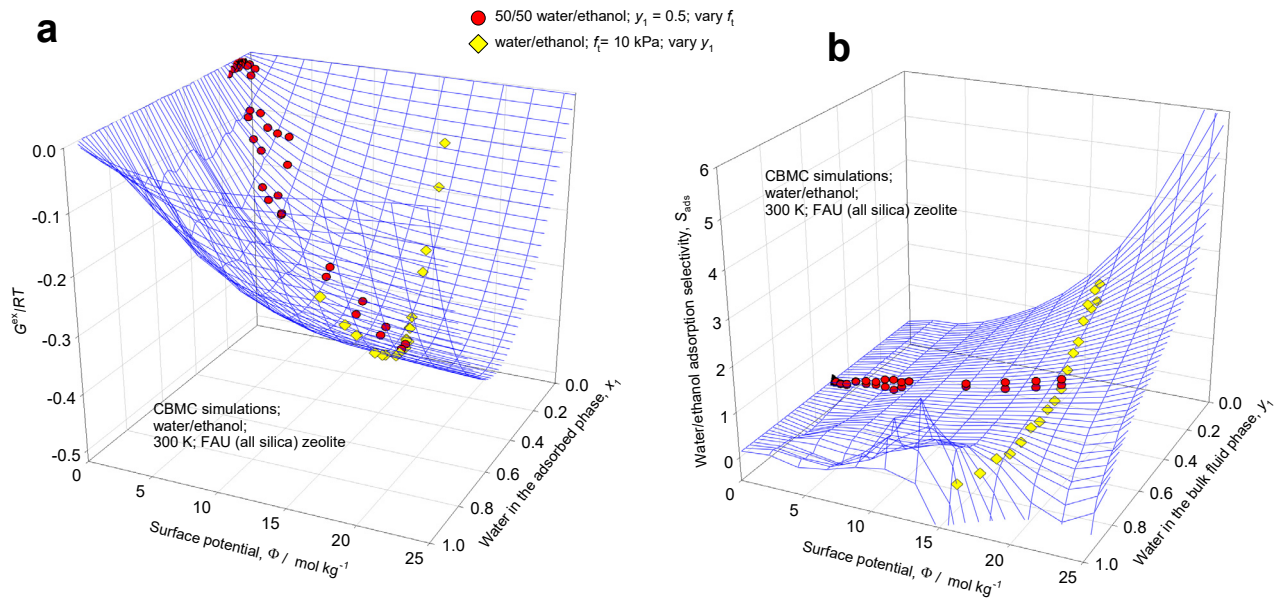

Figure S67. 3D plots of CBMC data for two different CBMC campaigns on (a) excess Gibbs free energy $G^{ex}/RT = x_1 \ln(\gamma_1) + x_2 \ln(\gamma_2)$, and (b) adsorption selectivity for water(1)/ethanol(2) mixture adsorption in FAU (all-silica) zeolite at 300 K. The 3D mesh is constructed using the Margules parameters provided in Table S12.

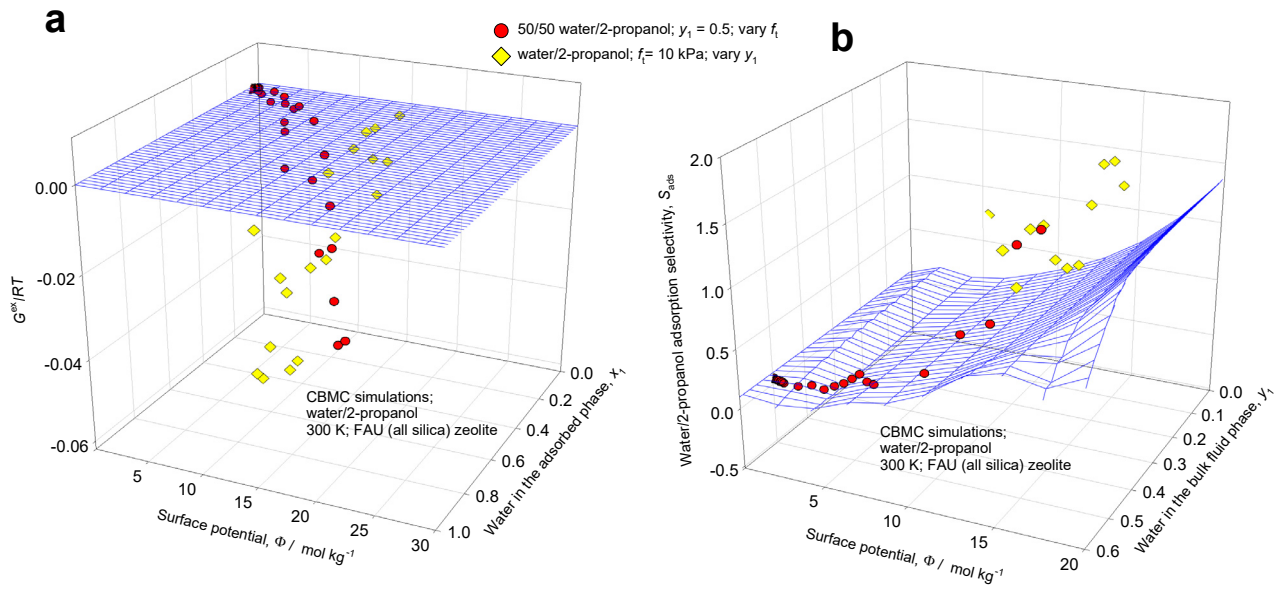

Figure S68. 3D plots of CBMC data for two different campaigns on (a) excess Gibbs free energy $G^{ex}/RT = x_1 \ln(\gamma_1) + x_2 \ln(\gamma_2)$, and (b) adsorption selectivity for water(1)/2-propanol(2) mixture adsorption in FAU (all-silica) zeolite at 300 K. The 3D mesh is constructed using the IAST using the unary isotherm fits provided in Table S12.

10 Mixture adsorption in LTA and LTA-4A zeolite

LTA (Linde Type A) all-silica zeolite consist of cages of 743 Å^3 volume, separated by 4.11 Å × 4.47 Å 8-ring windows; the pore landscapes and structural details are provided in Figure S1, and Figure S2. Figure S3 presents the structural details of cation-exchanged LTA-4A; per unit cell LTA-4A has 96 Si, 96 Al, 96 Na^+, Si/Al=1.

10.1 Mixture adsorption in LTA (all silica) zeolite

Figure S69 presents CBMC simulations of the selectivities for mixture adsorption, $S_{ads} = \frac{q_1/q_2}{f_1/f_2}$ in all silica LTA zeolite for 50/50 CO_2(1)/CH_4(2), CO_2(1)/N_2(2), and CH_4(1)/N_2(2) mixtures with $\left(y_1 = \frac{f_1}{f_1+f_2} = 0.5 \right)$ and varying total bulk gas phase fugacity, $f_t = f_1 + f_2$, at 300 K. The selecivities are plotted as function of the surface potential, Φ. Also shown are the simulations for equimolar $\left(f_1 = f_2 = f_3\right)$ CO_2(1)/CH_4(2)/N_2(3) mixtures. The selectivity for each of the three binary pairs are the same for binary mixtures and ternary mixture, provided the comparison is made at the same value of the surface potential, Φ; see eq (S12) and the related discussions. Put another way, the presence of component 3 in the ternary mixture has no influence of the adsorption selectivity for the 1-2 pair.

The dashed lines in Figure S69 are the IAST estimates of the adsorption selectivities. We note good agreement between CBMC simulations and IAST estimates.

10.2 CO_2/C_3H_8 mixture adsorption in LTA-4A zeolite

Two different campaigns were carried out for CBMC simulations of CO_2(1)/C_3H_8(2) mixture adsorption in LTA-4A zeolite at 300 K. In campaign A, the mole fraction of CO_2(1) in the bulk gas phase is held constant (at values of y_1 = 0.1, and y_1 = 0.8), and the bulk gas phase fugacity $f_t = f_1 + f_2$ was varied. In campaign B, the mole fraction of CO_2(1) in the bulk gas phase is held constant, and the bulk gas phase fugacity $f_t = f_1 + f_2$ was varied. . The CBMC results of these three campaigns are presented in Figure S70.

In Figure S70a,b CBMC data on adsorption selectivity, $S_{ads} = \frac{q_1/q_2}{f_1/f_2}$, are compared with IAST estimates indicated by the dashed lines.

The CBMC data in Figure S70c for Campaign A show with increasing values of the surface potential Φ, the selectivity S_{ads} becomes increasingly in favor of CO_2, due to strong coulombic interactions with the extra-framework cations Na^+. The IAST anticipates the CBMC data sets to have the same selectivity that depends uniquely on the surface potential Φ, independent of the bulk phase compositions (at values of $y_1 = 0.1$, and $y_1 = 0.8$). The IAST does not anticipate this selectivity reversal in favor of CO_2, for the CBMC data with $y_1 = 0.1$. The CBMC simulation data show that S_{ads} depends on the value of the bulk gas mixture composition, $y_1 = \frac{f_1}{f_1 + f_2}$.

For campaign B, with the bulk gas phase mixture $f_t = f_1 + f_2 = 1$ MPa we note that the $S_{ads} = \frac{q_1/q_2}{f_1/f_2}$ undergoes a selectivity reversal, that is not anticipated by the IAST; see Figure S70a.

The continuous solid lines in Figure S70 are the RAST calculations using fitted Wilson parameters as specified in Table S13. For the Wilson fits, we calculate the parameter C using $C = \frac{1}{\frac{x_1}{q_{1,sat}} + \frac{x_2}{q_{2,sat}}}$; $q_{i,sat} = q_{i,A,sat} + q_{i,B,sat}$; $i = 1, 2$, with the arbitrary assumption that $x_1 = x_2 = 0.5$.

Figure S70c,d,e plot the activity coefficients of the guest components in the adsorbed phase as function of (c) mole fraction of CO_2(1) in the adsorbed phase for campaign A, x_1, and (d, e) the surface potential Φ for campaigns B and C. For campaign A, we note the limiting behaviors $x_i \to 1$; $\gamma_i \to 1$. For campaigns A (at values of $y_1 = 0.1$, and $y_1 = 0.8$), we note that the activity coefficients are also dependent the surface potential Φ with the limiting characteristic $\Phi \to 0$; $\gamma_1 \to 1$; $\gamma_2 \to 1$. The introduction of $\left(1 - \exp\left(-C\Phi\right)\right)$ in the Wilson model, eq (S39), imparts the correct limiting behaviors $\Phi \to 0$; $\theta \to 0$; $\gamma_i \to 1$ for the activity coefficients in the Henry regime, $f_t \to 0$; $\Phi \to 0$, as the pore

occupancy tends to vanishingly small values. As pore saturation conditions are approached, this correction factor tends to unity: $\left(1-\exp\left(-C\Phi\right)\right)\to 1$.

The CBMC data in Figure S70c,d,e lead us to conclude that the activity coefficients are functions of both Φ and x_1. In Figure S71a, the CBMC data for the excess Gibbs free energy $G^{ex}/RT = x_1\ln\left(\gamma_1\right)+x_2\ln\left(\gamma_2\right)$ for the campaigns A, and B are plotted in 3D space as function of Φ and x_1. The entire CBMC data set resides on a 3D surface mesh determined from the fitted Wilson parameters; see Figure S71b.

Figure S71c presents a 3D plot of the CO_2(1)/C_3H_8(2) adsorption selectivity as function of the surface potential Φ and mole fraction of CO_2 in the bulk gas phase, y_1. The entire CBMC data set resides on a 3D surface mesh determined from the fitted Wilson parameters in Table S13. Figure S71c confirms that the adsorption selectivity is not uniquely determined by the surface potential, Φ, but is additionally dependent on the bulk phase mixture composition.

The rationale for the quantitative failures of IAST estimates can be traced to congregation of CO_2 near the Na^+ cations, as witnessed in the RDFs for various guest pairs CO_2-CO_2, CO_2-Na^+, CO_2-C_3H_8, and C_3H_8-C_3H_8 shown in Figure S72. It is noteworthy that the first peaks of CO_2-CO_2 and CO_2-Na^+ are close together. Also noteworthy is that the first peaks of CO_2-CO_2 and CO_2-C_3H_8 are farther apart, indicating segregation effects. Also noteworthy, is that a number of peaks occur for CO_2-CO_2 pairs; two of these peaks correspond to the window-to-window distances of 8.68, and 12.27 Å.

Figure S73 shows snapshots of the location of CO_2(1), and C_3H_8(2) molecules within the pore topology of LTA-4A zeolite. We note that the CO_2 is almost exclusively located at the windows, or near the window entrance regions. Due to configurational restraints C_3H_8 can only located at the cage interiors. Consequently, the competition between the adsorption of CO_2 and C_3H_8 is less severe than assumed in the homogenous distribution that is inherent in the IAST prescription.

10.3 CO_2/CH_4 mixture adsorption in LTA-4A zeolite

Two different campaigns were carried out for CBMC simulations of $CO_2(1)/CH_4(2)$ mixture adsorption in LTA-4A zeolite at 300 K. In campaign A, the mole fraction of $CO_2(1)$ in the bulk gas phase is held constant, $y_1 = 0.1$, and the bulk gas phase fugacity $f_t = f_1 + f_2$ was varied. In campaign B, the mole fraction of $CO_2(1)$ in the bulk gas phase is held constant, $y_1 = 0.5$, and the bulk gas phase fugacity $f_t = f_1 + f_2$ was varied. The CBMC results of these two campaigns are presented in Figure S74.

Figure S74c compares CBMC data on adsorption selectivity, $S_{ads} = \frac{q_1/q_2}{f_1/f_2}$, with IAST estimates indicated by the dashed lines for campaigns A, B. The CBMC simulation data show that S_{ads} depends on the value of the bulk gas mixture composition, $y_1 = \frac{f_1}{f_1 + f_2}$. The IAST (indicated by the dashed line) anticipates that the adsorption selectivity is uniquely dependent on the surface potential Φ, and independent of bulk gas phase composition.

Figure S74e shows the CBMC data for campaign B for the activity coefficients as function of the mole fraction of $CO_2(1)$ in the adsorbed phase, x_1. The continuous solid lines in Figure S74 are the RAST calculations using fitted Wilson parameters as specified in Table S13. For the Wilson fits, we calculate the parameter C using $C = \frac{1}{\frac{x_1}{q_{1,sat}} + \frac{x_2}{q_{2,sat}}}$; $q_{i,sat} = q_{i,A,sat} + q_{i,B,sat}$; $i = 1, 2$, taking $x_1 = x_2 = 0.5$.

In Figure S75a the CBMC data for the excess Gibbs free energy $G^{ex}/RT = x_1 \ln(\gamma_1) + x_2 \ln(\gamma_2)$ for the campaigns A, and B are plotted in 3D space as function of surface potential Φ and adsorbed phase mole fraction x_1. The entire CBMC data set resides on a 3D surface mesh determined from the fitted Wilson parameters; see Figure S75b.

Figure S75c presents a 3D plot of the $CO_2(1)/CH_4(2)$ adsorption selectivity as function of the surface potential Φ and mole fraction of CO_2 in the bulk gas phase, y_1. The entire CBMC data set resides on a 3D surface mesh determined from the fitted Wilson parameters in Table S13. Figure S75c confirms that

the adsorption selectivity is not uniquely determined by the surface potential, Φ, but is additionally dependent on the bulk phase mixture composition.

10.4 CH_4/C_3H_8 mixture adsorption in LTA-4A zeolite

Figure S76 presents CBMC simulation data for 90/10 $CH_4(1)/C_3H_8(2)$ mixture adsorption in LTA-4A zeolite at 300 K. The IAST underestimates the loadings of CH_4, as compared with CBMC data. This suggests some segregation of the two alkane guests. Note that C_3H_8 cannot locate at the window regions, as observed in Figure S73. CH_4, on the other hand, can locate at and near window regions.

The continuous solid lines in Figure S76b,c,d are the RAST calculations using fitted Wilson parameters as specified in Table S13. For the Wilson fits, we calculate the parameter C using $C = \frac{1}{\frac{x_1}{q_{1,sat}} + \frac{x_2}{q_{2,sat}}}$; $q_{i,sat} = q_{i,A,sat} + q_{i,B,sat}$; $i = 1, 2$, with the arbitrary assumption that $x_1 = x_2 = 0.5$.

In Figure S77a the CBMC data for the excess Gibbs free energy $G^{ex}/RT = x_1 \ln(\gamma_1) + x_2 \ln(\gamma_2)$ are plotted in 3D space as function of Φ and x_1. The entire CBMC data set resides on a 3D surface mesh determined from the fitted Wilson parameters; see Figure S77b.

10.5 $CO_2/CH_4/C_3H_8$ mixture adsorption in LTA-4A

CBMC simulations were carried out for 25/65/10 $CO_2/CH_4/C_3H_8$ mixtures in LTA-4A at 300 K for a range of total fugacities, f_t. In Figure S78a,b,c the component loadings from CBMC are compared with IAST and RAST estimates. For the RAST calculations, we use eq (S42). The Wilson parameters for the binary pairs $\Lambda_{12}, \Lambda_{21}, \Lambda_{13}, \Lambda_{31}, \Lambda_{23}, \Lambda_{32}$ are taken to the same as for the corresponding binary pairs as listed in Table S13. Our approach for ternary mixtures is to estimate C as $C = \frac{x_1}{q_{1,sat}} + \frac{x_2}{q_{2,sat}} + \frac{x_3}{q_{3,sat}}$, assuming, $x_1 = x_2 = x_3 = 1/3$. The RAST estimates are in reasonable agreement with the ternary CBMC data. Figure S78d plots the activity coefficients as function of the surface potential.

In Figure S79 the excess Gibbs free energy $G^{ex}/RT = \sum_{i=1}^{n} x_i \ln(\gamma_i)$ determined from CBMC data for 25/65/10 $CO_2/CH_4/C_3H_8$ mixtures in LTA-4A are plotted in 3D space as function of Φ and x_1. The continuous solid line represents the ternary RAST Wilson calculations. The agreement is good, validating the ternary RAST Wilson model.

10.6 CO_2/nC_4H_{10} mixture adsorption in LTA-4A zeolite

Thermodynamic non-ideality effects were also investigated for $CO_2(1)/nC_4H_{10}(2)$ mixture adsorption in LTA-4A zeolite at 300 K. Four different CBMC simulation campaigns were conducted.

(i) Campaign A (y_1= 0.5) for $CO_2(1)/nC_4H_{10}(2)$ mixture adsorption

(ii) Campaign A (y_1= 0.9) for $CO_2(1)/nC_4H_{10}(2)$ mixture adsorption

(iii) Campaign B (f_t = 100 kPa) for $CO_2(1)/nC_4H_{10}(2)$ mixture adsorption

(iv) Campaign B (f_t = 500 kPa) for $CO_2(1)/nC_4H_{10}(2)$ mixture adsorption

The CBMC data and analysis are presented in Figure S80, Figure S81, and Figure S82.

In Figure S82a the CBMC data for the excess Gibbs free energy $G^{ex}/RT = x_1 \ln(\gamma_1) + x_2 \ln(\gamma_2)$ determined from CBMC data for all four CBMC campaigns are plotted in 3D space as function of the surface potential Φ and mole fraction of CO_2 in the adsorbed phase, x_1. The entire CBMC data set resides on a 3D surface mesh determined from the fitted Wilson parameters provided in Table S13.

Figure S82b presents a 3D plot of the $CO_2(1)/CH_4(2)$ adsorption selectivity as function of the surface potential Φ and mole fraction of CO_2 in the bulk gas phase, y_1. The entire CBMC data set resides on a 3D surface mesh determined from the fitted Wilson parameters in Table S13. Figure S82b confirms that the adsorption selectivity is not uniquely determined by the surface potential, Φ, but is additionally dependent on the bulk phase mixture composition.

10.7 Water/alcohol mixture adsorption in LTA (all silica) zeolite

Due to molecular clustering, we should anticipate that water/methanol and water/ethanol mixture adsorption in LTA (all silica) zeolite will be subject to significant deviations from the estimations of the IAST.

For adsorption of water(1)/methanol(2) mixtures in LTA (all silica) zeolite at 300 K, three different CBMC simulations were carried out: Campaign A (with $y_1 = 0.5$, vary f_t), and campaign B, the mole fraction of water(1) in the bulk fluid phase, y_1 was varied from 0 to 1, keeping the bulk fluid phase mixture fugacity $f_t = f_1 + f_2$ constant at values of 1 kPa, and 10 kPa. The CBMC data on component loadings, adsorption selectivities, and activity coefficients are presented in Figure S83.

The dashed lines are the IAST estimates. The failure of the IAST to match the CBMC data presented in is a consequence of hydrogen bonding between guest molecules in water/alcohol mixtures. [15, 18, 47, 48, 60] One of the mandates of the IAST is violated because of the formation of water/alcohol clusters.[15, 46, 48]

The continuous solid lines in Figure S83 are the RAST calculations with fitted Margules parameters specified in Table S15

The CBMC data in Figure S83.f,g leads us to conclude that the activity coefficients are functions of both the surface potential Φ and mole fraction of water in the adsorbed phase mixture, x_1.

For adsorption of water(1)/ethanol(2) mixtures in LTA (all silica) zeolite at 300 K, two different CBMC simulations were carried out: Campaign A (with $y_1 = 0.5$, vary f_t), and campaign B, the mole fraction of water(1) in the bulk fluid phase, y_1 was varied from 0 to 1, keeping the bulk fluid phase mixture fugacity $f_t = f_1 + f_2$ constant at a value of 10 kPa. The CBMC data on component loadings, adsorption selectivities, and activity coefficients are presented in Figure S84. The continuous solid lines in Figure S84 are the RAST calculations with fitted Margules parameters specified in Table S15.

10.8 List of Tables for Mixture adsorption in LTA and LTA-4A zeolite

Table S13. Dual-site Langmuir-Freundlich parameters for pure components CO_2, CH_4, C_3H_8, and nC_4H_{10}, at 300 K in LTA-4A zeolite (96 Si, 96 Al, 96 Na^+, Si/Al=1). The fit parameters are based on the CBMC simulations of pure component isotherms.

	Site A			Site B		
	$\frac{q_{A,sat}}{\text{mol kg}^{-1}}$	$\frac{b_A}{\text{Pa}^{-\nu_A}}$	ν_A	$\frac{q_{B,sat}}{\text{mol kg}^{-1}}$	$\frac{b_B}{\text{Pa}^{-\nu_B}}$	ν_B
CO_2	3.25	6.981E-04	0.9	1.25	3.722E-08	1.2
CH_4	5	9.080E-09	1	3.9	1.689E-05	1
C_3H_8	2.4	3.272E-02	1	1.35	8.192E-03	0.38
nC_4H_{10}	1.8	1.140E+00	1	0.55	5.060E-03	1

Fitted Wilson non-ideality parameters for mixture adsorption in LTA-4A at 300 K.

	C / kg mol^{-1}	Λ_{12}	Λ_{12}
CO_2/C_3H_8	0.244	1.594	4.071
CO_2/CH_4	0.167	2.720	0.368
CH_4/C_3H_8	0.190	2.771	1.073
CO_2/nC_4H_{10}	0.748	0.095	4.861
$CO_2/CH_4/C_3H_8$	0.2	$\Lambda_{12}, \Lambda_{21}, \Lambda_{13}, \Lambda_{31}, \Lambda_{23}, \Lambda_{32}$ as above	

Table S14. Dual-site Langmuir-Freundlich parameters for guest molecules in LTA (all-silica) at 300 K. To convert from molecules uc^{-1} to mol kg^{-1}, multiply by 0.086683044.

	Site A			Site B		
	$\frac{\Theta_{A,sat}}{\text{molec uc}^{-1}}$	$\frac{b_A}{\text{Pa}^{-\nu_A}}$	ν_A	$\frac{\Theta_{B,sat}}{\text{molec uc}^{-1}}$	$\frac{b_B}{\text{Pa}^{-\nu_B}}$	ν_B
CO_2	36	1.513E-05	0.54	85	2.064E-07	1.15
CH_4	52	6.635E-08	0.82	65	3.772E-07	1
N_2	70	1.360E-07	1	60	5.029E-10	1

Table S15. Dual-site Langmuir-Freundlich parameters for adsorption of water, methanol, and ethanol at 300 K in all-silica LTA zeolite. The fit parameters are based on the CBMC simulations of pure component isotherms presented in earlier works.[27, 48]

Adsorbate	Site A			Site B		
	$\frac{q_{A,sat}}{\text{mol kg}^{-1}}$	$\frac{b_A}{\text{Pa}^{-\nu_A}}$	ν_A	$\frac{q_{B,sat}}{\text{mol kg}^{-1}}$	$\frac{b_B}{\text{Pa}^{-\nu_B}}$	ν_B
water	18	3.35353E-68	16	4.3	8.75008E-07	1.06
methanol	6.2	8.07492E-53	14.6	2.4	9.73382E-06	1.09
ethanol	3.6	2.94176E-17	5.4	1.2	0.000111202	1

Fitted Margules non-ideality parameters for binary mixture adsorption in all-silica LTA zeolite at 300 K. The fits are based on combining CBMC Campaigns A and B for each mixture.

	C / kg mol^{-1}	A_{12}	A_{21}
water/methanol	14.355	-0.693	-3.094
water/ethanol	22.657	-1.328	-2.451

10.9 List of Figures for Mixture adsorption in LTA and LTA-4A zeolite

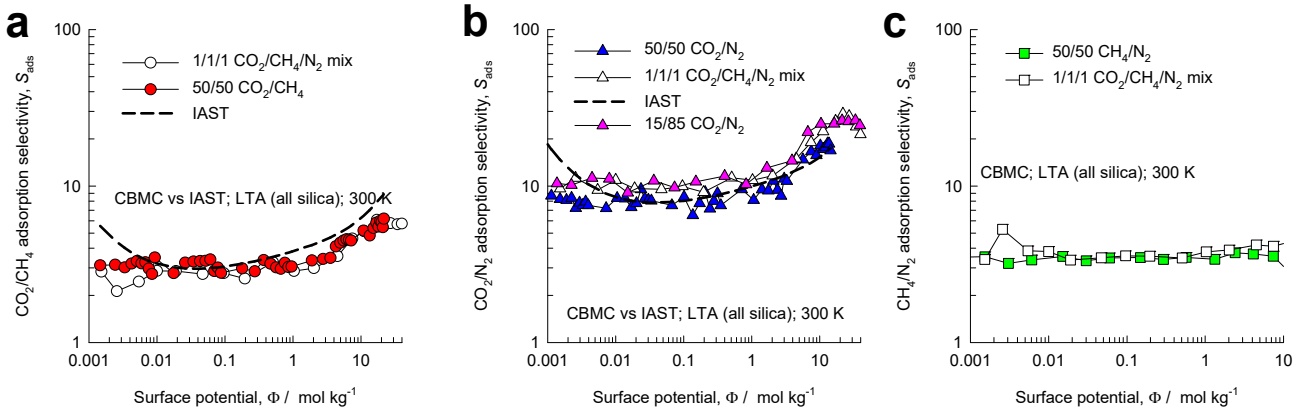

Figure S69. CBMC simulations of the selectivities for mixture adsorption, $S_{ads} = \frac{q_1/q_2}{f_1/f_2}$ in all silica LTA zeolite for 50/50 $CO_2(1)/CH_4(2)$, $CO_2(1)/N_2(2)$, and $CH_4(1)/N_2(2)$ mixtures (i.e. $y_1 = \frac{f_1}{f_1+f_2} = 0.5$) and varying total bulk gas phase fugacity, $f_t = f_1 + f_2$, at 300 K. The selecivities are plotted as function of the surface potential, Φ. Also shown are the simulations for equimolar $(f_1 = f_2 = f_3)$ $CO_2(1)/CH_4(2)/N_2(3)$ mixtures. The dashed lines are the IAST estimates of the adsorption selectivities. The unary isotherm fit parameters are provided in Table S14.

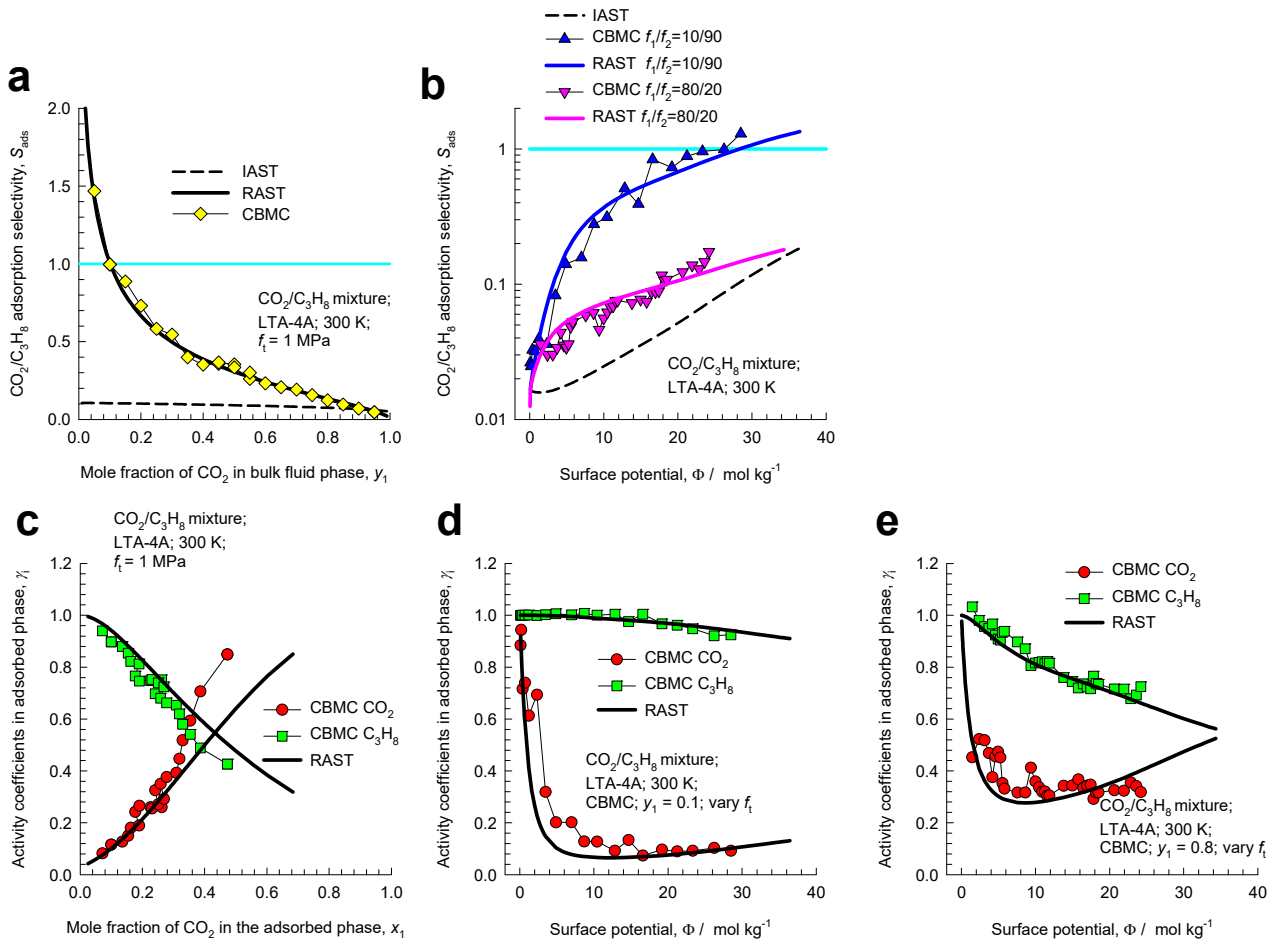

Figure S70. CBMC simulations data for CO_2(1)/C_3H_8(2) mixture adsorption in LTA-4A zeolite at 300 K. (a, b) CBMC data on adsorption selectivity compared with IAST (dashed lines) and RAST estimates (continuous solid lines). (c, d, e) CBMC data on activity coefficients in the adsorbed phase compared with RAST Wilson fits. The unary isotherm fit parameters and Wilson parameters are provided in Table S13.

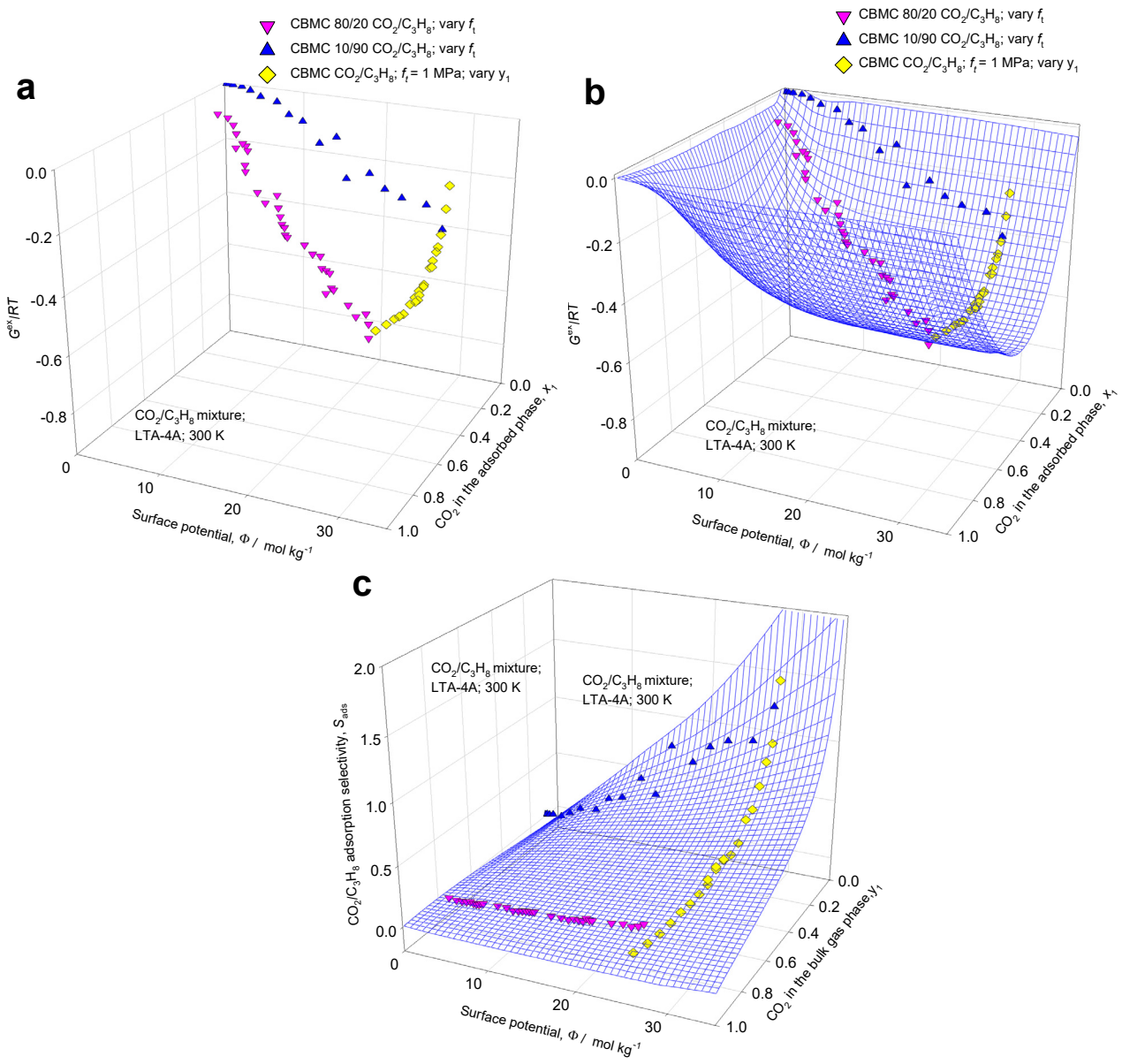

Figure S71. (a, b) 3D plots of CBMC data on excess Gibbs free energy $G^{ex}/RT = x_1 \ln(\gamma_1) + x_2 \ln(\gamma_2)$ for $CO_2(1)/C_3H_8(2)$ mixture adsorption in LTA-4A zeolite at 300 K. (c) 3D plot of the $CO_2(1)/C_3H_8(2)$ adsorption selectivity as function of the surface potential Φ and mole fraction of CO_2 in the bulk gas phase, y_1. The 3D mesh is constructed using the Wilson parameters provided in Table S13.

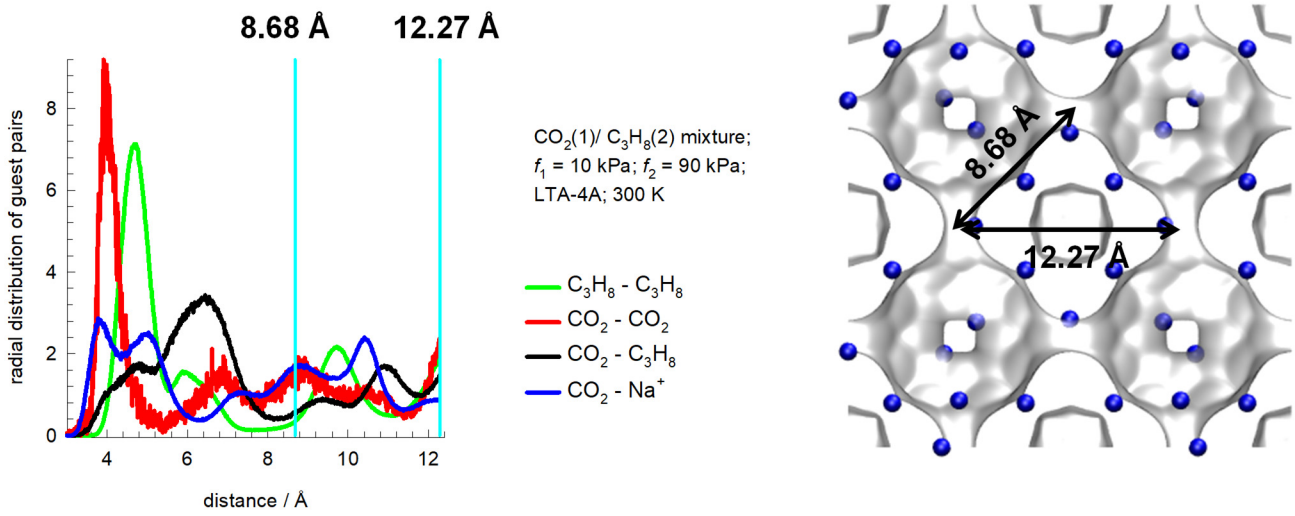

Figure S72. Radial distribution of guest pairs determined from CBMC simulations for adsorption of CO_2/C_3H_8 mixtures in LTA-4A zeolite at 300 K and total fugacity f_t = 100 kPa, and y_1=0.1.

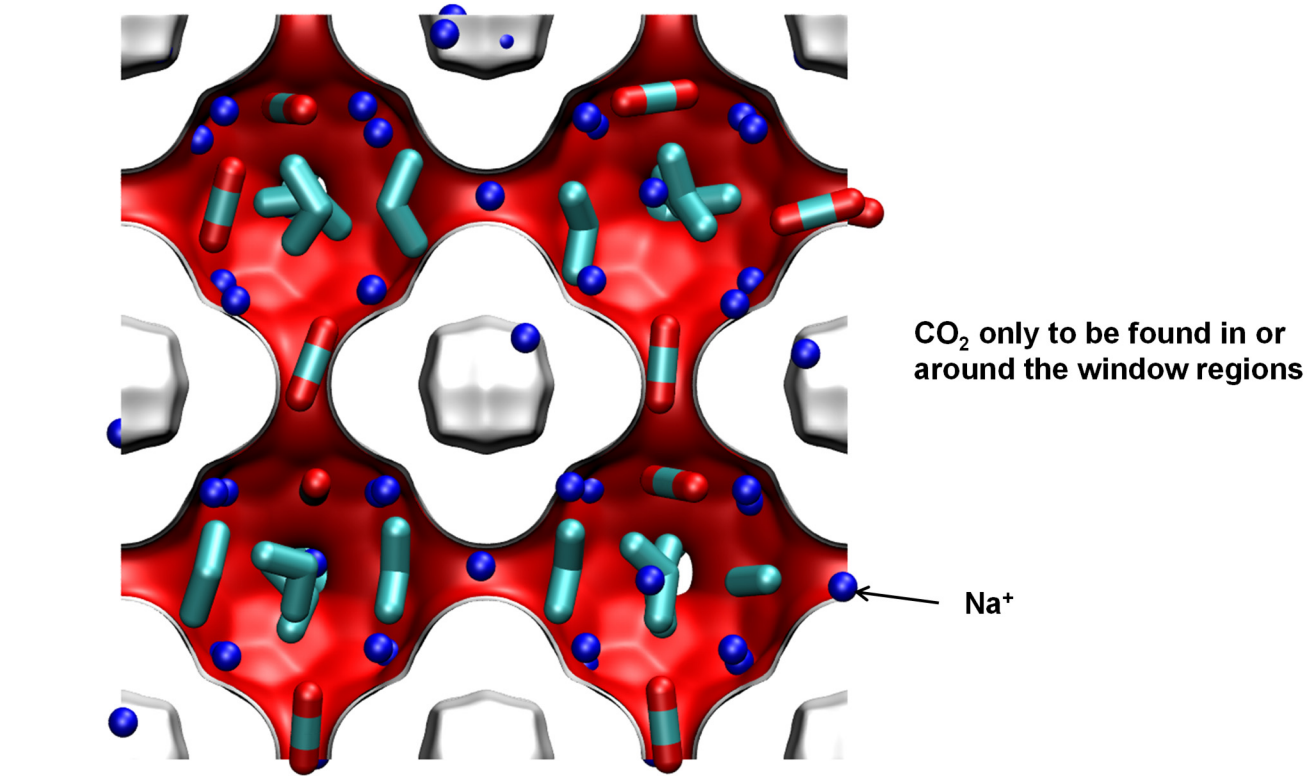

Figure S73. Computational snapshot showing the location of CO_2, and C_3H_8 within the cages of LTA-4A zeolite at 300 K and total fugacity f_t = 1 MPa. The component partial fugacities are f_1 = 0.8 MPa, and f_2 = 0.2 MPa.

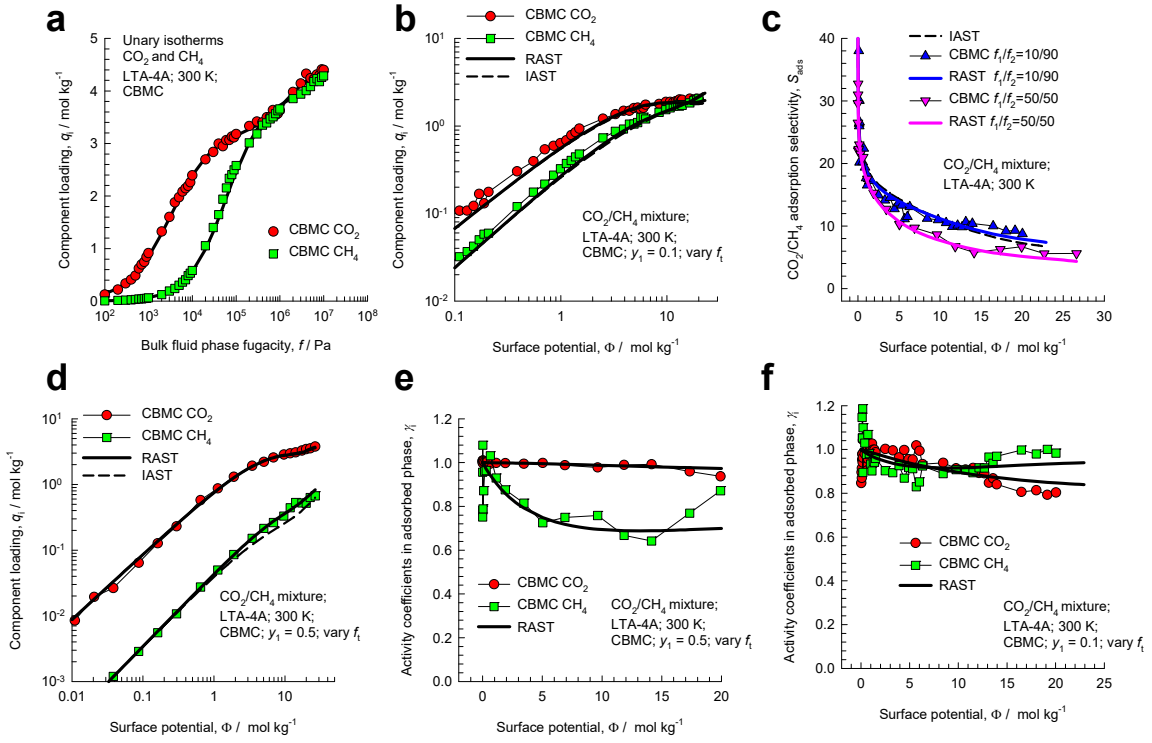

Figure S74. CBMC simulations data for CO_2(1)/CH_4(2) mixture adsorption in LTA-4A zeolite at 300 K. (a) CBMC data on adsorption selectivity compared with IAST (dashed lines) and RAST estimates (continuous solid lines). (be) CBMC data on activity coefficients in the adsorbed phase compared with RAST Wilson fits. The unary isotherm fit parameters and Wilson parameters are provided in Table S13.

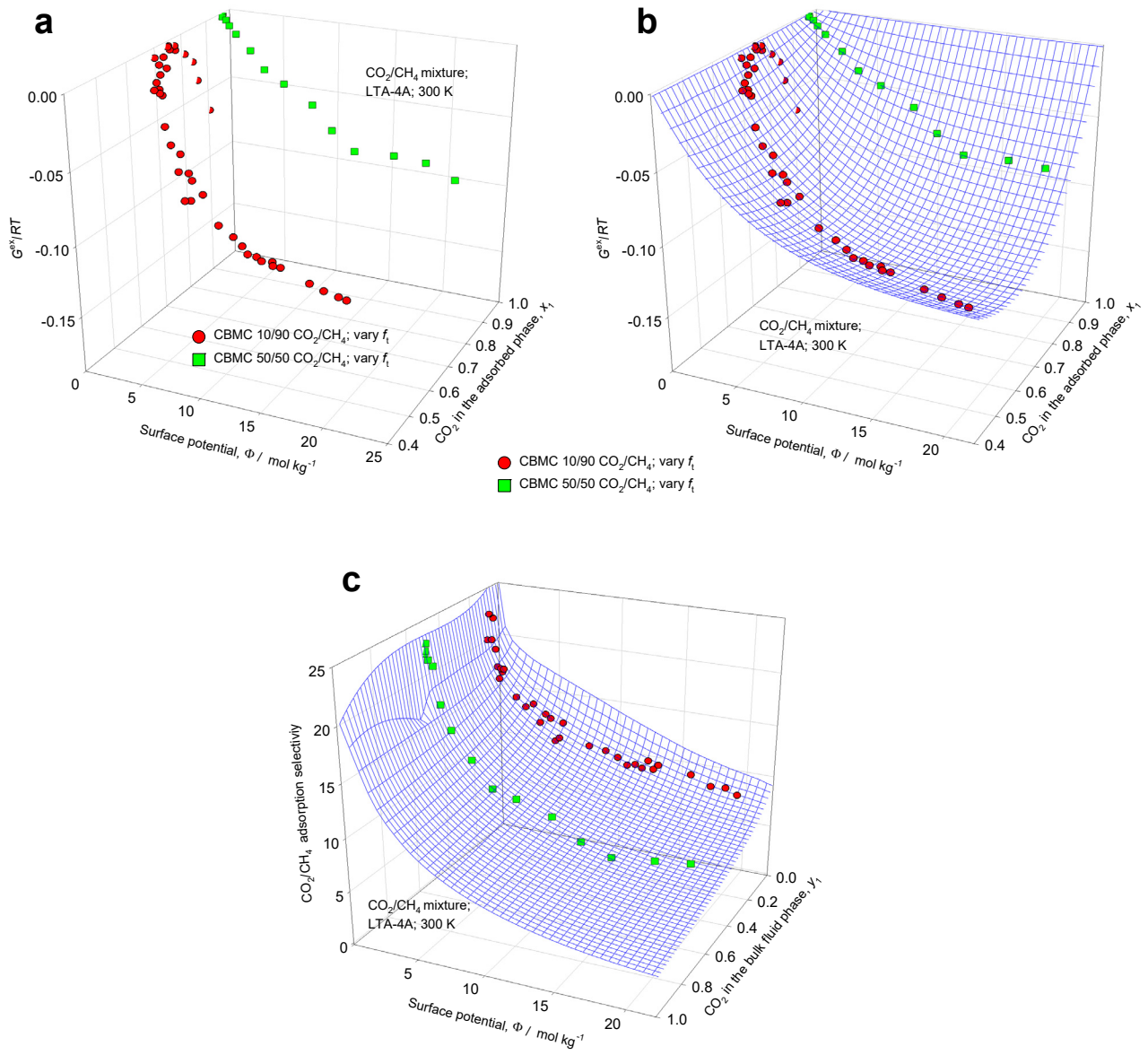

Figure S75. (a, b) 3D plots of CBMC data on excess Gibbs free energy $G^{ex}/RT = x_1 \ln(\gamma_1) + x_2 \ln(\gamma_2)$ for CO_2(1)/CH_4(2) mixture adsorption in LTA-4A zeolite at 300 K. (c) 3D plot of the CO_2(1)/CH_4(2) adsorption selectivity as function of the surface potential Φ and mole fraction of CO_2 in the bulk gas phase, y_1. The 3D mesh is constructed using the Wilson parameters provided in Table S13.

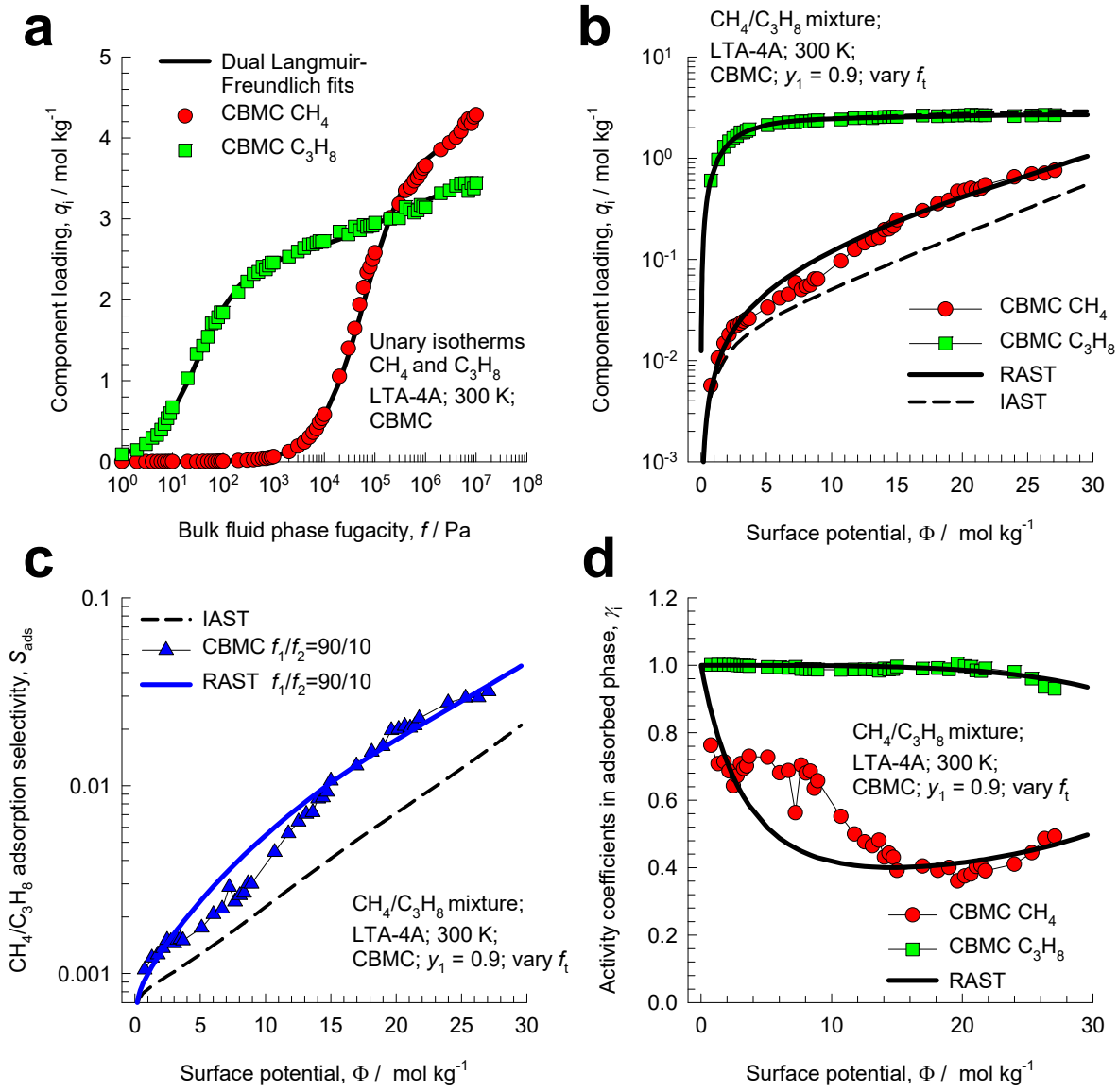

Figure S76. CBMC simulation data for 90/10 $CH_4(1)/C_3H_8(2)$ mixture adsorption in LTA-4A zeolite at 300 K. (a) Unary isotherms and fits. (b) Component loadings in mixture compared with IAST and RAST estimates (c) CBMC data for $CH_4(1)/C_3H_8(2)$ adsorption selectivity compared with IAST and RAST estimates. (d) Activity coefficients as function of the surface potential. The unary isotherm fits and the Wilson parameter fits are provided in Table S13.

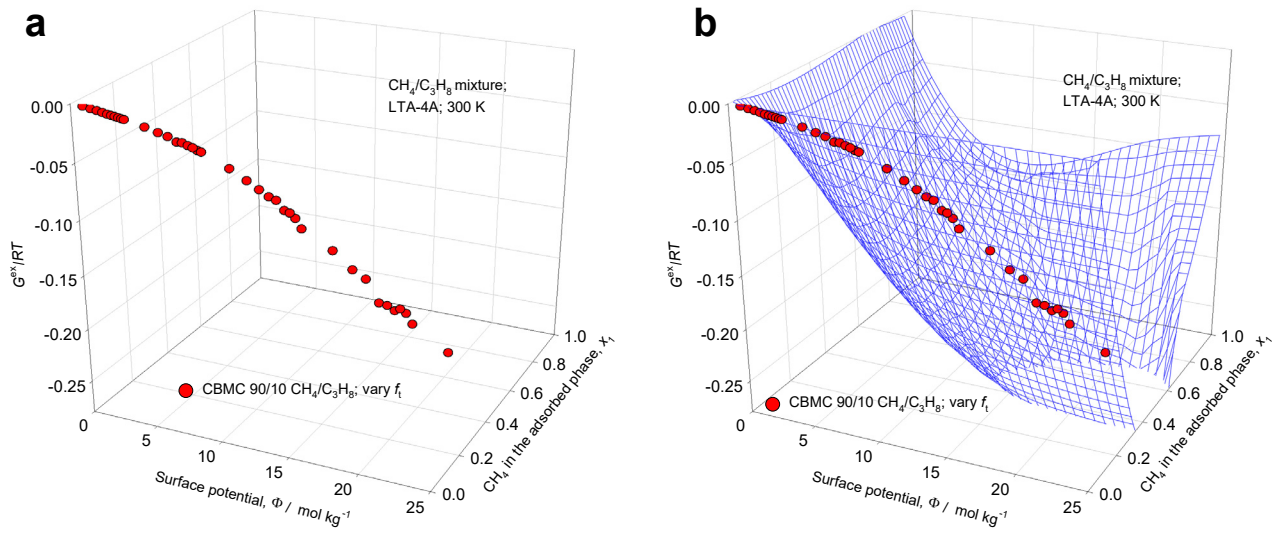

Figure S77. 3D plots of CBMC data on excess Gibbs free energy $G^{ex}/RT = x_1 \ln(\gamma_1) + x_2 \ln(\gamma_2)$ for 90/10 $CH_4(1)/C_3H_8(2)$ mixture adsorption in LTA-4A zeolite at 300 K. The 3D mesh is constructed using the Wilson parameters provided in Table S13.

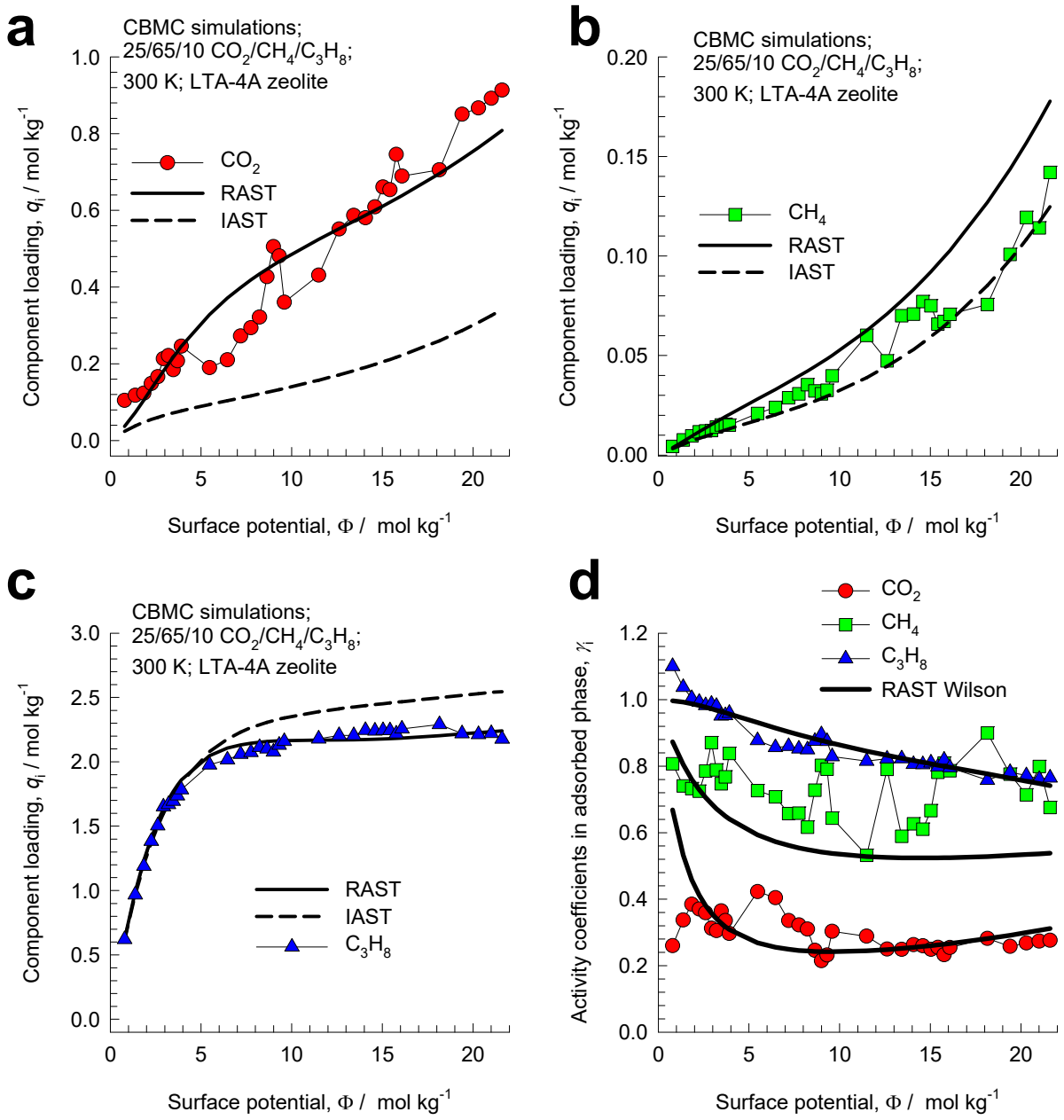

Figure S78. CBMC simulations (indicated by symbols) for 25/65/10 CO_2(1)//CH_4(2)/C_3H_8(3) mixtures in LTA-4A zeolite at 300 K. (a, b, c) Component loadings from CBMC are compared with IAST and RAST estimates. (d) Activity coefficients as function of the surface potential. The Wilson parameters for the binary pairs are as provided in Table S13.

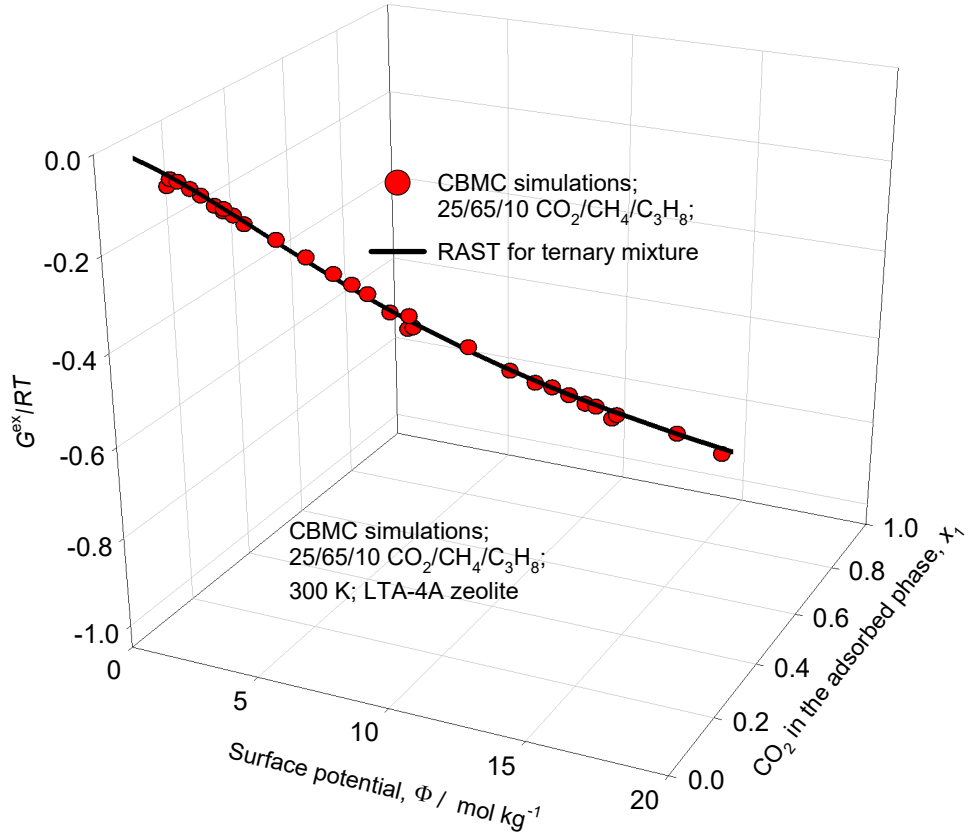

Figure S79. 3D plot of CBMC data on excess Gibbs free energy $G^{ex}/RT = \sum_{i=1}^{n} x_i \ln(\gamma_i)$ for 25/65/10 $CO_2(1)//CH_4(2)/C_3H_8(3)$ mixtures in LTA-4A zeolite at 300 K. Comparison is made with the estimates of the ternary Wilson RAST model. The Wilson parameters for the binary pairs are provided in Table S13.

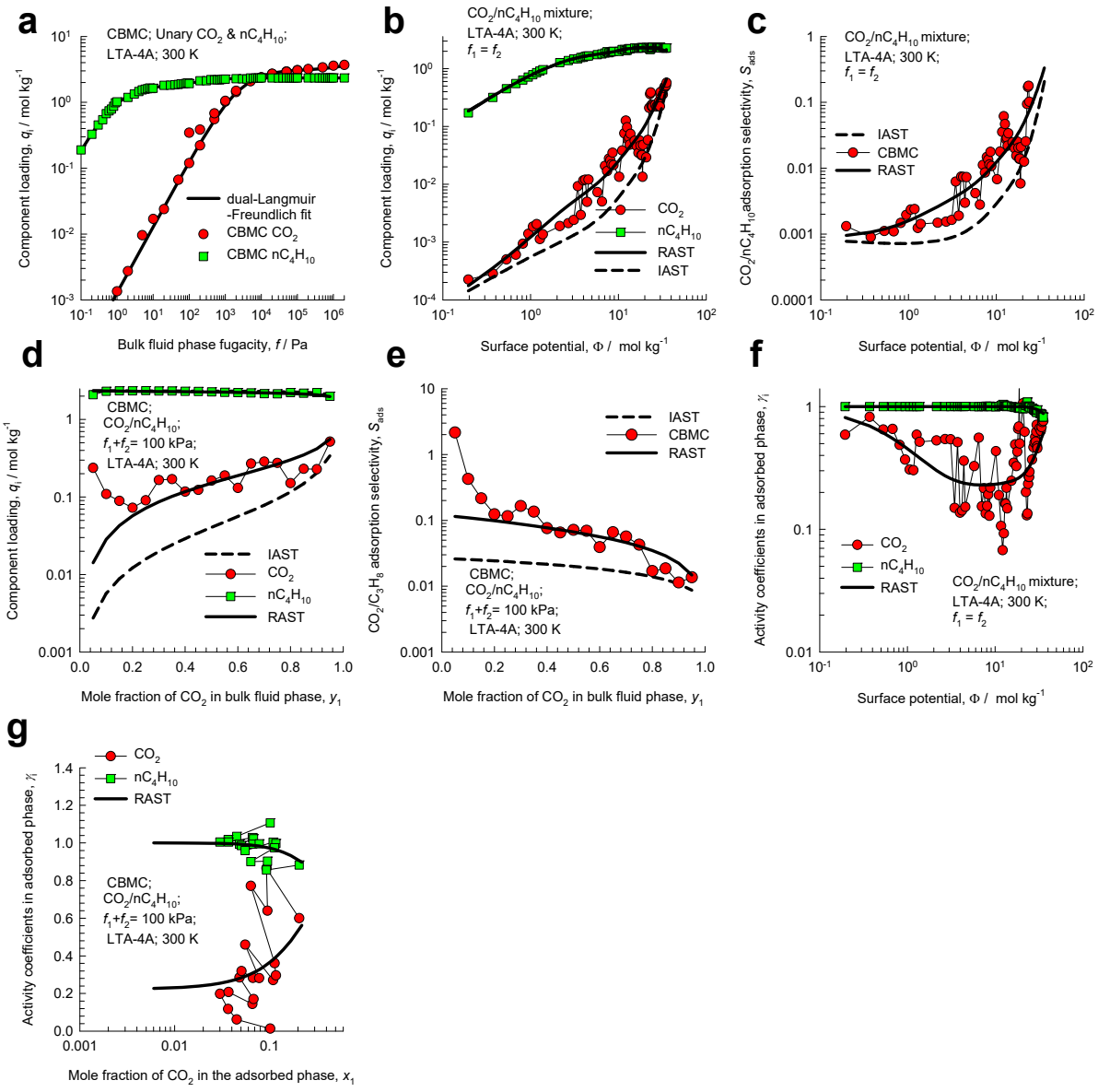

Figure S80. CBMC simulation data and analysis for Campaign A (y_1= 0.5) and Campaign B (f_t = 100 kPa) for CO_2(1)/nC_4H_{10}(2) mixture adsorption in LTA-4A zeolite at 300 K. (a) Unary isotherms and fits. (b, d) CBMC data for component loadings compared with IAST/RAST estimates. (c, e) CO_2(1)/nC_4H_{10}(2)/adsorption selectivity compared with IAST/RAST estimates. (e, f) Activity coefficients for Campaigns A and B.. The unary isotherm fits and Wilson parameters parameters are provided in Table S13.

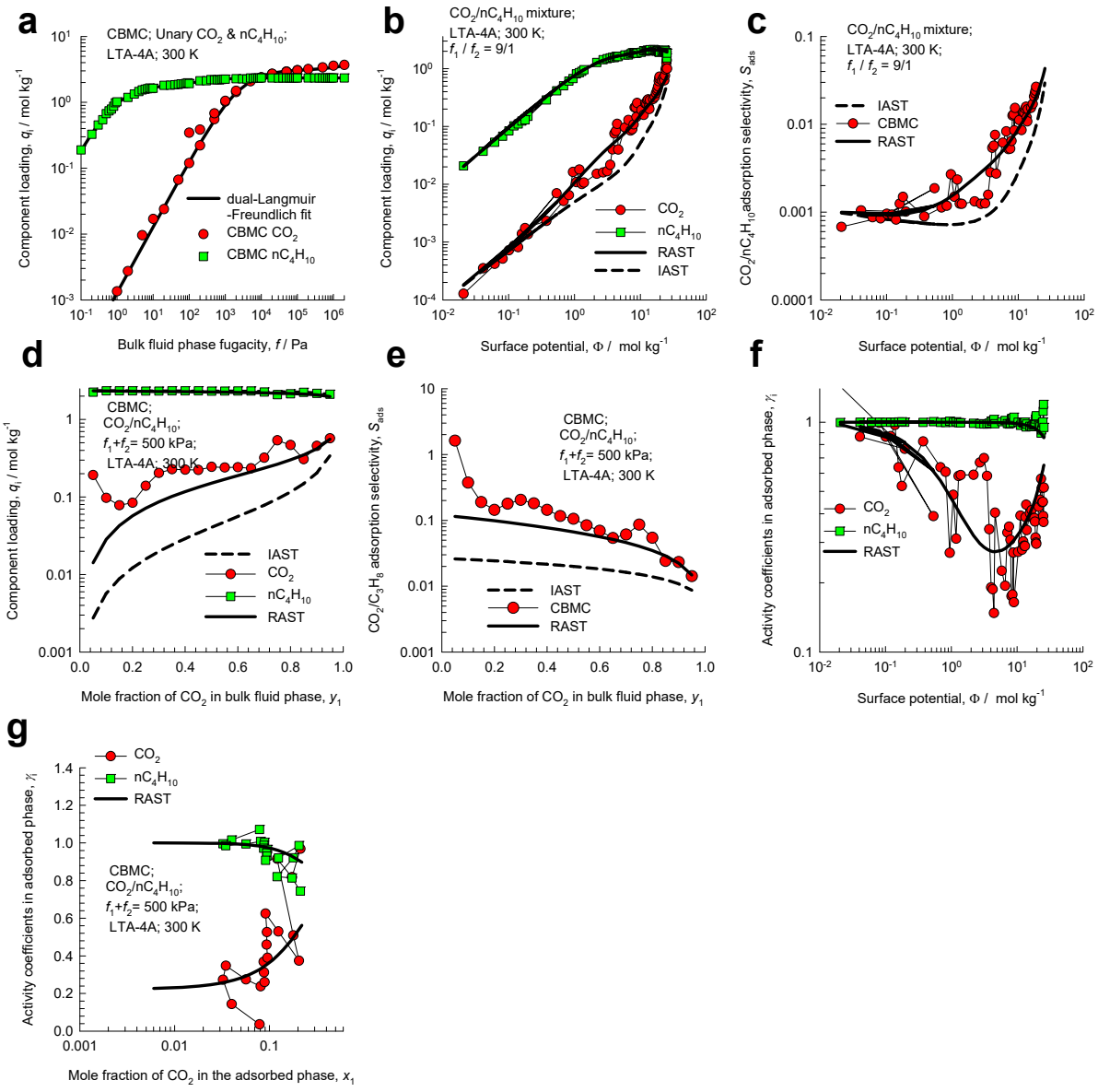

Figure S81. CBMC simulation data and analysis for Campaign A (y_1= 0.9) and Campaign B (f_t = 500 kPa) for CO_2(1)/nC_4H_{10}(2) mixture adsorption in LTA-4A zeolite at 300 K. (a) Unary isotherms and fits. (b, d) CBMC data for component loadings compared with IAST/RAST estimates. (c, e) CO_2(1)/nC_4H_{10}(2)/adsorption selectivity compared with IAST/RAST estimates. (e, f) Activity coefficients for Campaigns A and B.. The unary isotherm fits and Wilson parameters parameters are provided in Table S13.

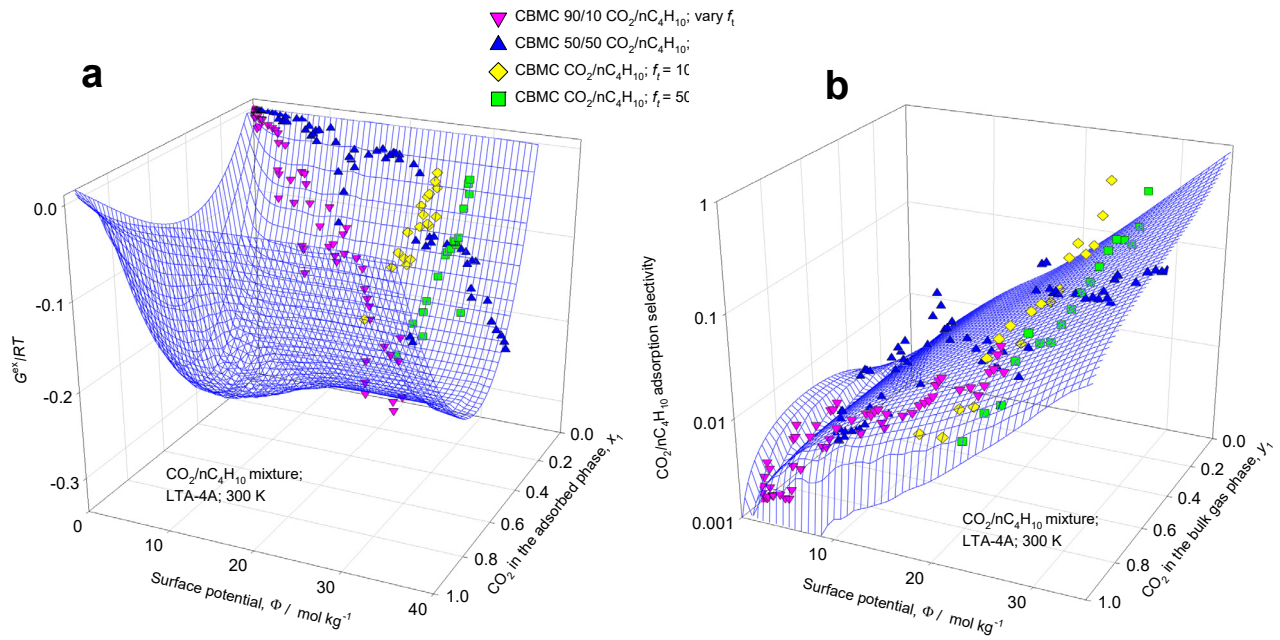

Figure S82. 3D plot of CBMC data on (a) excess Gibbs free energy $G^{ex}/RT = x_1 \ln(\gamma_1) + x_2 \ln(\gamma_2)$, and (b) adsorption selectivity for Campaigns A ($y_1 = 0.5$, $y_1 = 0.9$) and Campaigns B ($f_t = 100$ kPa and $f_t = 500$ kPa) for $CO_2(1)/nC_4H_{10}(2)$ mixture adsorption in LTA-4A zeolite at 300 K. The 3D mesh is created with the Wilson parameters provided in Table S13.

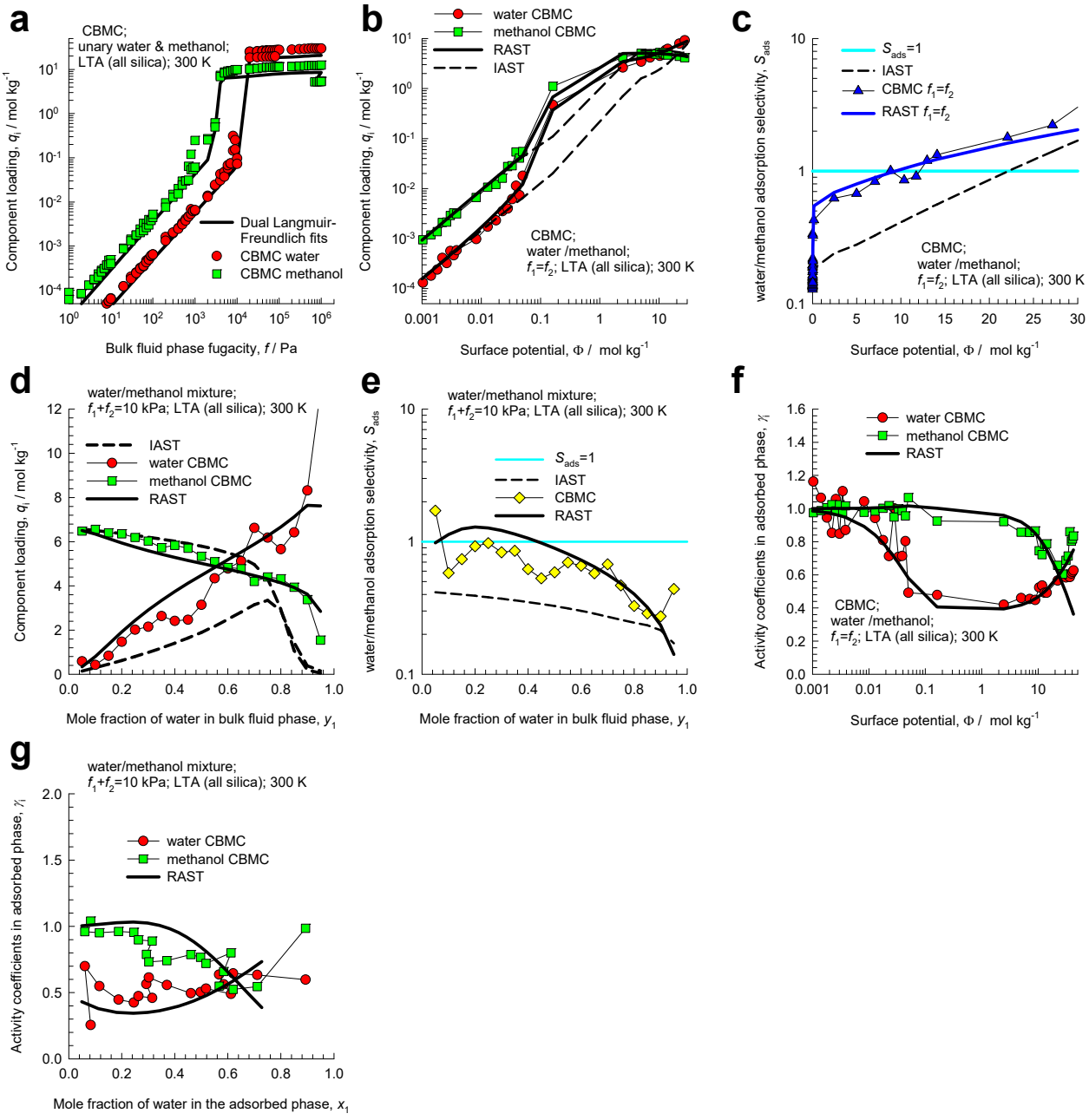

Figure S83. CBMC simulation data on component loadings, selectivities, and activity coefficients for Campaign A (y_1= 0.5) and Campaign B (f_t= 10 kPa) for water(1)/methanol(2) mixtures in LTA (all silica) at 300 K The CBMC data are compared with RAST calculations using fitted Margules parameters. The dashed lines are IAST calculations.

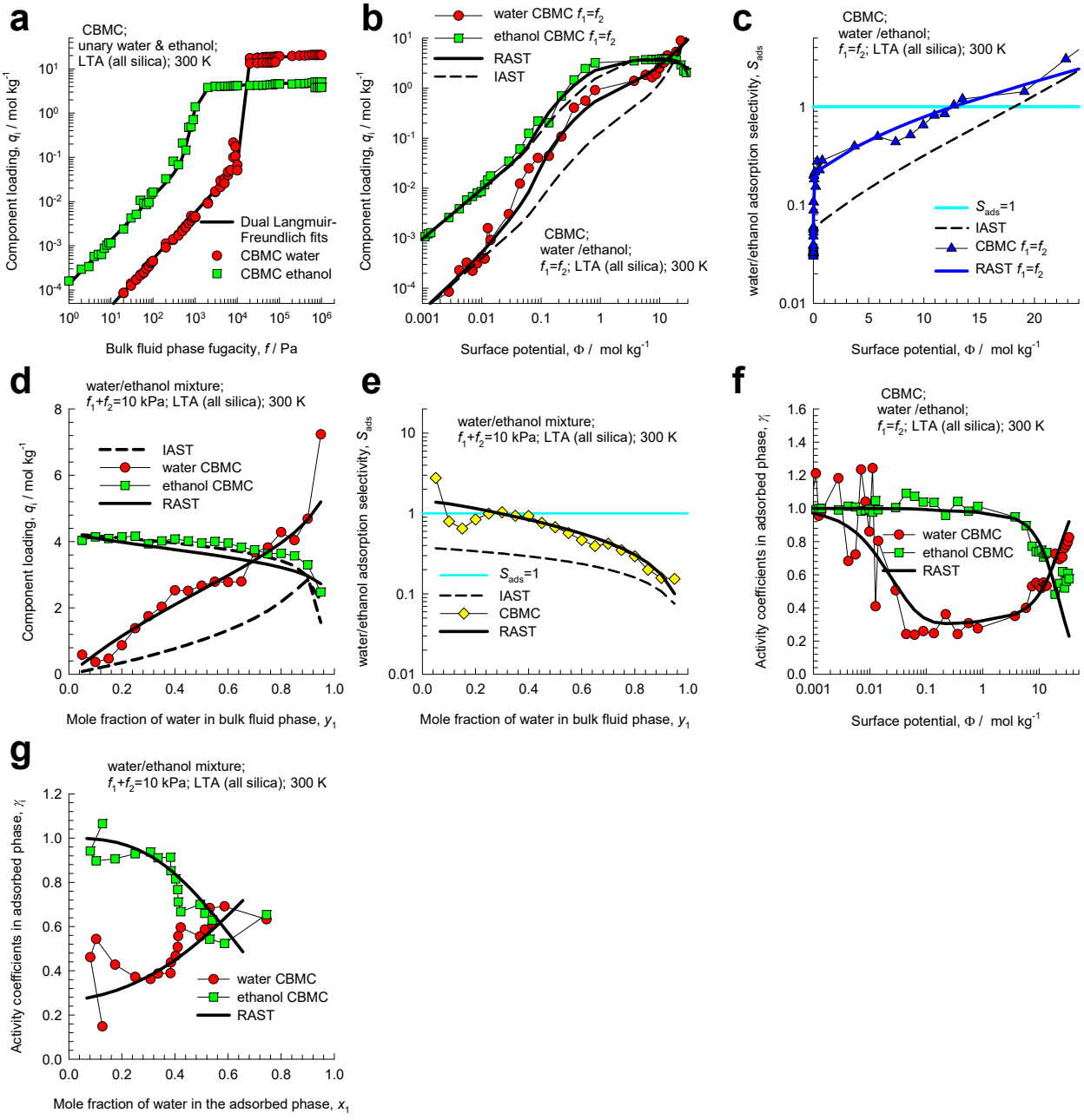

Figure S84. CBMC simulation data on component loadings, selectivities, and activity coefficients for Campaign A (y_1= 0.5) and Campaign B (f_t= 10 kPa) for water(1)/ethanol(2) mixtures in LTA (all silica) at 300 K The CBMC data are compared with RAST calculations using fitted Margules parameters. The dashed lines are IAST calculations.

11 Mixture adsorption in all-silica MFI zeolite

MFI zeolite (also called silicalite-1) has a topology consisting of a set of intersecting straight channels, and zig-zag (or sinusoidal) channels of 5.4 Å × 5.5 Å and 5.4 Å × 5.6 Å size. The pore landscapes and structural details are provided in Figure S85, and Figure S86. The crystal framework density $\rho = 1796$ kg m^{-3}. The pore volume $V_p = 0.165$ cm^3/g.

11.1 Adsorption of mixtures of light gaseous molecules in MFI zeolite

The applicability of Raoult's law analog, eq (S4), mandates that all of the adsorption sites within the microporous material are equally accessible to each of the guest molecules, implying a homogeneous distribution of guest adsorbates within the pore landscape, with no preferential locations of any guest species.[45, 47] This requirement of homogeneous distribution of guest molecules within MFI zeolite is fulfilled for light gaseous molecules such as H_2, N_2, CO_2, CH_4, C_2H_4, C_2H_6, C_3H_6, C_3H_8, and n-C_4H_{10}. Figure S87a shows computational snapshots for the adsorption of CO_2, and CH_4 within the intersecting channel topology of MFI zeolite. It is noticeable that neither guest species shows any preferential location and there is no visual indication of segregated adsorption. The only charged species is CO_2; the coulombic interactions with the negatively charged oxygen atoms in the zeolite framework are not strong enough to cause segregation between CO_2, and CH_4. We should therefore expect the mixture adsorption characteristics to be adequately well described by the IAST. Figure S87b shows CBMC simulations for the unary isotherms of light gaseous molecules in MFI zeolite at 300 K. The light gaseous guests can locate anywhere along the straight channels and zig-zag channels, and there are no perceptible isotherm inflections. The loadings, plotted on the *y*-axis are expressed in units of molecules per unit cell, Θ. To obtain the loading q, with units of mol kg^{-1}, the conversion factor is $1\ \text{molecule uc}^{-1} = 0.173366\ \text{mol kg}^{-1}$. These unary isotherms were each fitted with the dual-site Langmuir-Freundlich model (eq (S8)); the parameter values are defined in Table S16. The IAST calculations for the adsorption selectivity, S_{ads},

for five different binary mixtures CO_2/CH_4, CO_2/H_2, CO_2/N_2, CH_4/N_2, C_3H_8/CH_4, are compared with the corresponding S_{ads} values determined from CBMC simulations in Figure S88a,b. In Figure S88a the S_{ads} values are plotted as function of the surface potential, Φ . In Figure S88b the S_{ads} values are plotted as function of the pore occupancy, θ, determined from eq (S28). For all five mixtures the IAST estimations are in good agreement with the CBMC simulations. For CO_2/CH_4 and CO_2/N_2 mixtures, the S_{ads} increases as pore saturation conditions are approached, i.e. $\Phi > 10 \text{ mol kg}^{-1}$; $\theta > 0.5$ because of entropy effects that favor the guest CO_2 with the higher saturation capacity (cf. Figure S87b); the explanation of entropy effects are provided in the published literature.[66, 67]

For CO_2/H_2 and C_3H_8/CH_4 mixtures, the S_{ads} decreases as pore saturation conditions are approached, i.e. $\Phi > 10 \text{ mol kg}^{-1}$; $\theta > 0.5$ because entropy effects favor the smaller guests H_2 and CH_4, respectively.

The use of the mixed-gas Langmuir model with equal saturation capacities (eq (S24)) is unable to cater for entropy effects as evidenced for the four aforementioned CO_2/CH_4, CO_2/N_2, CO_2/H_2 and C_3H_8/CH_4 mixtures.

For CH_4/N_2 mixtures, the S_{ads} is practically independent of occupancy because the saturation capacities of CH_4, and N_2 are nearly the same, as evidenced in Figure S87b.

A further important point to note is that for the adsorption selectivity as defined in eq (S13) for component 1 with respect to component 2, also holds for the same guest components in the presence of other guest species, 3, 4, 5, .. etc. Equation (S6) implies that if the comparisons are made at the same surface potential Φ , the value of S_{ads} for component 1 with respect to component 2, remains the same irrespective of the presence of additional guest components in the same host.

Figure S89a presents a comparison of CO_2/CH_4, CO_2/N_2, and CH_4/N_2 adsorption selectivities determined from binary mixtures, with the corresponding values determined from CBMC simulations two different ternary mixtures: 5/15/80 $CO_2/CH_4/N_2$, and 20/30/50 $CO_2/CH_4/N_2$ in MFI zeolite at 300 K. Each of the three selectivities shows a unique dependence on Φ , as prescribed by eq (S13). Put another way,

the presence of component 3 in the ternary mixture has no influence of the adsorption selectivity for the 1-2 pair other than via the surface potential.

Figure S89b,c present a different way to demonstrate that the adsorption selectivity for ideal mixtures is dependent only on the surface potential Φ and not the bulk gas phase composition, y_1, Figure S89b,c are 3D plots the of CO_2/CH_4 and CO_2/N_2 selectivity as a function of Φ and y_1, The CBMC data for binary and ternary mixtures of varying compositions mixtures reside on a 3D mesh created by IAST calculations. The 3D plots confirm the unique S_{ads} vs Φ dependence, as prescribed by eq (S13). Put another way, the presence of component 3 in the ternary mixture has no influence of the adsorption selectivity for the 1-2 pair.

11.2 Water/methanol/ethanol mixture adsorption

For adsorption of water(1)/ethanol(2) mixtures in MFI zeolite at 300 K, two different CBMC simulations were carried out: Campaign A (with $y_1 = 0.5$, vary f_t), and campaign B, the mole fraction of water(1) in the bulk fluid phase, y_1 was varied from 0 to 1, keeping the bulk fluid phase mixture fugacity $f_t = f_1 + f_2$ constant at a value of 10 kPa. The CBMC data on component loadings, adsorption selectivities, and activity coefficients are presented in Figure S90,

The dashed lines are the IAST estimates. The failure of the IAST to match the CBMC data presented in Figure S90 is a consequence of hydrogen bonding between guest molecules in water/alcohol mixtures.[15, 18, 47, 48, 60] One of the mandates of the IAST is violated because of the formation of water/alcohol clusters.[15, 46, 48]

In order to demonstrate the occurrence of hydrogen bonding in water/methanol, and water/ethanol mixtures CBMC simulation data on the spatial locations of the guest molecules were sampled to determine the O···H distances of various pairs of molecules. By sampling a total of 10^6 simulation steps, the radial distribution functions (RDF) of O···H distances were determined for water-water, water-alcohol, and alcohol-alcohol pairs.

Figure S91 shows the RDF of O…H distances for molecular pairs of water(1)/ethanol(2) mixture adsorption in MFI zeolite at 300 K. The partial fugacities of components 1 and 2 are f_1= 9 kPa, f_2= 1 kPa. We note the first peaks in the RDFs occur at a distance less than 2 Å, that is characteristic of hydrogen bonding.[27, 61] The heights of the first peaks are a direct reflection of the degree of hydrogen bonding between the molecular pairs.

A visual appreciation of hydrogen bonding is gleaned from the snapshots in Figure S63 for water/methanol and water/ethanol mixture adsorption in MFI.

The continuous solid lines in Figure S90 are the RAST calculations with fitted NRTL parameters specified in Table S17.

The CBMC data in Figure S90 lead us to conclude that the activity coefficients are functions of both the surface potential Φ and mole fraction of water in the adsorbed phase mixture, x_1. In Figure S93 the CBMC data for the excess Gibbs free energy $G^{ex}/RT = x_1 \ln(\gamma_1) + x_2 \ln(\gamma_2)$ for the two CBMC campaigns for water/ethanol mixtures are plotted in 3D space as function of Φ and x_1. The entire CBMC data set resides on a 3D surface mesh determined from the fitted NRTL parameters specified in Table S17.

For adsorption of water(1)/methanol(2) mixtures in MFI zeolite at 300 K, CBMC simulations were carried out for Campaign A (with y_1 = 0.5, vary f_t). The CBMC data on component loadings, adsorption selectivities, and activity coefficients are presented in Figure S94. In Figure S95 the CBMC data for the excess Gibbs free energy $G^{ex}/RT = x_1 \ln(\gamma_1) + x_2 \ln(\gamma_2)$ for the CBMC campaign for water/methanol mixtures are plotted in 3D space as function of Φ and x_1. The entire CBMC data set resides on a 3D surface mesh determined from the fitted NRTL parameters specified in Table S17. The 3D plot reaffirms the dependence of the activity coefficients on both the surface potential Φ and mole fraction of water in the adsorbed phase mixture, x_1.

For adsorption of methanol(1)/ethanol(2) mixtures in MFI zeolite at 300 K, CBMC simulations were carried out for Campaign A (with $y_1 = 0.5$, vary f_t). The CBMC data on component loadings, adsorption selectivities, and activity coefficients are presented in Figure S96. In Figure S97 the CBMC data for the excess Gibbs free energy $G^{ex}/RT = x_1 \ln(\gamma_1) + x_2 \ln(\gamma_2)$ for the CBMC campaign for methanol/ethanol mixtures are plotted in 3D space as function of Φ and x_1. The entire CBMC data set resides on a 3D surface mesh determined from the fitted NRTL parameters specified in Table S17. The 3D plot reaffirms the dependence of the activity coefficients on both the surface potential Φ and mole fraction of water in the adsorbed phase mixture, x_1.

Figure S98a,b,c presents CBMC simulations of component loadings, q_i, for equimolar $f_1 = f_2 = f_3$ water(1)/methanol(2)/ethanol(3) mixture adsorption in MFI zeolite with varying total fugacity $f_t = f_1 + f_2 + f_3$, plotted as a function of the surface potential Φ . The component activity coefficients are plotted in Figure S98d. The dashed lines in Figure S98 are IAST estimates; the continuous solid lines are RAST calculations The continuous solid lines in Figure S98 are RAST calculations using the NRTL model. In these calculations the NRTL parameters $\tau_{12}, \tau_{21}, \alpha_{12}, \tau_{13}, \tau_{31}, \alpha_{13}, \tau_{23}, \tau_{32}, \alpha_{23}$ are taken to the same as for the corresponding binary pairs as listed in in Table S17. Our approach for ternary mixtures is to estimate C as $C = \frac{x_1}{q_{1,sat}} + \frac{x_2}{q_{2,sat}} + \frac{x_3}{q_{3,sat}}$, assuming, $x_1 = x_2 = x_3 = 1/3$. The RAST calculations are in reasonable agreement with CBMC data.

In Figure S99 the excess Gibbs free energy $G^{ex}/RT = \sum_{i=1}^{n} x_i \ln(\gamma_i)$ determined from CBMC data for equimolar $f_1 = f_2 = f_3$ water(1)/methanol(2)/ethanol(3) mixture adsorption in MFI zeolite are plotted in 3D space as function of the surface potential Φ and mole fraction of water in the adsorbed phase mixture, x_1. The continuous solid line represents the ternary RAST NRTL calculations. The agreement is good, validating the ternary RAST NRTL model.

11.3 List of Tables for Mixture adsorption in all-silica MFI zeolite

Table S16. Dual-site Langmuir-Freundlich parameters for guest molecules in MFI at 300 K. To convert from molecules uc^{-1} to mol kg^{-1}, multiply by 0.173367.

	Site A			Site B		
	$\frac{\Theta_{A,sat}}{\text{molec uc}^{-1}}$	$\frac{b_A}{\text{Pa}^{-\nu_A}}$	ν_A	$\frac{\Theta_{B,sat}}{\text{molec uc}^{-1}}$	$\frac{b_B}{\text{Pa}^{-\nu_B}}$	ν_B
H2	30	3.57E-08	1	42	1.39E-09	1
N2	16	6.37E-07	1	16	3.82E-07	0.7
CO2	19	6.12E-06	1	11	1.73E-08	1
CH4	7	5.00E-09	1	16	3.10E-06	1
C2H6	3.3	4.08E-07	1	13	7.74E-05	1
C2H4	6.9	1.988E-04	0.65	10.1	6.959E-06	1.2
C3H8	1.4	3.35E-04	0.67	10.7	6.34E-04	1.06
C3H6	0.6	2.912E-06	1	11.4	6.534E-04	1
nC4H10	1.5	2.24E-03	0.57	8.7	9.75E-03	1.12
iso-C4H10	4	2.29E-02	1	6	2.87E-05	1
nC6H14	6.6	7.08E-01	0.83	1.4	1.66E+01	1.5
2MP	4	4.513	1.05	4	7.92E-05	1.13
Benzene	4	1.359E-01	1.06	8	2.339E-03	0.52

Table S17. Dual-site Langmuir-Freundlich parameters for pure component water, methanol, and ethanol in MFI zeolite at 300 K. The fit parameters are based on the CBMC simulations of pure component isotherms presented in earlier works.[48, 62]

	Site A			Site B		
	$\frac{q_{A,sat}}{\text{mol kg}^{-1}}$	$\frac{b_A}{\text{Pa}^{-\nu_A}}$	ν_A	$\frac{q_{B,sat}}{\text{mol kg}^{-1}}$	$\frac{b_B}{\text{Pa}^{-\nu_B}}$	ν_B
water	6.7	6.369E-24	6.2	3.6	1.089E-05	1.04
methanol	2.4	1.002E-04	1.64	1.4	1.920E-03	0.7
ethanol	0.7	1.083E-18	13.6	2.03	1.775E-02	1

Fitted NRTL non-ideality parameters for binary mixture adsorption at 300 K in MFI zeolite.

	C / kg mol^{-1}	τ_{12}	τ_{21}	α
water/methanol	0.180	4.991	-1.044	0.302
water/ethanol	0.183	5.101	-0.902	0.216
methanol/ethanol	0.315	32.404	-22.485	0.013
water/methanol/ethanol	0.242	$\tau_{12},\tau_{21},\alpha_{12},\tau_{13},\tau_{31},\alpha_{13},\tau_{23},\tau_{32},\alpha_{23}$ as above		

11.4 List of Figures for Mixture adsorption in all-silica MFI zeolite

MFI pore landscape

	MFI
a /Å	20.022
b /Å	19.899
c /Å	13.383
Cell volume / Å^3	5332.025
conversion factor for [molec/uc] to [mol per kg Framework]	0.1734
conversion factor for [molec/uc] to [kmol/m^3]	1.0477
ρ [kg/m3]	1796.386
MW unit cell [g/mol(framework)]	5768.141
ϕ, fractional pore volume	0.297
open space / Å^3/uc	1584.9
Pore volume / cm^3/g	0.165
Surface area /m^2/g	487.0
DeLaunay diameter /Å	5.16

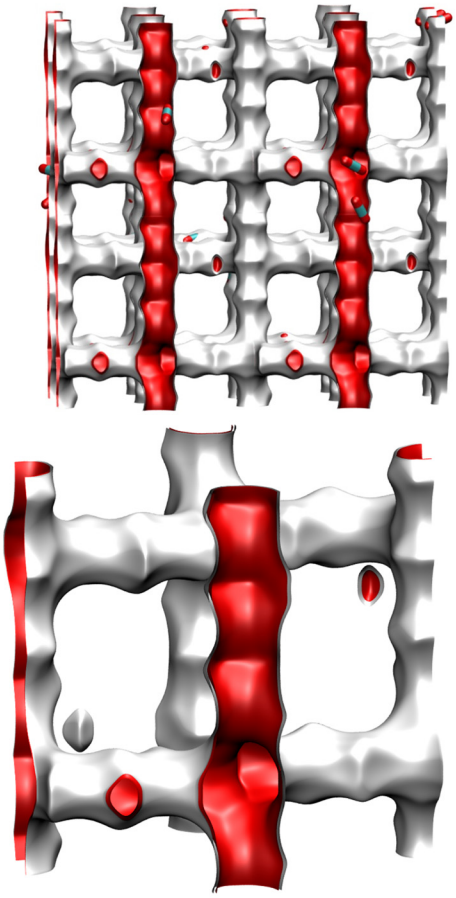

Figure S85. Pore landscape and structural data for MFI zeolite.

MFI channel dimensions

10 ring channel of MFI viewed along [100]

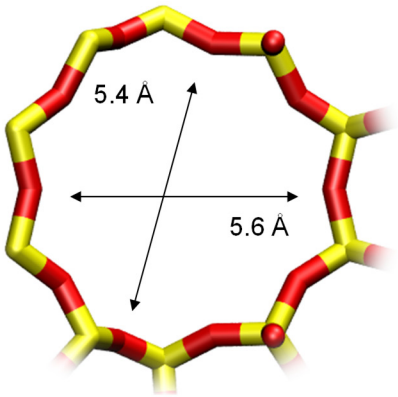

10 ring channel of MFI viewed along [010]

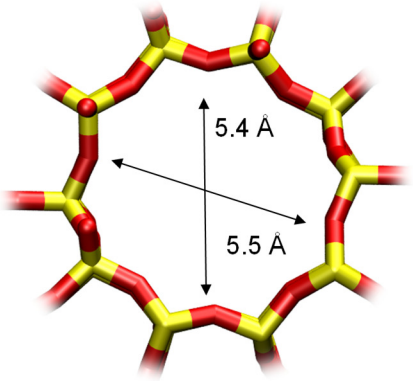

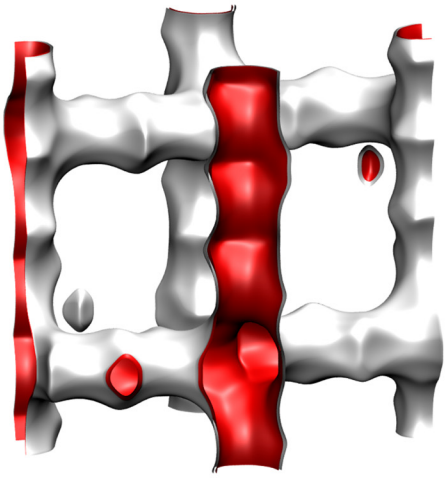

Figure S86. Pore landscape and structural data for MFI zeolite.

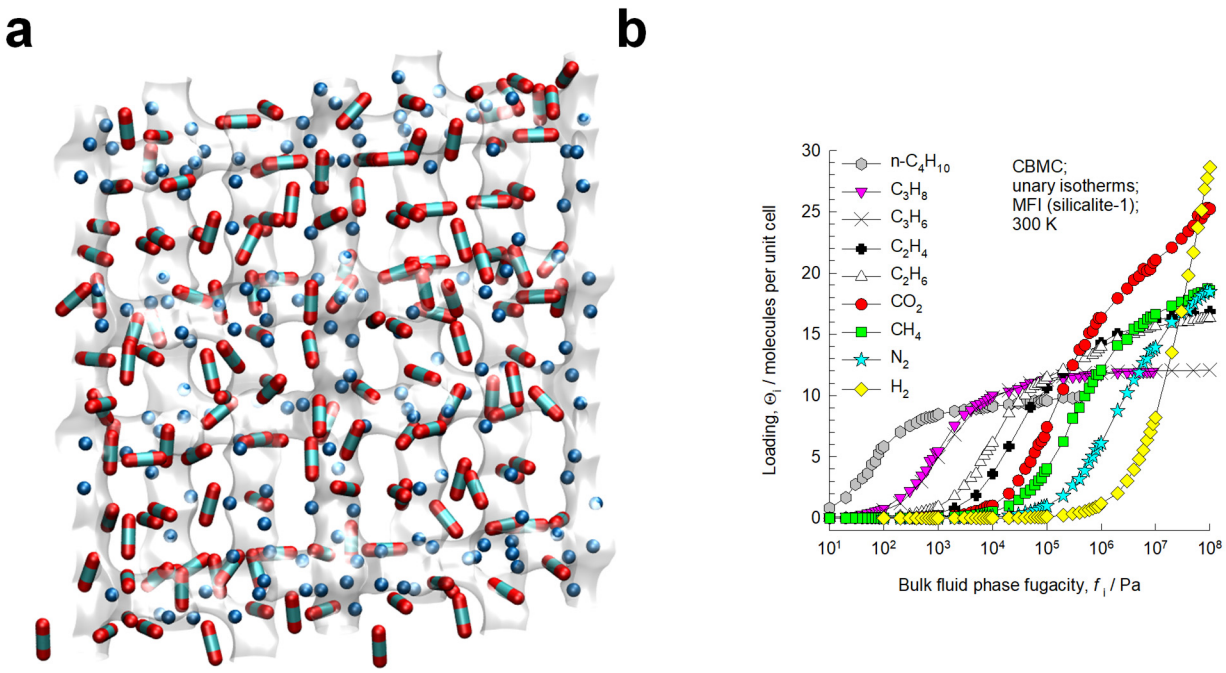

Figure S87. (a) Computational snapshots showing the distribution of. CO_2 and CH_4 for binary mixture adsorption. (b) CBMC simulations of unary isotherms for light gaseous molecules H_2, N_2, CO_2, CH_4, C_2H_4, C_2H_6, C_3H_6, C_3H_8, and n-C_4H_{10} in MFI zeolite at 300 K.

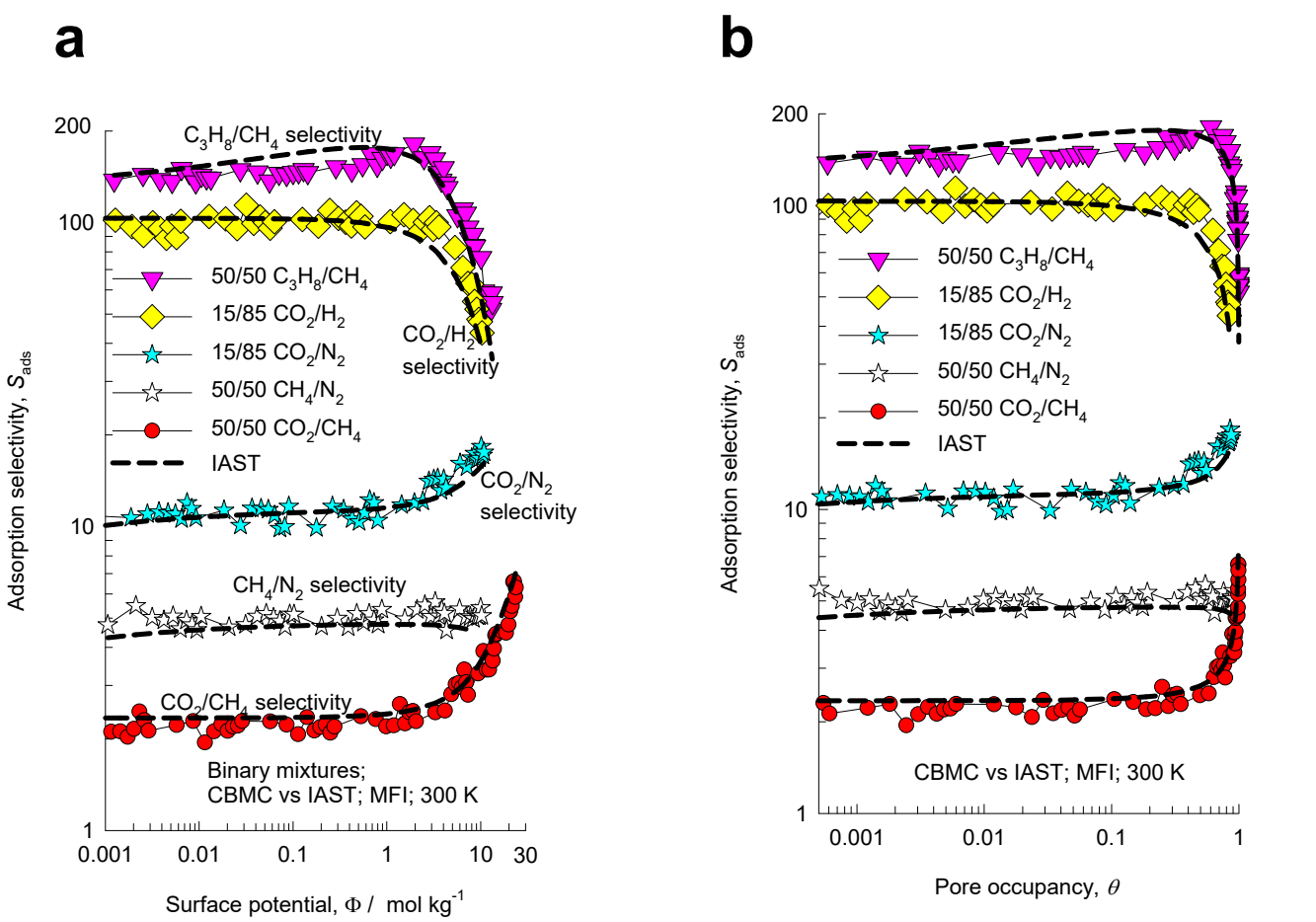

Figure S88. (a, b) CBMC simulations (indicated by symbols) of the adsorption selectivity, S_{ads} , for five different binary CO_2/CH_4, CO_2/H_2, CO_2/N_2, CH_4/N_2, C_3H_8/CH_4 mixtures compared with the IAST calculations (indicated by dashed lines) for corresponding S_{ads} values using the Dual-site Langmuir-Freundlich fits of unary isotherms. In (a) the S_{ads} values are plotted as function of the surface potential, Φ . In (b) the S_{ads} values are plotted as function of the pore occupancy, θ, determined from eq (S28).

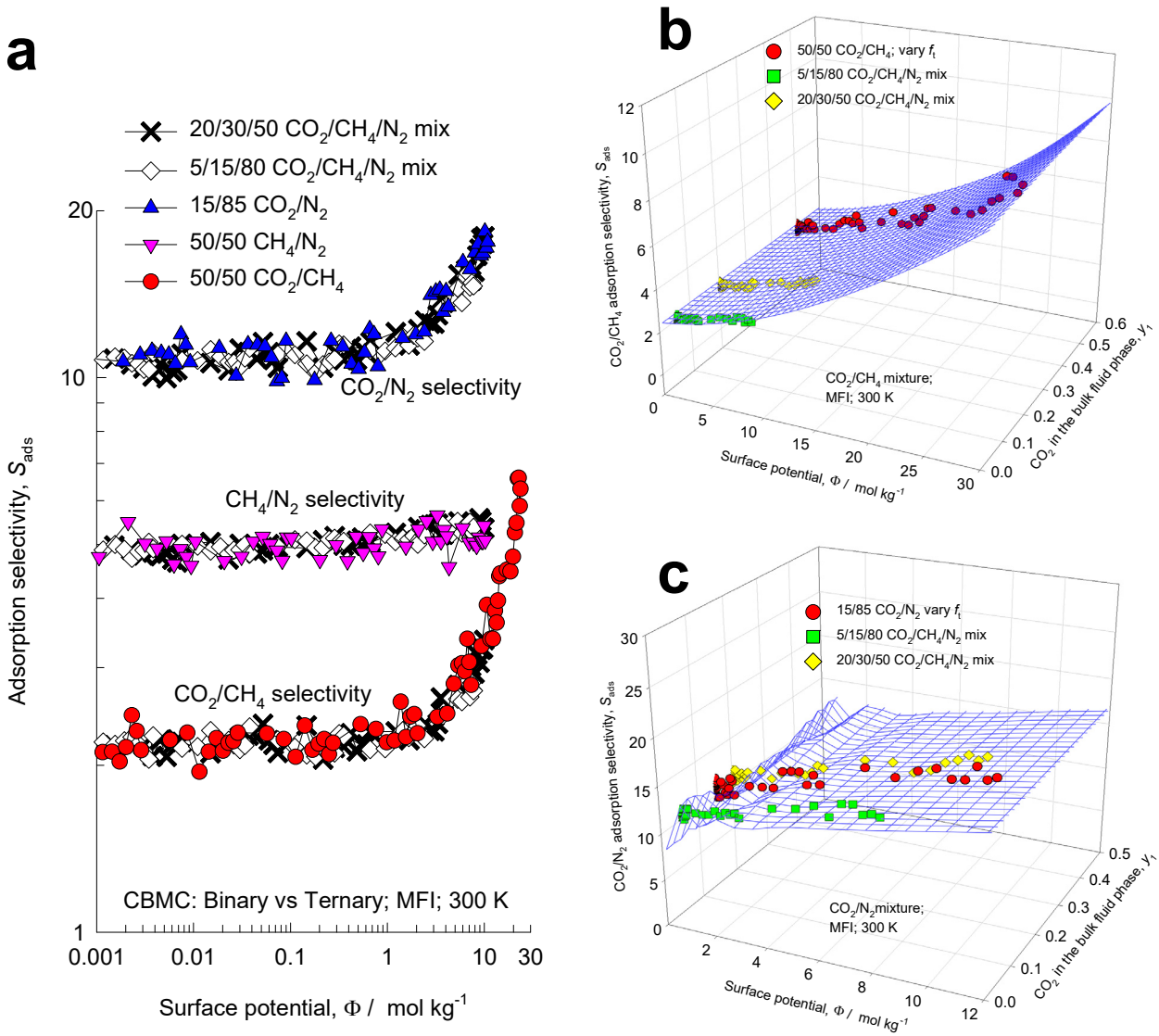

Figure S89. (a) Comparison of CO_2/CH_4, CO_2/N_2, and CH_4/N_2 adsorption selectivities determined from binary mixtures, with the corresponding values in two different ternary mixtures: 5/15/80 $CO_2/CH_4/N_2$, and 20/30/50 $CO_2/CH_4/N_2$. The *x*-axis represents the surface potential, Φ. (b, c) 3D plot of CBMC data on S_{ads} for CO_2/CH_4 and CO_2/N_2 mixture adsorption in MFI at 300 K, plotted as function of the surface potential, Φ, and the mole fraction of CO_2 in the bulk gas phase mixture, y_1. The 3D mesh is constructed using the IAST.

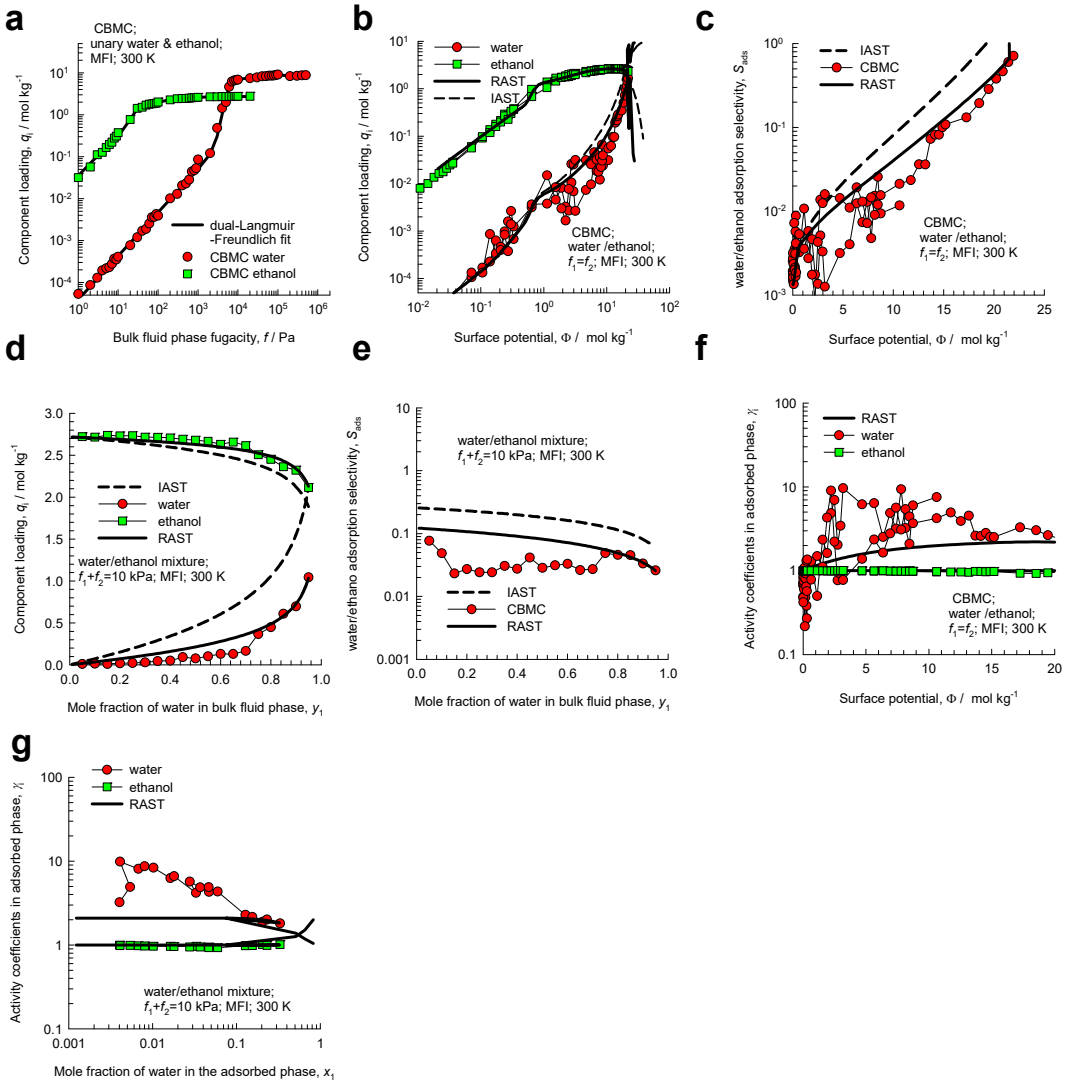

Figure S90. CBMC simulation data and analysis for Campaign A (y_1= 0.5) and for Campaign B (f_t = 10 kPa) for water(1)/ethanol(2) mixture adsorption in MFI zeolite at 300 K. (a) Unary isotherms and fits. (b, d) Component loadings in mixture compared with IAST/RAST estimates. (c, e) CBMC data for water(1)/ethanol(2) adsorption selectivity compared with IAST and RAST estimates. (f, g) Activity coefficients from CBMC compared with RAST model calculations. The unary isotherm fit parameters and NRTL parameters are provided in Table S17.

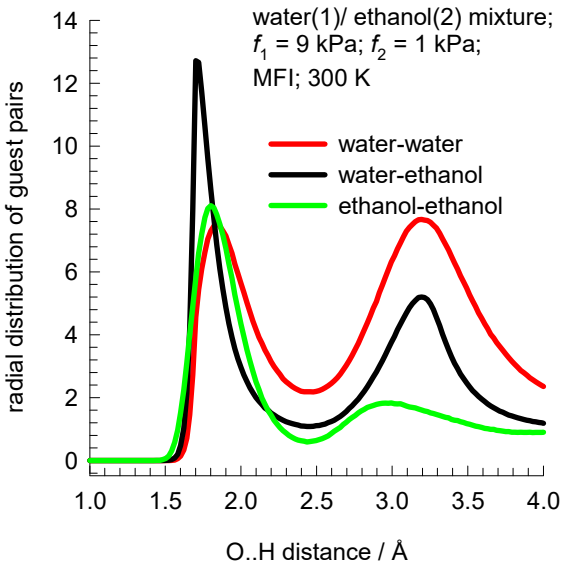

Figure S91. RDF of O···H distances for molecular pairs of water(1)/ethanol(2) mixture adsorption in MFI zeolite at 300 K. The partial fugacities of components 1 and 2 are f_1= 9 kPa, f_2= 1 kPa.

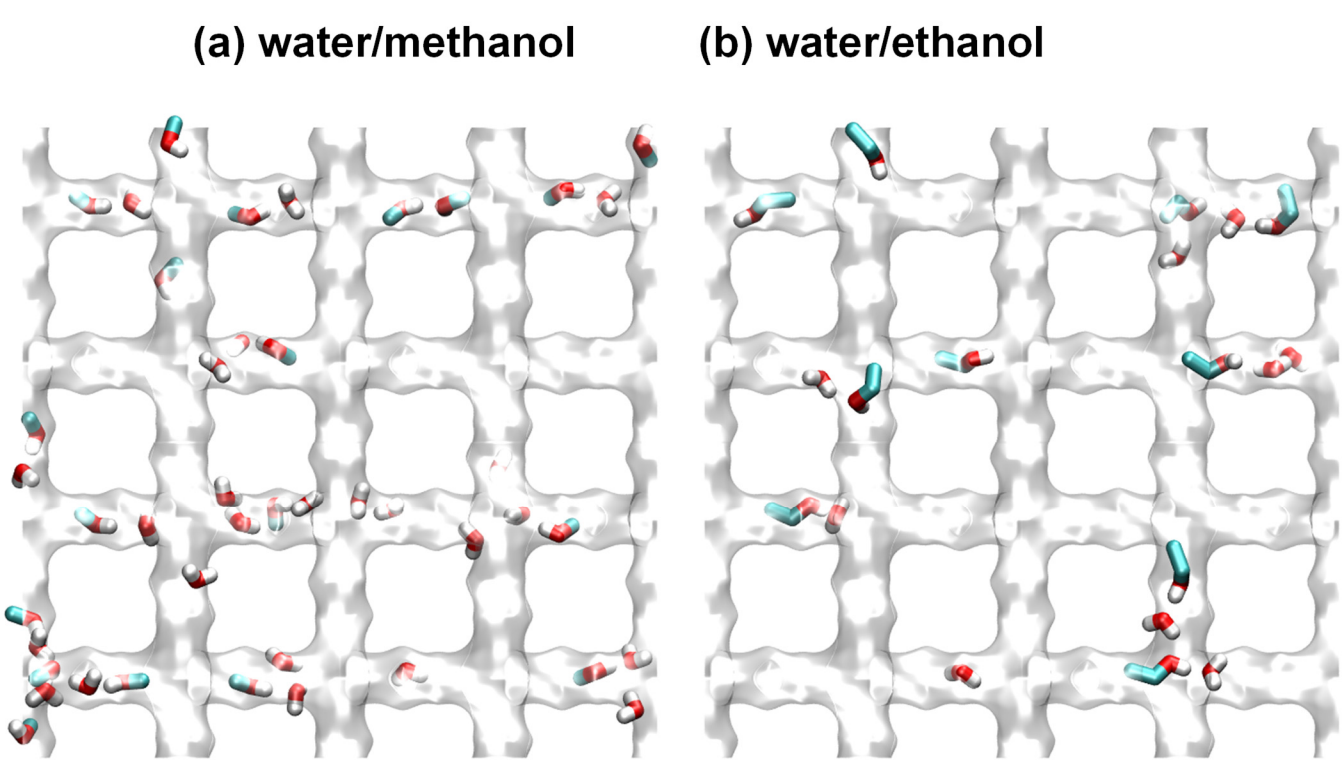

Figure S92. Snapshots showing location and conformations of guest molecules for adsorption of (a) water(1)/methanol(2), and (b) water(1)/ethanol(2) mixture adsorption in MFI zeolite at 300 K.

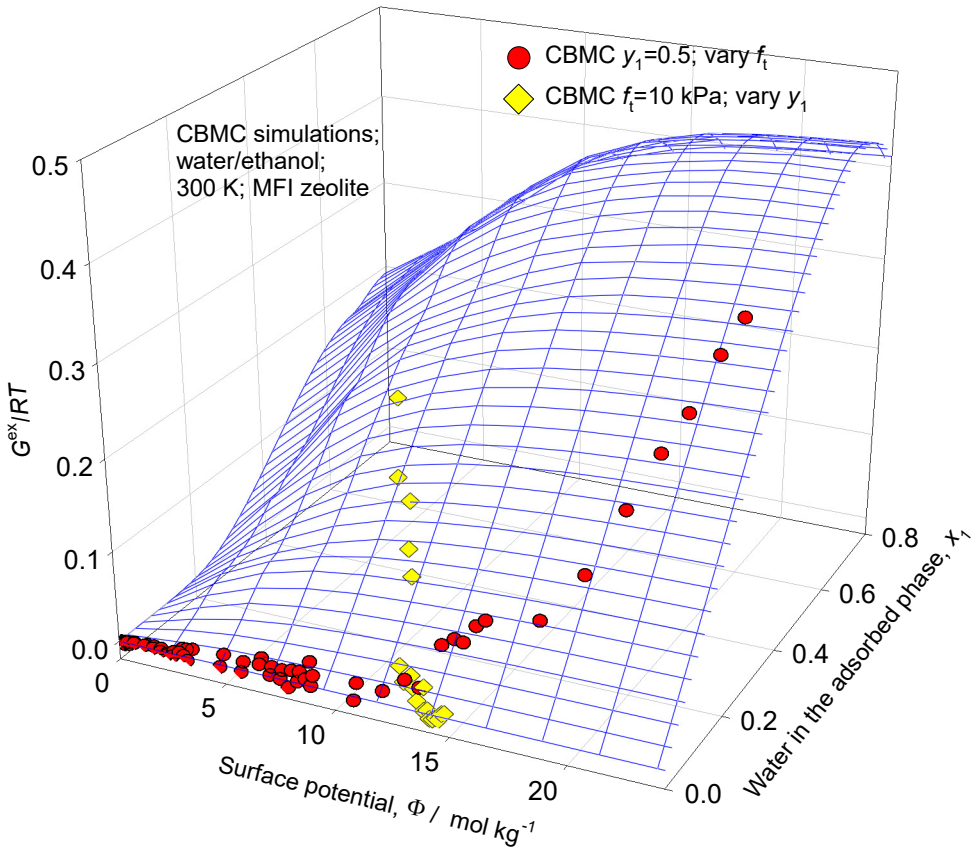

Figure S93. 3D plot of CBMC data on excess Gibbs free energy $G^{ex}/RT = x_1 \ln(\gamma_1) + x_2 \ln(\gamma_2)$ for water(1)/ethanol(2) mixture adsorption in MFI zeolite at 300 K. The 3D mesh is constructed using the NRTL parameters provided in Table S17.

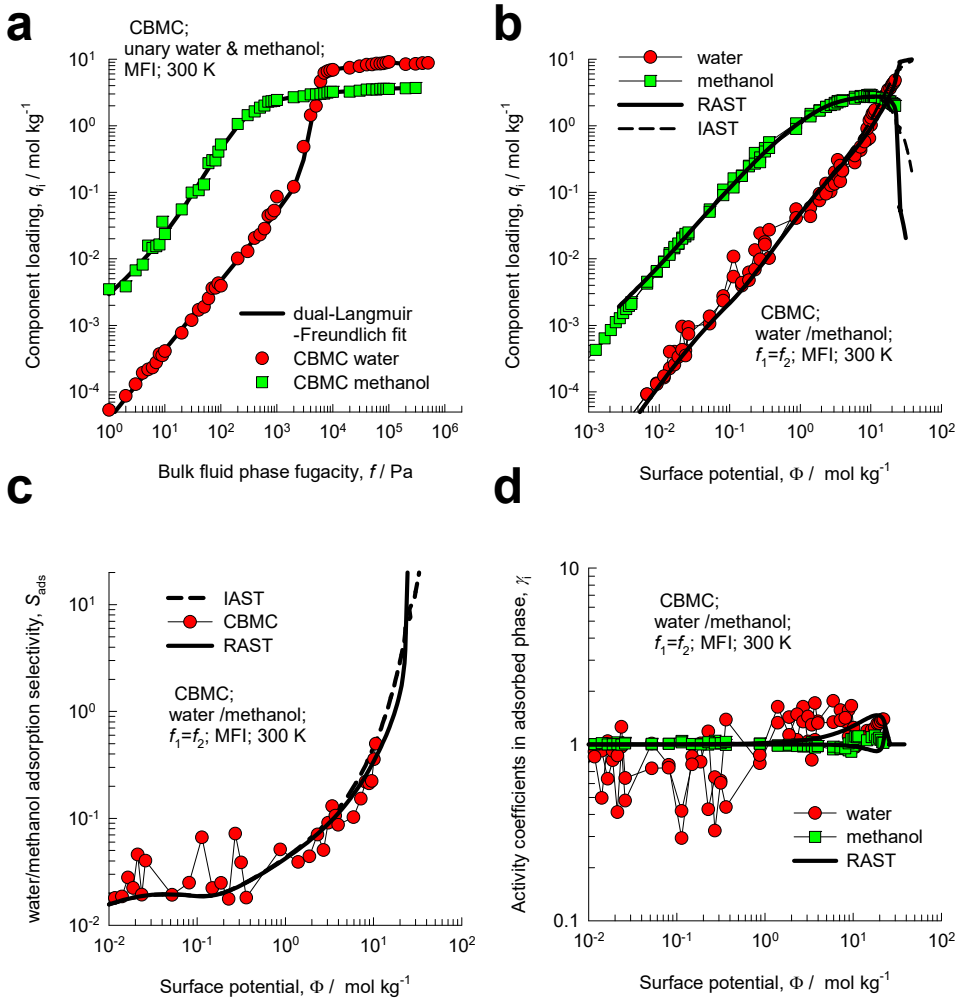

Figure S94. CBMC simulation data and analysis for Campaign A (y_1= 0.5) for water(1)/methanol(2) mixture adsorption in MFI zeolite at 300 K. (a) Unary isotherms and fits. (b) Component loadings in mixture compared with compared with IAST/RAST estimates. (c) CBMC data for water(1)/methanol(2) adsorption selectivity compared with IAST and RAST estimates. (d) CBMC data for activity coefficients from CBMC compared with RAST model calculations. The unary isotherm fit parameters and Margules parameters are provided in Table S17.

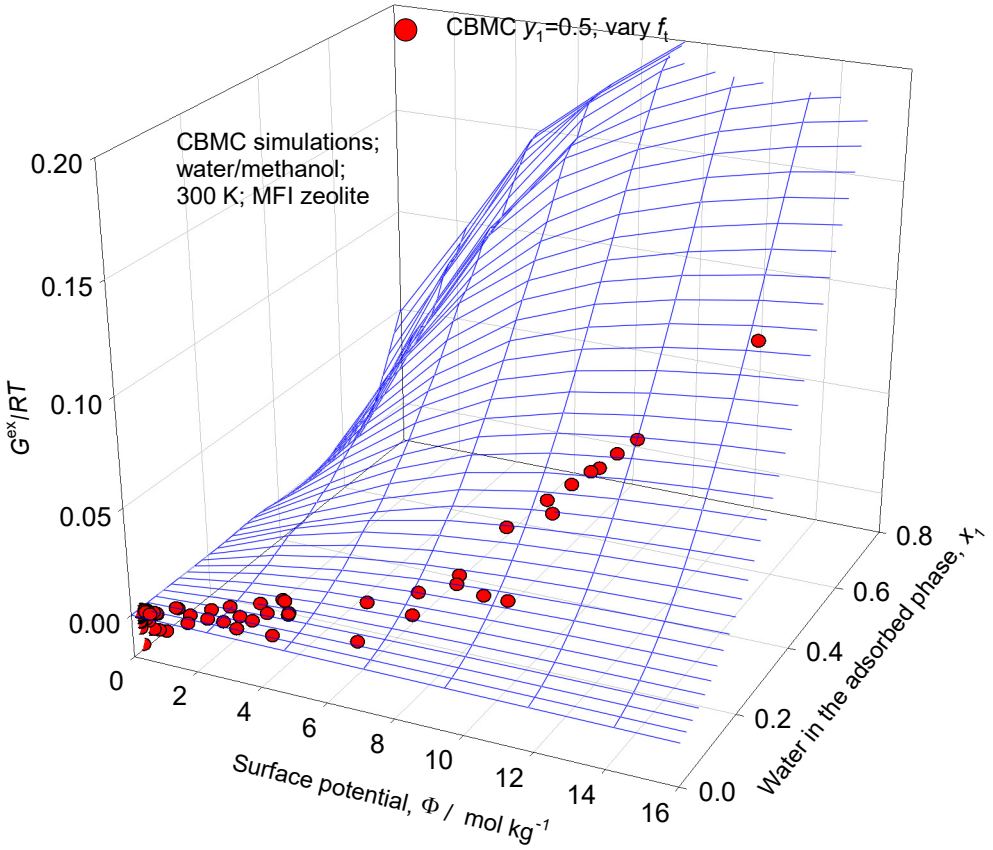

Figure S95. 3D plot of CBMC data on excess Gibbs free energy $G^{ex}/RT = x_1 \ln(\gamma_1) + x_2 \ln(\gamma_2)$ for water(1)/methanol(2) mixture adsorption in MFI zeolite at 300 K. The 3D mesh is constructed using the NRTL parameters provided in Table S17.

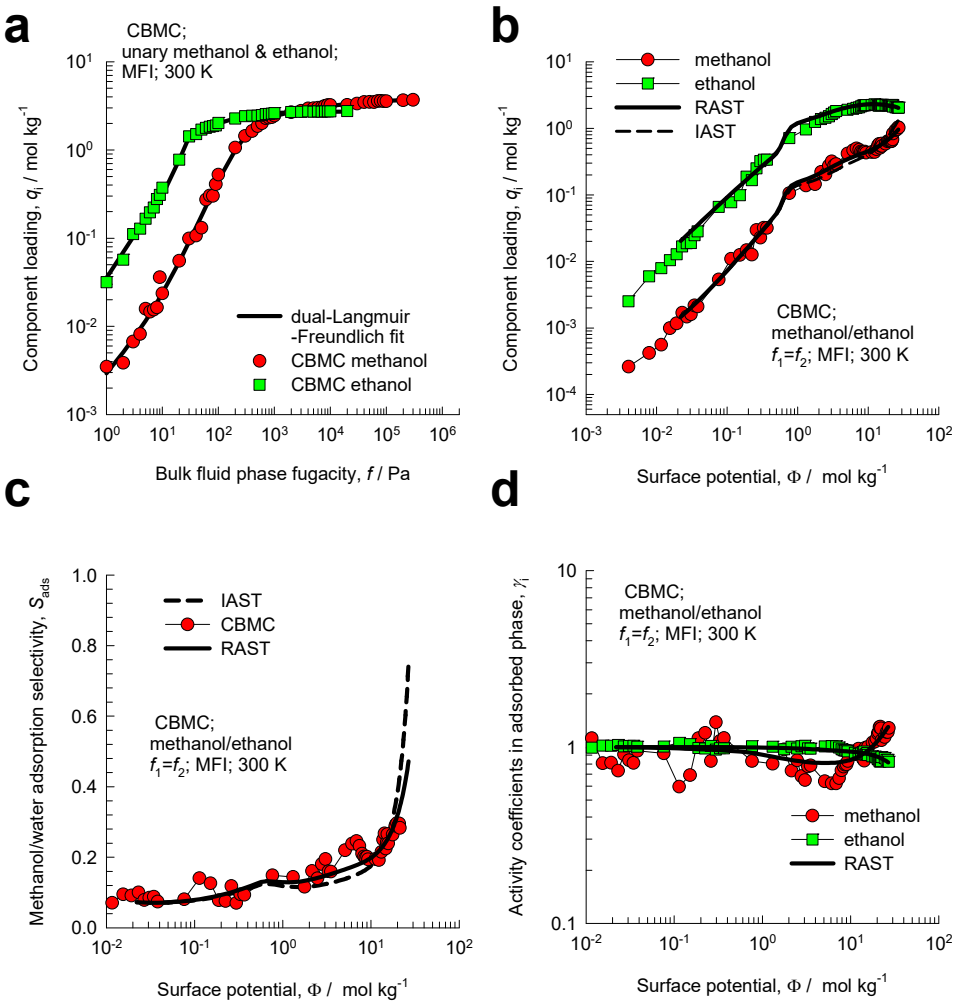

Figure S96. CBMC simulation data and analysis for Campaign A (y_1= 0.5) for methanol(1)/ethanol(2) mixture adsorption in MFI zeolite at 300 K. (a) Unary isotherms and fits. (b) Component loadings in mixture compared with compared with IAST/RAST estimates. (c) CBMC data for methanol(1)/ethanol(2) adsorption selectivity compared with IAST and RAST estimates. (d) CBMC data for activity coefficients from CBMC compared with RAST model calculations. The unary isotherm fit parameters and Margules parameters are provided in Table S17.

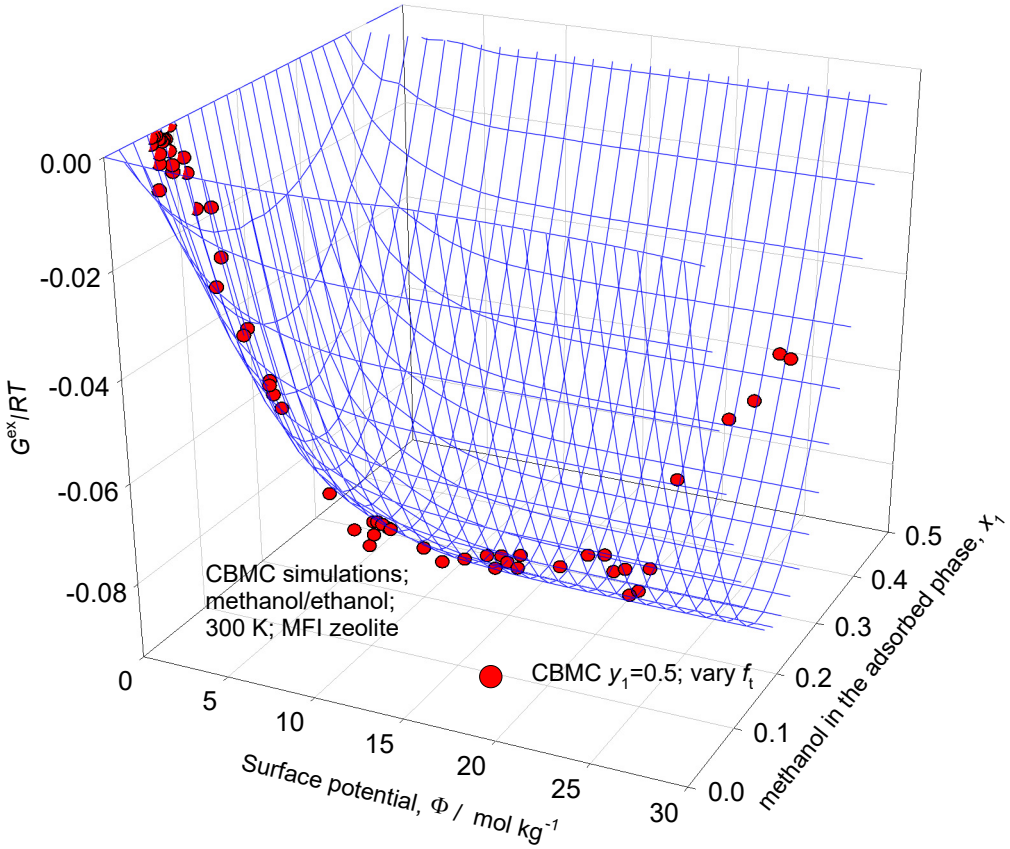

Figure S97. 3D plot of CBMC data on excess Gibbs free energy $G^{ex}/RT = x_1 \ln(\gamma_1) + x_2 \ln(\gamma_2)$ for methanol(1)/ethanol(2) mixture adsorption in MFI zeolite at 300 K. The 3D mesh is constructed using the NRTL parameters provided in Table S17.

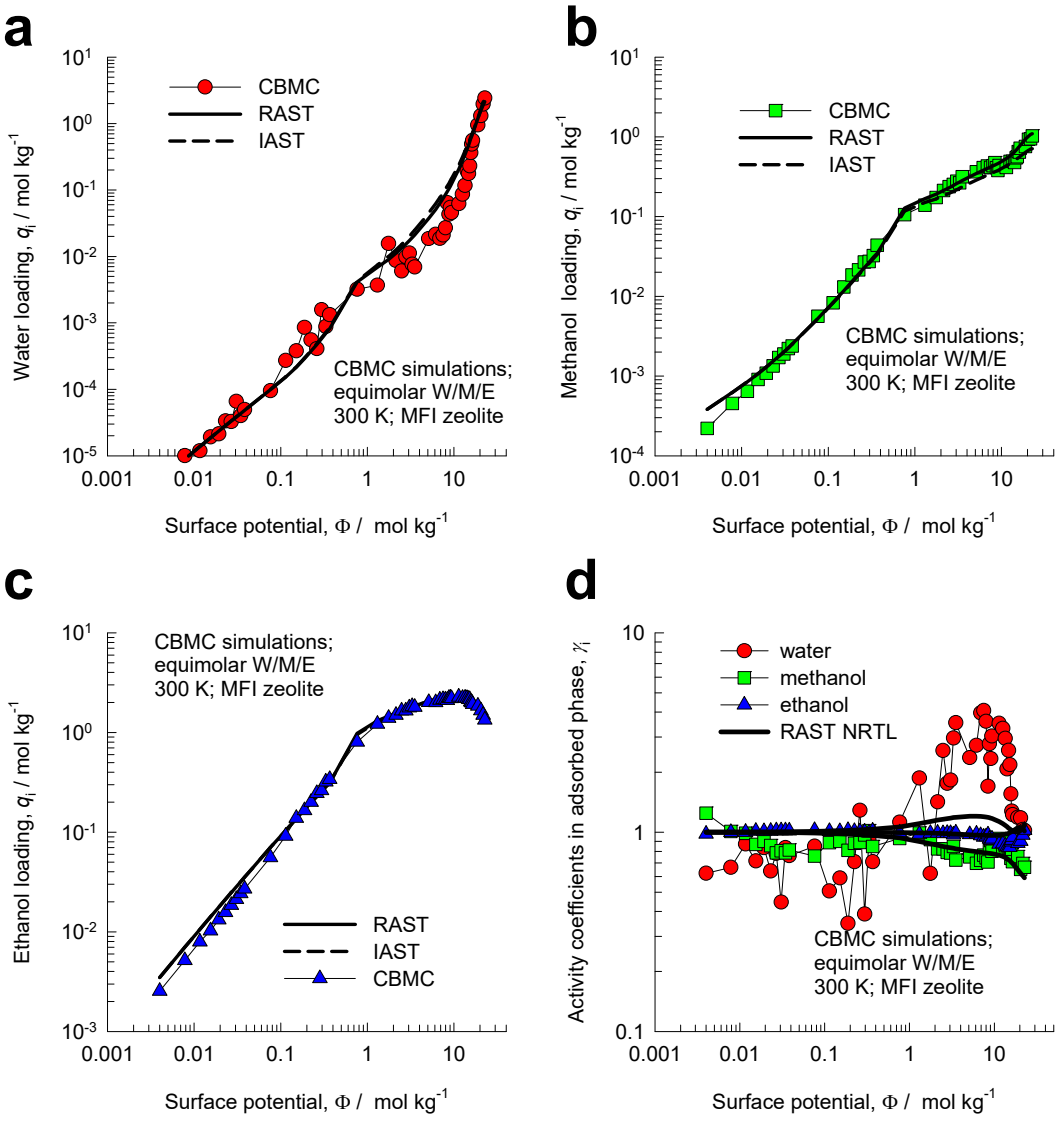

Figure S98. CBMC simulations (indicated by symbols) for equimolar $(f_1 = f_2 = f_3)$ water(1)/methanol(2)/ethanol(3) mixtures in MFI zeolite at 300 K. (a, b, c) Component loadings from CBMC are compared with IAST and RAST estimates. (d) Activity coefficients as function of the surface potential. The NRTL parameters are provided in Table S17.

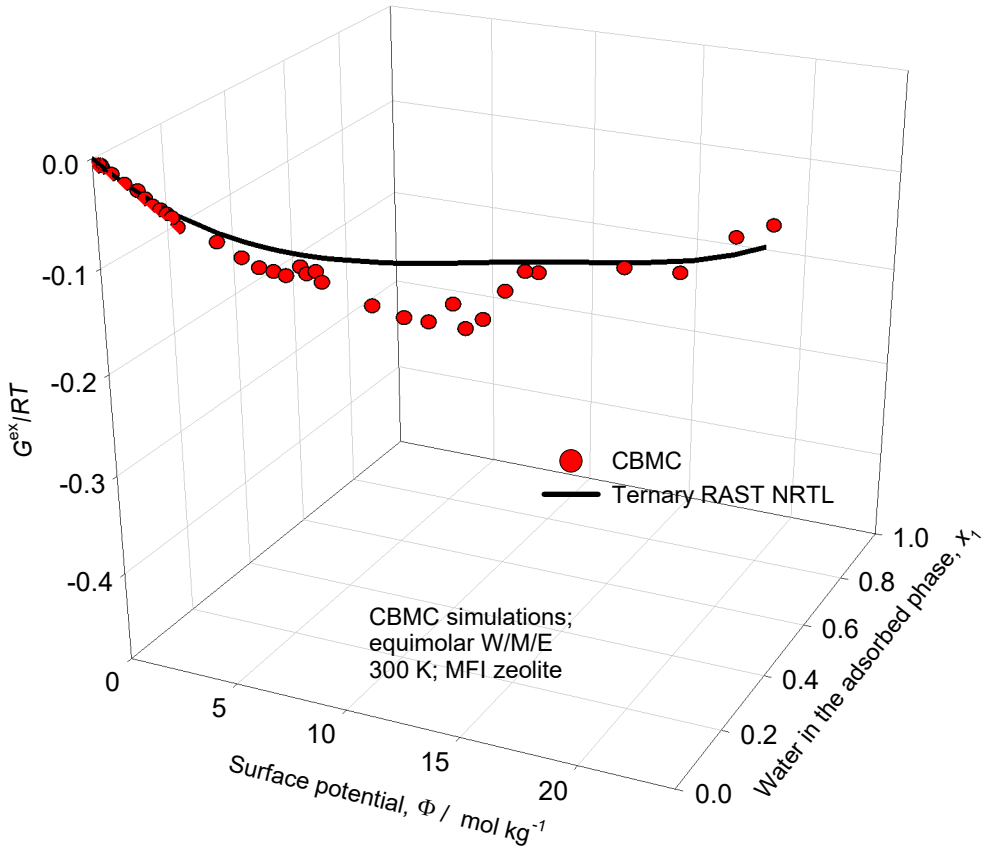

Figure S99. 3D plot of CBMC data on excess Gibbs free energy $G^{ex}/RT = \sum_{i=1}^{n} x_i \ln(\gamma_i)$ for equimolar $(f_1 = f_2 = f_3)$ water(1)/methanol(2)/ethanol(3) mixtures in MFI zeolite at 300 K. Comparison is made with the estimates of the ternary NRTL RAST model. The NRTL parameters for the binary pairs are as provided in Table S17.

12 Water/alcohol mixture adsorption in ZIF-8

ZIF-8 ($Zn(MeIm)_2$, MeIm = 2-methylimidazole) has a cage-window SOD (sodalite) topology with large cavities (≈ 11.6 Å) interconnected by small six-ring-openings (≈ 3.3 Å) (see pore landscapes in Figure S100, and Figure S101). Though the crystallographic size of the windows of ZIF-8 is 3.3 Å, the windows are flexible.

Watch also the presentations titled **ZIF-8 Membranes, Visualizing Motion of Guest Molecules in ZIF-8, Diffusion in ZIF-8** on YouTube https://www.youtube.com/@rajamanikrishna250/videos

Figure S102a shows the RDF of O…H distances for molecular pairs of water(1)/methanol(2) mixture adsorption in ZIF-8 at 300 K. We note the first peaks in the RDFs occur at a distance less than 2 Å, that is characteristic of hydrogen bonding. [27, 61] The heights of the first peaks are a direct reflection of the degree of hydrogen bonding between the molecular pairs, resulting in cluster formation and enhanced water ingress.[46] We may conclude, therefore that for water/methanol mixtures the degree of H-bonding between water-methanol pairs is significantly larger, by about an order of magnitude, than for water-water, and methanol-methanol pairs. Analogous set of conclusions can be drawn for water/ethanol mixtures, for which the RDF data are presented in Figure S102b; the degree of H-bonding between water-ethanol pairs is larger than for water-water, and ethanol-ethanol pairs.

Computational snapshots for water/methanol and water/ethanol mixture adsorption in ZIF-8 are provided in Figure S103a,b.

Due to molecular clustering, we should anticipate that the IAST would fail to provide a quantitative description of mixture adsorption equilibrium.

Figure S104 and Figure S105 present CBMC simulations for water(1)/methanol(2) and water(1)/ethanol(2) mixture adsorption in ZIF-8 at 300 K.

In CBMC campaign A, adsorption of Equimolar binary $\left(f_1 = f_2\right)$ water(1)/methanol(2) mixtures, and binary $\left(f_1/f_2 = 5/95\right)$ water(1)/methanol(2) mixtures were simulated and the bulk fluid phase fugacity $f_t = f_1 + f_2$ was varied over a wide range from the Henry regime of adsorption, $f_t \to 0; \quad \Phi \to 0$, to pore saturation conditions, typically $\Phi > 30$.

In Campaign B, the bulk fluid phase fugacity $f_t = f_1 + f_2$ was held at a constant value of 10 kPa, and the bulk fluid phase mixture composition y_1 was varied $0 < y_1 < 1$.

The CBMC data on activity coefficients confirm that mixture adsorption equilibrium is subject to strong thermodynamic non-idealities. Further, we note that the activity coefficients in the adsorbed phase are functions of both the surface potential Φ and mole fraction of water in the adsorbed phase mixture, x_1; see Figure S104f,g,i and Figure S105f,g,i.

12.1 List of Tables for Water/alcohol mixture adsorption in ZIF-8

Table S18. 3-site and 2-site Langmuir-Freundlich parameters for adsorption of water, methanol, and ethanol at 300 K in ZIF-8.

	Site A			Site B			Site C		
	$\frac{q_{A,sat}}{\text{mol kg}^{-1}}$	$\frac{b_A}{\text{Pa}^{-\nu_A}}$	ν_A	$\frac{q_{B,sat}}{\text{mol kg}^{-1}}$	$\frac{b_B}{\text{Pa}^{-\nu_B}}$	ν_B	$\frac{q_{c,sat}}{\text{mol kg}^{-1}}$	$\frac{b_c}{\text{Pa}^{-\nu_C}}$	ν_C
water	22	2.08 $\times 10^{-57}$	13.4	3.6	1.327 $\times 10^{-15}$	3.2	69	1.20 $\times 10^{-7}$	1

Adsorbate	Site A			Site B		
	$\frac{q_{A,sat}}{\text{mol kg}^{-1}}$	$\frac{b_A}{\text{Pa}^{-\nu_A}}$	ν_A	$\frac{q_{B,sat}}{\text{mol kg}^{-1}}$	$\frac{b_B}{\text{Pa}^{-\nu_B}}$	ν_B
methanol	8.4	1.736E-43	12	3.9	2.920E-05	1
ethanol	4.6	2.372E-12	3.9	2.3	2.396E-04	1

Fitted Margules non-ideality parameters for binary mixture adsorption in ZIF-8 at 300 K. The fits are based on combining CBMC Campaigns A and B for each mixture.

	C / kg mol^{-1}	A_{12}	A_{21}
water/methanol	1.335	-1.190	-0.949
water/ethanol	1.246	-2.515	-0.688

12.2 List of Figures for Water/alcohol mixture adsorption in ZIF-8

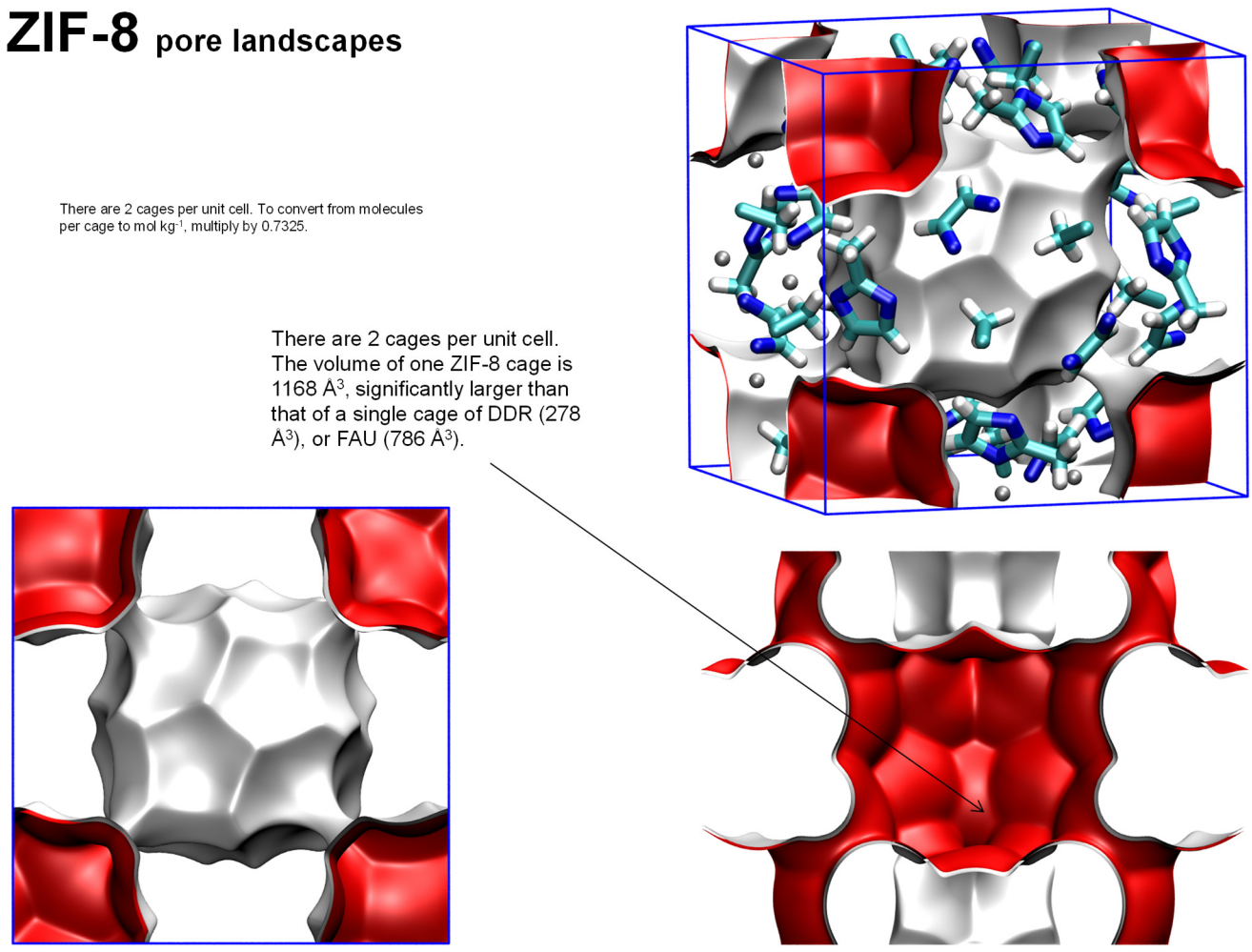

Figure S100. Pore landscape and structural details of ZIF-8.

ZIF-8 dimensions

	ZIF-8
a /Å	16.991
b /Å	16.991
c /Å	16.991
Cell volume / Å^3	4905.201
conversion factor for [molec/uc] to [mol per kg Framework]	0.3663
conversion factor for [molec/uc] to [kmol/m^3]	0.7106
ρ [kg/m3]	924.253
MW unit cell [g/mol(framework)]	2730.182
ϕ, fractional pore volume	0.476
open space / Å^3/uc	2337.0
Pore volume / cm^3/g	0.515
Surface area /m^2/g	1164.7
DeLaunay diameter /Å	3.26

Figure S101. Pore landscape and structural details of ZIF-8.

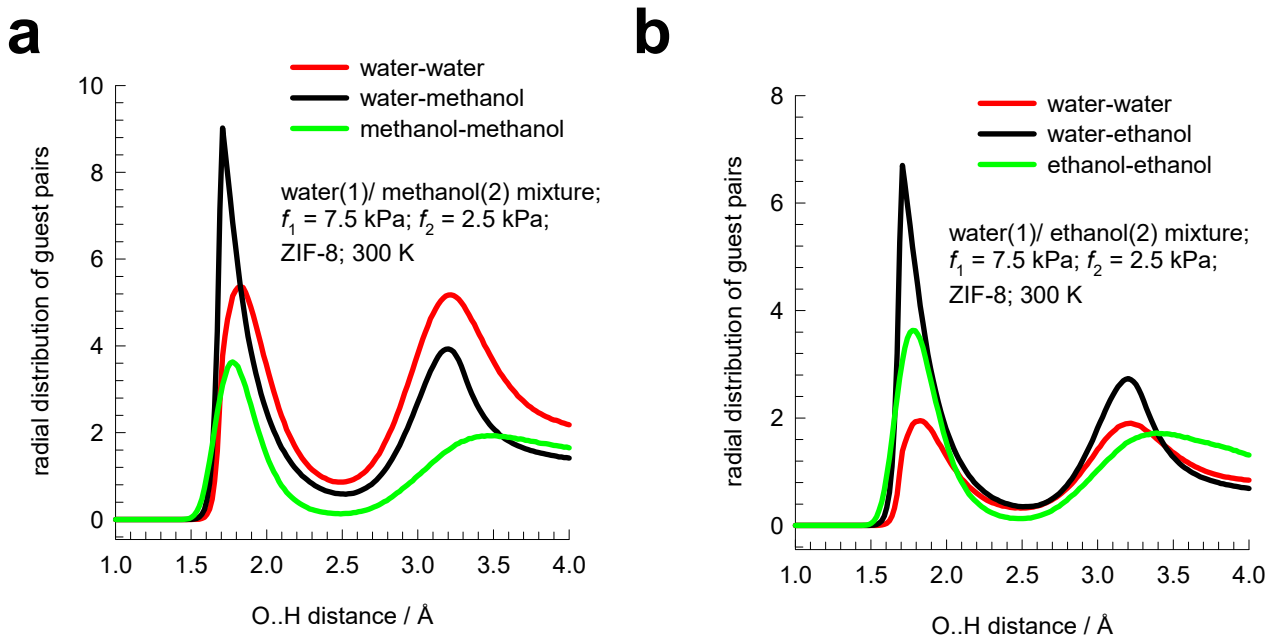

Figure S102. RDF of O···H distances for molecular pairs of (a) water(1)/methanol(2), and (b) water(1)/ethanol(2) mixture adsorption in ZIF-8 at 300 K. For both mixtures, the partial fugacities of components 1 and 2 are f_1= 7.5 kPa, f_2= 2.5 kPa. The *y*- axes are normalized in the same manner and, therefore, the magnitudes of the first peaks is a direct reflection of the degree of hydrogen bonding between the molecular pairs.

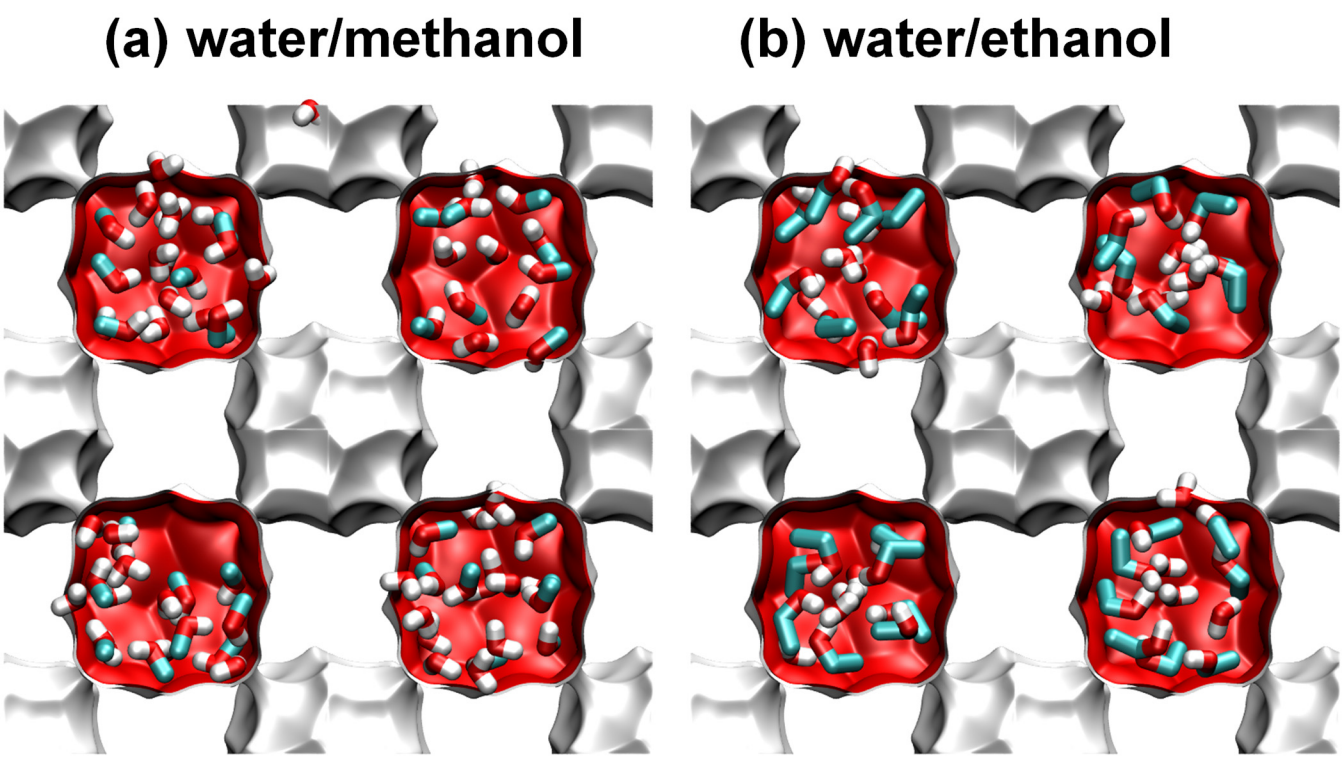

Figure S103. Snapshots showing location and conformations of guest molecules for adsorption of (a) water(1)/methanol(2), and (b) water(1)/ethanol(2) mixture adsorption in ZIF-8 at 300 K.

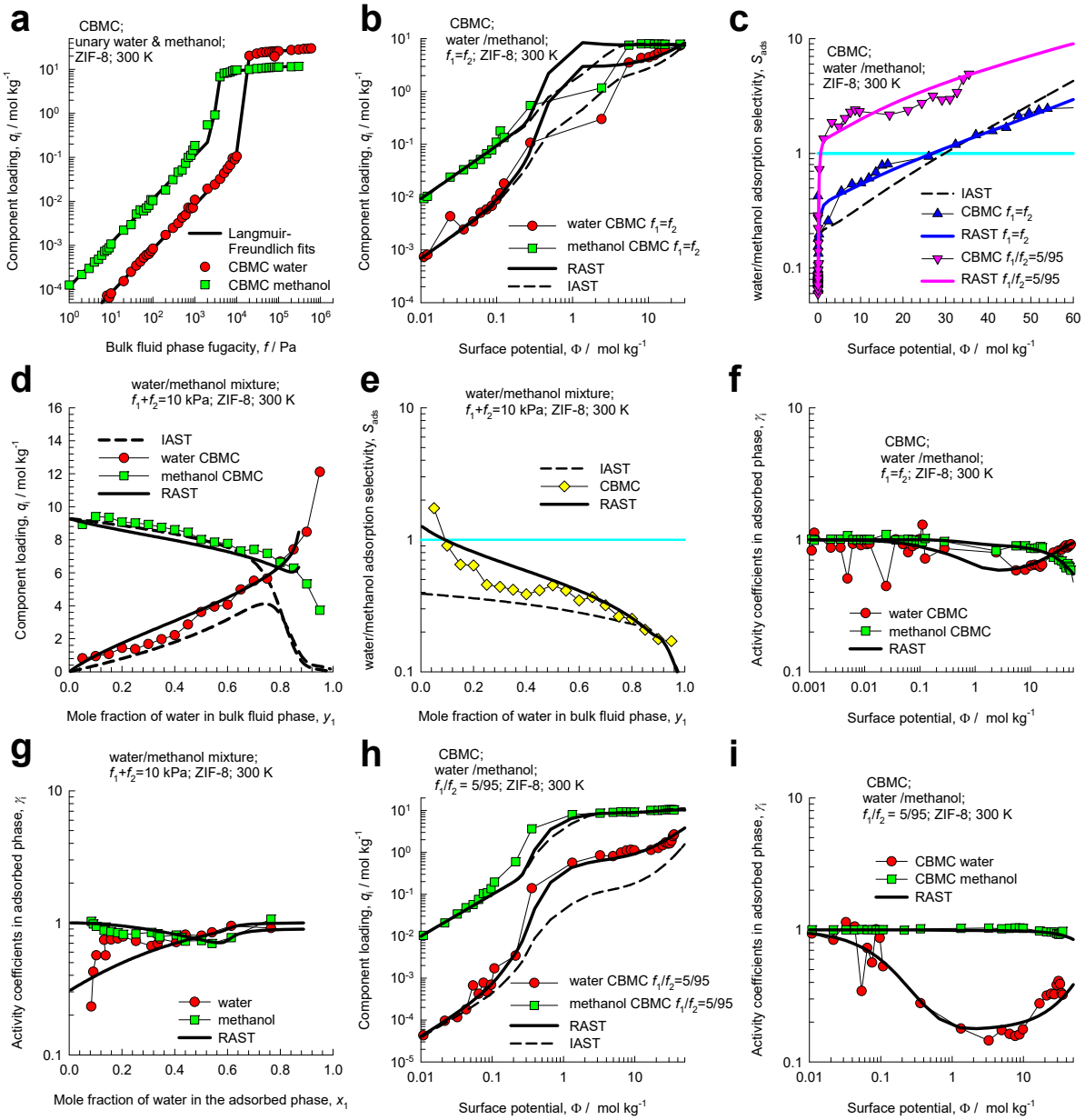

Figure S104. CBMC simulation data on component loadings, selectivities, and activity coefficients for Campaign A (y_1= 0.5 and y_1= 0.05) and Campaign B (f_i= 10 kPa) for water(1)/methanol(2) mixtures in ZIF-8 at 300 K The CBMC data are compared with RAST calculations using fitted Margules parameters. The dashed lines are IAST calculations.

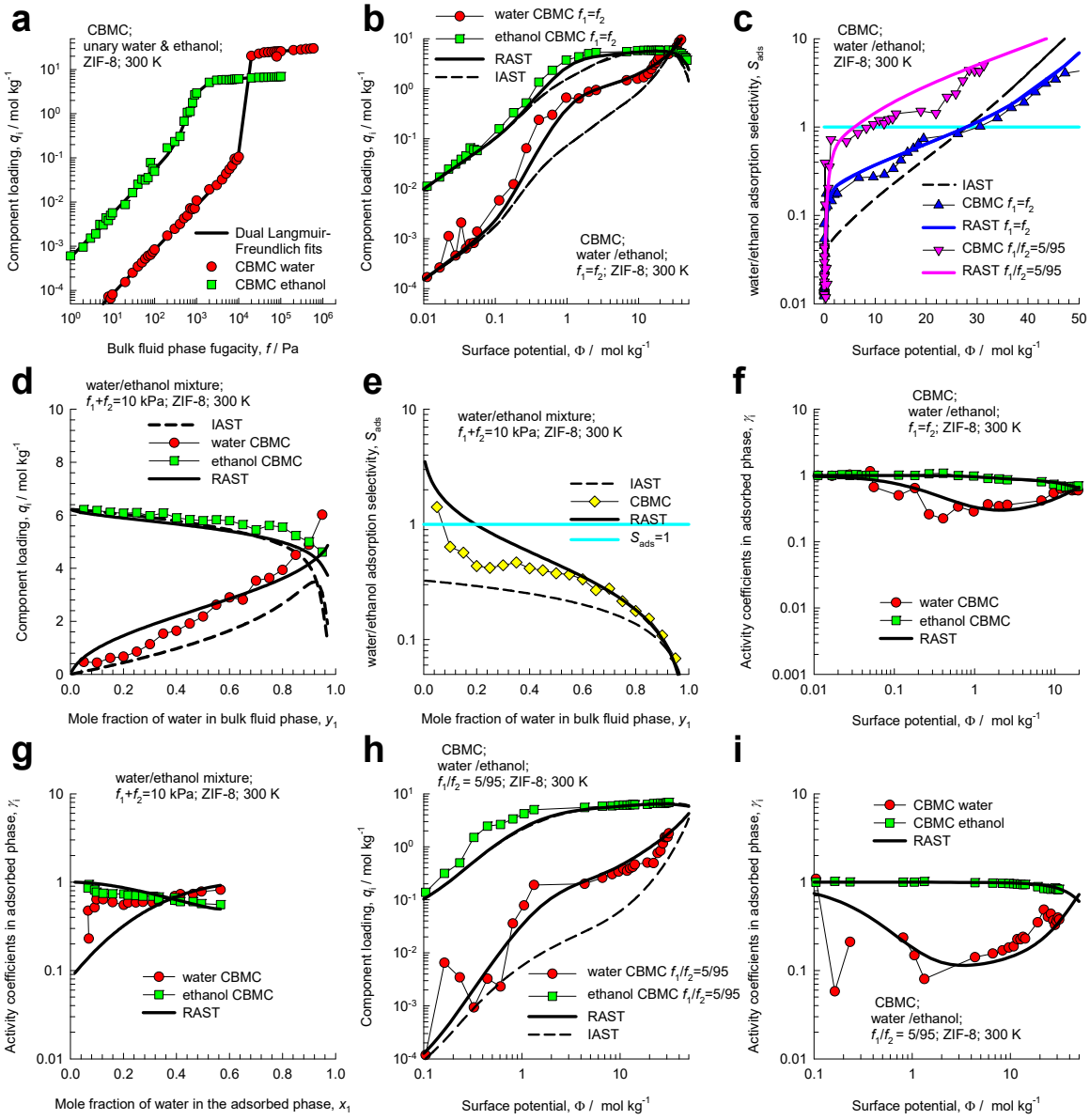

Figure S105. CBMC simulation data on component loadings, selectivities, and activity coefficients for Campaigns A (y_1= 0.5 and y_1= 0.05) and Campaign B (f_t= 10 kPa) for water(1)/ethanol(2) mixtures in ZIF-8 at 300 K The CBMC data are compared with RAST calculations using fitted Margules parameters. The dashed lines are IAST calculations.

13 Mixture adsorption in all-silica MOR zeolite

MOR zeolite (Mordenite) consists of 12-ring (7.0 Å × 6.5 Å) 1D channels, connected to 8-ring (5.7 Å × 2.6 Å) pockets; the pore landscapes and structural details are provided in Figure S106, and Figure S107.

13.1 CO_2/CH_4 mixture adsorption in all-silica MOR zeolite

Computational snapshots of the location of molecules for CO_2/CH_4 mixture adsorption show that CO_2 get preferentially ensconced in the side-pockets; see Figure S108a. The CH_4 molecules can also occupy the side pockets, but their preferred locations are the 12-ring channels. The RDF data in Figure S108b confirms the distances of CO_2-CH_4 pairs are significantly higher than for CH_4-CH_4 pairs.

Figure S109 presents CBMC simulation data for adsorption of equimolar (partial fugacities f_1=f_2) CO_2/CH_4 mixtures in MOR zeolite at 300 K. The conventional IAST calculation assumes that CH_4 molecules compete with *all* of the CO_2, making no allowance for segregation. We note that the IAST under-predicts the loading of the more weakly adsorbed CH_4 in the CO_2/CH_4 mixture. The conventional IAST calculation assumes that CH_4 molecules compete with *all* of the CO_2, making no allowance for segregation. Due to segregation effects the competition faced by CH_4 molecules within the 12-ring channels, where they almost exclusively reside, is *smaller* than that in the entire pore space. The IAST anticipates a stiffer competition between CO_2 and CH_4 as it assumes a uniform distribution of composition; consequently the separation selectivity is *over*estimated. Figure S109c compares CO_2/CH_4 adsorption selectivities obtained from CBMC with IAST and RAST estimations.

Figure S109d shows RAST calculations of the component activity coefficients γ_i, for CO_2 and CH_4.

13.2 CO_2/C_3H_8 mixture adsorption in all-silica MOR zeolite

For CO_2(1)/C_3H_8(2) mixture adsorption in all-silica MOR zeolite at 300 K, the computational snapshots for partial fugacities f_1 = f_2 = 20 kPa are shown in Figure S110. CO_2 get preferentially ensconced in the

side-pockets, but when the side pockets are fully occupied the CO_2 can also locate in the 12-ring 1D channels. The C_3H_8 molecules are unable to occupy the side pockets, but their preferred locations are the 12-ring channels.

Figure S111 present the CBMC data and analysis for two different campaigns. In Campaign A the ratio of partial fugacities $f_1/f_2 = 15/85$ and the bulk mixture fugacity, $f_t = f_1 + f_2$ is varied. In Campaign B in which total fugacity is held constant at the value f_t = 40 kPa and the bulk fluid phase mixture composition $y_1 = f_1/f_t$ is varied.

The unary isotherm data are shown in Figure S111a. In the Henry regime, the adsorption strengths are nearly equal. CO_2 has a significantly higher saturation capacity, and therefore entropy effects favor the adsorption of CO_2 at high pore occupancies. The CBMC data for Campaign A shows that the $CO_2(1)/C_3H_8(2)$ adsorption selectivity S_{ads} increases significantly with increasing values of the surface potential, Φ; see Figure S111c. Due to the segregated nature of adsorption, the IAST overestimates the S_{ads} for $\Phi_t > 10$ mol kg^{-1}. Interesting, the IAST underestimates the S_{ads} for $\Phi < 10$ mol kg^{-1}.

Segregation effects have the influence of moderating the influence of entropy effects that favor CO_2 that has the higher saturation capacity.

The results for Campaign B are even more interesting; see Figure S111d,e. For $y_1 = f_1/f_t < 0.6$, the adsorption selectivity $S_{ads} > 1$, i.e. the selectivity is in favor of CO_2. The CBMC simulations show that the adsorption selectivity S_{ads} is increasingly lowered below unity, i.e. in favor of the alkane, with increasing proportion of $CO_2(1)$ in the bulk gas phase; see Figure S111e. The IAST anticipates S_{ads} to be virtually independent of y_1. The conventional IAST calculation assumes that C_3H_8 molecules compete with *all* of the CO_2, making no allowance for segregation. Due to segregation effects the competition faced by C_3H_8 molecules within the 12-ring channels, where C_3H_8 exclusively reside, is *smaller* than that in the entire pore space. The IAST anticipates a stiffer competition between CO_2 and C_3H_8 as it assumes a uniform distribution of composition; consequently, the separation selectivity is *over*estimated to a significant extent.

We note that the activity coefficients plotted in Figure S111f, are dependent on the surface potential Φ with the limiting characteristic $\Phi \to 0;\ \ \gamma_1 \to 1;\ \ \gamma_2 \to 1$. We also note that the activity coefficients plotted in Figure S111g, are on the mole fraction in the adsorbed phase, x_1, with the limiting characteristic $x_i \to 0;\ \ \gamma_i \to 1$.

In Figure S112a the CBMC data for the excess Gibbs free energy $G^{ex}/RT = x_1 \ln(\gamma_1) + x_2 \ln(\gamma_2)$ for Campaigns A, and B are plotted in 3D space as function of Φ and x_1. The entire CBMC data set resides on a 3D surface mesh determined from the fitted Margules parameters in Table S19. The 3D plot reaffirms the dependence of γ_i on both Φ and x_1.

Figure S112b presents a 3D plot of the $CO_2(1)/C_3H_8(2)$ adsorption selectivity as function of the surface potential Φ and mole fraction of $CO_2(1)$ in the bulk gas phase, y_1. The entire CBMC data set resides on a 3D surface mesh determined from the fitted Wilson parameters in Table S19. Figure S112b reaffirms that the adsorption selectivity is not uniquely determined by the surface potential, Φ, but is additionally dependent on the bulk phase mixture composition.

13.3 List of Tables for Mixture adsorption in all-silica MOR zeolite

Table S19. Dual-site Langmuir parameters for CO_2, CH_4, and C_3H_8 at 300 K in all-silica MOR zeolite. The fit parameters are based on the CBMC simulations of pure component isotherms presented in earlier works.[11, 44, 68]

	Site A			Site B		
	$\frac{q_{A,sat}}{\text{mol kg}^{-1}}$	$\frac{b_A}{\text{Pa}^{-\nu_A}}$	ν_A	$\frac{q_{B,sat}}{\text{mol kg}^{-1}}$	$\frac{b_B}{\text{Pa}^{-\nu_B}}$	ν_B
CO_2	1.4	4.865E-04	1	4.65	1.234E-06	1
CH_4	1.05	1.587E-08	1	2.8	2.391E-06	1
C_3H_8	0.18	2.112E-06	1	1	3.551E-04	1

Fitted Margules non-ideality parameters for binary mixture adsorption in MOR at 300 K.

	C / kg mol^{-1}	A_{12}	A_{21}
CO_2/CH_4 in MOR	0.856	-1.246	-1.145
CO_2/C_3H_8 in MOR	0.071	-26.209	-17.143

13.4 List of Figures for Mixture adsorption in all-silica MOR zeolite

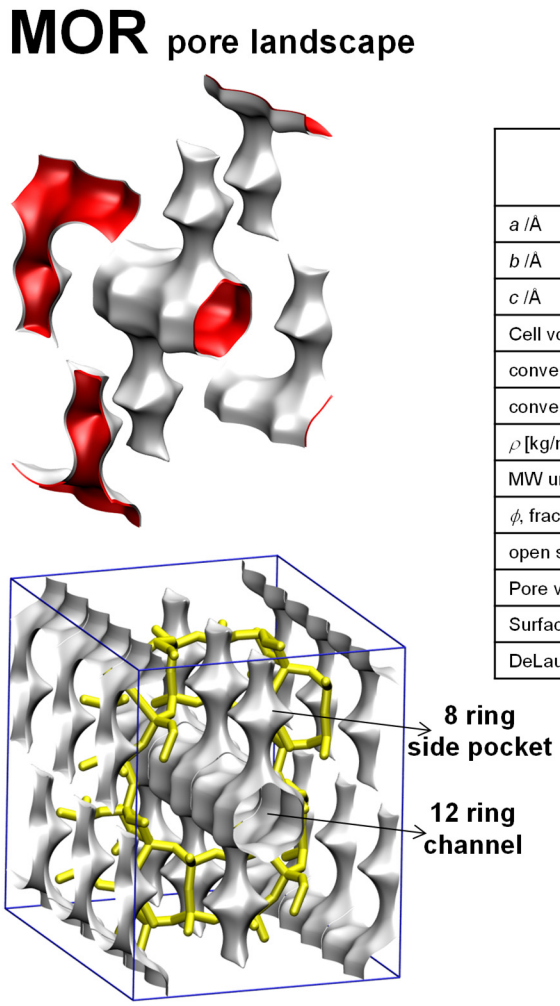

	MOR
a /Å	18.094
b /Å	20.516
c /Å	7.524
Cell volume / Å^3	2793.033
conversion factor for [molec/uc] to [mol per kg Framework]	0.3467
conversion factor for [molec/uc] to [kmol/m^3]	2.0877
ρ [kg/m3]	1714.691
MW unit cell [g/mol(framework)]	2884.07
ϕ, fractional pore volume	0.285
open space / Å^3/uc	795.4
Pore volume / cm^3/g	0.166
Surface area /m^2/g	417.0
DeLaunay diameter /Å	6.44

Figure S106. Pore landscape of all-silica MOR zeolite.

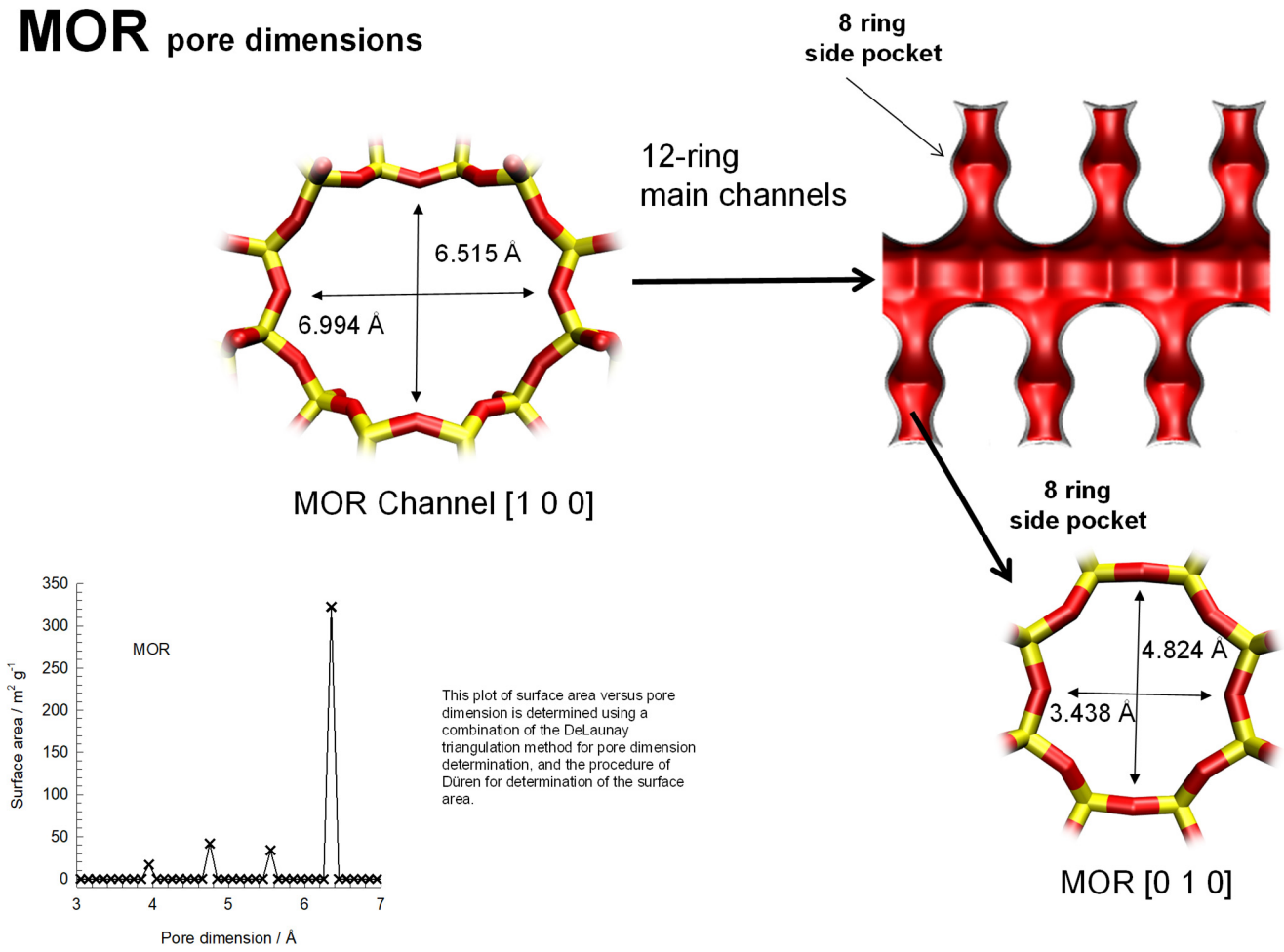

Figure S107. Structural details for MOR zeolite.

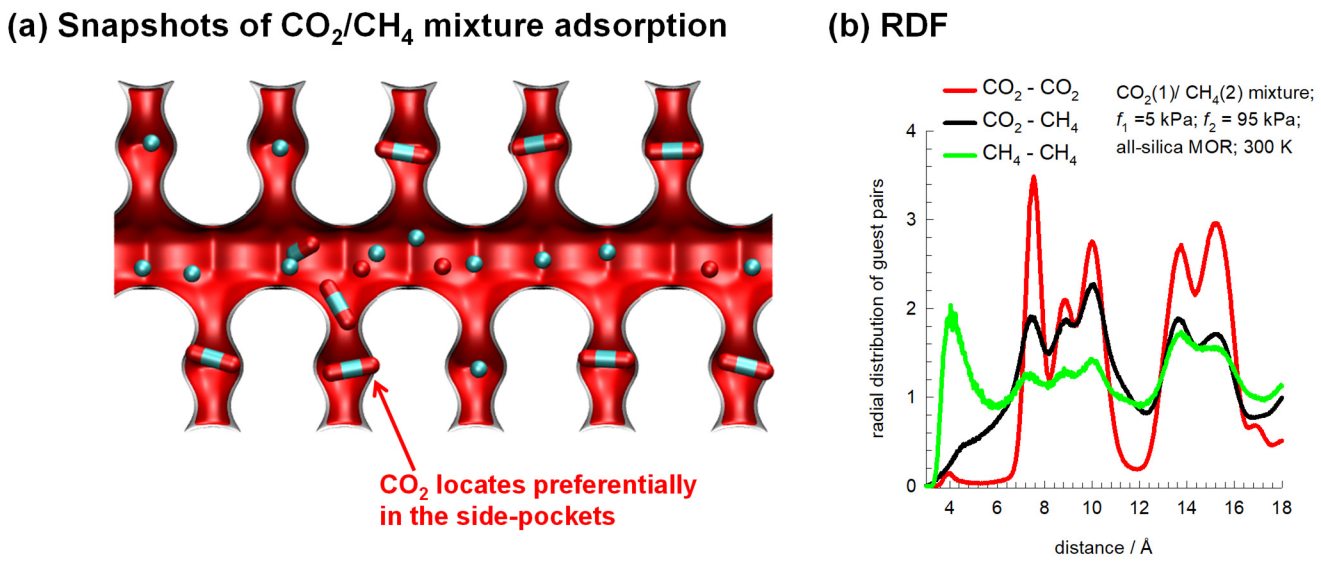

Figure S108. (a) Snapshots showing the location of guest molecules for CO_2(1)/CH_4(2) mixture adsorption in MOR zeolite at 300 K. (b) RDF for CO_2(1)/CH_4(2) mixture adsorption in MOR zeolite at 300 K

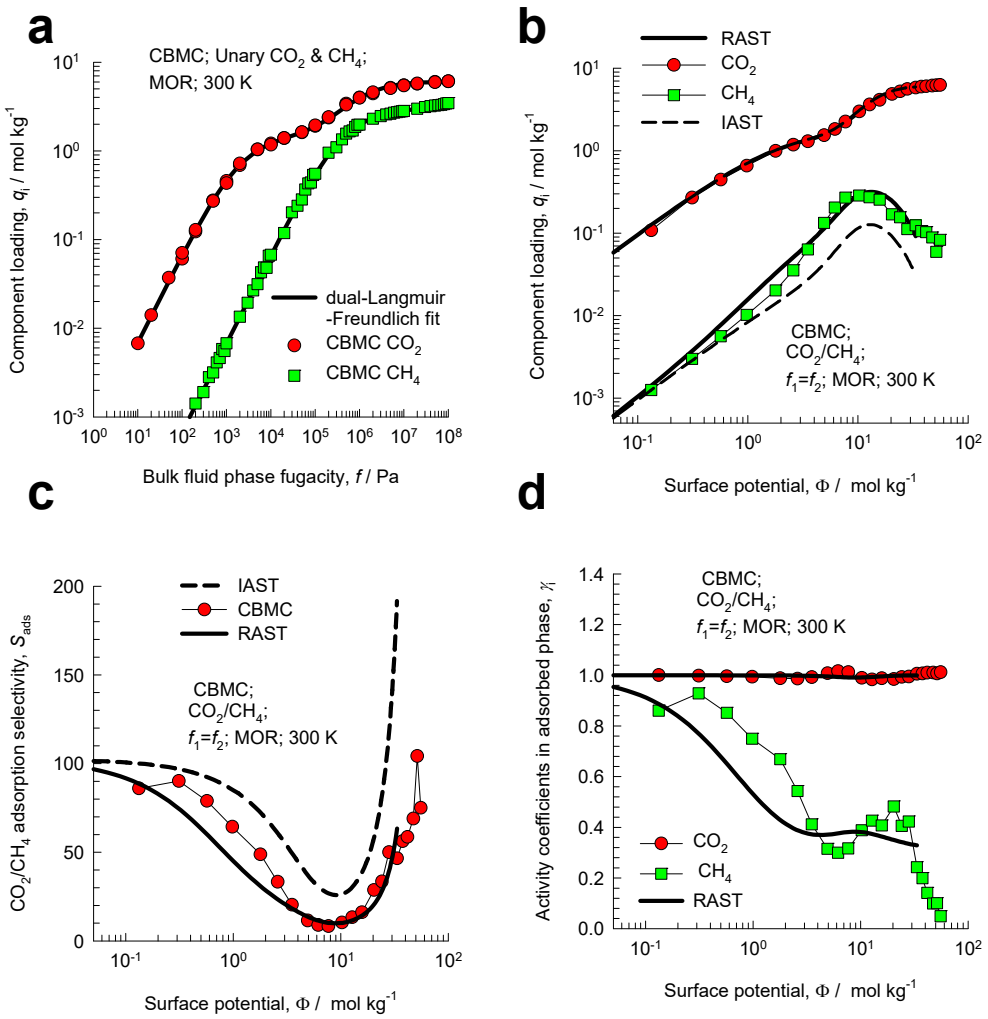

Figure S109. CBMC simulation data[44] and analysis for Campaign A (y_1= 0.5) for CO_2(1)/CH_4(2) mixture adsorption in MOR zeolite at 300 K. (a) Unary isotherms and fits. (b) Component loadings in mixture compared with compared with IAST/RAST estimates. (c) CBMC data for CO_2(1)/CH_4(2) adsorption selectivity compared with IAST and RAST estimates. (d) CBMC data for activity coefficients from CBMC compared with RAST model calculations. The unary isotherm fit parameters and Margules parameters are provided in Table S19.

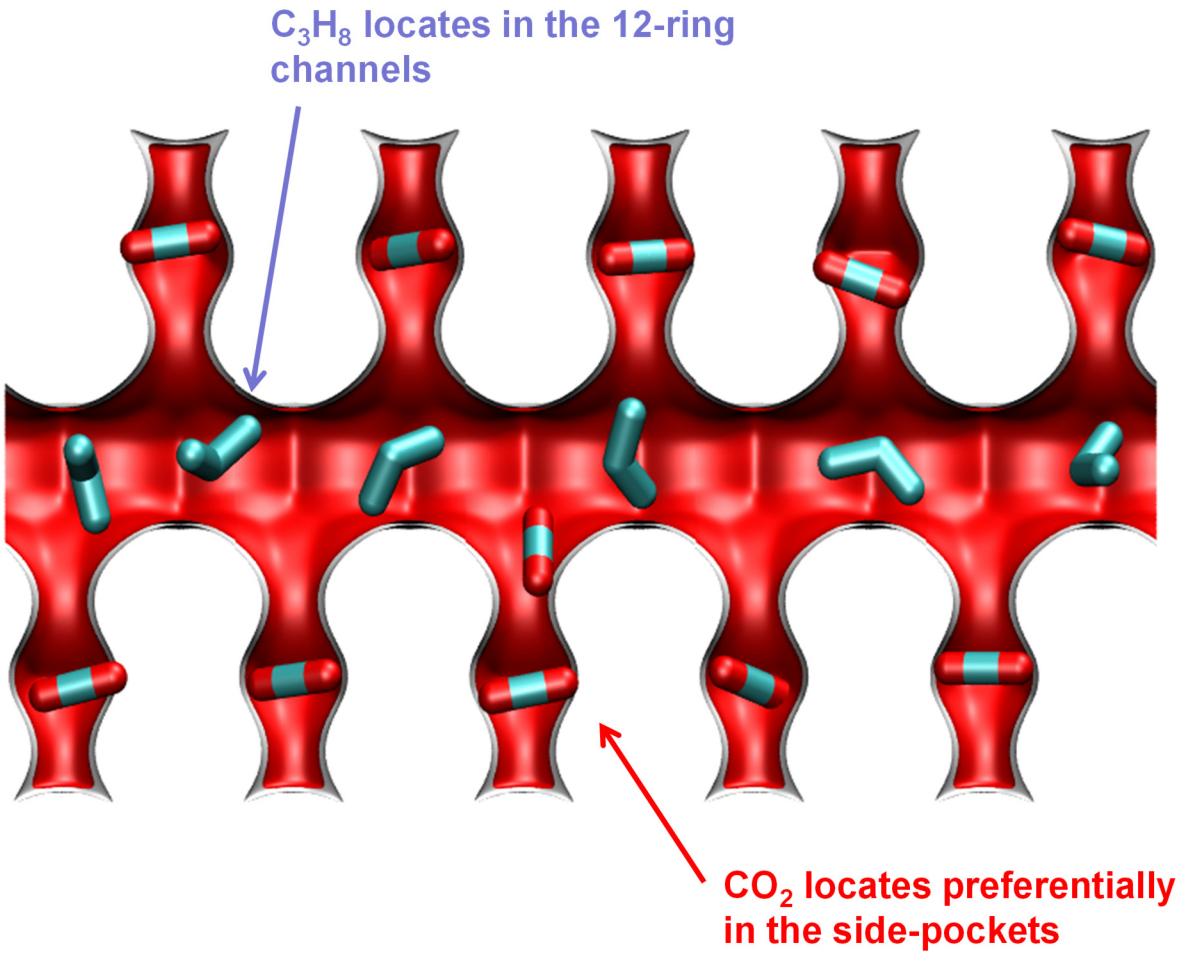

Figure S110. Snapshots[44] showing the location of guest molecules for CO_2(1)/C_3H_8(2) mixture adsorption in MOR zeolite at 300 K.

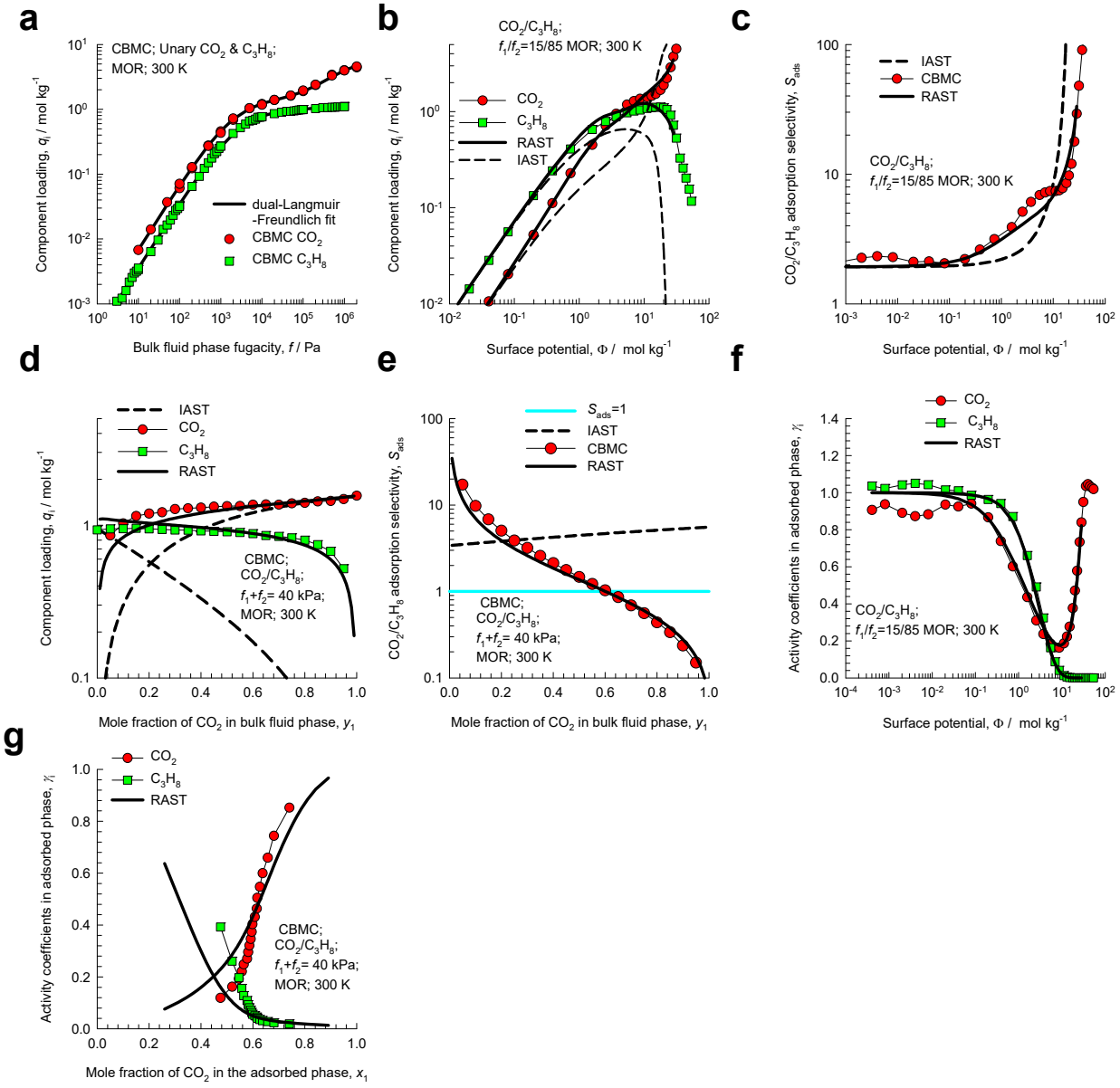

Figure S111. CBMC simulation data[44] and analysis for Campaign A (y_1= 0.15) and for Campaign B (f_t = 40 kPa) for CO_2(1)/C_3H_8(2) mixture adsorption in MOR zeolite at 300 K. (a) Unary isotherms and fits. (b, d) Component loadings in mixture compared with IAST/RAST estimates. (c, e) CBMC data for CO_2(1)/C_3H_8(2) adsorption selectivity compared with IAST and RAST estimates. (f, g) Activity coefficients from CBMC compared with RAST model calculations. The unary isotherm fit parameters and Margules parameters are provided in Table S19.

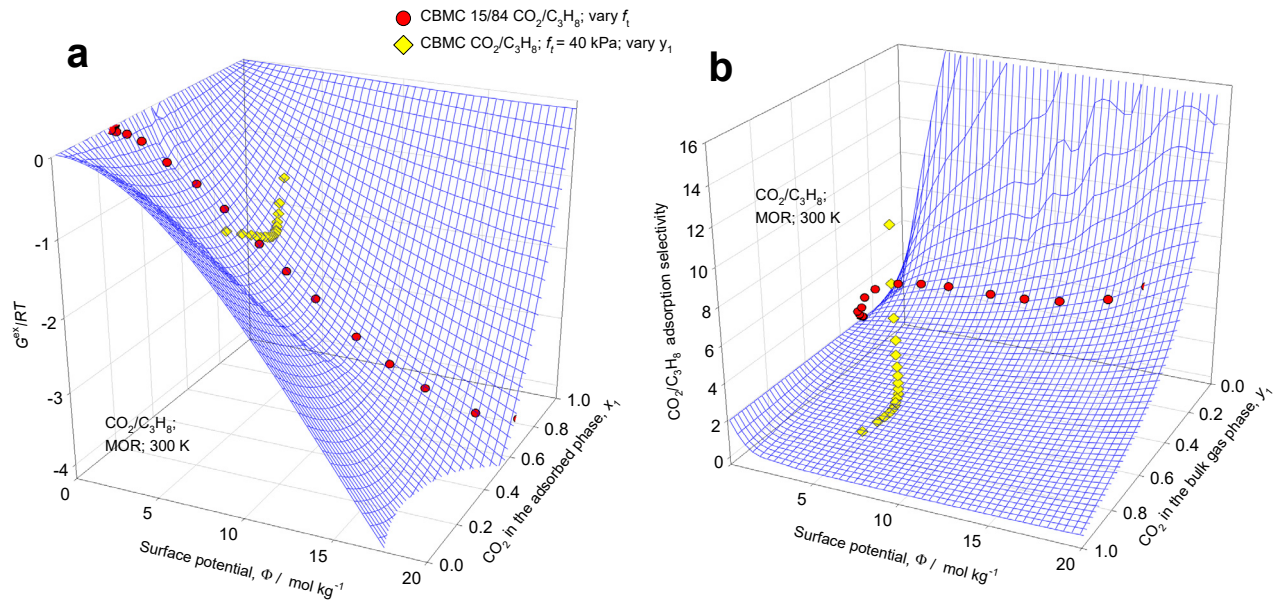

Figure S112. 3D plots of CBMC data on (a) excess Gibbs free energy $G^{ex}/RT = x_1 \ln(\gamma_1) + x_2 \ln(\gamma_2)$, and (b) adsorption selectivity for $CO_2(1)/C_3H_8(2)$ mixture adsorption in MOR zeolite at 300 K. The 3D mesh is constructed using the Margules parameters provided in Table S19.

14 Analysis of published experimental data

14.1 CO_2/N_2 mixture adsorption in 13X zeolite; Wilkins experiments

Figure S113a presents the unary isotherm data of CO_2, and N_2 in 13X zeolite at 298 K, as reported by in Table 1 and Table 2 of the Supplementary Material accompanying the publication of Wilkins and Rajendran.[49] The experimental CO_2 isotherms were fitted with a dual-Langmuir model; the experimental N_2 isotherms were fitted with a 1-site-Langmuir model. The isotherm fit parameters are provided in Table S20. Figure S113b presents the experimental data (indicated by symbols) of Wilkins and Rajendran[49] for component loadings, q_i, of CO_2, and N_2 for adsorption of CO_2/N_2 mixtures in 13X zeolite at 296 K and total pressure p_t = 97 kPa, as function of the mole fraction of CO_2 in the bulk gas phase, y_1. The dashed lines in Figure S113b are the IAST estimations using the unary isotherm fits provided in Table S20. The IAST estimations of the component loadings for N_2 are not in good agreement with the experimental data.

To match the experimental data on the component loadings, we need to introduce activity coefficients. Use of the RAST with fitted Wilson parameters $\Lambda_{12} = 8.5$; $\Lambda_{21} = 1$; $C = 0.025$ kg mol^{-1} results in a good match with the experiments. Figure S113c is a 3D plot of the excess Gibbs free energy $G^{ex}/RT = x_1 \ln(\gamma_1) + x_2 \ln(\gamma_2)$ as function of the surface potential Φ, and mole fraction of CO_2 in the bulk gas phase, y_1. The experimental data resides on the 3D mesh. Figure S113d plots the experimental data on the CO_2/N_2 adsorption selectivity as function of the mole fraction of CO_2 in the bulk gas phase, y_1. The IAST severely overestimates the adsorption selectivity.

The explanation for the failure of the IAST and the need to quantify non-idealities is to be found in the CBMC simulation data and analysis in Figure S59, Figure S60, and Figure S61. Indeed, the experimental data in Figure S113 is precisely analogous to the CBMC data in Figure S59.

14.2 CO_2/N_2 mixture adsorption in 13X zeolite; Hefti experiments

Hefti et al.[50] report the results of a comprehensive experimental investigation of adsorption equilibrium for CO_2/N_2 mixtures in ZSM-5 and 13X zeolites for pressures ranging to 1 MPa. As illustration, Figure S114a present experimental data (indicated by symbols) of Hefti et al.[50] for component loadings, q_i, of CO_2, and N_2 for adsorption of CO_2/N_2 mixtures in 13X zeolite at 298 K and total pressure p_t = 1 MPa, as function of the mole fraction of CO_2 in the bulk gas phase. The IAST (shown by the dashed lines) overestimates the CO_2 loading, and underestimates the N_2 loading; consequently, the adsorption selectivities (see Figure S114b) are overly optimistic. Use of the RAST model, shown by the continuous solid line, with fitted Wilson parameters $\Lambda_{12} = 6.758$; $\Lambda_{21} = 0.4844$; $C = 0.0744$ kg mol^{-1} is able to model non-ideality effects mixture adsorption. The fitted Wilson parameters are based on the entire data set at 298 K, at total pressures ranging from 0.12 MPa to 1.02 MPa, as reported in Section 2.2 of the Supplementary Material of Hefti et al.[50]

Figure S114c is a 3D plot of the excess Gibbs free energy c for the entire data set at total pressures ranging from 0.12 MPa to 1.02 MPa, as function of the surface potential Φ, and mole fraction of CO_2 in the bulk gas phase, y_1. The experimental data resides on the 3D mesh.

The explanation for the failure of the IAST and the need to quantify non-idealities is to be found in the CBMC simulation data and analysis in Figure S59, Figure S60, and Figure S61. Indeed, the experimental data in Figure S114 is precisely analogous to the CBMC data in Figure S59.

14.3 CO_2/CH_4 mixture adsorption in 13X zeolite; UWA experiments

Avijegon et al.[69] from the University of Western Australia (UWA) present experimental data on adsorption of CO_2/CH_4 mixtures in 13X zeolite. Figure S115 presents data on excess Gibbs free energy $G^{ex}/RT = x_1 \ln(\gamma_1) + x_2 \ln(\gamma_2)$ for adsorption of CO_2/CH_4 mixtures at 273 K in NaX (=13X) zeolite. The experimental data lie on a 3D mesh that is constructed using the Wilson parameters provided in Table S27.

The explanation for the failure of the IAST and the need to quantify non-idealities is to be found in the CBMC simulation data and analysis in Figure S47, Figure S48, and Figure S49.

Indeed, the experimental data in Figure S115 is precisely analogous to the 3D plot of CBMC simulation data in Figure S48,

14.4 CO_2/C_2H_4 mixture adsorption in 5A zeolite

The paper by Basmadjian and Hsieh[70] presents evidence of strong non-idealities for adsorption of $CO_2(1)/C_2H_4(2)$ mixtures in LTA-5A zeolite. Their experimental data, obtained at 238 K and total pressure of 1.07 bar as presented in Figure 1 of their paper has been redrawn for further analysis in Figure S116a,b. The experimental data displays selectivity reversals in favor of $C_2H_4(2)$ for bulk gas phase mole fractions of $CO_2(1)$, $y_1 > 0.7$. The IAST does not anticipate the selectivity reversal, and severely overestimates the $CO_2(1)/C_2H_4(2)$ mixture adsorption selectivity S_{ads}. The selectivity reversal can be quantified adequately by the Real Adsorbed Solution Theory (RAST) with the choice of the Wilson parameters as specified in Table S21. Figure S116c is a 3D plot of the excess Gibbs free energy $G^{ex}/RT = x_1 \ln(\gamma_1) + x_2 \ln(\gamma_2)$ as function of the surface potential Φ, and mole fraction of CO_2 in the adsorbed phase, x_1. The activity coefficients are dependent on both Φ, and x_1.

The explanation for the failure of the IAST and the need to quantify non-idealities is to be found in the CBMC simulation data for $CO_2(1)/CH_4(2)$ mixtures in LTA4A zeolite in Figure S74, and Figure S75. Indeed, the experimental data in Figure S116 is precisely analogous to the 3D plot of CBMC data for G^{ex}/RT in Figure S75.

Basmadjian and Hsieh[70] also present experimental data for adsorption of $CO_2(1)/C_2H_4(2)$ mixtures in LTA-5A zeolite at temperatures of 273 K, and 323 K. The analysis and RAST modeling of these sets of data are presented in Figure S117, and Figure S118. With increasing temperature, the influence of thermodynamic non-idealities are of diminishing importance; this is verified in Figure S119 that compares

the values of the excess Gibbs free energy $G^{ex}/RT = x_1 \ln(\gamma_1) + x_2 \ln(\gamma_2)$ for the three data sets. These data show that with increasing temperatures, G^{ex}/RT deviate from $G^{ex}/RT = 0$ to a diminished extent.

Further evidence of the selectivity reversal phenomena with LTA-5A zeolite is available in the transient breakthrough experiments reported by van Zandvoort et al.[51, 52] In the transient breakthrough experiments the feed mixtures consist of $C_2H_4/CO_2/N_2/Ar$ mixtures using different C_2H_4/CO_2 ratios; N_2 forms about 58%, and Ar about 2%. Four sets of breakthrough experiments with LTA-5A zeolite, operating at 100 kPa and 313 K are shown in Figure S120a,b,c,d for four different runs: Run 1 (C_2H_4/CO_2 = 3.4), Run 2 (C_2H_4/CO_2 = 1.8), Run 3 (C_2H_4/CO_2 = 0.9), and Run 4 (C_2H_4/CO_2 = 0.75). We note that for Runs 1 and 2, the breakthrough of C_2H_4 occurs earlier than that of CO_2, indicating that CO_2 adsorbs more strongly. For Run 3, we note that the breakthroughs of C_2H_4 and CO_2 occur at nearly the same time, suggesting that the adsorption selectivity $S_{ads} \approx 1$. For Run 4, we note that the breakthrough of C_2H_4 occurs later than that of CO_2, indicating that C_2H_4 adsorbs more strongly than CO_2. The selectivity reversal in favor of C_2H_4 at feed compositions poorer in C_2H_4, i.e. richer in CO_2, is analogous to the experimental data of Basmadjian and Hsieh,[70] witnessed in Figure S116a,b.

Figure S121a compares the experimental breakthroughs for Run 4 (C_2H_4/CO_2 = 0.75) with transient breakthrough simulations in which the IAST is used to described mixture adsorption equilibrium; the unary isotherm fits are provided by van Zandvoort et al.[51, 52, 71] The methodology for performing transient breakthrough simulations are discussed in our earlier works.[72-75] In these simulations, the intra-crystalline diffusional influences are considered to be of negligible importance, i.e. $Đ_i/r_c^2 >> 1$. The IAST based simulations do not anticipate selectivity reversals in favor of C_2H_4, and predicts that C_2H_4 breaks through earlier than CO_2.

Figure S121b compares the experimental data in Run 4 with transient breakthrough simulations using the RAST, along with Wilson parameters for the binary $CO_2(1)/C_2H_4(2)$ mixture: $\Lambda_{12} = 0.03$; $\Lambda_{21} = 32$; $C = 1$ kg mol^{-1}. The RAST correctly anticipates selectivity reversal phenomenon in favor of C_2H_4, predicting that C_2H_4 breaks through last.

14.5 C_2H_4/C_2H_6 mixture adsorption in 5A zeolite

Mofarahi and Salehi[76] present experimental data adsorption of $C_2H_4(1)/C_2H_6(2)$ mixtures in LTA-5A zeolite at 283 K for three different mole fractions, 0.2, 0.5, and 0.8, of $C_2H_4(1)$ in the bulk gas phase. The unary isotherm data fits are provided in Table S21. Figure S122a is a 3D plot of the excess Gibbs free energy $G^{ex}/RT = x_1 \ln(\gamma_1) + x_2 \ln(\gamma_2)$ as function of the surface potential Φ, and mole fraction of CO_2 in the adsorbed phase, x_1. The 3D mesh is constructed using the Wilson parameters provided in Table S21. The 3D plot confirms that strong thermodynamic non-idealites influence mixture adsorption. and that the activity coefficients in the adsorbed phase are functions of both Φ, and x_1. The explanation for the failure of the IAST and the need to quantify non-idealities is to be found in the CBMC simulation data for $CH_4(1)/C_3H_8(2)$ mixtures in LTA-4A zeolite in Figure S77.

Figure S122b is a 3D plot of the $C_2H_4(1)/C_2H_6(2)$ adsorption selectivity, S_{ads}, as function of the surface potential Φ, and mole fraction of CO_2 in the bulk gas phase, y_1. Figure S122b demonstrates that S_{ads} is not uniquely dependent on surface potential Φ, as is anticipated by the IAST, but is also dependent on the mole fraction of CO_2 in the bulk gas phase, y_1.

14.6 CO_2/CH_4 mixture adsorption in 5A zeolite; Mofarahi experiments

Mofarahi and Gholipour[77] report the results of a comprehensive experimental investigation of adsorption equilibrium of describe CO_2/CH_4 mixture adsorption in LTA-5A zeolite at 303 K, 0.4 MPa, and varying compositions of the bulk gas mixture. We present a re-analysis of their binary experimental data as presented in Table 4, Table 9, and Table 11 of their paper. Figure S123a presents a plot of the adsorbed phase mole fraction of CO_2 as a function of the mole fraction of CO_2 in the bulk gas mixture; the plotted data is for 0.4 MPa total pressure. As compared to the experimental data, the IAST severely overpredicts the mole fraction of the adsorbed phase mole fraction of CO_2. The corresponding values of the CO_2/CH_4 adsorption selectivity are plotted in Figure S123b.

As compared to the experimental data, the IAST severely overpredicts the selectivity values to a significant extent. The explanation for the failure of the IAST and the need to quantify non-idealities is to be found in the CBMC simulation data for CO_2(1)/CH_4(2) mixtures in LTA-4A zeolite in Figure S74, and Figure S75.

14.7 Mixture adsorption in NaX zeolite; Siperstein experiments

Siperstein and Myers[43] report experimental data for adsorption of CO_2(1)/C_3H_8(2) mixtures in NaX zeolite at 293 K. The adsorption selectivity, S_{ads}, plotted as a function of the surface potential, Φ, does not exhibit a unique dependence as anticipated by the IAST, indicated by the dashed lines in Figure S124a.

In Figure S124b, the adsorbed phase mole fraction of CO_2(1), x_1, is plotted as function of mole fraction of CO_2(1) in the bulk gas phase mixture, y_1. It is noteworthy that at high mole fractions of CO_2(1) in the bulk gas phase mixture, y_1, there is a tendency towards adsorption azeotropy, i.e. $x_1 = y_1$. The analysis of azeotropic adsorption and the rationalization of the Siperstein experiments are provided by Krishna and van Baten.[44] The activity coefficients of CO_2(1), and C_3H_8(2) mixtures in NaX zeolite at 293 K are functions of both adsorbed phase compositions, and the surface potential; see Figure S124c,d. Particularly noteworthy is that $\Phi \to 0; \quad \theta \to 0; \quad \gamma_i \to 1$.

The Wilson parameters obtained by data fitting, following eq (S47). are listed in Table S22.

In Figure S125a, the experimental data on the excess Gibbs free energy $G^{ex}/RT = x_1 \ln(\gamma_1) + x_2 \ln(\gamma_2)$ for adsorption of CO_2(1)/C_3H_8(2) mixtures in NaX zeolite at 293 K are plotted in 3D space as function of the surface potential Φ and mole fraction of CO_2 in the adsorbed phase, x_1. The entire data set resides on a 3D surface mesh determined from the fitted Wilson parameters in Table S22.

Figure S125b presents a 3D plot of the CO_2(1)/C_3H_8(2) adsorption selectivity as function of the surface potential Φ and mole fraction of CO_2 in the bulk gas phase, y_1. The entire data set resides on a 3D surface mesh determined from the fitted Wilson parameters in Table S22. Figure S125b confirms that the

adsorption selectivity is not uniquely determined by the surface potential, Φ, but is additionally dependent on the bulk phase mixture composition.

The explanation for the failure of the IAST and the need to quantify non-idealities is to be found in the CBMC simulation data and analysis in Figure S52, Figure S53, Figure S54, Figure S55, and Figure S56. Indeed, the experimental data on G^{ex}/RT and S_{ads} in Figure S125 is precisely analogous to the corresponding 3D plots of CBMC data in Figure S54.

In Figure S126a the experimental data on the excess Gibbs free energy $G^{ex}/RT = x_1 \ln(\gamma_1) + x_2 \ln(\gamma_2)$ for adsorption of CO_2(1)/C_2H_4(2) mixtures in NaX zeolite at 293 K are plotted in 3D space as function of Φ and x_1. The entire data set resides on a 3D surface mesh determined from the fitted Wilson parameters in Table S22. Figure S126b presents a 3D plot of the CO_2(1)/C_2H_4(2) adsorption selectivity as function of the surface potential Φ and mole fraction of CO_2 in the bulk gas phase, y_1. The entire data set resides on a 3D surface mesh determined from the fitted Wilson parameters in Table S22. Figure S126b confirms that the adsorption selectivity is not uniquely determined by the surface potential, Φ, but is additionally dependent on the bulk phase mixture composition.

In Figure S127a the experimental data on the excess Gibbs free energy $G^{ex}/RT = x_1 \ln(\gamma_1) + x_2 \ln(\gamma_2)$ for adsorption of CO_2(1)/C_2H_6(2) mixtures in NaX zeolite at 293 K are plotted in 3D space as function of the surface potential Φ and mole fraction of CO_2 in the adsorbed phase, x_1. The entire data set resides on a 3D surface mesh determined from the fitted Wilson parameters in Table S22. Figure S127b presents a 3D plot of the CO_2(1)/C_2H_6(2) adsorption selectivity as function of the surface potential Φ and mole fraction of CO_2 in the bulk gas phase, y_1. The entire data set resides on a 3D surface mesh determined from the fitted Wilson parameters in Table S22. Figure S127b confirms that the adsorption selectivity is not uniquely determined by the surface potential, Φ, but is additionally dependent on the bulk phase mixture composition.

The rationalization of the non-idealities in the adsorption of CO_2(1)/C_2H_4(2) and CO_2(1)/C_2H_6(2) mixtures in NaX zeolite is due to the inhomogeneous distribution of guest adsorbates within the pore landscape of NaX, as witnessed in the RDFs in Figure S56.

In Figure S128a the experimental data on the excess Gibbs free energy $G^{ex}/RT = x_1 \ln(\gamma_1) + x_2 \ln(\gamma_2)$ for adsorption of C_2H_4(1)/C_2H_6(2) mixtures in NaX zeolite at 293 K are plotted in 3D space as function of the surface potential Φ and mole fraction of CO_2 in the adsorbed phase, x_1. The entire data set resides on a 3D surface mesh determined from the fitted Wilson parameters in Table S22. Figure S128b presents a 3D plot of the CO_2(1)/C_2H_6(2) adsorption selectivity as function of the surface potential Φ and mole fraction of CO_2 in the bulk gas phase, y_1. The entire data set resides on a 3D surface mesh determined from the fitted Wilson parameters in Table S22. Figure S128b confirms that the adsorption selectivity is not uniquely determined by the surface potential, Φ, but is additionally dependent on the bulk phase mixture composition.

Siperstein and Myers[43] also report experimental data on the component loadings for CO_2(1)/C_2H_4(2)/C_2H_6(3) mixture adsorption in 13X zeolite at 293 K. Figure S129 presents parity plots comparing the experimental data with IAST and RAST estimates. The unary isotherm fits and Wilson parameters are provided in Table S22. Our approach for ternary mixtures is to estimate C as $C = \frac{x_1}{q_{1,sat}} + \frac{x_2}{q_{2,sat}} + \frac{x_3}{q_{3,sat}}$, assuming, $x_1 = x_2 = x_3 = 1/3$. For ternary mixture adsorption, the Wilson parameters for the binary pairs $\Lambda_{12}, \Lambda_{21}, \Lambda_{13}, \Lambda_{31}, \Lambda_{23}, \Lambda_{32}$ are taken to the same as for the corresponding binary pairs as listed in Table S22. The RAST estimates are in better agreement with the experimental data as compared to the IAST estimates.

14.8 Mixture adsorption in NaX zeolite; Costa/Calleja experiments

Costa et al.[63] and Calleja et al.[58] report experimental data for adsorption of CO_2(1)/C_3H_8(2) mixtures in NaX zeolite at 293 K, that are analogous to those analyzed in the foregoing section for the experimental data of Siperstein and Myers[43]. The adsorption selectivity S_{ads} for CO_2(1)/C_3H_8(2) mixture adsorption in

NaX zeolite, is not a unique function of the surface potential, as anticipated by the IAST estimates (indicated by the dashed line); see Figure S130a. The unary isotherm fit parameters, along with the Wilson parameters, are specified in Table S23. Furthermore, the activity coefficients in the adsorbed phase are not uniquely determined by the mole fraction of CO_2 in the adsorbed phase, x_1; Figure S130b.

In Figure S131, the experimental data on the excess Gibbs free energy $G^{ex}/RT = x_1 \ln(\gamma_1) + x_2 \ln(\gamma_2)$ for adsorption of $CO_2(1)/C_3H_8(2)$ mixtures in NaX zeolite at 293 K are plotted in 3D space as function of the surface potential Φ and mole fraction of CO_2 in the adsorbed phase, x_1. The entre data set resides on a 3D surface mesh determined from the fitted Wilson parameters in Table S23.

The explanation for the failure of the IAST and the need to quantify non-idealities is to be found in the CBMC simulation data and analysis in Figure S52, Figure S53, Figure S54, Figure S55, and Figure S56. Indeed, the experimental data on G^{ex}/RT in Figure S131.the is precisely analogous to the corresponding 3D plots of CBMC data in Figure S54.

In Figure S132a the experimental data on the excess Gibbs free energy $G^{ex}/RT = x_1 \ln(\gamma_1) + x_2 \ln(\gamma_2)$ for adsorption of $CO_2(1)/C_3H_6(2)$ mixtures in NaX zeolite at 293 K are plotted in 3D space as function of the surface potential Φ and mole fraction of CO_2 in the adsorbed phase, x_1. The entire data set resides on a 3D surface mesh determined from the fitted Wilson parameters in Table S23.

In Figure S132b the experimental data on the $CO_2(1)/C_3H_6(2)$ adsorption selectivity are plotted in 3D space as function of the surface potential Φ and the mole fraction of CO_2 in the bulk gas phase, y_1. The entire data set resides on a 3D surface mesh determined from the fitted Wilson parameters in Table S23. Figure S132b confirms that the adsorption selectivity is not uniquely determined by the surface potential, Φ, but is additionally dependent on the bulk phase mixture composition.

The explanation for the failure of the IAST for

In Figure S133a the experimental data on the excess Gibbs free energy $G^{ex}/RT = x_1 \ln(\gamma_1) + x_2 \ln(\gamma_2)$ for adsorption of $C_3H_6(1)/C_3H_8(2)$ mixtures in NaX zeolite at 293 K are plotted in 3D space as function of Φ and x_1, the mole fraction of C_3H_6 in the adsorbed phase. The entire data set resides on a 3D surface mesh determined from the fitted Wilson parameters in Table S23.

In Figure S133b the experimental data on the $C_3H_6(1)/C_3H_8(2)$ adsorption selectivity are plotted in 3D space as function of the surface potential Φ and the mole fraction of C_3H_6 in the bulk gas phase, y_1. The entire data set resides on a 3D surface mesh determined from the fitted Wilson parameters in Table S23. Figure S133b confirms that the adsorption selectivity is not uniquely determined by the surface potential, Φ, but is additionally dependent on the bulk phase mixture composition.

In Figure S134, the experimental data on the excess Gibbs free energy $G^{ex}/RT = x_1 \ln(\gamma_1) + x_2 \ln(\gamma_2)$ for adsorption of $CO_2(1)/C_2H_4(2)$ mixtures in NaX zeolite at 293 K are plotted in 3D space as function of Φ and x_1. The entre data set resides on a 3D surface mesh determined from the fitted Wilson parameters in Table S23.

In Figure S135, the experimental data on the excess Gibbs free energy $G^{ex}/RT = x_1 \ln(\gamma_1) + x_2 \ln(\gamma_2)$ for adsorption of $C_2H_4(1)/C_3H_8(2)$ mixtures in NaX zeolite at 293 K are plotted in 3D space as function of Φ and x_1. The entre data set resides on a 3D surface mesh determined from the fitted Wilson parameters in Table S23.

Calleja et al.[58] report experimental data on the component loadings for $CO_2(1)/C_3H_6(2)/C_3H_8(3)$ mixture adsorption in 13X zeolite at 293 K. Figure S136 presents parity plots comparing the experimental data with IAST and RAST estimates. The unary isotherm fits and Wilson parameters are provided in Table S23. Our approach for ternary mixtures is to estimate C as $C = \frac{x_1}{q_{1,sat}} + \frac{x_2}{q_{2,sat}} + \frac{x_3}{q_{3,sat}}$, assuming, $x_1 = x_2 = x_3 = 1/3$. For ternary mixture adsorption, the Wilson parameters for the binary pairs

$\Lambda_{12}, \Lambda_{21}, \Lambda_{13}, \Lambda_{31}, \Lambda_{23}, \Lambda_{32}$ are taken to the same as for the corresponding binary pairs as listed in Table S23. The RAST estimates are in good agreement with the experimental data.

Calleja et al.[58] also report experimental data on the component loadings for $CO_2(1)/C_2H_4(2)/C_3H_8(3)$ mixture adsorption in 13X zeolite at 293 K. Figure S137 presents parity plots comparing the experimental data with IAST and RAST estimates. The unary isotherm fits and Wilson parameters are provided in Table S23. Our approach for ternary mixtures is to estimate C as $C = \frac{x_1}{q_{1,sat}} + \frac{x_2}{q_{2,sat}} + \frac{x_3}{q_{3,sat}}$, assuming, $x_1 = x_2 = x_3 = 1/3$. For ternary mixture adsorption, the Wilson parameters for the binary pairs $\Lambda_{12}, \Lambda_{21}, \Lambda_{13}, \Lambda_{31}, \Lambda_{23}, \Lambda_{32}$ are taken to the same as for the corresponding binary pairs as listed in Table S23. The RAST estimates are in good agreement with the experimental data. For this ternary mixture, the non-idealities are not strong; therefore, the IAST estimates are close to the RAST estimates.

14.9 Mixture adsorption in 13X zeolite; Hyun/Danner experiments

Congregation effects also manifest for adsorption of unsaturated alkenes in zeolites containing extra-framework cations. Hyun and Danner[78] report experimental data for adsorption of $C_2H_4(1)$/iso-$C_4H_{10}(2)$ mixtures in 13X zeolite. For adsorption at 298 K and 137.8 kPa, their experimental data clearly demonstrates the occurrence of the phenomenon of azeotropic adsorption, i.e. $y_1 = x_1$; see Figure S138a. The phenomenon of azeotropy is not anticipated by the IAST (indicated by dashed lines). To account for azeotropic adsorption, activity coefficients need to be introduced; see RAST NRTL calculations in Figure S138a. In Figure S138c, the experimental data on the excess Gibbs free energy $G^{ex}/RT = x_1 \ln(\gamma_1) + x_2 \ln(\gamma_2)$ are plotted in 3D space as function of the surface potential Φ and adsorbed phase mole fraction of $C_2H_4(1)$, x_1.

In Figure S138d, the experimental data on the $C_2H_4(1)$/iso-$C_4H_{10}(2)$ adsorption selectivity are plotted in 3D space as function of the surface potential Φ and mole fraction of $C_2H_4(1)$ in the bulk gas phase, y_1. The entre data set resides on a 3D surface mesh determined from the fitted NRTL parameters in Table

S24. This 3D plot demonstrates that the selectivity is dependent on both the surface potential Φ and gas phase composition of $C_2H_4(1)$, y_1.

14.10 CO_2/C_3H_8 mixture adsorption in ZSM-5 zeolite; Calleja experiments

We investigate the experimental data of Calleja et al.[79] for adsorption of the binary mixtures of CO_2/C_2H_4, CO_2/C_3H_8 in ZSM-5 (with MFI topology) zeolite with Si/Al ratio = 15, as reported in Table 5 of their paper.

In Figure S139a, the adsorbed phase mole fraction of $CO_2(1)$, x_1, is plotted as function of mole fraction of $CO_2(1)$ in the bulk gas phase mixture, y_1. The experimental data clearly demonstrates the occurrence of the phenomenon of azeotropic adsorption, i.e. $x_1 = y_1$. The phenomenon of azeotropy is not anticipated by the IAST; as demonstrated the IAST calculations of adsorption selectivity S_{ads} for a total pressure of 90 kPa; see Figure S139b. It is noteworthy that for $y_1 \approx 0.35$, we have mixture adsorption azeotropy, $x_1 = y_1; S_{ads} = 1$. The IAST is unable to anticipate the strong decrease in S_{ads} with increased mole fraction of $CO_2(1)$ in the bulk gas phase mixture, y_1. Interestingly, the IAST anticipates the selectivity to be practically independent of y_1, whereas the experiments show a decreasing trend.

Introduction of the activity coefficients in the adsorbed phase is required for quantitative modeling of mixture adsorption. The deviations from ideality are adequately described with the Wilson parameters listed in Table S25. The RAST model, with Wilson parameters fitted to match the experimental data, anticipates the phenomenon of azeotropy for bulk vapor phase mole fraction $y_1 \approx 0.35$, at a total pressure of 90 kPa; see Figure S139b.

In Figure S139c, the adsorption selectivity S_{ads} for $CO_2(1)/C_3H_8(2)$ mixture adsorption in NaX zeolite is plotted as a function of the surface potential Φ. The experimental data clearly show that S_{ads} is not uniquely determined by Φ, as anticipated by the IAST.

In Figure S140a the experimental data for the excess Gibbs free energy $G^{ex}/RT = x_1 \ln(\gamma_1) + x_2 \ln(\gamma_2)$ are plotted in 3D space as function of Φ and x_1. The entire CBMC data set resides on a 3D surface mesh determined from the fitted Wilson parameters in Table S25.

In Figure S140b the experimental data on the $CO_2(1)/C_3H_8(2)$ adsorption selectivity are plotted in 3D space as function of the surface potential Φ and the mole fraction of CO_2 in the bulk gas phase, y_1. The entire data set resides on a 3D surface mesh determined from the fitted Wilson parameters in Table S25. Figure S140b confirms that the adsorption selectivity is not uniquely determined by the surface potential, Φ, but is additionally dependent on the bulk phase mixture composition.

14.11 CO_2/C_3H_8 mixture adsorption in H-MOR; Talu-Zwiebel experiments

Talu and Zwiebel[55] report experimental data of adsorption of CO_2/C_3H_8 mixtures at 303 K in H-MOR (= H-Mordenite) that provides insights into the influence of thermodynamic non-idealities on mixture adsorption. Two sets of experimental data are reported: (a) 17/83 $CO_2(1)/C_3H_8(2)$ mixtures and varying total gas phase pressures, p_t, and (b) $CO_2(1)/C_3H_8(2)$ mixtures at a total gas phase pressure p_t = 41 kPa, and varying CO_2 mole fractions in the bulk gas phase, y_1.

Figure S141a the adsorption selectivity S_{ads} for $CO_2(1)/C_3H_8(2)$ mixture adsorption in H-MOR zeolite is plotted as a function of the surface potential Φ. The experimental data clearly show that S_{ads} is not uniquely determined by Φ, as anticipated by the IAST.

Figure S141b presents the data on the adsorption selectivity S_{ads} for $CO_2(1)/C_3H_8(2)$ mixture adsorption as a function of the mole fraction of CO_2 in the bulk gas phase, y_1; the total gas phase pressure $p_t = p_1 + p_2 = 41$ kPa. For $y_1 < 0.6$, the selectivity is in favor of $CO_2(1)$, whereas for bulk gas phase mole fractions $y_1 > 0.6$, $S_{ads} < 1$ and the adsorption is C_3H_8-selective. The experimental data for adsorption of $CO_2(1)/C_3H_8(2)$ mixtures clearly show the phenomenon of azeotropy, $S_{ads} = 1$, at $y_1 \approx 0.6$. The IAST does not anticipate selectivity reversal phenomena, and the adsorption is anticipated to be CO_2-

selective over the entire composition range. With the fitted Wilson parameters, are reported in Table S26, the correct experimental trends in Figure S141a,b can be reproduced.

The experimental data presented in Figure S141b is in remarkable quantitative agreement with the corresponding CBMC simulations presented in Figure S111e.

In Figure S141c the experimental data for the excess Gibbs free energy $G^{ex}/RT = x_1 \ln(\gamma_1) + x_2 \ln(\gamma_2)$ are plotted in 3D space as function of the surface potential Φ and mole fraction of CO_2 in the adsorbed phase, x_1. The entre data set resides on a 3D surface mesh determined from the fitted Wilson parameters in Table S26. This plot demonstrates the dependence of activity coefficients on both Φ and x_1. The experimental data presented in Figure S141c is analogous to the corresponding 3D plot of CBMC simulations presented in Figure S112a.

Experimental data of Talu and Zwiebel[55] for adsorption of (a) CO_2/H_2S, and (b) C_3H_8/H_2S mixtures at 303 K in H-MOR are presented in Figure S142a,b. These are 3D plots of experimental data on excess Gibbs free energy $G^{ex}/RT = x_1 \ln(\gamma_1) + x_2 \ln(\gamma_2)$ plotted as a function of the surface potential Φ and mole fraction in the adsorbed phase mixture. The 3D mesh is constructed using the Wilson parameters provided in Table S26. These plot demonstrate the strong thermodynamic non-idealities that are adequately captured by the RAST Wilson model.

14.12 Toluene/1-propanol mixture adsorption in DAY-13; Sakuth experiments

In Figure S143a,b the experimental data of Sakuth et al.[80, 81] for component loadings, q_i, selectivity S_{ads}, and activity coefficients, γ_i, for toluene/1-propanol mixture adsorption in DAY-13 (dealuminated Y zeolite) at $T = 298.15$ K and total pressure (a, b, c) $p_t = 0.36$ kPa, and (d, e, f) $p_t = 1.06$ kPa. are presented. For both sets of data, selectivity reversals are experienced. The IAST estimations of the S_{ads}, shown by the dashed lines, do not anticipate such selectivity reversals.

Use of the RAST, with fitted Wilson parameters with fitted parameters as specified in Table S28, enables the correct experimental trends to be reproduced; see the continuous solid lines in Figure S143.

In Figure S144a the experimental data for the excess Gibbs free energy $G^{ex}/RT = x_1 \ln(\gamma_1) + x_2 \ln(\gamma_2)$ are plotted in 3D space as function of the surface potential Φ and mole fraction of toluene in the adsorbed phase, x_1. The entre data set resides on a 3D surface mesh determined from the fitted Wilson parameters in Table S28, Figure S144a confirms that the activity coefficients are functions of both Φ and x_1.

In Figure S144b the experimental data for the adsorption selectivity, S_{ads}, are plotted in 3D space as function of the surface potential Φ and mole fraction of toluene in the bulk fluid phase, y_1. The entre data set resides on a 3D surface mesh determined from the fitted Wilson parameters in Table S28, Figure S144a confirms that S_{ads} depend on both Φ and y_1. Noteworthily, the IAST anticipates the adsorption selectivity to be solely dependent on the surface potential Φ and not on the composition of the bulk phase mixture, y_1.

14.13 1-butanol/p-xylene mixture adsorption in Y zeolite; Takeuchi experiments

The experimental data of Takeuchi et al.[82] for adsorption of 1-butanol(1)/p-xylene(2) mixtures in high silica Y zeolite, obtained at 298 K and total pressure of 60 Pa present strong evidence of thermodynamic non-idealities in mixture adsorption; their data is redrawn for further analysis in Figure S145a,b. The IAST calculations anticipate that the selectivity is in favor of 1-butanol(1) for the entire range compositions. The experimental data, on the other hand, displays selectivity reversal in favor of p-xylene(2) for bulk vapor phase compositions $y_1 > 0.5$. This selectivity reversal phenomena is well described by the Real Adsorbed Solution Theory (RAST) with the choice of the fitted Wilson parameters specified in Table S29.

In Figure S145c the experimental data for the excess Gibbs free energy $G^{ex}/RT = x_1 \ln(\gamma_1) + x_2 \ln(\gamma_2)$ are plotted in 3D space as function of the surface potential Φ and mole fraction of 1-butanol in the adsorbed phase, x_1. The entre data set resides on a 3D surface mesh determined from the fitted Wilson parameters in Table S29. This plot demonstrates the dependence of activity coefficients on both Φ and x_1.

14.14 Methanol/nC6 mixture adsorption in MSC; Konno experiments

One of the early experimental investigations demonstrating inadequacies of the IAST for description of mixture adsorption equilibria is by Konno et al.[83] who investigated adsorption of mixtures containing one or more polar compounds: methanol, acetone, benzene, and n-hexane (nC6) in three different adsorbents: 13 X zeolite, Takeda Molecular Sieve Carbon MSC-5A, and activated carbon G-2X. As illustration, Figure S146a presents data on the component loadings of methanol and nC6 in MSC-5A at a total pressure of 4 kPa and 303.15 K, as a function of the mole fraction of methanol in the bulk vapor phase, y_1. In Figure S146b, the data on the adsorbed phase mole fraction of methanol, x_1, is plotted as a function the mole fraction of methanol in the bulk vapor phase, y_1. It is interesting to note that mixture adsorption exhibits azeotropic behavior. The phenomenon of azeotropic mixture adsorption is characterized by the equality of mole fractions in the bulk vapor phase and in the adsorbed phase, $y_1 = x_1$. For bulk vapor phase methanol fractions lower than 0.5, the adsorbed phase is richer in methanol, the adsorbate of the smaller molecular size. However, for bulk vapor phase richer in methanol, the adsorbed phase is richer in n-hexane, the adsorbate with the larger molecular size.

For the IAST calculations, the pure component Langmuir isotherm fits used are taken from Table S1 of Bartholdy et al.[84] The IAST estimations of the adsorbate composition, shown by the dashed line, does not anticipate such selectivity reversals. Use of the RAST, shown by the continuous solid line, with fitted Wilson parameters are $C = 0.144$ kg mol^{-1}; $\Lambda_{12} = 1.438; \Lambda_{21} = 68.567$ is able to capture the selectivity reversal phenomena reasonably accurately. Figure S146c presents the RAST calculations of the activity coefficients in the adsorbed phase. It is interesting to note that the activity coefficients are below unity, whereas the corresponding activity coefficients for bulk liquid phase mixtures, both exceed unity; Figure S146d. In Figure S146e the experimental data for the excess Gibbs free energy $G^{ex}/RT = x_1 \ln(\gamma_1) + x_2 \ln(\gamma_2)$ are plotted as function of the mole fraction of methanol in the adsorbed phase, x_1. The agreement with RAST Wilson calculations is excellent.

14.15 Methanol/nC6 mixture adsorption in CuBTC; Van Assche experiments

Figure S147 presents an analysis of the experimental of van Assche et al.[85] for adsorption of methanol, and n-hexane at 313 K in CuBTC. Figure S147a presents the unary isotherm data of van Assche et al.[85] for adsorption of methanol, and n-hexane at 313 K in CuBTC; the dual-site Langmuir-Freundlich parameters are provided in Table S30. Figure S147b,c plot the experimental data of van Assche et al.[85] for component loadings and adsorption selectivities, S_{ads}, for equimolar $\left(f_1 = f_2\right)$ methanol/n-hexane mixture adsorption in CuBTC as a function of the surface potential, Φ. The IAST overestimates the methanol/n-hexane adsorption selectivity to a significant extent. The experimentally determined activity coefficients are compared with RAST Margules fits in Figure S147d; the fitted parameters are specified in Table S30. The activity coefficients follow the limiting characteristics $\Phi \to 0; \gamma_i \to 1/$

14.16 List of Tables for Analysis of published experimental data

Table S20. Dual-site Langmuir parameters for pure components CO_2, and N_2 at 298 K in 13X zeolite. These fits are based on the 298 K unary isotherm data in Table 1 and Table 2 of the Supplementary Material accompanying the publication of Wilkins and Rajendran.[49]

	Site A		Site B	
	$\frac{q_{A,sat}}{\text{mol kg}^{-1}}$	$\frac{b_A}{\text{Pa}^{-1}}$	$\frac{q_{B,sat}}{\text{mol kg}^{-1}}$	$\frac{b_B}{\text{Pa}^{-1}}$
CO_2	3.8	1.16×10^{-4}	1.8	1.04×10^{-2}
N_2	4.0	1.1×10^{-6}		

Fitted Wilson non-ideality parameters for binary CO_2/N_2 mixture adsorption in 13X.

	Λ_{12}	Λ_{21}	C / kg mol^{-1}
CO_2/N_2 in 13X	8.5	1	0.025

Table S21. Dual-site Langmuir parameter fits for CO_2, C_2H_4, C_2H_6, and CH_4 in LTA-5A zeolite. The unary isotherm data are culled from Mofarahi and Salehi[76] and Mofarahi and Gholipour[77].

	Site A			Site B		
	$\frac{q_{A,sat}}{\text{mol kg}^{-1}}$	$\frac{b_{A0}}{\text{Pa}^{-1}}$	$\frac{E_A}{\text{kJ mol}^{-1}}$	$\frac{q_{B,sat}}{\text{mol kg}^{-1}}$	$\frac{b_{B0}}{\text{Pa}^{-1}}$	$\frac{E_B}{\text{kJ mol}^{-1}}$
CO_2	1.5	3.216E-10	24	2.5	2.864E-12	49
C_2H_4	2.4	3.373E-06	9	0.8	1.578E-17	66
C_2H_6	2.1	1.581E-08	19.6	0.33	1.299E-23	99
CH_4	5	4.007E-09	15			

Wilson non-ideality parameters for binary mixtures in LTA-5A zeolite.

	C / kg mol^{-1}	Λ_{12}	Λ_{12}
C_2H_4/C_2H_6 at 283 K	12.015	0.259	3.859
CO_2/C_2H_4 at 238 K	0.119	2.033	183.022
CO_2/C_2H_4 at 273 K	0.036	0.00693	1446.771
CO_2/C_2H_4 at 323 K	0.0126	0.23202818	2014405.774

Table S22. Dual-site Langmuir-Freundlich parameters for pure components at 293 K in NaX zeolite.[43] The fit parameters were determined by fitting the unary isotherm data presented in Figure 1 of Siperstein and Myers.[43]

	Site A			Site B		
	$\frac{q_{A,sat}}{\text{mol kg}^{-1}}$	$\frac{b_A}{\text{Pa}^{-\nu_A}}$	ν_A	$\frac{q_{B,sat}}{\text{mol kg}^{-1}}$	$\frac{b_B}{\text{Pa}^{-\nu_B}}$	ν_B
CO_2	5.7	2.938E-03	0.64	1.1	1.633E-02	0.92
C_3H_8	1.8	1.475E-05	1.75	1.5	3.555E-03	0.75
C_2H_4	1.8	2.095E-03	1	2.6	1.190E-03	0.76
C_2H_6	1.1	1.054E-09	2.2	2.75	5.922E-05	1

Wilson non-ideality parameters for binary and ternary mixtures at 293 K in NaX zeolite.

	C / kg mol^{-1}	Λ_{12}	Λ_{12}
CO_2/C_3H_8	0.225	1.760	2.751
CO_2/C_2H_4	0.187	2.070	0.483
CO_2/C_2H_6	0.203	0.114	8.816
C_2H_4/C_2H_6	0.244	1.177	1.431
$CO_2/C_2H_4/C_2H_6$	0.211	$\Lambda_{12}, \Lambda_{21}, \Lambda_{13}, \Lambda_{31}, \Lambda_{23}, \Lambda_{32}$ as above	

Table S23. Dual-site Langmuir parameters for pure components at 293 K in 13X (= NaX) zeolite. The fit parameters were determined by fitting the unary isotherm data presented in Table I of Costa et al.[63]

	Site A			Site B		
	$\frac{q_{A,sat}}{\text{mol kg}^{-1}}$	$\frac{b_{A0}}{\text{Pa}^{-1}}$	$\cdot\frac{E_A}{\text{kJ mol}^{-1}}\cdot$	$\frac{q_{B,sat}}{\text{mol kg}^{-1}}$	$\frac{b_{B0}}{\text{Pa}^{-1}}$	$\frac{E_B}{\text{kJ mol}^{-1}}$
CO_2	2	4.813E-08	23	2.5	1.129E-12	42
C_2H_4	1.35	3.403E-05	4.6	1.4	8.508E-17	70
C_3H_8	1.24	3.451E-11	41	0.96	3.451E-11	41
C_3H_6	0.95	7.490E-10	33	1.5	1.436E-16	82

Wilson non-ideality parameters for binary and ternary mixtures at 293 K in NaX zeolite.

	C / kg mol^{-1}	Λ_{12}	Λ_{12}
CO_2/C_3H_6	0.315	7.223	0.138
CO_2/C_3H_8	0.338	0.000	5.403
C_3H_6/C_3H_8	0.431	0.125	7.968
CO_2/C_2H_4	0.293	3.221	0.086
C_2H_4/C_3H_8	0.409	0.000	3.750
$CO_2/C_3H_6/C_3H_8$	0.362	$\Lambda_{12},\Lambda_{21},\Lambda_{13},\Lambda_{31},\Lambda_{23},\Lambda_{32}$ as above	
$CO_2/C_2H_4/C_3H_8$	0.347	$\Lambda_{12},\Lambda_{21},\Lambda_{13},\Lambda_{31},\Lambda_{23},\Lambda_{32}$ as above	

Table S24. Dual-site Langmuir parameter fits for C_2H_4, and iso-C_4H_{10} in 13X zeolite. The unary isotherm data are from Table 1 of Hyun and Danner.[78]

	Site A			Site B		
	$\frac{q_{A,sat}}{\text{mol kg}^{-1}}$	$\frac{b_{A0}}{\text{Pa}^{-1}}$	$\frac{E_A}{\text{kJ mol}^{-1}}$	$\frac{q_{B,sat}}{\text{mol kg}^{-1}}$	$\frac{b_{B0}}{\text{Pa}^{-1}}$	$\frac{E_B}{\text{kJ mol}^{-1}}$
C_2H_4	0.75	2.089E-10	40	2.15	9.284E-11	35
iso-C_4H_{10}	0.52	2.448E-16	65	1.4	3.270E-10	42

Fitted NRTL non-ideality parameters for binary mixture adsorption.

	C / kg mol^{-1}	τ_{12}	τ_{21}	α
C_2H_4/iso-C_4H_{10}	0.052	859.064	-787.085	1.091E-04

Table S25. Dual-site Langmuir parameters for pure components CO_2, and C_3H_8 at 293 K in ZSM-5 (with MFI topology) zeolite with Si/Al ratio = 15. The fit parameters were determined by fitting the unary isotherm data presented in Table 2 of Calleja et al.[79]

	Site A		Site B	
	$\frac{q_{A,sat}}{\text{mol kg}^{-1}}$	$\frac{b_A}{\text{Pa}^{-1}}$	$\frac{q_{B,sat}}{\text{mol kg}^{-1}}$	$\frac{b_B}{\text{Pa}^{-1}}$
CO_2	1.35	3.32×10^{-5}	1.1	4.5×10^{-3}
C_3H_8	0.76	3.62×10^{-4}	0.9	1×10^{-2}

Wilson non-ideality parameters for binary mixtures at 293 K in ZSM-5 (with MFI topology) zeolite with Si/Al ratio = 15. These are determined by fitting to the experimental data of Calleja et al.[79] as reported in Table 5 of their paper.

	C / kg mol^{-1}	Λ_{12}	Λ_{12}
CO_2/C_3H_8	0.92	0.19	5.1

Table S26. Dual-site Langmuir parameters for pure components CO_2, C_3H_8, and H_2S in H-MOR. The fit parameters were determined by fitting the unary isotherm data, reported for different temperatures in Table 4 of Talu and Zwiebel.[55]

	Site A			Site B		
	$\frac{q_{A,sat}}{\text{mol kg}^{-1}}$	$\frac{b_{A0}}{\text{Pa}^{-1}}$	$\frac{E_A}{\text{kJ mol}^{-1}}$	$\frac{q_{B,sat}}{\text{mol kg}^{-1}}$	$\frac{b_{B0}}{\text{Pa}^{-1}}$	$\frac{E_B}{\text{kJ mol}^{-1}}$
CO_2	2.4	9.155E-11	31	0.6	7.860E-11	42
C_3H_8	0.65	4.974E-11	32	0.72	1.449E-10	41
H_2S	1.5	2.002E-10	33	1.2	9.436E-10	39

Wilson non-ideality parameters for binary mixtures at 303 K in H-MOR. These are determined by fitting to the experimental data of Talu and Zwiebel[55] as reported in Table 5 of their paper.

	C / kg mol^{-1}	Λ_{12}	Λ_{12}
CO_2/C_3H_8	0.769	3.988	7.268
CO_2/H_2S	0.352	0.642	1.557
C_3H_8/H_2S	0.550	4.560	12.004

Table S27. Dual-site Langmuir parameters for pure components CO_2, CH_4, and N_2 in 13X (= NaX) zeolite. The fit parameters were determined by re-fitting the unary isotherm data presented in Figure 2 and Table 2 of Avijegon et al.[69]

	Site A			Site B		
	$\frac{q_{A,sat}}{\text{mol kg}^{-1}}$	$\frac{b_{A0}}{\text{Pa}^{-1}}$	$\frac{E_A}{\text{kJ mol}^{-1}}$	$\frac{q_{B,sat}}{\text{mol kg}^{-1}}$	$\frac{b_{B0}}{\text{Pa}^{-1}}$	$\frac{E_B}{\text{kJ mol}^{-1}}$
CO_2	2	1.066E-07	28.8	4	2.087E-07	22.7
CH_4	4	5.091E-09	14.4	0.24	8.324E-10	13
N_2	0.2	1.744E-08	13.6	3.3	3.471E-09	13.6

Wilson non-ideality parameters for binary CO_2/CH_4 mixtures at 273 K in NaX zeolite.

	C / kg mol^{-1}	Λ_{12}	Λ_{12}
CO_2/C_3H_8	0.201	4.133	4.020

Table S28. Langmuir-Freundlich fits of the unary isotherms of toluene, and 1-propanol in DAY-13 zeolite at 298 K. The parameters were obtained by fitting the unary isotherm data in Table 1 of Sakuth et al.[80]

	$\frac{q_{sat}}{\text{mol kg}^{-1}}$	$\frac{b}{\text{Pa}^{-\nu}}$	ν
toluene	2.26	0.2585	0.74
1-propanol	3.26	0.09743	0.56

The fitted Wilson parameters using the data from Table 3 of Sakuth et al.[80] for toluene/1-propanol mixture adsorption in DAY-13.

	C / kg mol^{-1}	Λ_{12}	Λ_{12}
Toluene/1-propanol	0.375	0.687	11.112

Table S29. Langmuir fits of the unary isotherms of 1-butanol, and p-xylene in Y zeolite at 298 K. The parameters correspond to those presented in Table 4 of Takeuchi et al.[82] for dry conditions in the vapor phase.

	$\frac{q_{sat}}{\text{mol kg}^{-1}}$	$\frac{b}{\text{Pa}^{-\nu}}$
1-butanol	2.17	0.2239
p-xylene	1.39	0.5268

Fitted Wilson non-ideality parameters for binary mixture adsorption in Y zeolite at 298 K.

	C / kg mol^{-1}	Λ_{12}	Λ_{12}
1-butanol/p-xylene	0.048	2.5	210

Table S30. Dual-site Langmuir-Freundlich parameters for adsorption of methanol, and n-hexane at 313 K in CuBTC. The unary isotherm fits are based on the data scanned from Figure 2 of van Assche et al.[85]

	Site A			Site B		
	$\frac{q_{A,sat}}{\text{mol kg}^{-1}}$	$\frac{b_A}{\text{Pa}^{-\nu_A}}$	ν_A	$\frac{q_{B,sat}}{\text{mol kg}^{-1}}$	$\frac{b_B}{\text{Pa}^{-\nu_B}}$	ν_B
methanol	13.5	8.568E-03	0.62	6.5	2.499E-03	1.56
n-hexane	2.3	1.057E-01	0.6	2.8	4.813E-08	6.85

The fitted Margules parameters using the data scanned from Figure 4 of van Assche et al.[85] The units of C are kg mol^{-1}.

	C / kg mol^{-1}	A_{12}	A_{21}
Methanol/n-hexane	0.123	-6.172	-15.625

14.17 List of Figures for Analysis of published experimental data

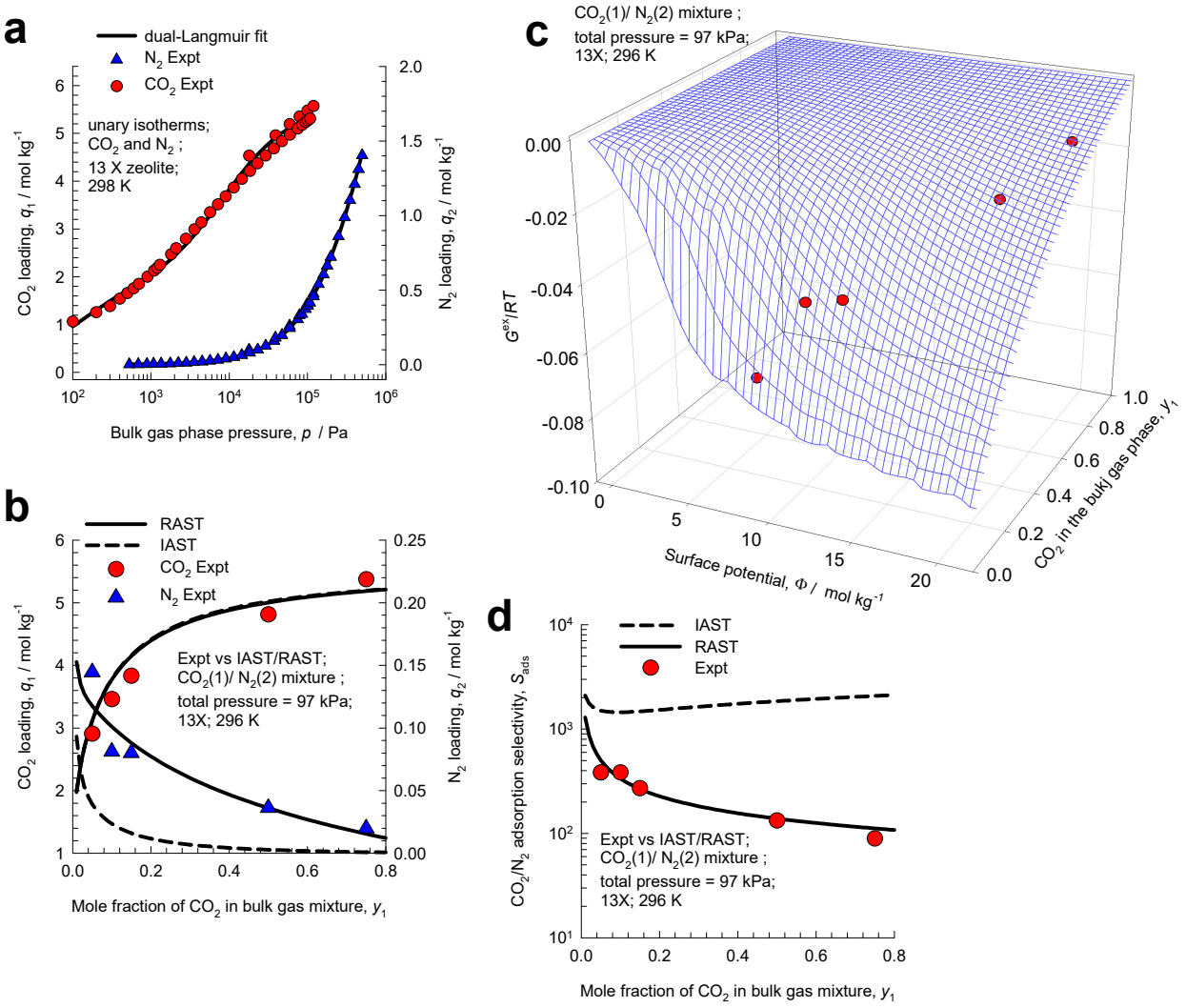

Figure S113. (a) Unary isotherm data of CO_2, and N_2 in 13X zeolite at 298 K. The isotherm fit parameters are provided in Table S20. (b) Experimental data (indicated by symbols) of Wilkins and Rajendran[49] for component loadings, q_i, of CO_2, and N_2 for adsorption of CO_2/N_2 mixtures in 13X zeolite at 296 K and total pressure p_t = 97 kPa, as function of the mole fraction of CO_2 in the bulk gas phase, y_1. (c) Excess Gibbs free energy G^{ex}/RT, as function of Φ, and y_1. (d) CO_2/N_2 adsorption selectivity S_{ads}, as function of y_1.

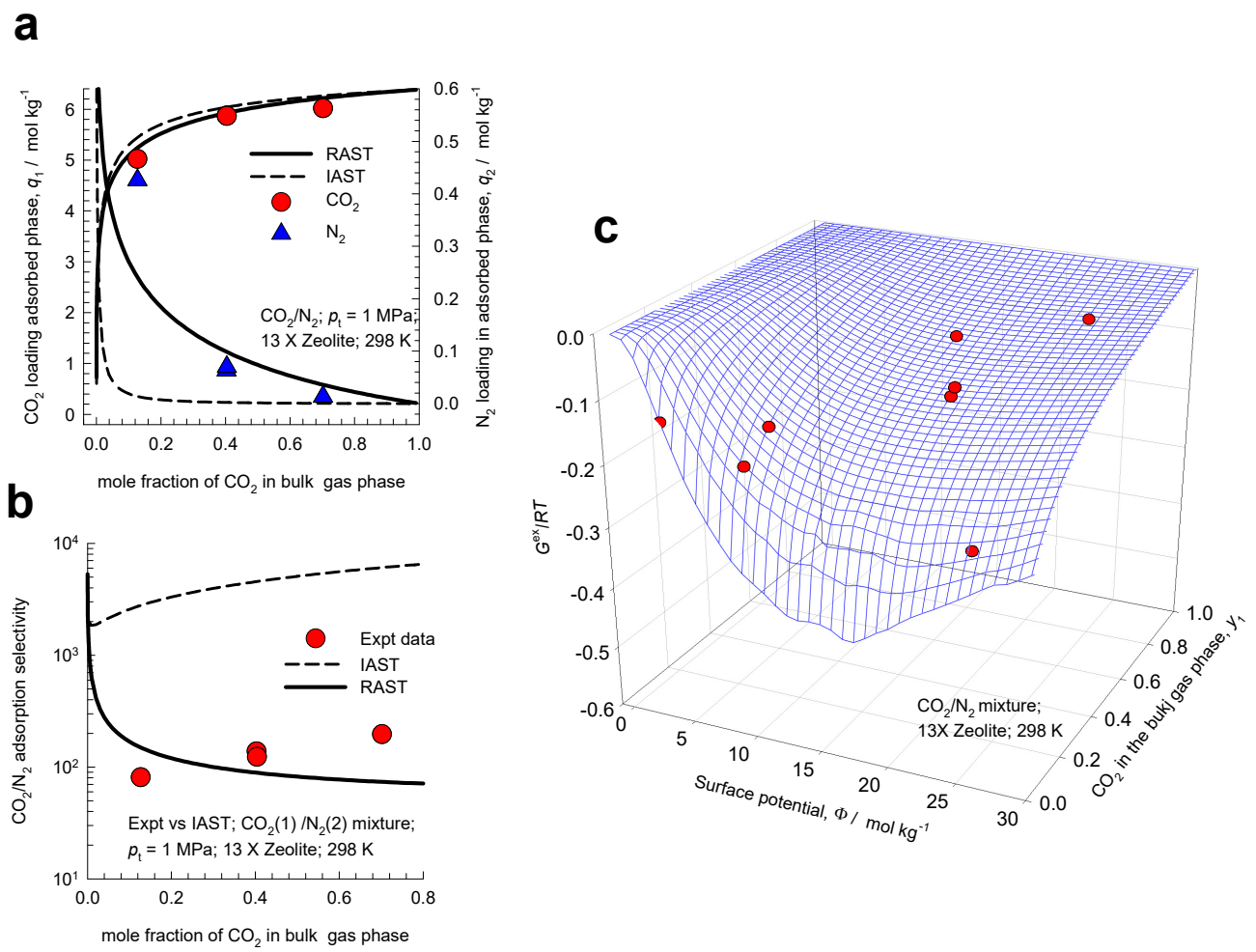

Figure S114. (a) Experimental data (indicated by symbols) of Hefti et al.[50] for component loadings, q_i, of CO_2, and N_2 for adsorption of CO_2/N_2 mixtures in 13X zeolite at 298 K and total pressure p_t = 1 MPa, as function of the mole fraction of CO_2 in the bulk gas phase. (b) CO_2/N_2 adsorption selectivity as function of the mole fraction of CO_2 in the bulk gas phase. The dashed lines in (a), and (b) are the IAST estimations, using the unary isotherm fits provided in Table 2 of Hefti et al.[50] The continuous solid lines in (a), and (b) are the estimations using RAST using Wilson parameters: $\Lambda_{12} = 6.758$; $\Lambda_{21} = 0.4844$; $C = 0.0744$ kg mol^{-1}. (c) Excess Gibbs free energy G^{ex}/RT, as function of Φ, and y_1.

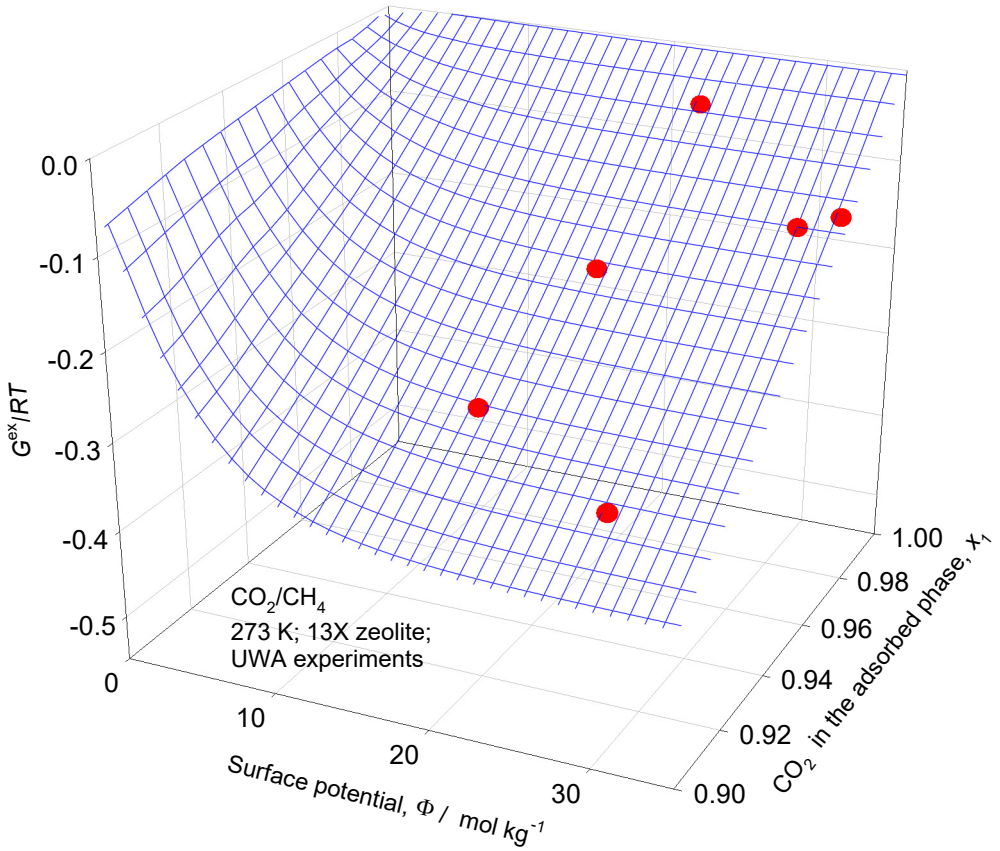

Figure S115. 3D plots of experimental data of Avijegon et al.[69] on excess Gibbs free energy $G^{ex}/RT = x_1 \ln(\gamma_1) + x_2 \ln(\gamma_2)$ for adsorption of CO_2/CH_4 mixtures at 273 K in NaX (=13X) zeolite. The 3D mesh is constructed using the Wilson parameters provided in Table S27.

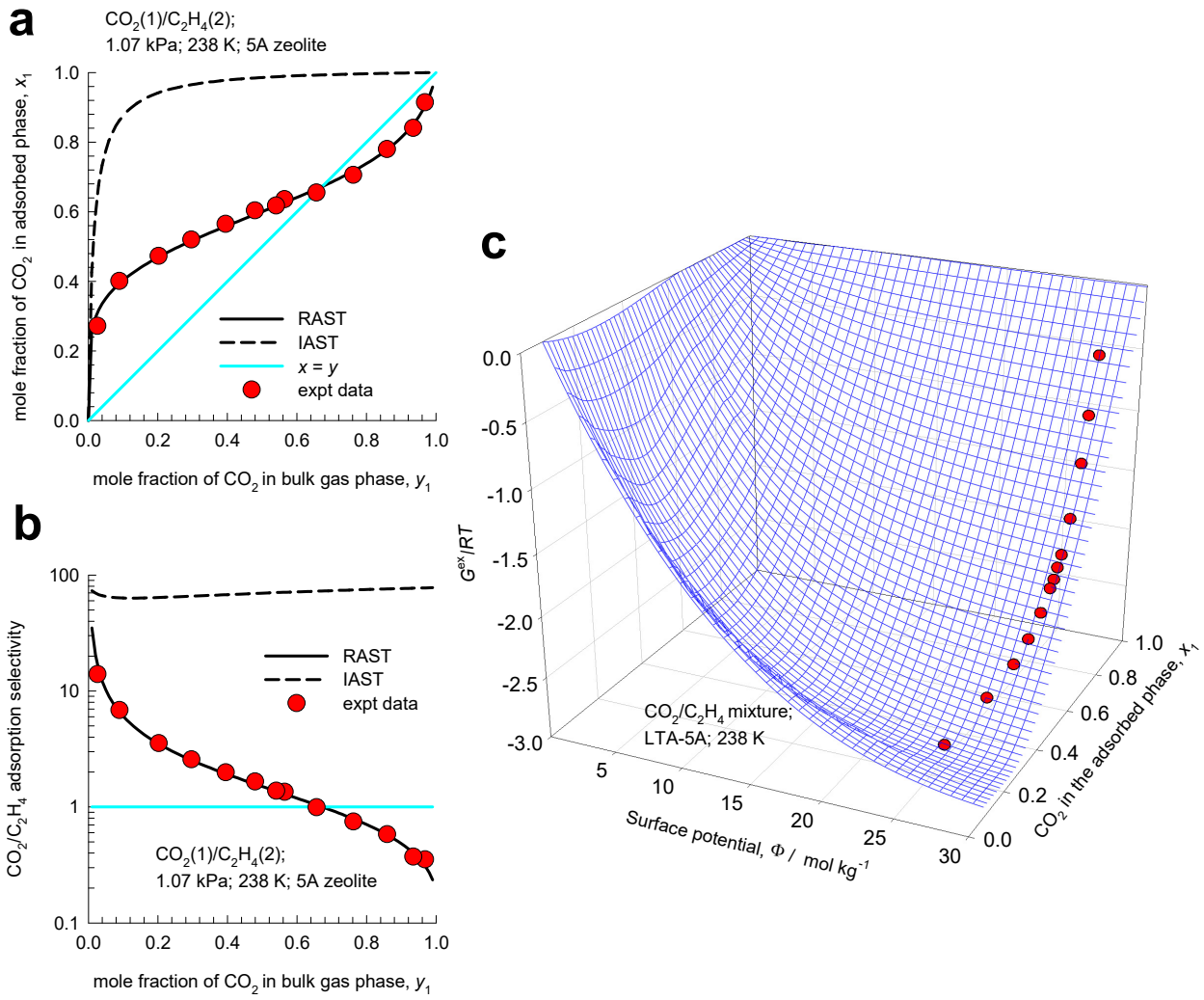

Figure S116. Experimental data of Basmadjian and Hsieh[70] for adsorption of $CO_2(1)/C_2H_4(2)$ mixtures in LTA-5A zeolite, obtained at 238 K and total pressure of 1.07 bar. (a) The adsorbed phase mole fraction of CO_2, x_1, is plotted as function of mole fraction of CO_2 in the bulk gas phase mixture, y_1. (b) The adsorption selectivity S_{ads} plotted as function as function of mole fraction of CO_2 in the bulk gas phase mixture, y_1. (c) The excess Gibbs free energy $G^{ex}/RT = x_1 \ln(\gamma_1) + x_2 \ln(\gamma_2)$ as function of the surface potential Φ and mole fraction of CO_2 in the adsorbed phase, x_1. The unary isotherm DSL parameters and Wilson fits are specified in Table S21.

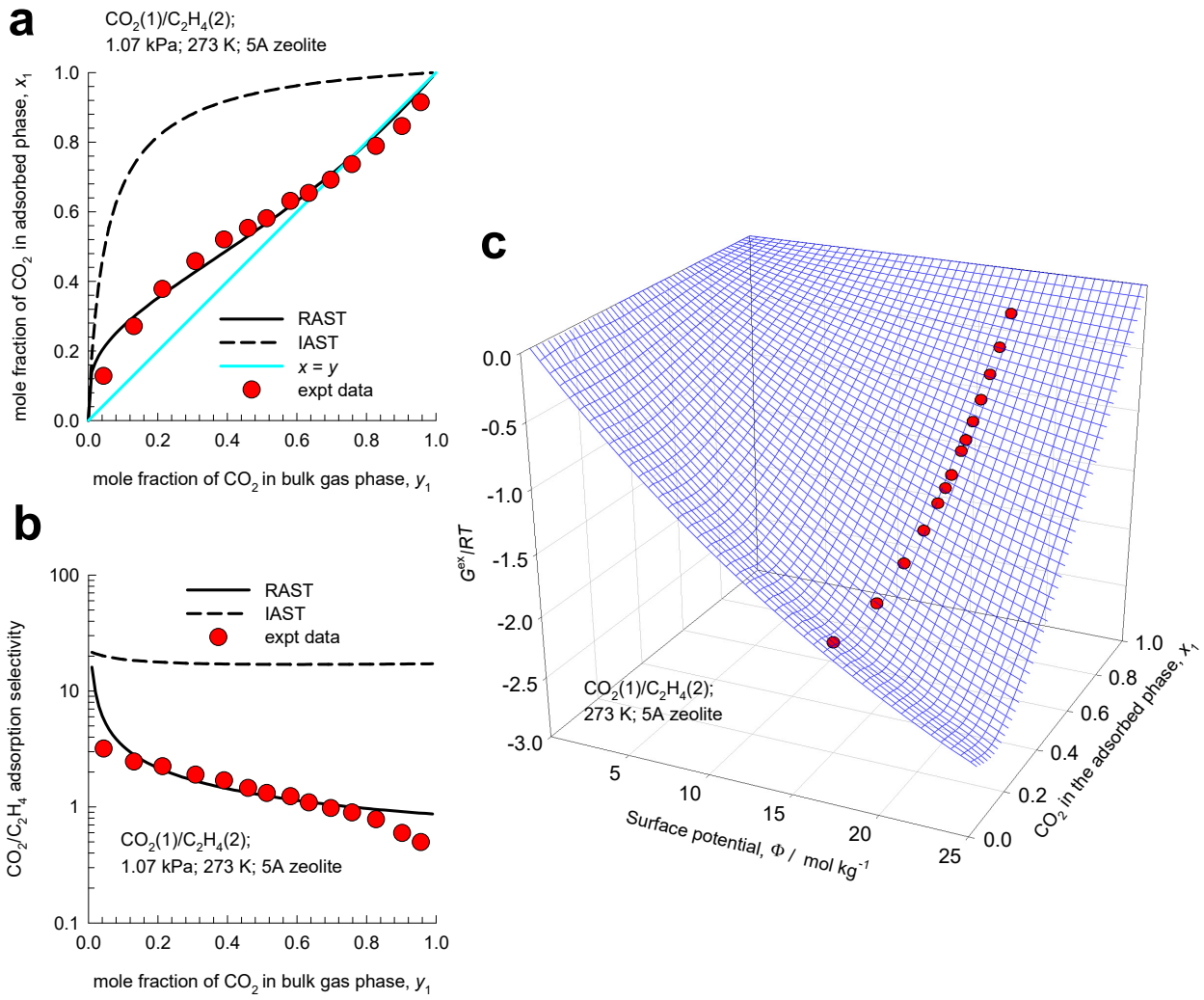

Figure S117. Experimental data of Basmadjian and Hsieh[70] for adsorption of $CO_2(1)/C_2H_4(2)$ mixtures in LTA-5A zeolite, obtained at 273 K and total pressure of 1.07 bar. (a) The adsorbed phase mole fraction of CO_2, x_1, is plotted as function of mole fraction of CO_2 in the bulk gas phase mixture, y_1. (b) The adsorption selectivity S_{ads} plotted as function as function of mole fraction of CO_2 in the bulk gas phase mixture, y_1. (c) The excess Gibbs free energy $G^{ex}/RT = x_1 \ln(\gamma_1) + x_2 \ln(\gamma_2)$ as function of the surface potential Φ and mole fraction of CO_2 in the adsorbed phase, x_1. The unary isotherm DSL parameters and Wilson fits are specified in Table S21.

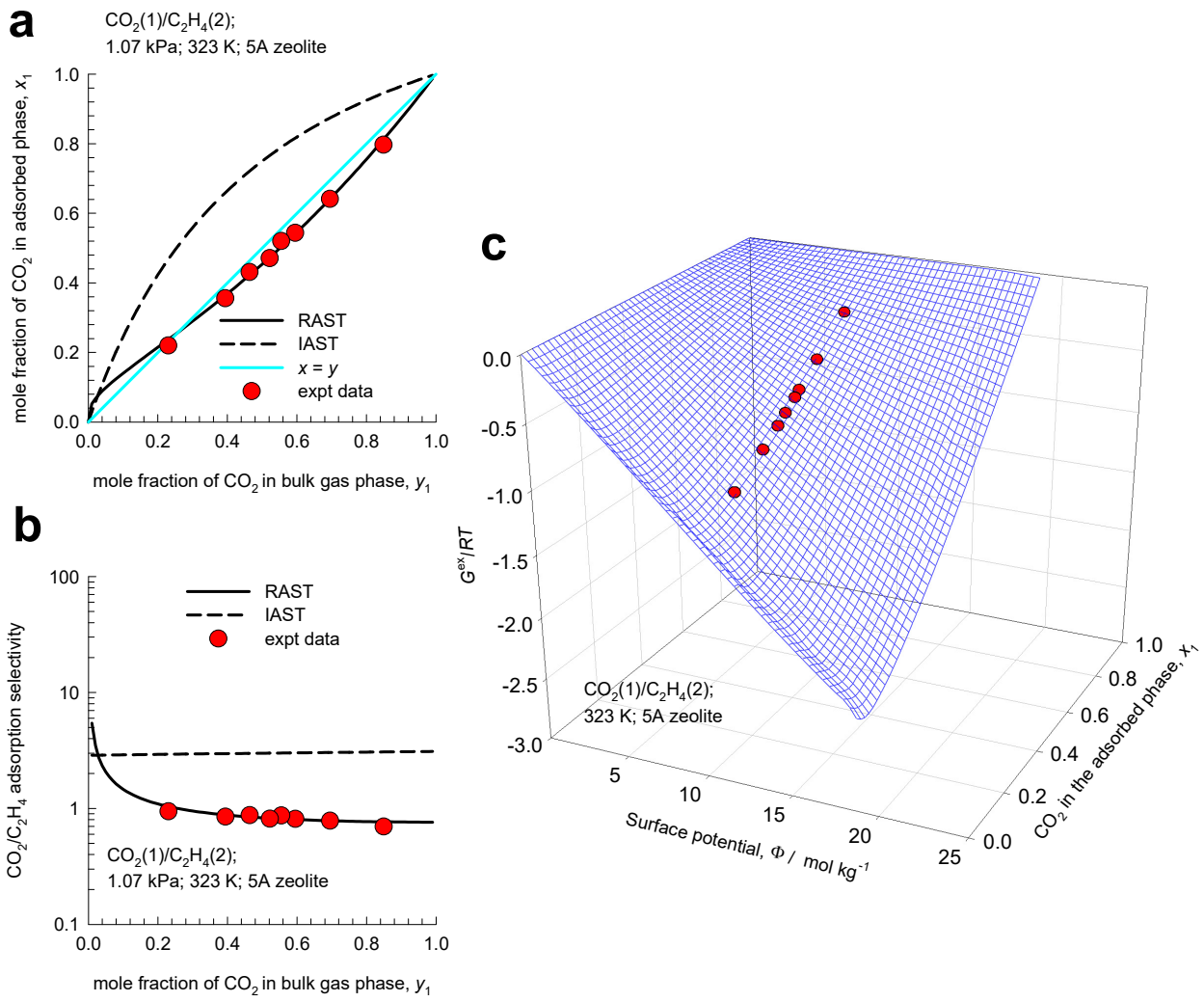

Figure S118. Experimental data of Basmadjian and Hsieh[70] for adsorption of $CO_2(1)/C_2H_4(2)$ mixtures in LTA-5A zeolite, obtained at 323 K and total pressure of 1.07 bar. (a) The adsorbed phase mole fraction of CO_2, x_1, is plotted as function of mole fraction of CO_2 in the bulk gas phase mixture, y_1. (b) The adsorption selectivity S_{ads} plotted as function as function of mole fraction of CO_2 in the bulk gas phase mixture, y_1. (c) The excess Gibbs free energy $G^{ex}/RT = x_1 \ln(\gamma_1) + x_2 \ln(\gamma_2)$ as function of the surface potential Φ and mole fraction of CO_2 in the adsorbed phase, x_1. The unary isotherm DSL parameters and Wilson fits are specified in Table S21.

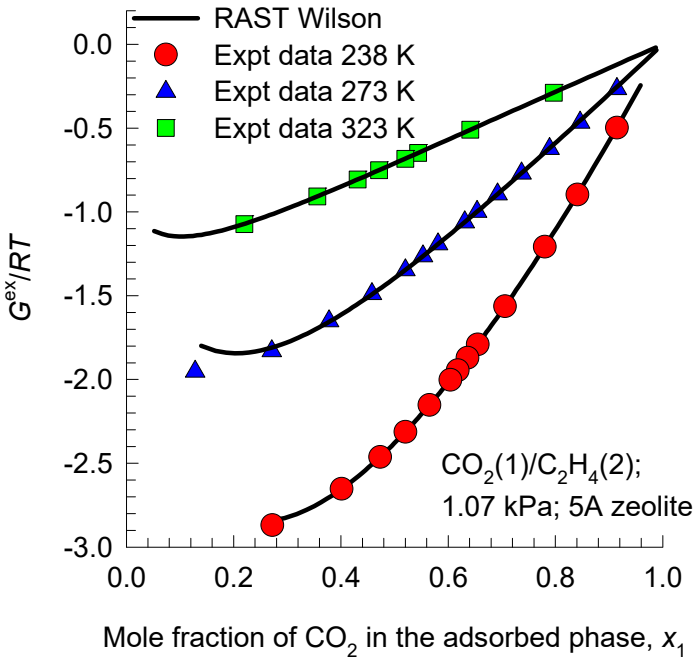

Figure S119. Experimental data of Basmadjian and Hsieh[70] for the excess Gibbs free energy $G^{ex}/RT = x_1 \ln(\gamma_1) + x_2 \ln(\gamma_2)$ for adsorption of $CO_2(1)/C_2H_4(2)$ mixtures in LTA-5A zeolite at total pressure of 1.07 bar. The data at 238 K, 273 K, and 323 K are plotted as function of the mole fraction of CO_2 in the adsorbed phase, x_1. The continuous solid lines are RAST calculations using the Wilson fits are specified in Table S21.

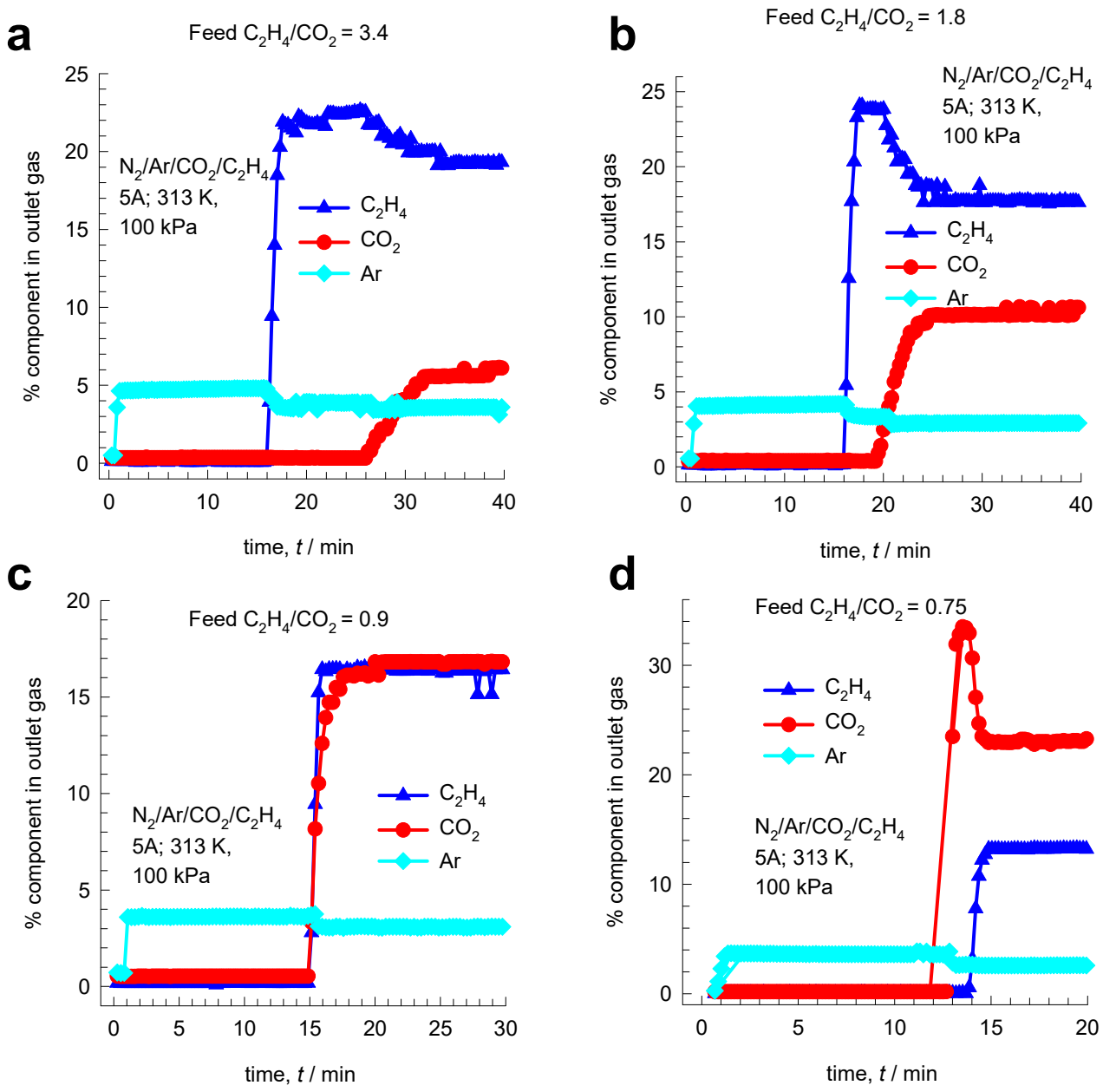

Figure S120. Experimental breakthroughs of van Zandvoort et al.[51, 52] for Ar/C2H4/CO2/N2 mixtures in LTA-5A zeolite at 313 K and total pressure of 1 bar for (a) Run1, (b) Run 2, (c) Run 3, and (d) Run 4. The % N2 in the outlet gas can be determined by the taking the sum of the mole % = 100. In (e) the experimental breakthroughs are compared with transient breakthrough simulations invoking the RAST.

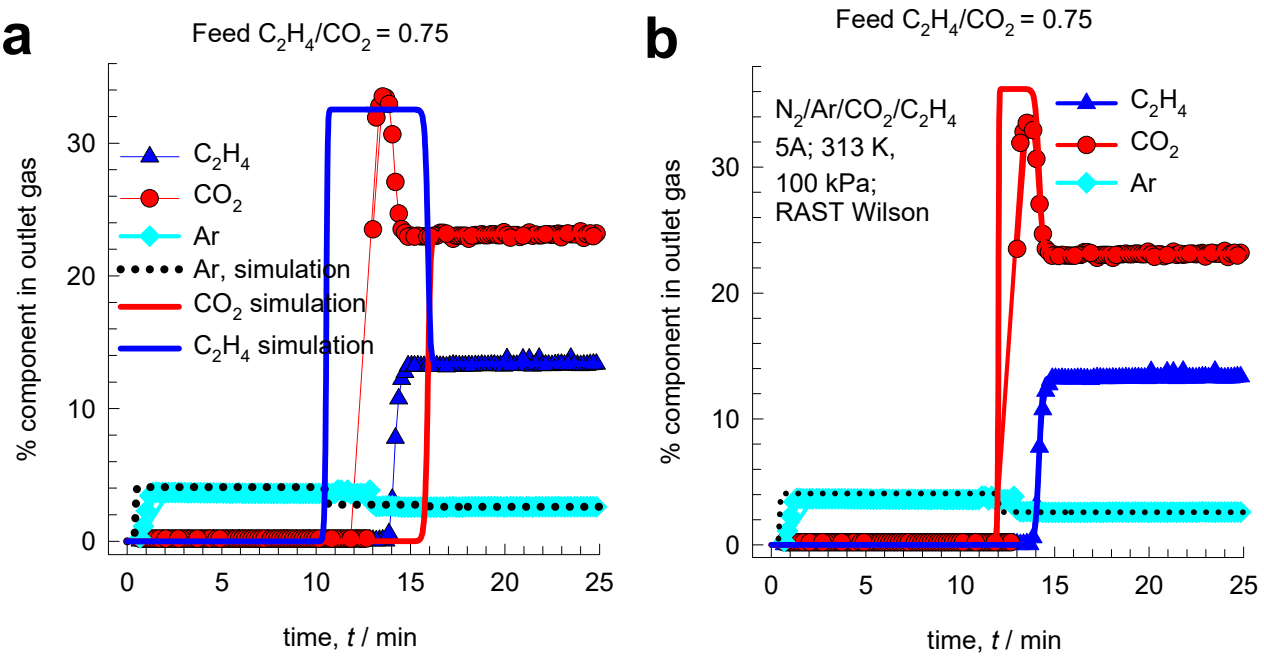

Figure S121. Experimental breakthroughs for $Ar/C_2H_4/CO_2/N_2$ mixtures in 5A zeolite. The total pressure is 1 bar, temperature T = 313 K, and the feed mixture composition corresponds to Run 4 (C_2H_4/CO_2 = 0.75). (a) The experimental breakthroughs are compared with simulations invoking the IAST. (b) The experimental breakthroughs are compared with simulation in which the RAST Wilson model is used to model thermodynamic non-idealities.

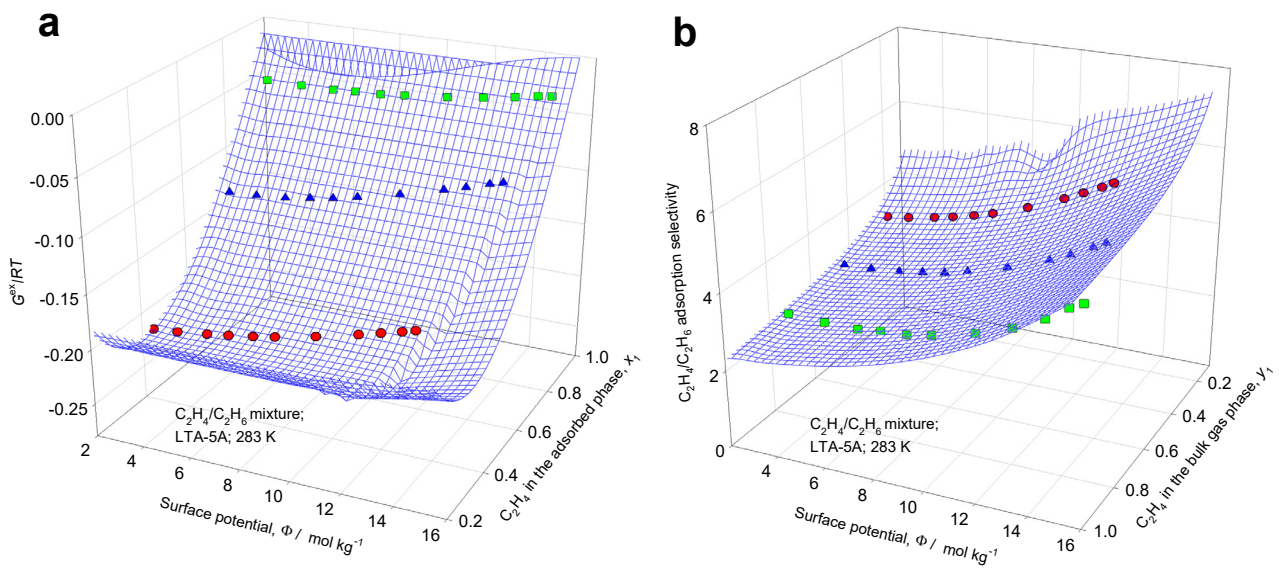

Figure S122. Experimental data of Mofarahi and Salehi[76] for adsorption of $C_2H_4(1)/C_2H_6(2)$ mixtures in LTA-5A zeolite at 283 K for three different mole fractions, 0.2, 0.5, and 0.8, of $C_2H_4(1)$ in the bulk gas phase, y_1. (a) The Gibbs free energy $G^{ex}/RT = x_1 \ln(\gamma_1) + x_2 \ln(\gamma_2)$ as function of the surface potential Φ and mole fraction of CO_2 in the adsorbed phase, x_1. (b) The $C_2H_4(1)/C_2H_6(2)$ adsorption selectivity for as function of the surface potential Φ and mole fraction of CO_2 in the bulk gas phase, y_1. The 3D mesh in (a, b) is constructed using the Wilson parameters provided in Table S21.

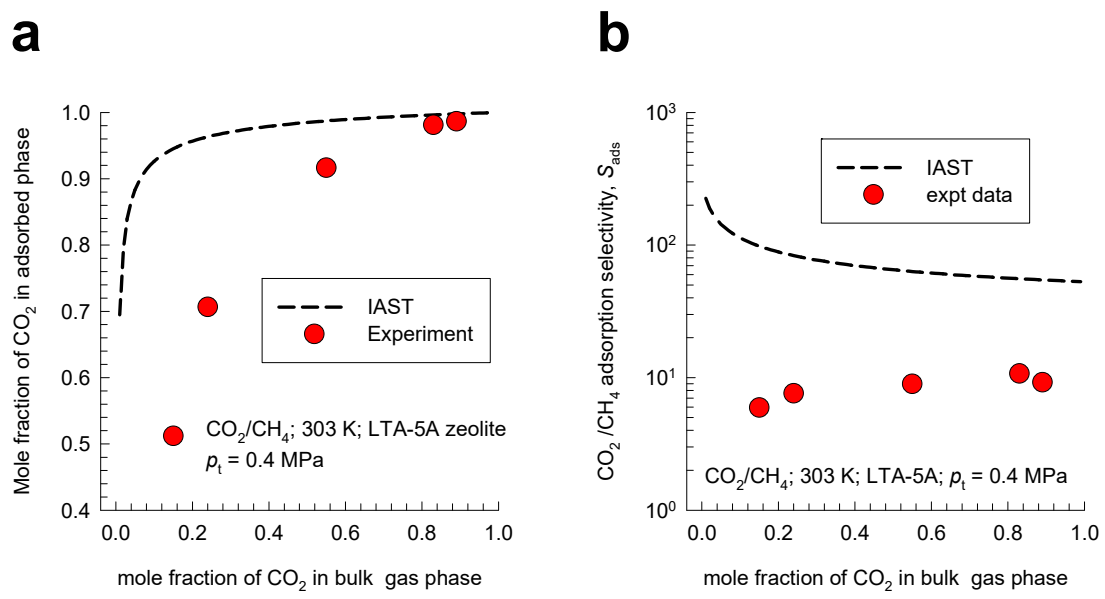

Figure S123 Re-analysis of the experimental data of Mofarahi and Gholipour[77] for $CO_2(1)/CH_4(2)$ mixture adsorption at 303 K in LTA-5A zeolite. (a) Experimental data (indicated by symbols) of adsorbed phase mole fractions, x_1, of CO_2, as function of the mole fraction of CO_2 in the bulk gas phase, y_1. (b) $CO_2(1)/CH_4(2)$ adsorption selectivity as function of the mole fraction of CO_2 in the bulk gas phase. The unary isotherm fit parameters are specified in Table S21.

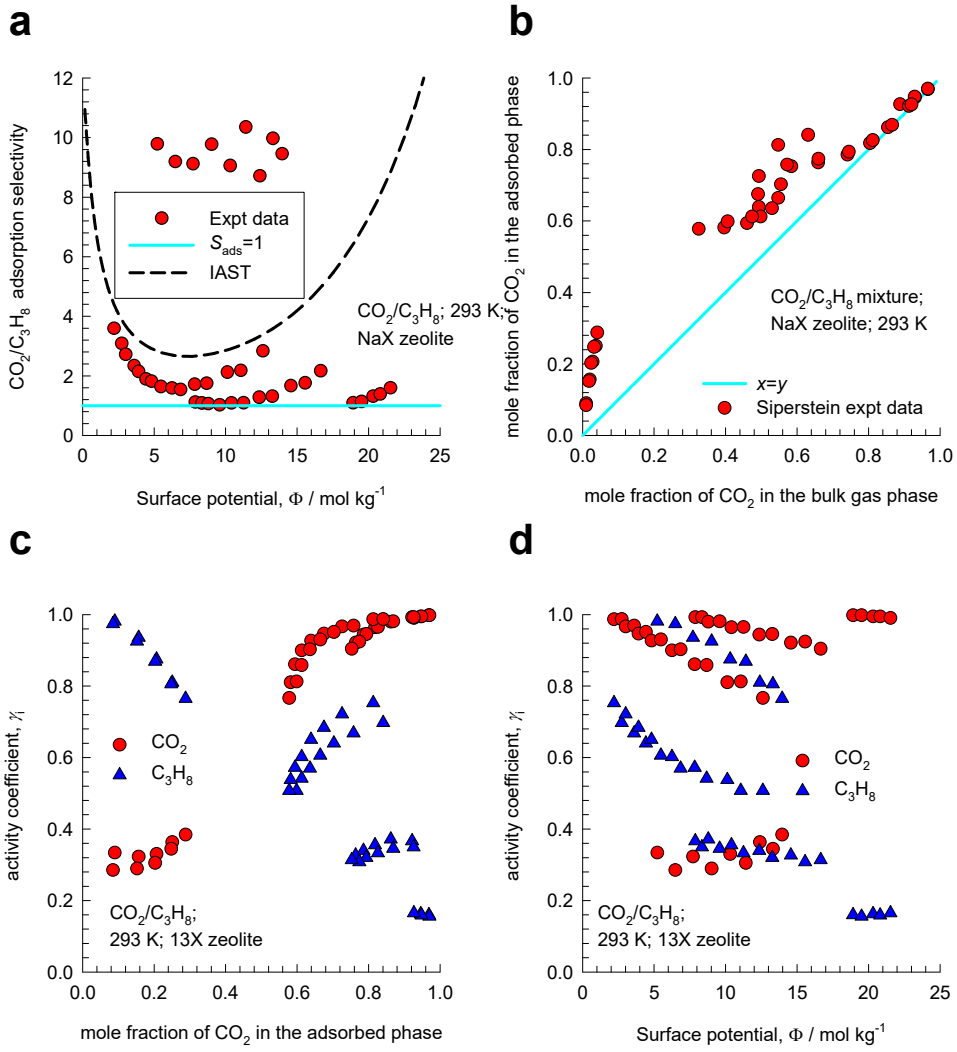

Figure S124. Experimental data of Siperstein and Myers[43] for adsorption of $CO_2(1)/C_3H_8(2)$ mixtures in NaX zeolite at 293 K, as reported in Table C1 of their paper. (a) The adsorption selectivity S_{ads} for $CO_2(1)/C_3H_8(2)$ mixture adsorption in NaX zeolite is plotted as a function of the surface potential Φ. The IAST estimation of S_{ads} are shown by dashed lines. (b) The adsorbed phase mole fraction of $CO_2(1)$, x_1, is plotted as function of mole fraction of $CO_2(1)$ in the bulk gas phase mixture, y_1. (c, d) Activity coefficients in the adsorbed phase as function of x_1, and Φ. The unary isotherm fit parameters, along with the Wilson parameters, are specified in Table S22.

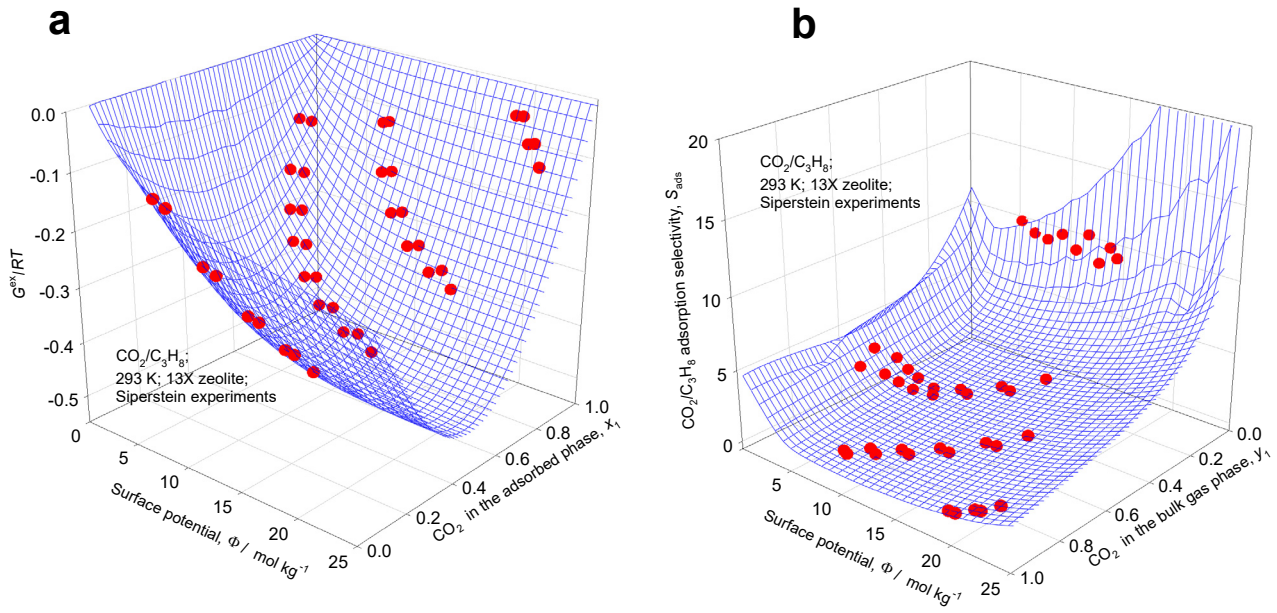

Figure S125. 3D plots of experimental data of Siperstein and Myers[43] on (a) excess Gibbs free energy $G^{ex}/RT = x_1 \ln(\gamma_1) + x_2 \ln(\gamma_2)$, and (b) adsorption selectivity for adsorption of CO_2/C_3H_8 mixtures at 293 K in NaX (=13X) zeolite. The 3D mesh is constructed using the Wilson parameters provided in Table S22.

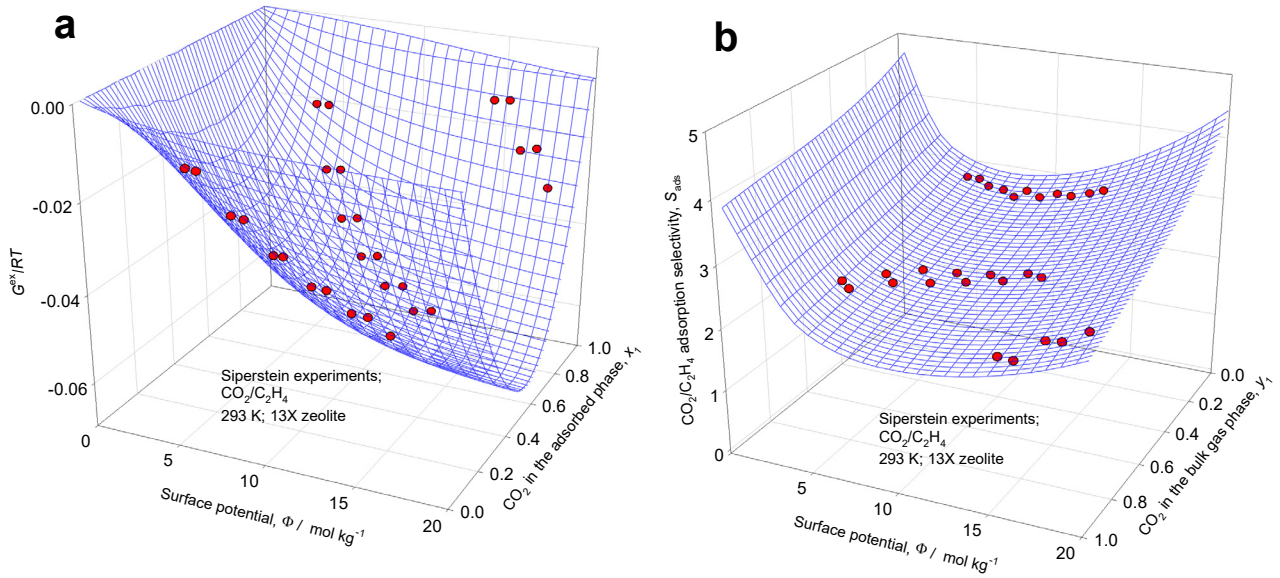

Figure S126. 3D plots of experimental data of Siperstein and Myers[43] on (a) excess Gibbs free energy $G^{ex}/RT = x_1 \ln(\gamma_1) + x_2 \ln(\gamma_2)$, and (b) adsorption selectivity for adsorption of CO_2/C_2H_4 mixtures at 293 K in NaX (=13X) zeolite. The 3D mesh is constructed using the Wilson parameters provided in Table S22.

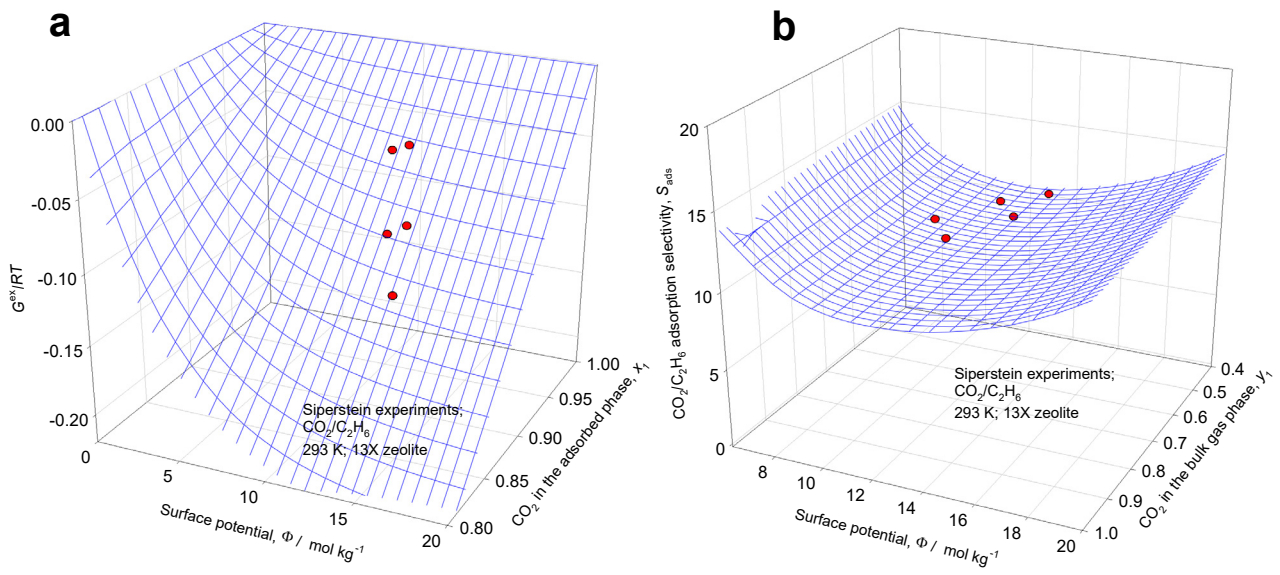

Figure S127. 3D plots of experimental data of Siperstein and Myers[43] on a) excess Gibbs free energy $G^{ex}/RT = x_1 \ln(\gamma_1) + x_2 \ln(\gamma_2)$, and (b) adsorption selectivity adsorption of CO_2/C_2H_6 mixtures at 293 K in NaX (=13X) zeolite. The 3D mesh is constructed using the Wilson parameters provided in Table S22.

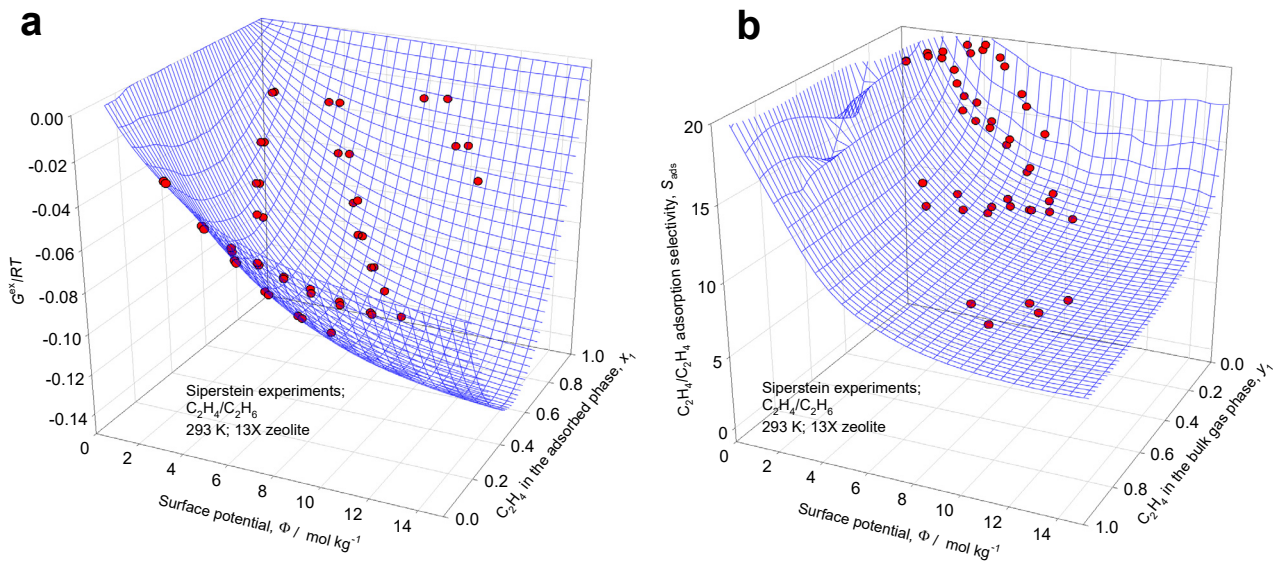

Figure S128. 3D plots of experimental data of Siperstein and Myers[43] on (a) excess Gibbs free energy $G^{ex}/RT = x_1 \ln(\gamma_1) + x_2 \ln(\gamma_2)$, and (b) adsorption selectivity for adsorption of C_2H_4/C_2H_6 mixtures at 293 K in NaX (=13X) zeolite. The 3D mesh is constructed using the Wilson parameters provided in Table S22.

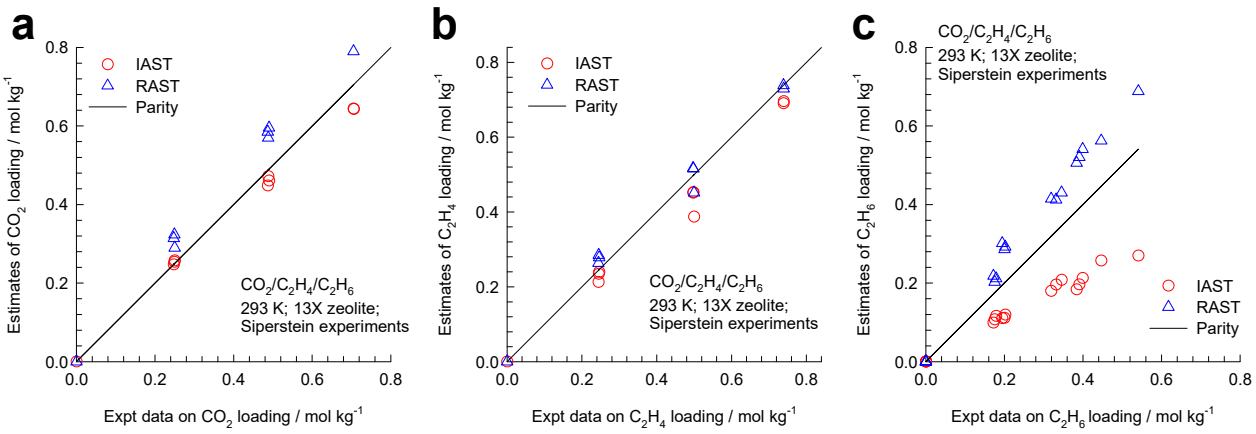

Figure S129. Experimental data of Siperstein and Myers[43] on the component loadings for CO_2(1)/C_2H_4(2)/C_2H_6(3) mixture adsorption in 13X (= NaX) zeolite at 293 K. The parity plots compare the experimental data with IAST and RAST estimates. The unary isotherm fits and Wilson parameters are provided in Table S22.

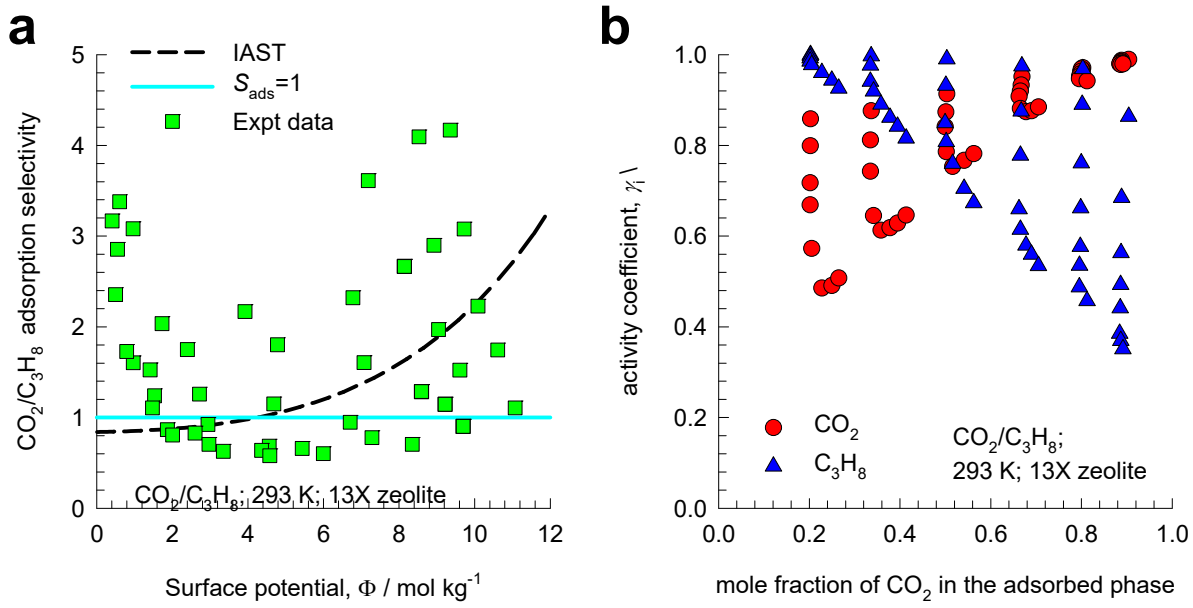

Figure S130. Experimental data of Costa et al.[63] and Calleja et al.[58] for adsorption of CO_2/C_3H_8 mixtures at 293 K in NaX (=13X) zeolite. (a) The adsorption selectivity S_{ads} for $CO_2(1)/C_3H_8(2)$ mixture adsorption in NaX zeolite,s plotted as a function of the surface potential Φ. (b) Plot of the activity coefficients in the adsorbed phase as function of the mole fraction of CO_2 in the adsorbed phase, x_1. The unary isotherm fit parameters, along with the Wilson parameters, are specified in Table S23.

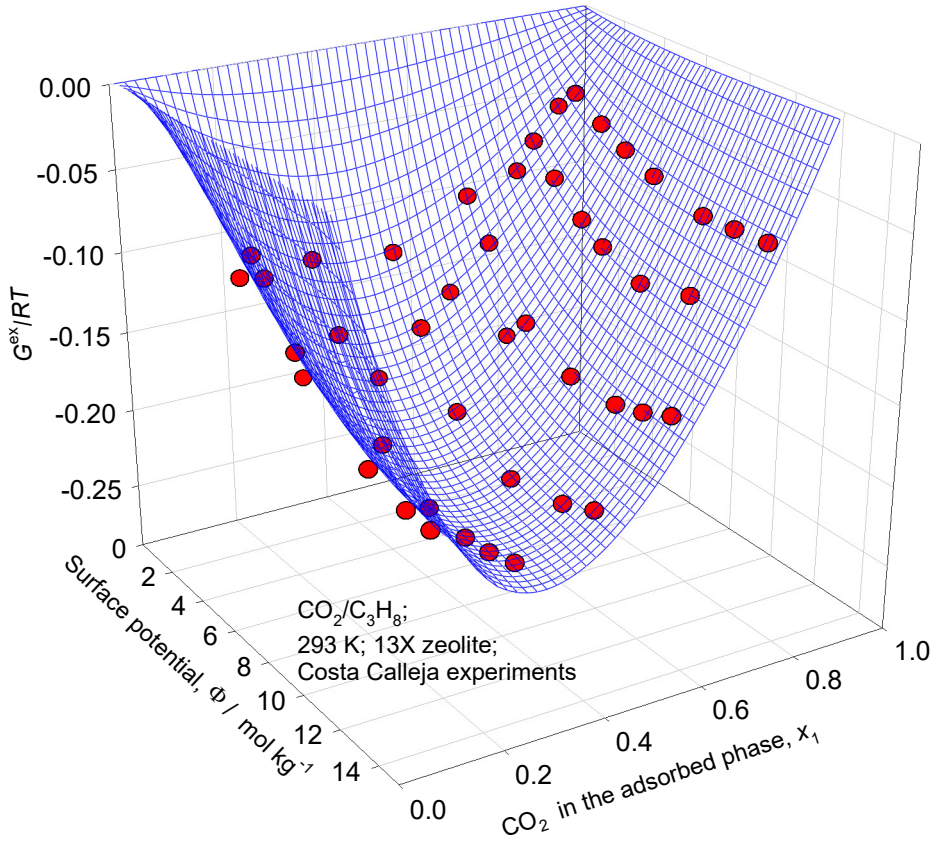

Figure S131. 3D plots of experimental data of Costa et al.[63] and Calleja et al.[58] on excess Gibbs free energy $G^{ex}/RT = x_1 \ln(\gamma_1) + x_2 \ln(\gamma_2)$ for adsorption of CO_2/C_3H_8 mixtures at 293 K in NaX (=13 X) zeolite. The 3D mesh is constructed using the Wilson parameters provided in Table S23.

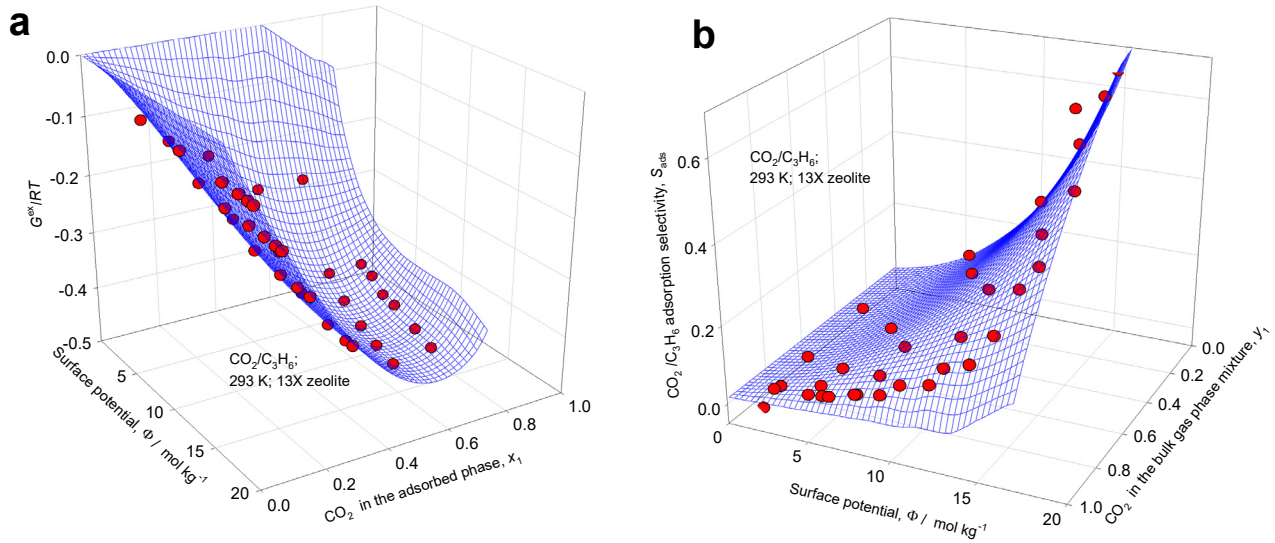

Figure S132. 3D plots of experimental data of Costa et al.[63] and Calleja et al.[58] on (a) excess Gibbs free energy $G^{ex}/RT = x_1 \ln(\gamma_1) + x_2 \ln(\gamma_2)$ and (b) $CO_2(1)/C_3H_6(2)$ adsorption selectivity for $CO_2(1)/C_3H_6(2)$ mixture adsorption in 13X zeolite at 293 K. The 3D mesh is constructed using the Wilson parameters provided in Table S23.

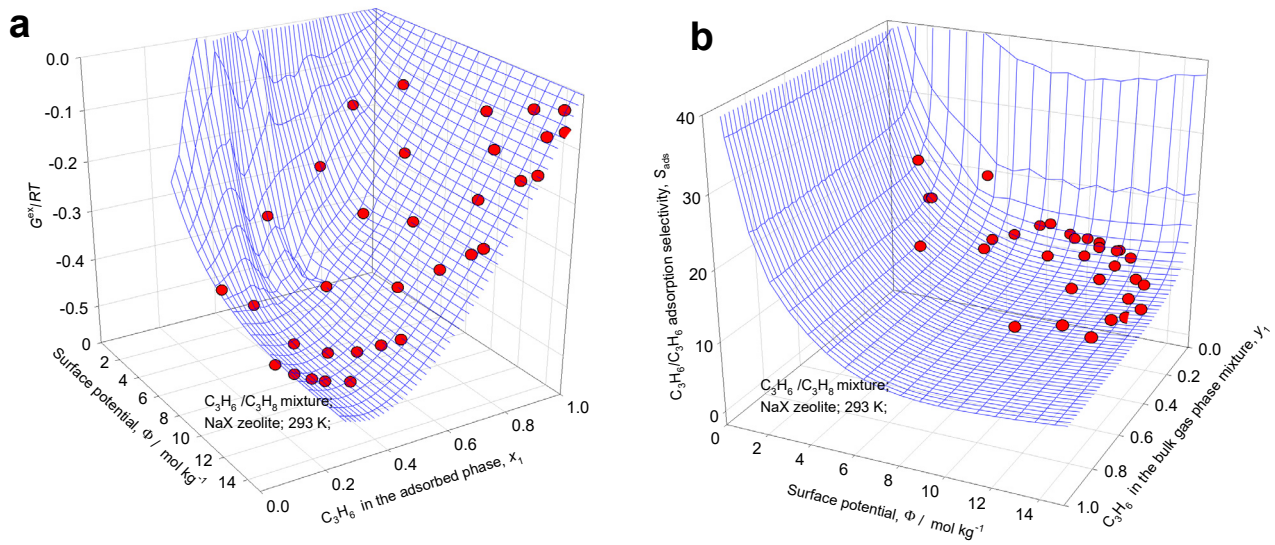

Figure S133. 3D plots of experimental data of Costa et al.[63] and Calleja et al.[58] on (a) excess Gibbs free energy $G^{ex}/RT = x_1 \ln(\gamma_1) + x_2 \ln(\gamma_2)$ and (b) $C_3H_6(1)/C_3H_8(2)$ adsorption selectivity for $C_3H_6(1)/C_3H_8(2)$ mixture adsorption in 13X zeolite at 293 K. The 3D mesh is constructed using the Wilson parameters provided in Table S23.

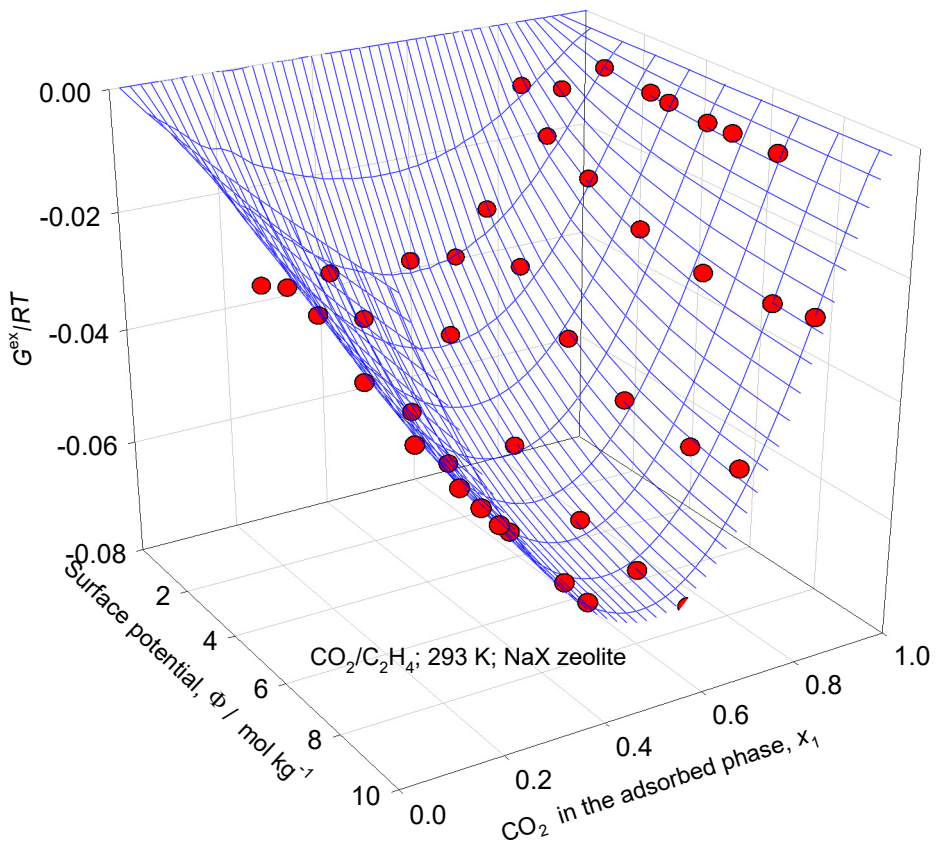

Figure S134. 3D plots of experimental data of Costa et al.[63] and Calleja et al.[58] on excess Gibbs free energy $G^{ex}/RT = x_1 \ln(\gamma_1) + x_2 \ln(\gamma_2)$ for adsorption of CO_2/C_2H_4 mixtures at 293 K in NaX (=13 X) zeolite. The 3D mesh is constructed using the Wilson parameters provided in Table S23.

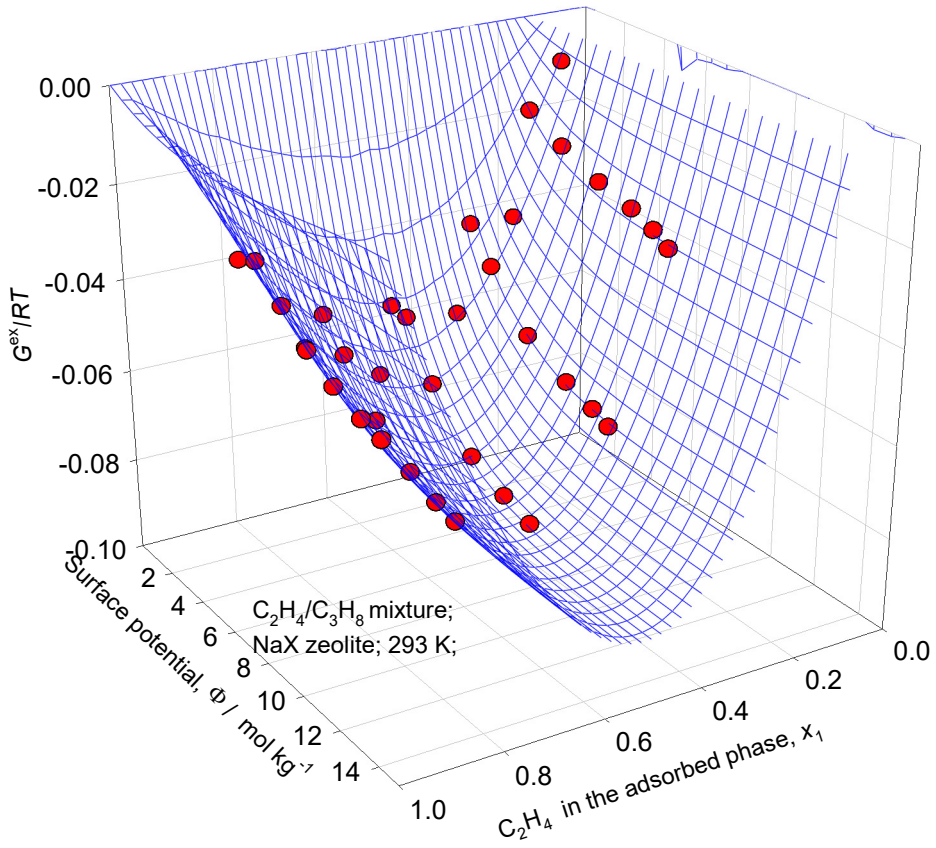

Figure S135. 3D plots of experimental data of Costa et al.[63] and Calleja et al.[58] on excess Gibbs free energy $G^{ex}/RT = x_1 \ln(\gamma_1) + x_2 \ln(\gamma_2)$ for adsorption of C2H4(1)/C3H8(2) mixtures at 293 K in NaX (=13 X) zeolite. The 3D mesh is constructed using the Wilson parameters provided in Table S23.

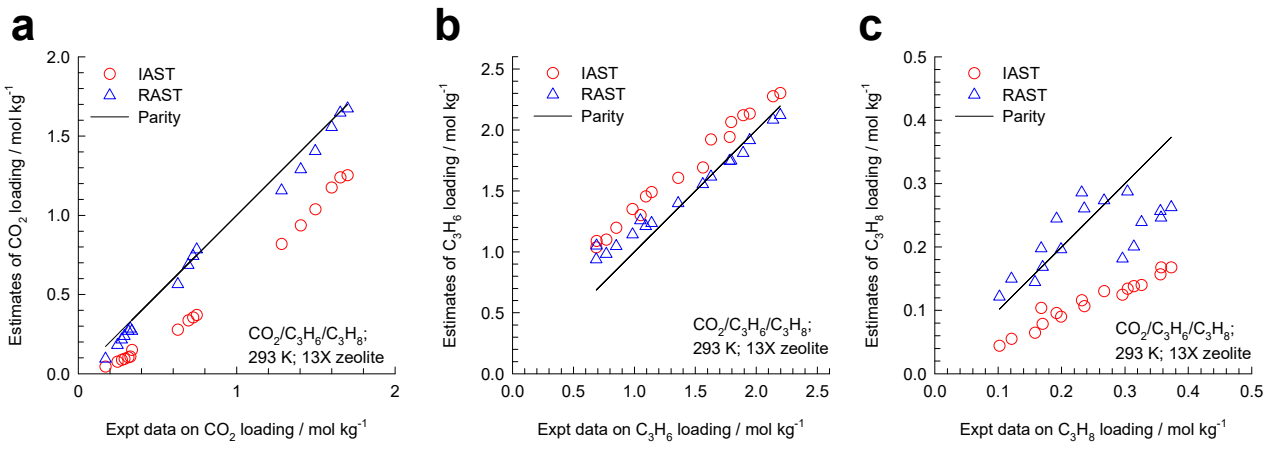

Figure S136. Experimental data of Calleja et al.[58] on the component loadings for CO_2(1)/C_3H_6(2)/C_3H_8(3) mixture adsorption in 13X zeolite at 293 K. The parity plots compare the experimental data with IAST and RAST estimates. The unary isotherm fits and Wilson parameters are provided in Table S23.

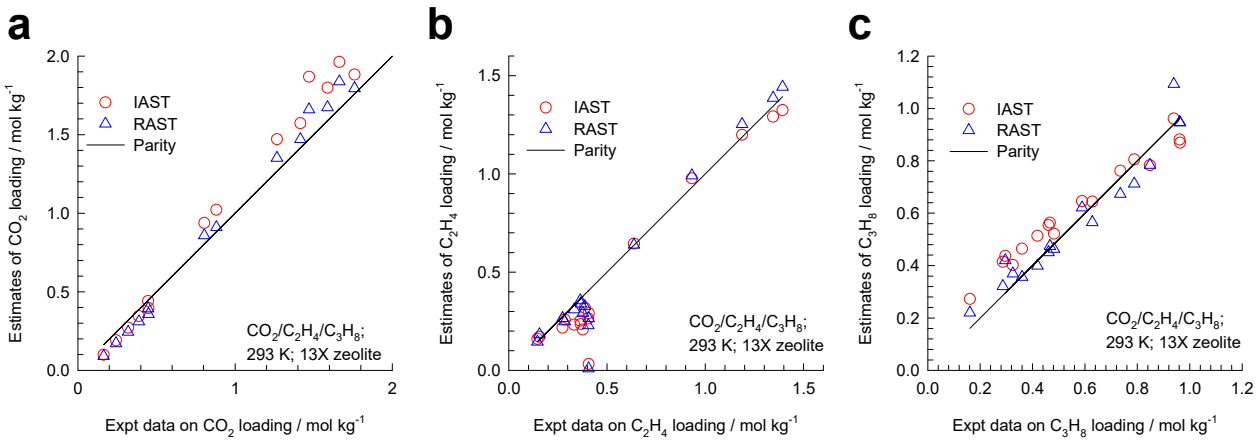

Figure S137. Experimental data of Calleja et al.[58] on the component loadings for $CO_2(1)/C_2H_4(2)/C_3H_8(3)$ mixture adsorption in 13X zeolite at 293 K. The parity plots compare the experimental data with IAST and RAST estimates. The unary isotherm fits and Wilson parameters are provided in Table S23.

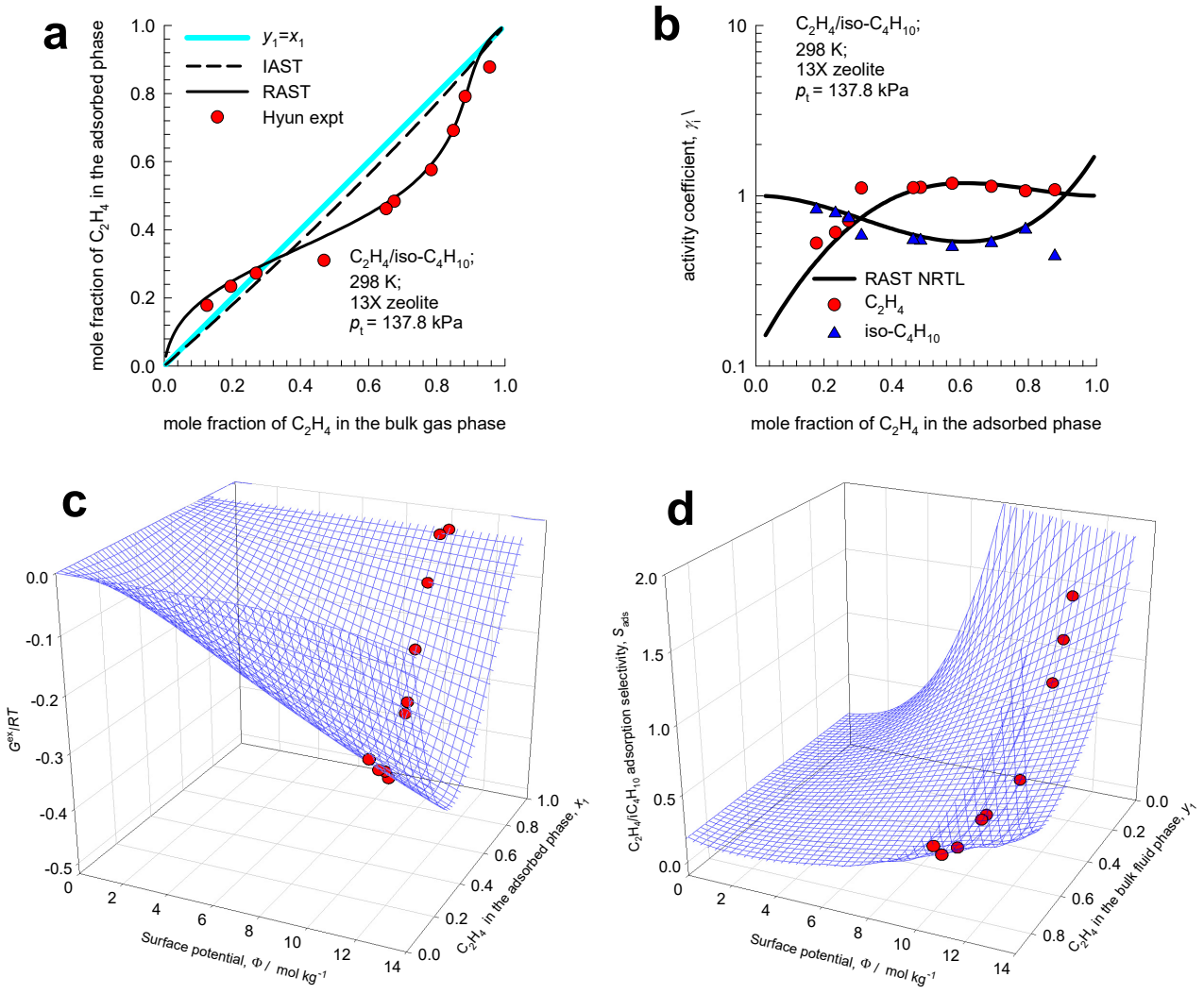

Figure S138. Experimental data of Hyun and Danner[78] for adsorption of C_2H_4/iso-C_4H_{10} mixtures at 298 K and 137.8 kPa in 13X zeolite, as reported in Table III of their paper. (b) Activity coefficients of C_2H_4, and iso-C_4H_{10} plotted as a function of the adsorbed phase mole fraction of C_2H_4. (c, d) 3D plots of the excess Gibbs free energy G^{ex}/RT and the C_2H_4/iso-C_4H_{10} adsorption selectivity. The unary isotherm fit parameters, along with the NRTL parameters, are specified in Table S24.

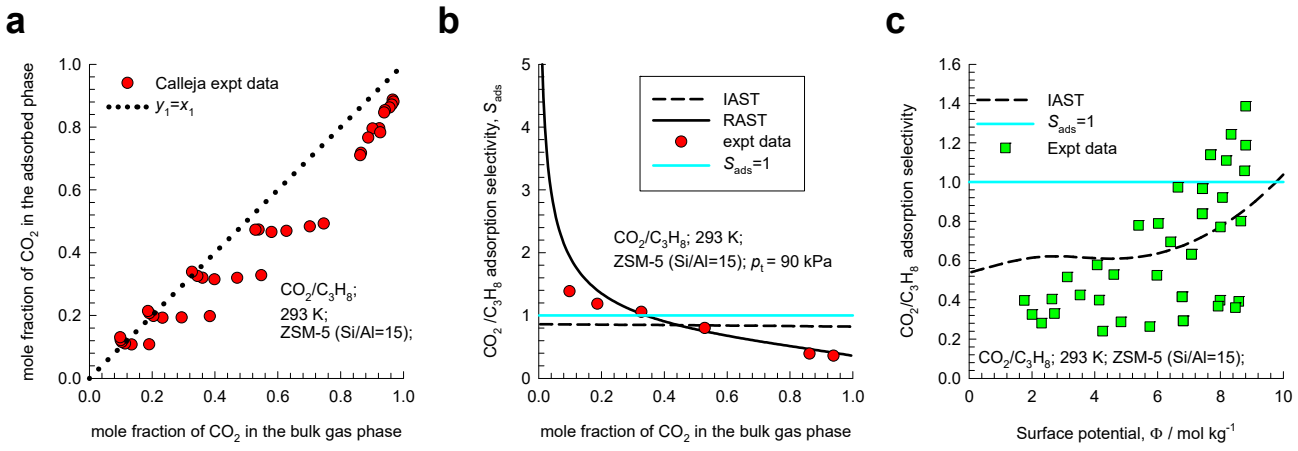

Figure S139. Experimental data of Calleja et al.[79] for adsorption of CO_2/C_3H_8 mixtures at 293 K in ZSM-5 (with MFI topology) zeolite with Si/Al ratio = 15, as reported in Table 5 of their paper. (a) Plot of the experimental data on mole fraction of CO_2 in the bulk gas phase, y_1, versus the mole fraction of CO_2 in the adsorbed phase, x_1. (b) The adsorption selectivity S_{ads} for $CO_2(1)/C_3H_8(2)$ mixture adsorption as a function of the mole fraction of CO_2 in the bulk gas phase, y_1. In this graph only data at total pressure = 90 kPa are plotted. (c) The adsorption selectivity S_{ads} for $CO_2(1)/C_3H_8(2)$ mixture adsorption in ZSM-5 zeolite, plotted as a function of the surface potential Φ. The unary isotherm fits and Wilson parameters are specified in Table S25.

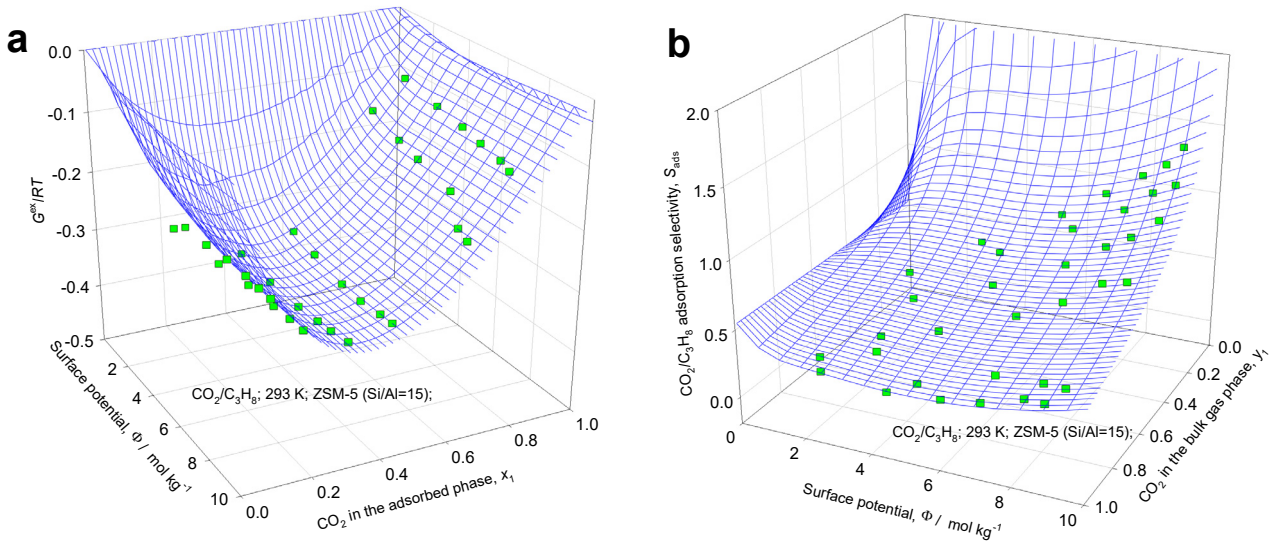

Figure S140. 3D plots of CBMC data on (a) excess Gibbs free energy $G^{ex}/RT = x_1 \ln(\gamma_1) + x_2 \ln(\gamma_2)$ and (b) $CO_2(1)/C_3H_8(2)$ adsorption selectivity for $CO_2(1)/C_3H_8(2)$ mixture adsorption in ZSM-5 zeolite at 293 K. The 3D mesh is constructed using the Wilson parameters provided in Table S25.

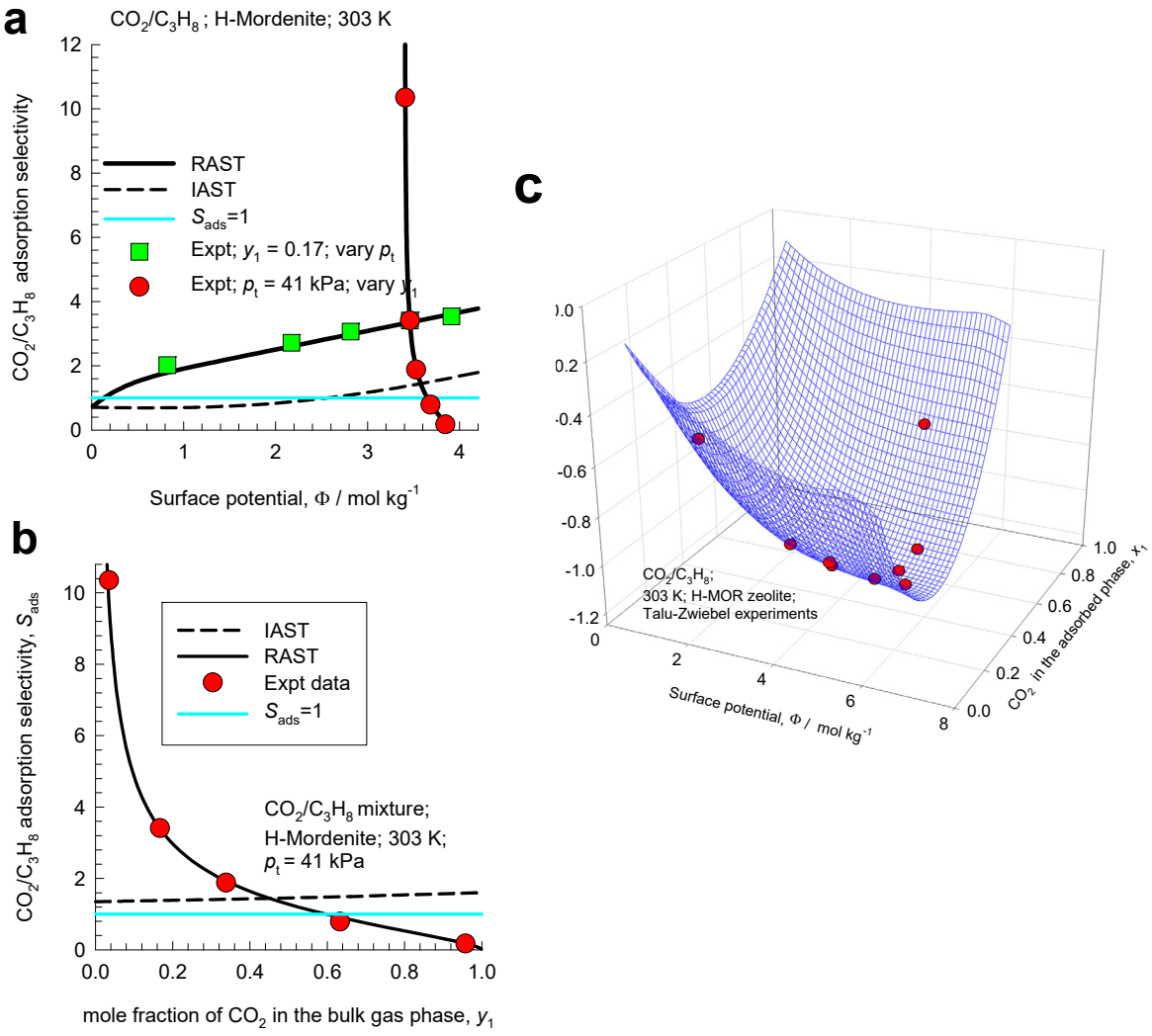

Figure S141. Experimental data of Talu and Zwiebel[55] for adsorption of CO_2/C_3H_8 mixtures at 303 K in H-MOR, as reported in Table 5 of their paper. (a) The data sets on the adsorption selectivity S_{ads} plotted in Figure S141a,b for $CO_2(1)/C_3H_8(2)$ mixture adsorption in H-MOR is plotted as a function of the the surface potential Φ. (b) The adsorption selectivity S_{ads} for $CO_2(1)/C_3H_8(2)$ mixture adsorption as a function of the mole fraction of CO_2 in the bulk gas phase, y_1; the total gas phase pressure $p_t = p_1 + p_2 = 41$ kPa. (c) 3D plots of experimental data on excess Gibbs free energy $G^{ex}/RT = x_1 \ln(\gamma_1) + x_2 \ln(\gamma_2)$. The 3D mesh is constructed using the Wilson parameters provided in Table S26.

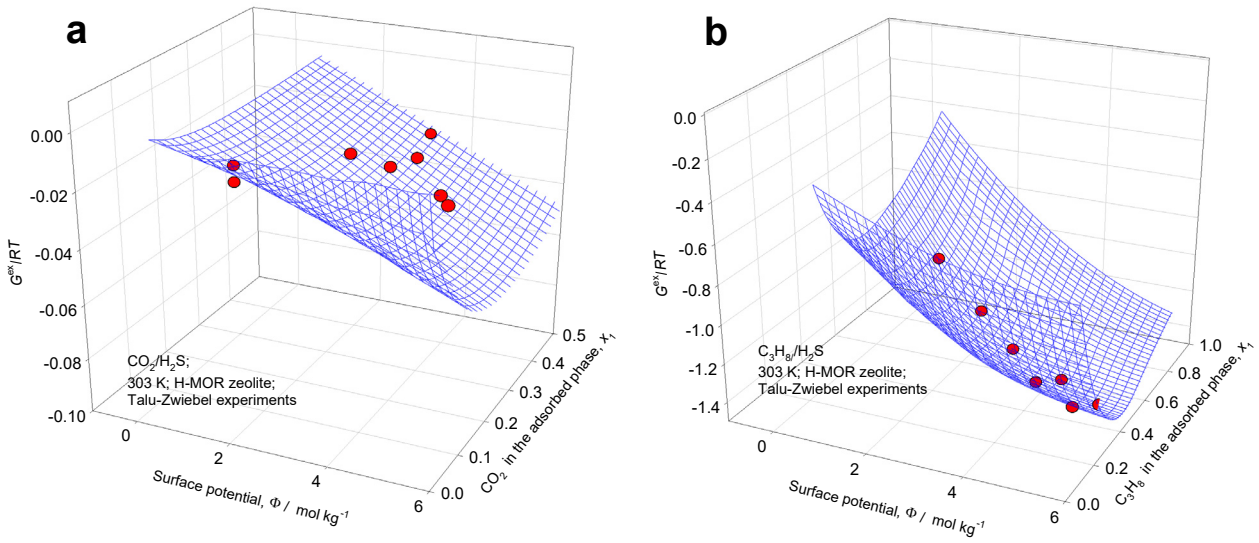

Figure S142. Experimental data of Talu and Zwiebel[55] for adsorption of (a) CO_2/H_2S, and (b) C_3H_8/H_2S mixtures at 303 K in H-MOR. 3D plots of experimental data on excess Gibbs free energy $G^{ex}/RT = x_1 \ln(\gamma_1) + x_2 \ln(\gamma_2)$, plotted as a function of the surface potential Φ and mole fraction in the adsorbed phase mixture. The 3D mesh is constructed using the Wilson parameters provided in Table S26.

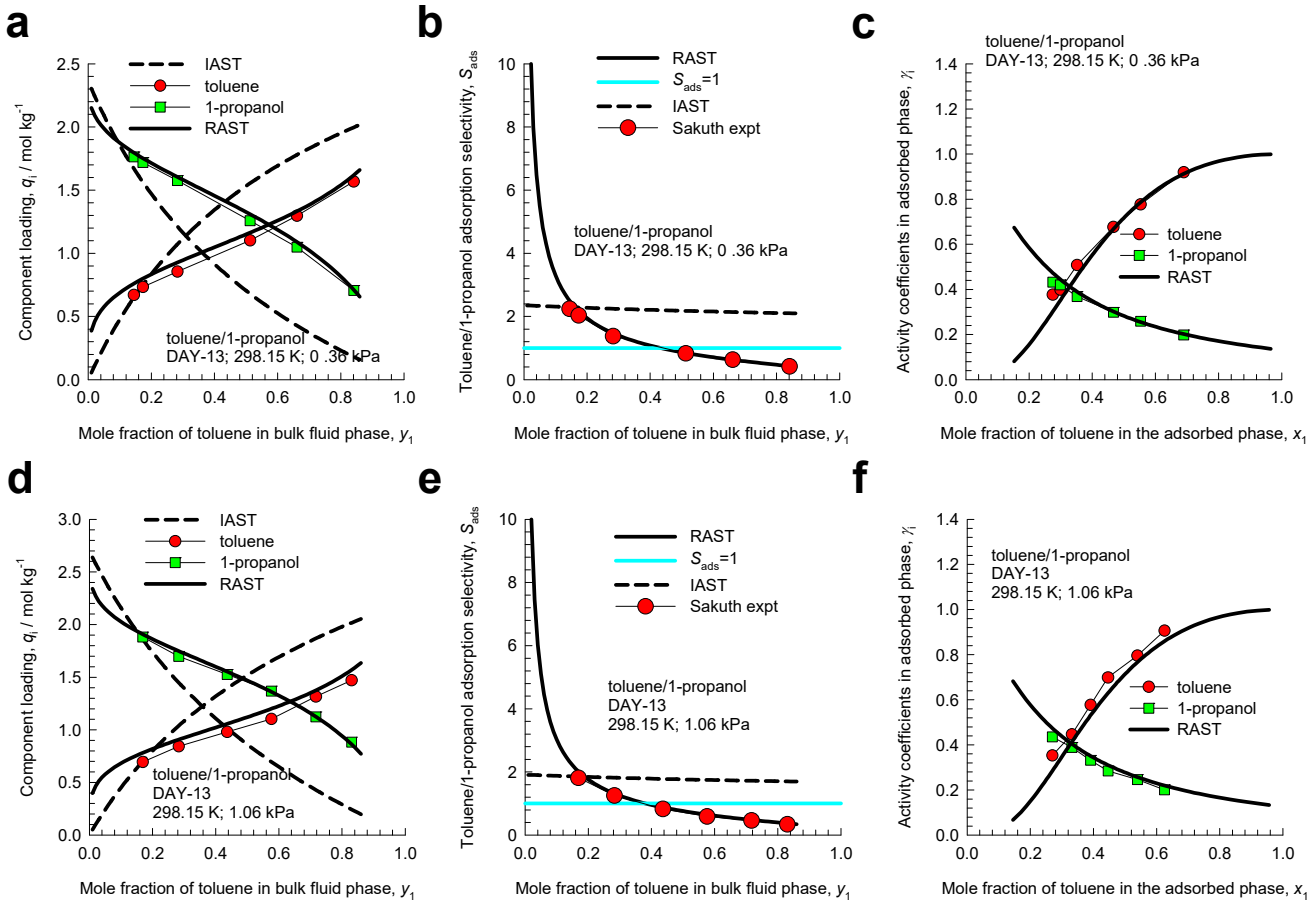

Figure S143. Experimental data of Sakuth et al.[80] for component loadings, q_i, selectivity S_{ads}, and activity coefficients, γ_i, for toluene/1-propanol mixture adsorption in DAY-13 (dealuminated Y zeolite) at T = 298.15 K and total pressure (a, b, c) p_t = 0.36 kPa, and (d, e, f) p_t = 1.06 kPa. Also shown in (a, b, c) are IAST (dashed lines) and RAST calculations (continuous solid lines) of q_i, S_{ads}, and γ_i, The unary isotherm fit parameters, along with the Wilson parameters, are specified in Table S28.

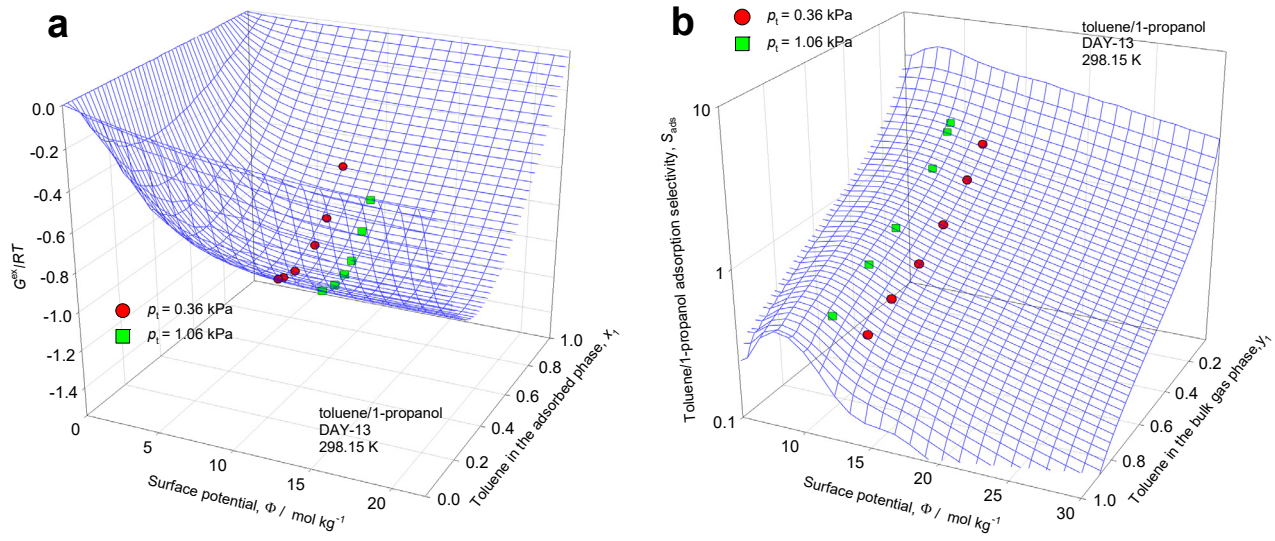

Figure S144. 3D plots of experimental data of Sakuth et al.[80] on (a) excess Gibbs free energy $G^{ex}/RT = x_1 \ln(\gamma_1) + x_2 \ln(\gamma_2)$, and (b) adsorption selectivity S_{ads} for toluene/1-propanol mixture adsorption in DAY-13 (dealuminated Y zeolite) at T = 298.15 K and total pressure p_t = 0.36 kPa, and p_t = 1.06 kPa. The 3D mesh is constructed using the Wilson parameters provided in Table S28.

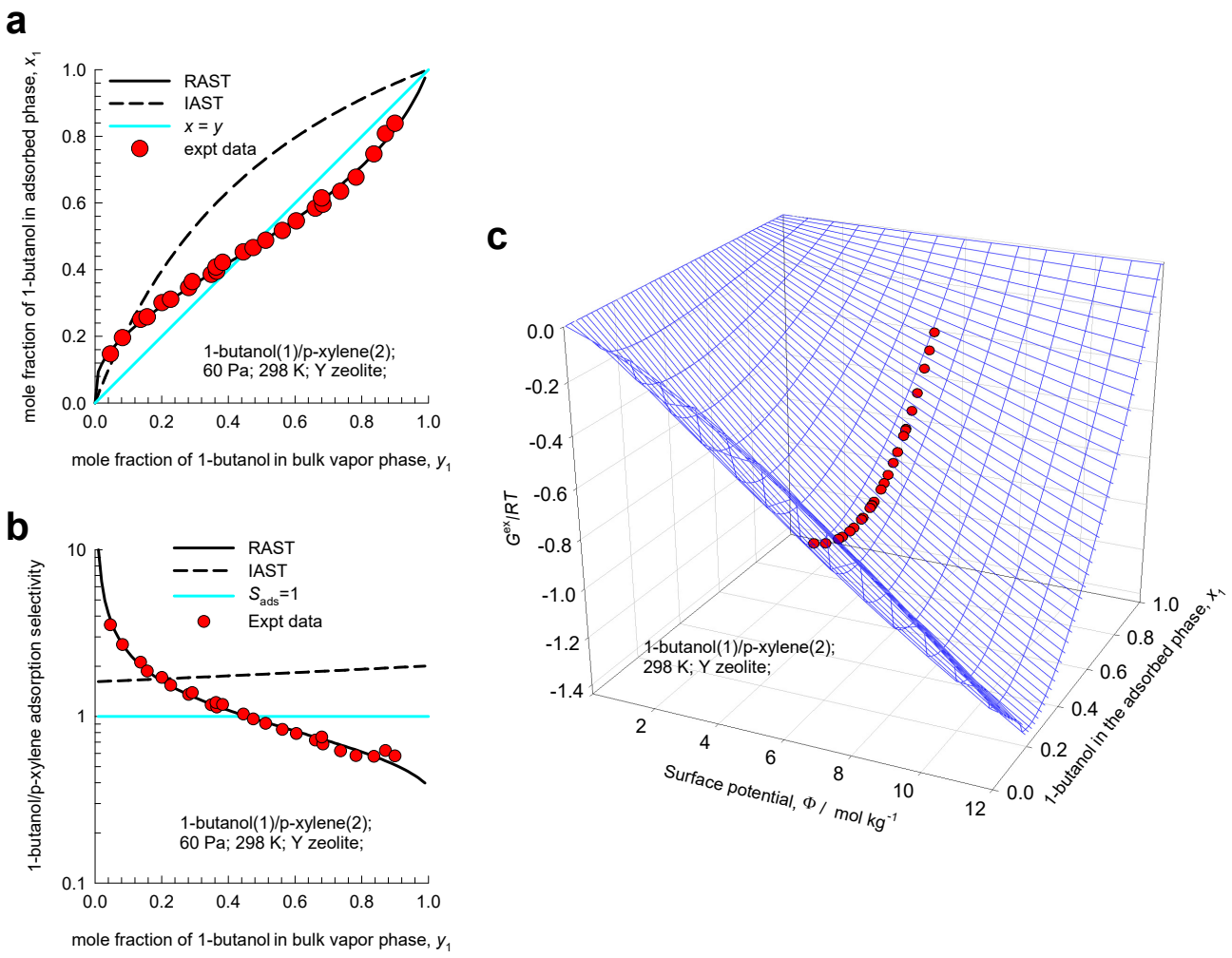

Figure S145. Experimental data of Takeuchi et al.[82] for adsorption of 1-butanol(1)/p-xylene(2) mixtures in high silica Y zeolite, obtained at 298 K and total pressure of 60 Pa. (a) The adsorbed phase mole fraction of 1-butanol(1), x_1, is plotted as function of mole fraction of 1-butanol(1) in the bulk vapor phase mixture, y_1. (b) The adsorption selectivity S_{ads} plotted as function as function of mole fraction of 1-butanol(1) in the bulk vapor mixture, y_1. (c) 3D plot of experimental data on excess Gibbs free energy $G^{ex}/RT = x_1 \ln(\gamma_1) + x_2 \ln(\gamma_2)$, The 3D mesh is constructed using the Wilson parameters provided in Table S29.

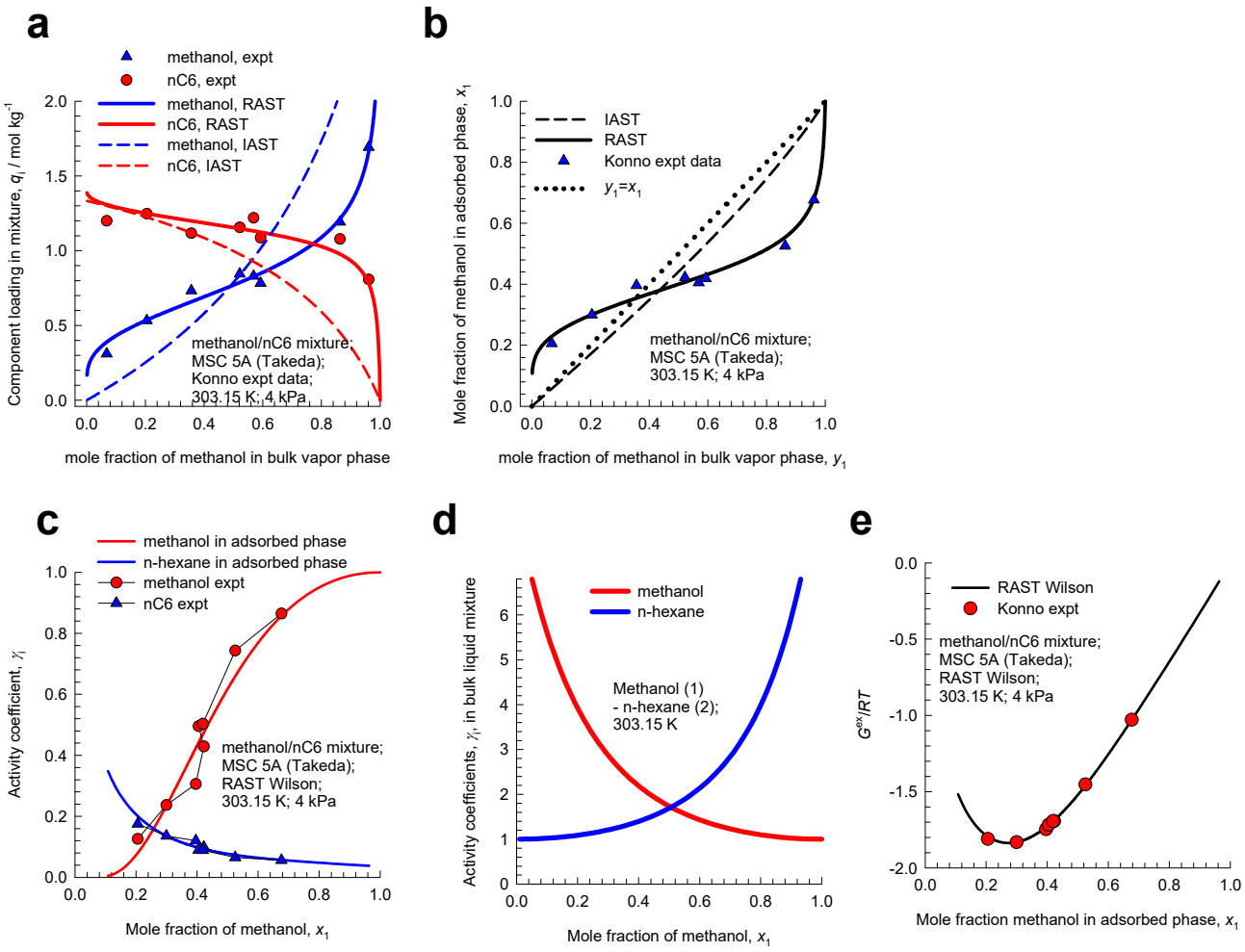

Figure S146. (a) Experimental data of Konno et al.[83] for component loadings for methanol and n-hexane (nC6) in MSC-5A (Takeda) at 4 kPa and 303.15 K as a function of the mole fraction of methanol in the bulk vapor phase. (b) Plot of the adsorbed phase mole fraction of methanol, x_1, vs the mole fraction of methanol in the bulk vapor phase, y_1. The dashed line represents IAST estimations; the continuous solid line are the RAST calculations. (c) Activity coefficients in the adsorbed phase. The unary Langmuir isotherm fits are provided in Table S1 of Bartholdy et al.[84] The "fitted" Wilson parameters are Λ_{12} = 1.2; Λ_{21}= 68; C = 0.15 kg mol^{-1}. (e) Activity coefficient in bulk liquid mixtures, calculated using the NRTL parameters of Clark and Rowley.[86] (e) Excess Gibbs free energy $G^{ex}/RT = x_1 \ln(\gamma_1) + x_2 \ln(\gamma_2)$ vs x_1.

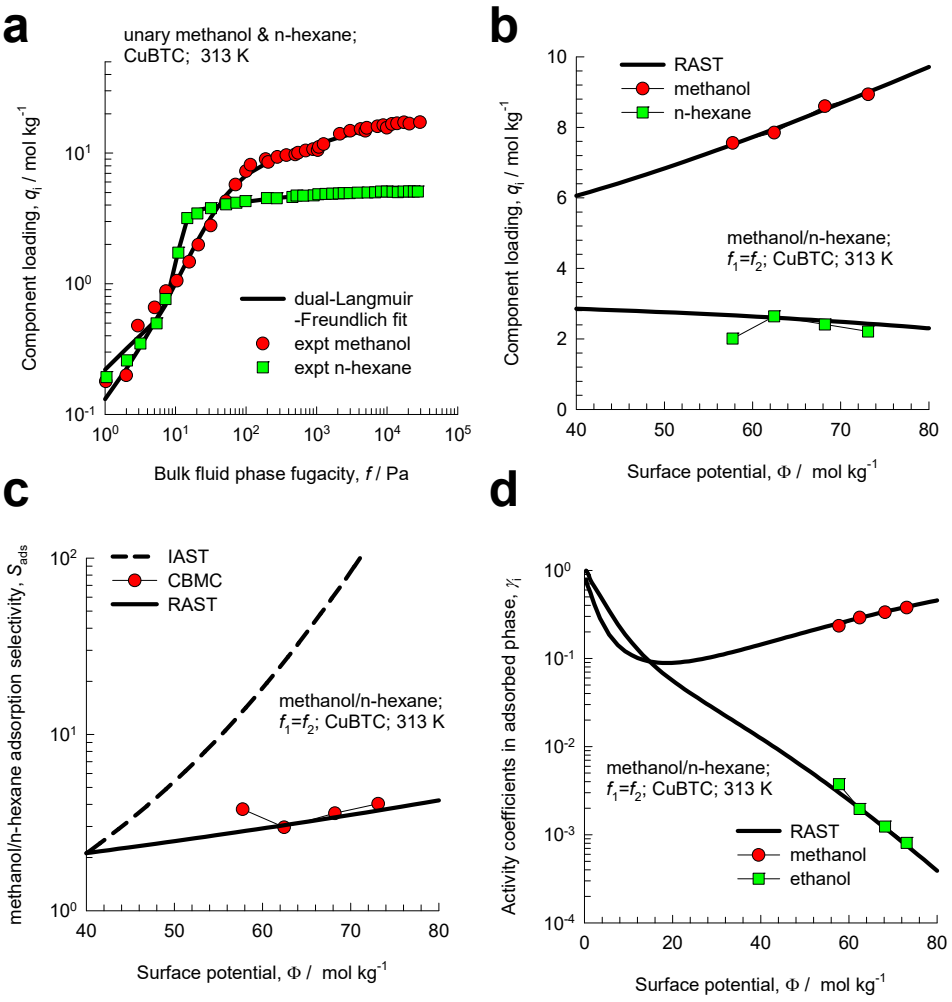

Figure S147. (a) Unary isotherm data of van Assche et al.[85] for adsorption of methanol, and n-hexane at 313 K in CuBTC; the dual-site Langmuir-Freundlich parameters are provided in Table S30. (b) Experimental data of van Assche et al.[85] for component loadings for equimolar $\left(f_1 = f_2\right)$ methanol/n-hexane mixture adsorption in CuBTC as a function of the surface potential, Φ. (c) Comparison of the experimental data on the methanol/n-hexane adsorption selectivity, as a function of Φ, with IAST and RAST calculations. (d) Experimentally determined activity coefficients compared with RAST model calculations.

15 CBMC Simulations vs Experimental Data

15.1 Unary isotherms

Published experimental data for unary isotherms for linear, mono-branched, and di-branched alkanes in a number of zeolite host materials are in good agreement with the CBMC simulation data on unary isotherms.[20, 87-92]

Experimental data on the unary isotherms for CO_2 in a number of all-silica and cation-exchanged zeolites are used to set up the force fields.[22, 26, 93]

The CBMC simulations of unary CO_2, CH_4, N_2 and H_2 isotherms are in good agreement with experimental isotherm data for a variety of host zeolites.[6, 8, 9, 12, 22, 26, 60, 64, 65, 68, 93]

15.2 Mixture adsorption

The breakthrough experimental data of van Zandvoort et al.[51, 52] demonstrate the phenomenon of selectivity reversals for $CO_2(1)/C_2H_4(2)$ mixture separation using in LTA-5A zeolite (see Figures . The selectivity reversal phenomena can be rationalized on the basis of the CBMC simulations for cation-exchanged zeolites.[15, 44, 45, 47]

Water/alcohol pervaporation membranes may be constructed as thin films of zeolites (e.g. CHA [94-96], DDR [30, 97], LTA [98-101], MFI [102, 103], FAU [104]) or zeolitic imidazolate frameworks (ZIFs) [105, 106]. In published works in which the composition of the water/alcohol mixture in the upstream compartment is varied, the permeation selectivity S_{perm} becomes increasingly in favor of water as the alcohol content in the feed mixture increases.[99, 101, 107, 108] Experimental data on adsorption of water/alcohol mixtures clearly demonstrate the failure of the IAST for variety of host materials/ [48, 99, 101, 107, 108] The influences of thermodynamic non-idealites on membrane pervaporation are rationalized and quantified by a combination of CBMC and MD (= Molecular Dynamics) simulations.[15, 27, 29, 46, 48, 109, 110]

The occurrence of hydrogen bonding in water/alcohol mixtures causes mutual slowing-down for diffusion that is observed in several experimental studies.[27-29, 48, 109, 111]

Membrane technologies find applications for separation a variety of gaseous mixtures, such as CO_2/CH_4, CO_2/N_2, CO_2/H_2, and CH_4/N_2.[112-117] The perm-selective membrane layers often consist of crystalline microporous materials such as zeolites (e.g. CHA, DDR, MFI, LTA, and FAU) [118-129] metal-organic frameworks (MOFs) [130], or zeolitic imidazolate frameworks (ZIFs). [131-133] The experimental data on component permeances can be rationalized, often quantitatively by a combination of CBMC simulations of adsorption (unary components, binary and ternary mixtures), along with MD simulations of guest diffusivities.[3, 5, 7, 8, 11-13, 16, 54, 60, 111, 117, 131-144]

The adsorption and intra-crystalline diffusion of n-butane (nC4), iso-butane (iC4), 2-methylbutane (2MB), and 2,2-dimethylpropane (neoP) in CuBTC ($Cu_3(BTC)_2$ where BTC = benzene-1,3,5-tricarboxylate) has been investigated by Chmelik et al.[145] using infrared microscopy (IRM). The experimental trends are in agreement with CBMC and MD data.[145]

The adsorption and intra-crystalline diffusion of iso-C_4H_{10} in MFI zeolite have been investigated by Chmelik et al.[146] using infrared microscopy (IRM). The experimental data agree well with CBMC and KMC (= Kinetic Monte Carlo) simulations.[146]

The intra-crystalline diffusion of n-C_4H_{10}/iso-C_4H_{10} mixtures in MFI zeolite have been investigated using infrared microscopy (IRM) and PFG-NMR.[147, 148] The experimental data can be rationalized using a combination of CBMC, KMC, and MD simulations.[47, 148, 149]

The experimental data of Herm et al.[150, 151] on unary isotherms of CO_2, CH_4, N_2, and H_2 in Mg-MOF-74 are in reasonable agreement with CBMC data.[11, 142, 150, 151] The CBMC data for adsorption of binary of mixtures were used to establish the suitability of the use of the IAST to quantify mixture adsorption equilibrium. [142, 150, 151] However, thermodynamic non-ideality effects are in play at high pore occupancies; for which CBMC data for adsorption of binary of CO_2/CH_4, and CO_2/N_2 mixtures exhibited deviations from the IAST estimates,[15] Thermodynamic non-idealities stem from inhomogeneous distribution of guest adsorbates within the pore landscape.

The experimental data of Herm et al.[152] on unary isotherms of hexane isomers (nC6, 2MP, 3MP, 22DMB, 23DMB) in $Fe_2(BDP)_3$ are in good agreement with the CBMC simulation data.[4, 73, 136, 152, 153] The CBMC data for adsorption of 5-component hexane isomers mixtures were found to be in reasonably good agreement with the IAST estimates.[4, 73, 152]

Titze et al.[154] have investigated adsorption and diffusion of hexane isomers (unary nC6, 2MP, and binary nC6/2MP) in MFI zeolite using IRM. The adsorption data for unary isotherms in good agreement with the CBMC data.[11, 12, 154, 155] The adsorption data for binary mixture isotherms show slight deviations from the IAST estimates.[11, 12, 154, 155] The CBMC data for adsorption of 5-component hexane isomers (nC6, 2MP, 3MP, 22DMB, 23DMB) mixtures were found to be in reasonable agreement with the IAST estimates.[4, 73, 89]

Configurational-Bias Monte Carlo (CBMC) simulations, using the methodologies as detailed in earlier publications,[3, 5, 9, 11-14] were carried out to determine the adsorption isotherms for unary C_2H_2, unary C_2H_4, and 1/99 C_2H_2/C_2H_4 mixtures in ZUL-100 and ZUL-200 at 298 K. The CBMC unary isotherms are in good agreement with the experimental isotherms reported by Shen et al.[156] The CBMC data for 1/99 mixtures is in good agreement with IAST estimates.[15, 156]

The preferential perching of CO_2 in the window regions of CHA, DDR, LTA, ERI, and AFX zeolites, as demonstrated in CBMC and MD simulations[60, 157] allows the rationalization of experimental data of unary and mixture permeation across zeolite membranes.[3, 5, 7, 8, 60, 110, 117, 143, 144, 158]

The preferential location of CO_2 in the side-pockets of MOR zeolite (see Figures S106 – S112) and inhomogeneous of guest adsorbates for mixture adsorption rationalizes the deviations from thermodynamic idealities and selectivity reversals as witnessed in the experiments of Talu and Zwiebel[55] for CO_2/C_3H_8 mixtures in H-MOR. The experimental data presented in Figure S141b is in remarkable quantitative agreement with the corresponding CBMC simulations presented in Figure S111e. The influences of thermodynamic non-idealities are precisely analogous.

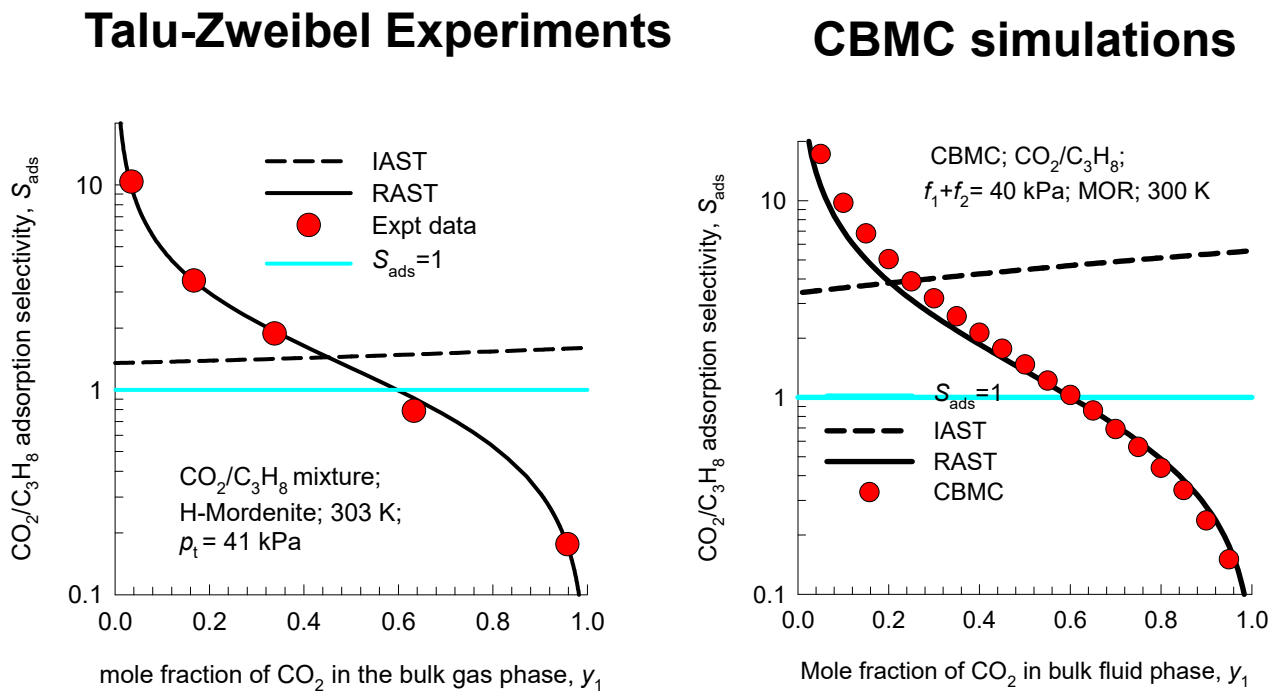

The experimental data of Moreton et al.[159] for CO_2/H_2O adsorption in CALF-20 show strong thermodynamic non-idealities; their experiments at 298 K are in quantitative agreement with the CBMC simulations.[17, 71]

The breakthrough experimental data of Nguyen et al.[160] for CO_2/H_2O adsorption in CALF-20 demonstrate the failure of the IAST. CBMC simulations[17, 71] provide elucidation and quantification of thermodynamic non-idealities.

16 Nomenclature

Latin alphabet

A	surface area per kg of framework, m^2 kg^{-1}
A_{12}, A_{21}	Margules parameters, dimensionless
b	Langmuir-Freundlich constant, $Pa^{-\nu}$
C	constant used in eq (S39), kg mol^{-1}
f_i	partial fugacity of species *i*, Pa
f_t	total fugacity of bulk fluid mixture, Pa
G^{ex}	excess Gibbs free energy, J mol^{-1}
G_{ij}	NRTL parameters, dimensionless
n	number of species in the mixture, dimensionless
p_i	partial pressure of species *i*, Pa
p_t	total system pressure, Pa
P_i^0	sorption pressure, Pa
q_i	molar loading of species *i*, mol kg^{-1}
q_t	total molar loading of mixture, mol kg^{-1}
$q_{i,sat}$	molar loading of species *i* at saturation, mol kg^{-1}
R	gas constant, 8.314 J mol^{-1} K^{-1}
S_{ads}	adsorption selectivity, dimensionless
T	absolute temperature, K
V_p	pore volume, m^3 kg^{-1}
x_i	mole fraction of species *i* in adsorbed phase, dimensionless
y_i	mole fraction of species *i* in bulk fluid mixture, dimensionless

Greek letters

α	NRTL parameters, dimensionless
γ_i	activity coefficient of component *i* in adsorbed phase, dimensionless
Λ_{ij}	Wilson parameters, dimensionless
μ_i	molar chemical potential, J mol^{-1}
θ	fractional pore occupancy, dimensionless
ν	Freundlich exponent, dimensionless
π	spreading pressure, N m^{-1}
ρ	framework density, kg m^{-3}
τ_{ij}	NRTL parameters, dimensionless
Φ	surface potential, mol kg^{-1}

Subscripts

i,j	components in mixture
t	referring to total mixture
sat	referring to saturation conditions

Superscripts

0	referring to pure component loading
ex	referring to excess parameter

17 References

(1) Baerlocher, C.; Meier, W. M.; Olson, D. H. *Atlas of Zeolite Framework Types*. 5th Edition, Elsevier: Amsterdam, 2002; pp

(2) Baerlocher, C.; McCusker, L. B. Database of Zeolite Structures. http://www.iza-structure.org/databases/, International Zeolite Association, 10 January 2002.

(3) Krishna, R. Diffusion in Porous Crystalline Materials. *Chem. Soc. Rev.* **2012**, *41*, 3099-3118. https://doi.org/10.1039/C2CS15284C.

(4) Krishna, R. The Maxwell-Stefan Description of Mixture Diffusion in Nanoporous Crystalline Materials. *Microporous Mesoporous Mater.* **2014**, *185*, 30-50. https://doi.org/10.1016/j.micromeso.2013.10.026.

(5) Krishna, R. Describing the Diffusion of Guest Molecules inside Porous Structures. *J. Phys. Chem. C* **2009**, *113*, 19756-19781. https://doi.org/10.1021/jp906879d.

(6) Krishna, R.; van Baten, J. M. Investigating the Relative Influences of Molecular Dimensions and Binding Energies on Diffusivities of Guest Species Inside Nanoporous Crystalline Materials *J. Phys. Chem. C* **2012**, *116*, 23556-23568. https://doi.org/10.1021/jp308971w.

(7) Krishna, R.; van Baten, J. M. Investigating the Influence of Diffusional Coupling on Mixture Permeation across Porous Membranes *J. Membr. Sci.* **2013**, *430*, 113-128. https://doi.org/10.1016/j.memsci.2012.12.004.

(8) Krishna, R.; van Baten, J. M. Influence of Adsorption Thermodynamics on Guest Diffusivities in Nanoporous Crystalline Materials. *Phys. Chem. Chem. Phys.* **2013**, *15*, 7994-8016.

(9) Krishna, R.; van Baten, J. M. Insights into diffusion of gases in zeolites gained from molecular dynamics simulations. *Microporous Mesoporous Mater.* **2008**, *109*, 91-108.

(10) Krishna, R.; van Baten, J. M. Diffusion of alkane mixtures in MFI zeolite. *Microporous Mesoporous Mater.* **2008**, *107*, 296-298.

(11) Krishna, R.; van Baten, J. M. In silico screening of metal-organic frameworks in separation applications. *Phys. Chem. Chem. Phys.* **2011**, *13*, 10593-10616. https://doi.org/10.1039/C1CP20282K.

(12) Krishna, R.; van Baten, J. M. In Silico Screening of Zeolite Membranes for CO_2 Capture. *J. Membr. Sci.* **2010**, *360*, 323-333. https://doi.org/10.1016/j.memsci.2010.05.032.

(13) Krishna, R.; van Baten, J. M. Describing Mixture Diffusion in Microporous Materials under Conditions of Pore Saturation. *J. Phys. Chem. C* **2010**, *114*, 11557-11563.

(14) Krishna, R.; van Baten, J. M. Diffusion of alkane mixtures in zeolites. Validating the Maxwell-Stefan formulation using MD simulations. *J. Phys. Chem. B* **2005**, *109*, 6386-6396.

(15) Krishna, R.; Van Baten, J. M. How Reliable is the Ideal Adsorbed Solution Theory for Estimation of Mixture Separation Selectivities in Microporous Crystalline Adsorbents? *ACS Omega* **2021**, *6*, 15499–15513. https://doi.org/10.1021/acsomega.1c02136.

(16) Krishna, R.; van Baten, J. M. Using the Spreading Pressure to Inter-Relate the Characteristics of Unary, Binary and Ternary Mixture Permeation across Microporous Membranes. *J. Membr. Sci.* **2022**, *643*, 120049. https://doi.org/10.1016/j.memsci.2021.120049.

(17) Krishna, R.; Van Baten, J. M. Elucidating the Failure of the Ideal Adsorbed Solution Theory for CO_2/H_2O Mixture Adsorption in CALF-20. *Sep. Purif. Technol.* **2025**, *352*, 128269. https://doi.org/10.1016/j.seppur.2024.128269.

(18) Krishna, R.; van Baten, J. M.; Baur, R. Highlighting the Origins and Consequences of Thermodynamic Nonidealities in Mixture Separations using Zeolites and Metal-Organic Frameworks. *Microporous Mesoporous Mater.* **2018**, *267*, 274-292. http://dx.doi.org/10.1016/j.micromeso.2018.03.013.

(19) Ryckaert, J. P.; Bellemans, A. Molecular dynamics of liquid alkanes. *Faraday Discuss. Chem. Soc.* **1978**, *66*, 95-106.

(20) Dubbeldam, D.; Calero, S.; Vlugt, T. J. H.; Krishna, R.; Maesen, T. L. M.; Smit, B. United Atom Forcefield for Alkanes in Nanoporous Materials. *J. Phys. Chem. B* **2004**, *108*, 12301-12313.

(21) Harris, J. G.; Yung, K. H. Carbon Dioxide's Liquid-Vapor Coexistence Curve And Critical Properties as Predicted by a Simple Molecular Model. *J. Phys. Chem.* **1995**, *99*, 12021-12024.

(22) García-Sánchez, A.; Ania, C. O.; Parra, J. B.; Dubbeldam, D.; Vlugt, T. J. H.; Krishna, R.; Calero, S. Development of a Transferable Force Field for Carbon Dioxide Adsorption in Zeolites. *J. Phys. Chem. C* **2009**, *113*, 8814-8820. https://doi.org/10.1021/jp810871f.

(23) Murthy, C. S.; Singer, K.; Klein, M. L.; McDonald, I. R. Pairwise additive effective potentials for nitrogen. *Mol. Phys.* **1980**, *41*, 1387-1399.

(24) Makrodimitris, K.; Papadopoulos, G. K.; Theodorou, D. N. Prediction of permeation properties of CO_2 and N_2 through silicalite via molecular simulations. *J. Phys. Chem. B* **2001**, *105*, 777-788.

(25) Kumar, A. V. A.; Jobic, H.; Bhatia, S. K. Quantum effects on adsorption and diffusion of hydrogen and deuterium in microporous materials *J. Phys. Chem. B* **2006**, *110*, 16666-16671.

(26) García-Pérez, E.; Parra, J. B.; Ania, C. O.; García-Sánchez, A.; Van Baten, J. M.; Krishna, R.; Dubbeldam, D.; Calero, S. A computational study of CO_2, N_2 and CH_4 adsorption in zeolites. *Adsorption* **2007**, *13*, 469-476.

(27) Krishna, R.; van Baten, J. M. Hydrogen Bonding Effects in Adsorption of Water-alcohol Mixtures in Zeolites and the Consequences for the Characteristics of the Maxwell-Stefan Diffusivities. *Langmuir* **2010**, *26*, 10854-10867. https://doi.org/10.1021/la100737c.

(28) Krishna, R.; van Baten, J. M. Mutual slowing-down effects in mixture diffusion in zeolites. *J. Phys. Chem. C* **2010**, *114*, 13154-13156. https://doi.org/10.1021/jp105240c.

(29) Krishna, R.; van Baten, J. M. Highlighting Pitfalls in the Maxwell-Stefan Modeling of Water-Alcohol Mixture Permeation across Pervaporation Membranes. *J. Membr. Sci.* **2010**, *360*, 476-482. https://doi.org/10.1016/j.memsci.2010.05.049.

(30) Kuhn, J.; Castillo-Sanchez, J. M.; Gascon, J.; Calero, S.; Dubbeldam, D.; Vlugt, T. J. H.; Kapteijn, F.; Gross, J. Adsorption and Diffusion of Water, Methanol, and Ethanol in All-Silica DD3R: Experiments and Simulation. *J. Phys. Chem. C* **2009**, *113*, 14290-14301.

(31) Rick, S. W. A Reoptimization of the Five-site Water Potential (TIP5P) for use with Ewald Sums. *J. Chem. Phys.* **2004**, *120*, 6085-6093. https://doi.org/10.1063/1.1652434.

(32) Chen, B.; Potoff, J. J.; Siepmann, J. I. Monte Carlo Calculations for Alcohols and Their Mixtures with Alkanes. Transferable Potentials for Phase Equilibria. 5. United-Atom Description of Primary, Secondary, and Tertiary Alcohols. *J. Phys. Chem. B* **2001**, *105*, 3093-3104.

(33) Kiselev, A. V.; Lopatkin, A. A.; Shul'ga, A. A. Molecular statistical calculation of gas adsorption by silicalite. *Zeolites* **1985**, *5*, 261-267.

(34) Mayo, S. L.; Olafson, B. D.; Goddard, W. A. DREIDING: A Generic Force Field for Molecular Simulations. *J. Phys. Chem.* **1990**, *94*, 8897-8909.

(35) Yang, Q.; Zhong, C. Understanding Hydrogen Adsorption in Metal-Organic Frameworks with Open Metal Sites: A Computational Study. *J. Phys. Chem. B* **2006**, *110*, 655-658.

(36) Jorgensen, W. L.; Maxwell, D. S.; Tirado-Rives, J. Development and Testing of the OPLS All-Atom Force Field on Conformational Energetics and Properties of Organic Liquids. *J. Am. Chem. Soc.* **1996**, *118*, 11225-11236.

(37) Zhou, M.; Wang, Q.; Zhang, L.; Liu, Y. C.; Kang, Y. Adsorption Sites of Hydrogen in Zeolitic Imidazolate Frameworks. *J. Phys. Chem. B* **2009**, *113*, 11049-11053.

(38) Xu, Q.; Zhong, C. A General Approach for Estimating Framework Charges in Metal-Organic Frameworks. *J. Phys. Chem. C* **2010**, *114*, 5035-5042.

(39) Frenkel, D.; Smit, B. *Understanding Molecular Simulations: From Algorithms to Applications*. 2nd Edition, Academic Press: San Diego, 2002; pp

(40) Ruthven, D. M. *Principles of Adsorption and Adsorption Processes*. John Wiley: New York, 1984; pp 1-433.

(41) Myers, A. L.; Prausnitz, J. M. Thermodynamics of Mixed Gas Adsorption. *A.I.Ch.E.J.* **1965**, *11*, 121-130. https://doi.org/10.1002/aic.690110125.

(42) Talu, O.; Myers, A. L. Rigorous Thermodynamic Treatment of Gas-Adsorption. *A.I.Ch.E.J.* **1988**, *34*, 1887-1893.

(43) Siperstein, F. R.; Myers, A. L. Mixed-Gas Adsorption. *A.I.Ch.E.J.* **2001**, *47*, 1141-1159. https://doi.org/10.1002/aic.690470520.

(44) Krishna, R.; Van Baten, J. M. Elucidation of Selectivity Reversals for Binary Mixture Adsorption in Microporous Adsorbents. *ACS Omega* **2020**, *5*, 9031-9040. https://doi.org/10.1021/acsomega.0c01051.

(45) Krishna, R.; Van Baten, J. M. Using Molecular Simulations for Elucidation of Thermodynamic Non-Idealities in Adsorption of CO_2-containing Mixtures in NaX Zeolite. *ACS Omega* **2020**, *5*, 20535-20542. https://doi.org/10.1021/acsomega.0c02730.

(46) Krishna, R.; Van Baten, J. M. Water/Alcohol Mixture Adsorption in Hydrophobic Materials: Enhanced Water Ingress caused by Hydrogen Bonding. *ACS Omega* **2020**, *5*, 28393-28402. https://doi.org/10.1021/acsomega.0c04491.

(47) Krishna, R.; Van Baten, J. M. Investigating the Non-idealities in Adsorption of CO_2-bearing Mixtures in Cation-exchanged Zeolites. *Sep. Purif. Technol.* **2018**, *206*, 208-217. https://doi.org/10.1016/j.seppur.2018.06.009.

(48) Krishna, R.; van Baten, J. M. Fundamental Insights into the Variety of Factors that Influence Water/Alcohol Membrane Permeation Selectivity *J. Membr. Sci.* **2024**, *698*, 122635. https://doi.org/10.1016/j.memsci.2024.122635.

(49) Wilkins, N. S.; Rajendran, A. Measurement of competitive CO_2 and N_2 adsorption on Zeolite 13X for post-combustion CO_2 capture. *Adsorption* **2019**, *25*, 115-133. https://doi.org/10.1007/s10450-018-00004-2.

(50) Hefti, M.; Marx, D.; Joss, L.; Mazzotti, M. Adsorption Equilibrium of Binary Mixtures of Carbon Dioxide and Nitrogen on Zeolites ZSM-5 and 13X. *Microporous Mesoporous Mater.* **2015**, *215*, 215-228.

(51) van Zandvoort, I.; Ras, E.-J.; de Graaf, R.; Krishna, R. Using Transient Breakthrough Experiments for Screening of Adsorbents for Separation of C_2H_4/CO_2 Mixtures *Sep. Purif. Technol.* **2020**, *241*, 116706. https://doi.org/10.1016/j.seppur.2020.116706.

(52) van Zandvoort, I.; van der Waal, J. K.; Ras, E.-J.; de Graaf, R.; Krishna, R. Highlighting non-idealities in C_2H_4/CO_2 mixture adsorption in 5A zeolite. *Sep. Purif. Technol.* **2019**, *227*, 115730. https://doi.org/10.1016/j.seppur.2019.115730.

(53) Wang, Y.; LeVan, M. D. Adsorption Equilibrium of Binary Mixtures of Carbon Dioxide and Water Vapor on Zeolites 5A and 13X. *J. Chem. Eng. Data* **2010**, *55*, 3189-3195. https://doi.org/10.1021/je100053g.

(54) Krishna, R. Occupancy Dependency of Maxwell−Stefan Diffusivities in Ordered Crystalline Microporous Materials. *ACS Omega* **2018**, *3*, 15743-15753. https://doi.org/10.1021/acsomega.8b02465.

(55) Talu, O.; Zwiebel, I. Multicomponent Adsorption Equilibria of Nonideal Mixtures. *A.I.Ch.E.J.* **1986**, *32*, 1263-1276.

(56) Sochard, S.; Fernandes, N.; Reneaume, J.-M. Modeling of Adsorption Isotherm of a Binary Mixture with Real Adsorbed Solution Theory and Nonrandom Two-Liquid Model. *A.I.Ch.E.J.* **2010**, *56*, 3109-3119. https://doi.org/10.1002/aic.12220.

(57) Mittal, N.; Bai, P.; Siepmann, I.; Daoutidis, P.; Tsapatsis, M. Bioethanol Enrichment using Zeolite Membranes: Molecular Modeling, Conceptual Process Design and Techno-Economic Analysis. *J. Membr. Sci.* **2017**, *540*, 464-476.

(58) Calleja, G.; Jimenez, A.; Pau, J.; Domínguez, L.; Pérez, P. Multicomponent Adsorption Equilibrium of Ethylene, Propane, Propylene and CO_2 on 13X Zeolite. *Gas Sep. Purif.* **1994**, *8*, 247-256. https://doi.org/10.1016/0950-4214(94)80005-7.

(59) Kaur, H.; Marshall, B. D. Real adsorbed solution theory model for the adsorption of CO_2 from humid gas on CALF-20. *ChemRxiv* **2023**, 1-18. https://doi.org/10.26434/chemrxiv-2023-2cp2c.

(60) Krishna, R.; van Baten, J. M. Segregation effects in adsorption of CO_2 containing mixtures and their consequences for separation selectivities in cage-type zeolites. *Sep. Purif. Technol.* **2008**, *61*, 414-423. https://doi.org/10.1016/j.seppur.2007.12.003.

(61) Zhang, C.; Yang, X. Molecular dynamics simulation of ethanol/water mixtures for structure and diffusion properties. *Fluid Phase Equilib.* **2005**, *231*, 1-10. https://doi.org/10.1016/j.fluid.2005.03.018.

(62) Krishna, R.; van Baten, J. M. Entropy-based Separation of Linear Chain Molecules by Exploiting Differences in the Saturation Capacities in Cage-type Zeolites. *Sep. Purif. Technol.* **2011**, *76*, 325-330. https://doi.org/10.1016/j.seppur.2010.10.023.

(63) Costa, E.; Calleja, G.; Jimenez, A.; Pau, J. Adsorption Equilibrium of Ethylene, Propane, Propylene, Carbon Dioxide, and Their Mixtures in 13X Zeolite. *J. Chem. Eng. Data* **1991**, *36*, 218-224. https://doi.org/10.1021/je00002a020.

(64) Krishna, R.; van Baten, J. M. Investigating cluster formation in adsorption of CO_2, CH_4, and Ar in zeolites and metal organic frameworks at sub-critical temperatures. *Langmuir* **2010**, *26*, 3981-3992. https://doi.org/10.1021/la9033639.

(65) Krishna, R.; van Baten, J. M. Highlighting a variety of unusual characteristics of adsorption and diffusion in microporous materials induced by clustering of guest molecules. *Langmuir* **2010**, *26*, 8450-8463. https://doi.org/10.1021/la904895y.

(66) Krishna, R. Separating Mixtures by Exploiting Molecular Packing Effects in Microporous Materials. *Phys. Chem. Chem. Phys.* **2015**, *17*, 39-59. https://doi.org/10.1039/C4CP03939D.

(67) Krishna, R. Elucidation and Characterization of Entropy Effects in Mixture Separations with Micro-porous Crystalline Adsorbents. *Sep. Purif. Technol.* **2019**, *215*, 227-241. https://doi.org/10.1016/j.seppur.2019.01.014.

(68) Krishna, R.; van Baten, J. M. A comparison of the CO_2 capture characteristics of zeolites and metal-organic frameworks. *Sep. Purif. Technol.* **2012**, *87*, 120-126. https://doi.org/10.1016/j.seppur.2011.11.031.

(69) Avijegon, G.; Xiao, G.; Li, G.; May, E. F. Binary and ternary adsorption equilibria for CO2/CH4/N2 mixtures on Zeolite 13X beads from 273 to 333 K and pressures to 900 kPa. **2018**, *24*, 381-392. https://doi.org/10.1007/s10450-018-9952-3.

(70) Basmadjian, D.; Hsieh, S. T. Isothermal Column Sorption of Ethylene-Carbon Dioxide Mixtures with Azeotropic Behaviour. *Can. J. Chem. Eng.* **1980**, *58*, 185-189. https://doi.org/10.1002/cjce.5450580208.

(71) Krishna, R.; van Baten, J. M. Non-Idealities in adsorption thermodynamics for CO_2 capture from humid natural gas using CALF-20. *Sep. Purif. Technol.* **2025**, *355, Part A*, 129553. https://doi.org/10.1016/j.seppur.2024.129553.

(72) Krishna, R. Highlighting the Influence of Thermodynamic Coupling on Kinetic Separations with Microporous Crystalline Materials. *ACS Omega* **2019**, *4*, 3409-3419. https://doi.org/10.1021/acsomega.8b03480.

(73) Krishna, R. Metrics for Evaluation and Screening of Metal-Organic Frameworks for Applications in Mixture Separations. *ACS Omega* **2020**, *5*, 16987−17004. https://doi.org/10.1021/acsomega.0c02218.

(74) Krishna, R. Synergistic and Antisynergistic Intracrystalline Diffusional Influences on Mixture Separations in Fixed Bed Adsorbers. *Precision Chemistry* **2023**, *1*, 83-93. https://doi.org/10.1021/prechem.2c00003.

(75) Krishna, R. Fundamental Insights into Intra-Crystalline Diffusional Influences on Mixture Separations in Fixed Bed Adsorbers. *Chem Bio Eng.* **2024**, *1*, 53-66. https://doi.org/10.1021/cbe.3c00057.

(76) Mofarahi, M.; Salehi, S. M. Pure and Binary Adsorption Isotherms of Ethylene and Ethane on Zeolite 5A. *Adsorption* **2013**, *19*, 101-110. https://doi.org/10.1007/s10450-012-9423-1.

(77) Mofarahi, M.; Gholipour, F. Gas Adsorption Separation of CO_2/CH_4 System using Zeolite 5A. *Microporous Mesoporous Mater.* **2014**, *200*, 47-54. https://doi.org/10.1016/j.micromeso.2014.08.022.

(78) Hyun, S. H.; Danner, R. P. Equiilbrium Adsorption of Ethane, Ethylene, Isobutane, Carbon Dioxide, and Their Binary Mixtures on 13X Molecular Sieves. *J. Chem. Eng. Data* **1982**, *27*, 196-200. https://doi.org/10.1021/je00028a029.

(79) Calleja, G.; Pau, J.; Calles, J. A. Pure and Multicomponent Adsorption Equilibrium of Carbon Dioxide, Ethylene, and Propane on ZSM-5 Zeolites with Different Si/Al Ratios. *J. Chem. Eng. Data* **1998**, *43*, 994-1003.

(80) Sakuth, M.; Meyer, J.; Gmehling, J. Vapor Phase Adsorption Equilibria of Toluene + 1-Propanol Mixtures on Y-Zeolites with Different Silicon to Aluminum Ratios. *J. Chem. Eng. Data* **1995**, *40*, 895-899.

(81) Sakuth, M.; Meyer, J.; Gmehling, J. Measurement and Prediction of Binary Adsorption Equilibria of Vapors on Dealuminated Y-zeolites (DAY). *Chem. Eng. Process.* **1998**, *37*, 267-277.

(82) Takeuchi, Y.; Iwamoto, H.; Miyata, N.; Asano, S.; Harada, M. Adsorption of l-butanol and p-xylene vapor with high silica zeolites. *Separations Technology* **1995**, *5*, 23-24.

(83) Konno, M.; Teranayabashi, M.; Takako, Y.; Saato, S. Adsorption Equilibria of Hydrocarbon Gaseous Mixtures Containing Polar Components. *J. Chem. Eng. Japan.* **1985**, *18*, 398-408.

(84) Bartholdy, S.; Bjørner, M. G.; Solbraa, E.; Shapiro, A.; Kontogeorgis, G. M. Capabilities and Limitations of Predictive Engineering Theories for Multicomponent Adsorption. *Ind. Eng. Chem. Res.* **2013**, *52*, 11552-11563.

(85) Van Assche, T. R. C.; Duerinck, T.; Van der Perre, S.; Baron, G. V.; Denayer, J. F. M. Prediction of Molecular Separation of Polar−Apolar Mixtures on Heterogeneous Metal−Organic Frameworks: HKUST-1. *Langmuir* **2014**, *30*, 7878−7883.

(86) Clark, W. M.; Rowley, R. L. The mutual diffusion coefficient of methanol - n-hexane near the consolute point. *A.I.Ch.E.J.* **1986**, *32*, 1125-1131.

(87) Vlugt, T. J. H.; Krishna, R.; Smit, B. Molecular Simulations of Adsorption Isotherms for Linear and Branched Alkanes and Their Mixtures in Silicalite. *J. Phys. Chem. B* **1999**, *103*, 1102-1118. https://doi.org/10.1021/jp982736c.

(88) Dubbeldam, D.; Calero, S.; Vlugt, T. J. H.; Krishna, R.; Maesen, T. L. M.; Beerdsen, E.; Smit, B. Force Field Parametrization through Fitting on Inflection Points in Isotherms. *Phys. Rev. Lett.* **2004**, *93*, 088302.

(89) Dubbeldam, D.; Krishna, R.; Calero, S.; Yazaydın, A. Ö. Computer-Assisted Screening of Ordered Crystalline Nanoporous Adsorbents for Separation of Alkane Isomers. *Angew. Chem. Int. Ed.* **2012**, *51*, 11867-11871. https://doi.org/10.1002/anie.201205040.

(90) Schenk, M.; Vidal, S. L.; Vlugt, T. J. H.; Smit, B.; Krishna, R. Separation of alkane isomers by exploiting entropy effects during adsorption on silicalite-1: A configurational-bias Monte Carlo simulation study. *Langmuir* **2001**, *17*, 1558-1570.

(91) van Baten, J. M.; Krishna, R. Entropy effects in adsorption and diffusion of alkane isomers in mordenite: An investigation using CBMC and MD simulations. *Microporous Mesoporous Mater.* **2005**, *84*, 179-191. https://doi.org/10.1016/j.micromeso.2005.05.025.

(92) García-Sánchez, A.; García-Pérez, E.; Dubbeldam, D.; Krishna, R.; Calero, S. A Simulation Study of Alkanes in Linde Type A Zeolites. *Adsorpt. Sci. Technol.* **2007**, *25*, 417-427.

(93) Calero, S.; Dubbeldam, D.; Krishna, R.; Smit, B.; Vlugt, T. J. H.; Denayer, J. F. M.; Martens, J. A.; Maesen, T. L. M. Understanding the role of sodium during adsorption. A force field for alkanes in sodium exchanged faujasites. *J. Am. Chem. Soc.* **2004**, *126*, 11377-11386.

(94) Hasegawa, Y.; Abe, C.; Ikeda, A. Pervaporative Dehydration of Organic Solvents Using High-Silica CHA-Type Zeolite Membrane. *Membranes* **2021**, *11*, 229. https://doi.org/10.3390/membranes11030229.

(95) Hasegawa, Y.; Abe, C.; Nishioka, M.; Sato, K.; Nagase, T.; Hanaoka, T. Formation of high flux CHA-type zeolite membranes and their application to the dehydration of alcohol solutions. *J. Membr. Sci.* **2010**, *364*, 318-324.

(96) Sato, K.; Sugimoto, K.; Shimosuma, N.; Kikuchi, T.; Kyotani, T.; Kurata, T. Development of practically available up-scaled high-silica CHA-type zeolite membranes for industrial purpose in dehydration of N-methyl pyrrolidone solution. *J. Membr. Sci.* **2012**, *409-410*, 82-95.

(97) Kuhn, J.; Yajima, K.; Tomita, T.; Gross, J.; Kapteijn, F. Dehydration performance of a hydrophobic DD3R zeolite membrane. *J. Membr. Sci.* **2008**, *321*, 344-349.

(98) Morigami, Y.; Kondo, M.; Abe, J.; Kita, H.; Okamoto, K. The First Large-scale Pervaporation Plant Using Tubular-type Module with Zeolite NaA Membrane. *Sep. Purif. Technol.* **2001**, *25*, 251-260.

(99) Pera-Titus, M.; Fité, C.; Sebastián, V.; Lorente, E.; Llorens, J.; Cunill, F. Modeling Pervaporation of Ethanol/Water Mixtures within 'Real' Zeolite NaA Membranes. *Ind. Eng. Chem. Res.* **2008**, *47*, 3213-3224.

(100) Pera-Titus, M.; Llorens, J.; Tejero, J.; Cunill, F. Description of the pervaporation dehydration performance of A-type zeolite membranes: A modeling approach based on the Maxwell–Stefan theory. *Catal. Today* **2006**, *118*, 73-84.

(101) Liu, B.; Kita, H.; Yogo , K. Preparation of Si-rich LTA membrane using organic template-free solution for methanol dehydration *Sep. Purif. Technol.* **2020**, *239*, 116533. https://doi.org/10.1016/j.seppur.2020.116533.

(102) Yu, M.; Falconer, J. L.; Noble, R. D.; Krishna, R. Modeling Transient Permeation of Polar Organic Mixtures through a MFI Zeolite Membrane using the Maxwell-Stefan Equations. *J. Membr. Sci.* **2007**, *293*, 167-173.

(103) Mittal, N.; Bai, P.; Siepmann, J. I.; Daoutidis, P.; Tsapatsis, M. Bioethanol Enrichment using Zeolite Membranes: Molecular Modeling, Conceptual Process Design and Techno-Economic Analysis. *J. Membr. Sci.* **2017**, *540*, 464-476. https://doi.org/10.1016/j.memsci.2017.06.075.

(104) Sawamura, K.; Furuhata, T.; Sekine, Y.; Kikuchi, E.; Subramanian, B.; Matsukata, M. Zeolite Membrane for Dehydration of Isopropylalcohol-Water Mixture by Vapor Permeation. *ACS Appl. Mater. Interfaces* **2015**, *7*, 13728–13730. https://doi.org/10.1021/acsami.5b04085.

(105) Yao, J.; Wang, H. Zeolitic Imidazolate Framework Composite Membranes and Thin Films: Synthesis and Applications. *Chem. Soc. Rev.* **2014**, *43*, 4470-4493. https://doi.org/10.1039/C3CS60480B.

(106) Zhang, K.; Lively, R. P.; Zhang, C.; Koros, W. J.; Chance, R. R. Investigating the Intrinsic Ethanol/Water Separation Capability of ZIF-8: An Adsorption and Diffusion Study. *J. Phys. Chem. C* **2013**, *117*, 7214-7225. https://doi.org/10.1021/jp401548b.

(107) Wu, J. Y.; Liu, Q. L.; Xiong, Y.; Zhu, A. M.; Chen, Y. Molecular Simulation of Water/Alcohol Mixtures Adsorption and Diffusion in Zeolite 4A Membranes. *J. Phys. Chem. B* **2009**, *113*, 4267-4274.

(108) Guo, S.; Yua, C.; Gua, X.; Jin, W.; Zhong, J.; Chen, C.-J. Simulation of adsorption, diffusion, and permeability of water and ethanol in NaA zeolite membranes. *J. Membr. Sci.* **2011**, *376*, 40-49. https://doi.org/10.1016/j.memsci.2011.03.043.

(109) Krishna, R. Highlighting Thermodynamic Coupling Effects in Alcohol/Water Pervaporation across Polymeric Membranes. *ACS Omega* **2019**, *4*, 15255-15264. https://doi.org/10.1021/acsomega.9b02255.

(110) Krishna, R.; van Baten, J. M. Unified Maxwell-Stefan Description of Binary Mixture Diffusion in Micro- and Meso- Porous Materials. *Chem. Eng. Sci.* **2009**, *64*, 3159-3178.

(111) Krishna, R.; van Baten, J. M. Maxwell-Stefan modeling of slowing-down effects in mixed gas permeation across porous membranes. *J. Membr. Sci.* **2011**, *383*, 289-300. https://doi.org/10.1016/j.memsci.2011.08.067.

(112) Baker, R. W. *Membrane Technology and Applications*. 3rd Edition, John Wiley: New York, 2012; pp

(113) Wesselingh, J. A.; Krishna, R. *Mass transfer in multicomponent mixtures*. VSSD: Delft, 2000; pp

(114) Caro, J. Are MOF membranes better in gas separation than those made of zeolites? *Curr. Opin. Chem. Eng.* **2011**, *1*, 77-83.

(115) Rangnekar, N.; Mittal, N.; Elyassi, B.; Caro, J.; Tsapatsis , M. Zeolite Membranes –A Review and Comparison with MOFs. *Chem. Soc. Rev.* **2015**, *44*, 7128-7154. https://doi.org/10.1039/C5CS00292C.

(116) Pera-Titus, M. Porous Inorganic Membranes for CO2 Capture: Present and Prospects. *Chem. Rev.* **2014**, *114*, 1413-1492.

(117) Krishna, R. Using the Maxwell-Stefan formulation for Highlighting the Influence of Interspecies (1-2) Friction on Binary Mixture Permeation across Microporous and Polymeric Membranes. *J. Membr. Sci.* **2017**, *540*, 261-276. https://doi.org/10.1016/j.memsci.2017.06.062.

(118) Krishna, R.; Li, S.; van Baten, J. M.; Falconer, J. L.; Noble, R. D. Investigation of slowing-down and speeding-up effects in binary mixture permeation across SAPO-34 and MFI membranes. *Sep. Purif. Technol.* **2008**, *60*, 230-236. https://doi.org/10.1016/j.seppur.2007.08.012.

(119) Li, S.; Falconer, J. L.; Noble, R. D.; Krishna, R. Modeling permeation of CO_2/CH_4, CO_2/N_2, and N_2/CH_4 mixtures across SAPO-34 membrane with the Maxwell-Stefan equations. *Ind. Eng. Chem. Res.* **2007**, *46*, 3904-3911. https://doi.org/10.1021/ie0610703.

(120) Li, S.; Falconer, J. L.; Noble, R. D.; Krishna, R. Interpreting unary, binary and ternary mixture permeation across a SAPO-34 membrane with loading-dependent Maxwell-Stefan diffusivities. *J. Phys. Chem. C* **2007**, *111*, 5075-5082. https://doi.org/10.1021/jp067404j.

(121) Feng, X.; Zong, Z.; Elsaidi, S.; Jasinski, J. B.; Krishna, R.; Thallapally, P. K.; Carreon, M. A. Kr/Xe Separation over a Chabazite Zeolite Membrane *J. Am. Chem. Soc.* **2016**, *138*, 9791-9794.

(122) Sandström, L.; Sjöberg, E.; Hedlund, J. Very high flux MFI membrane for CO_2 separation. *J. Membr. Sci.* **2011**, *380*, 232-240.

(123) van den Bergh, J.; Zhu, W.; Gascon, J.; Moulijn, J. A.; Kapteijn, F. Separation and Permeation Characteristics of a DD3R Zeolite Membrane. *J. Membr. Sci.* **2008**, *316*, 35-45.

(124) van de Graaf, J. M.; Kapteijn, F.; Moulijn, J. A. Modeling permeation of binary mixtures through zeolite membranes. *A.I.Ch.E.J.* **1999**, *45*, 497-511.

(125) Zito, P. F.; Brunetti, A.; Caravella, A.; Drioli, E.; Barbieri, G. Mutual influence in permeation of CO_2-containing mixtures through a SAPO-34 membrane. *J. Membr. Sci.* **2020**, *595*, 117534. https://doi.org/10.1016/j.memsci.2019.117534.

(126) Yu, L.; Nobandegani, M. S.; Hedlund, J. Industrially relevant CHA membranes for CO_2/CH_4 separation *J. Membr. Sci.* **2021**, *XX*, XXX. https://doi.org/10.1016/j.memsci.2021.119888.

(127) Hasegawa, Y.; Nishida, K.; Oguro, S.; Fujimura, Y.; Yajima, K.; Niino, M.; Isomura, M.; Tomita, T. Gas separation process for CO_2 removal from natural gas with DDR-type zeolite membrane. *Energy Procedia* **2017**, *114*, 32-36.

(128) Himeno, S.; Tomita, T.; Suzuki, K.; Nakayama, K.; Yoshida, S. Synthesis and Permeation Properties of a DDR-type zeolite membrane for Separation of CO_2/CH_4 Gaseous Mixtures. *Ind. Eng. Chem. Res.* **2007**, *46*, 6989-6997.

(129) van den Bergh, J.; Zhu, W.; Groen, J. C.; Kapteijn, F.; Moulijn, J. A.; Yajima, K.; Nakayama, K.; Tomita, T.; Yoshida, S. Natural Gas Purification with a DDR Zeolite Membrane; Permeation Modelling with Maxwell-Stefan Equations. *Stud. Surf. Sci. Catal.* **2007**, *170*, 1021-1027.

(130) Qian, Q.; Asinger, P. A.; Lee, M. J.; Han, G.; Rodriguez, K. M.; Lin, S.; Benedetti, F. M.; Wu, A. X.; Chi, W. S.; Smith, Z. P. MOF-Based Membranes for Gas Separations. *Chem. Rev.* **2020**, *120*, 8161-8266. https://doi.org/10.1021/acs.chemrev.0c00119.

(131) Bux, H.; Chmelik, C.; Krishna, R.; Caro, J. Ethene/Ethane Separation by the MOF Membrane ZIF-8: Molecular Correlation of Permeation, Adsorption, Diffusion. *J. Membr. Sci.* **2011**, *369*, 284-289.

(132) Bux, H.; Chmelik, C.; Van Baten, J. M.; Krishna, R.; Caro, J. Novel MOF-Membrane for Molecular Sieving Predicted by IR-Diffusion Studies and Molecular Modeling. *Adv. Mater.* **2010**, *22*, 4741-4743. https://doi.org/10.1002/adma.201002066.

(133) Chmelik, C.; van Baten, J. M.; Krishna, R. Hindering effects in diffusion of CO_2/CH_4 mixtures in ZIF-8 crystals. *J. Membr. Sci.* **2012**, *397-398*, 87-91. https://doi.org/10.1016/j.memsci.2012.01.013.

(134) Krishna, R.; Van Baten, J. M. Using Molecular Simulations to Unravel the Benefits of Characterizing Mixture Permeation in Microporous Membranes in Terms of the Spreading Pressure. *ACS Omega* **2020**, *5*, 32769−32780. https://dx.doi.org/10.1021/acsomega.0c05269.

(135) Krishna, R. Thermodynamic Insights into the Characteristics of Unary and Mixture Permeances in Microporous Membranes. *ACS Omega* **2019**, *4*, 9512-9521. https://doi.org/10.1021/acsomega.9b00907.

(136) Krishna, R. Methodologies for Screening and Selection of Crystalline Microporous Materials in Mixture Separations. *Sep. Purif. Technol.* **2018**, *194*, 281-300. https://doi.org/10.1016/j.seppur.2017.11.056.

(137) Krishna, R. A Maxwell-Stefan-Glueckauf Description of Transient Mixture Uptake in Microporous Adsorbents. *Sep. Purif. Technol.* **2018**, *191*, 392-399. https://doi.org/10.1016/j.seppur.2017.09.057.

(138) Krishna, R. Diffusing Uphill with James Clerk Maxwell and Josef Stefan. *Chem. Eng. Sci.* **2019**, *195*, 851-880. https://doi.org/10.1016/j.ces.2018.10.032.

(139) Krishna, R. Tracing the Origins of Transient Overshoots for Binary Mixture Diffusion in Microporous Crystalline Materials. *Phys. Chem. Chem. Phys.* **2016**, *18*, 15482-15495. https://doi.org/10.1039/C6CP00132G.

(140) Krishna, R. Uphill Diffusion in Multicomponent Mixtures. *Chem. Soc. Rev.* **2015**, *44*, 2812-2836. https://doi.org/10.1039/C4CS00440J.

(141) Krishna, R.; van Baten, J. M. Using Molecular Dynamics Simulations for Elucidation of Molecular Traffic in Ordered Crystalline Microporous Materials. *Microporous Mesoporous Mater.* **2018**, *258*, 151-169. https://doi.org/10.1016/j.micromeso.2017.09.014.

(142) Krishna, R.; van Baten, J. M. Investigating the potential of MgMOF-74 membranes for CO_2 capture. *J. Membr. Sci.* **2011**, *377*, 249-260.

(143) Krishna, R.; van Baten, J. M. Influence of Adsorption on the Diffusion Selectivity for Mixture Permeation across Mesoporous Membranes. *J. Membr. Sci.* **2011**, *369*, 545-549.

(144) Krishna, R.; van Baten, J. M. A molecular dynamics investigation of the diffusion characteristics of cavity-type zeolites with 8-ring windows. *Microporous Mesoporous Mater.* **2011**, *137*, 83-91. https://doi.org/10.1016/j.micromeso.2010.08.026.

(145) Chmelik, C.; Kärger, J.; Wiebcke, M.; Caro, J.; van Baten, J. M.; Krishna, R. Adsorption and Diffusion of Alkanes in CuBTC Crystals Investigated Using Infrared Microscopy and Molecular Simulations. *Microporous Mesoporous Mater.* **2009**, *117*, 22-32. https://doi.org/10.1016/j.micromeso.2008.06.003.

(146) Chmelik, C.; Heinke, L.; Kärger, J.; Shah, D. B.; Schmidt, W.; van Baten, J. M.; Krishna, R. Inflection in the Loading Dependence of the Maxwell-Stefan Diffusivity of Iso-butane in MFI Zeolite. *Chem. Phys. Lett.* **2008**, *459*, 141-145.

(147) Chmelik, C.; Heinke, L.; van Baten, J. M.; Krishna, R. Diffusion of *n*-butane/*iso*-butane Mixtures in Silicalite-1 Investigated Using Infrared (IR) Microscopy. *Microporous Mesoporous Mater.* **2009**, *125*, 11-16.

(148) Fernandez, M.; Kärger, J.; Freude, D.; Pampel, A.; van Baten, J. M.; Krishna, R. Mixture Diffusion in Zeolites Studied by MAS PFG NMR and Molecular Simulation. *Microporous Mesoporous Mater.* **2007**, *105*, 124-131. https://doi.org/10.1016/j.micromeso.2007.05.042.

(149) Krishna, R.; Van Baten, J. M. Elucidating Traffic Junction Effects in MFI Zeolite using Kinetic Monte Carlo Simulations. *ACS Omega* **2019**, *4*, 10761-10766. https://doi.org/10.1021/acsomega.9b01369.

(150) Herm, Z. R.; Krishna, R.; Long, J. R. CO_2/CH_4, CH_4/H_2 and $CO_2/CH_4/H_2$ separations at high pressures using Mg_2(dobdc). *Microporous Mesoporous Mater.* **2012**, *151*, 481-487.

(151) Herm, Z. R.; Swisher, J. A.; Smit, B.; Krishna, R.; Long, J. R. Metal-Organic Frameworks as Adsorbents for Hydrogen Purification and Pre-Combustion Carbon Dioxide Capture *J. Am. Chem. Soc.* **2011**, *133*, 5664-5667.

(152) Herm, Z. R.; Wiers, B. M.; Van Baten, J. M.; Hudson, M. R.; Zajdel, P.; Brown, C. M.; Maschiocchi, N.; Krishna, R.; Long, J. R. Separation of Hexane Isomers in a Metal-Organic Framework with Triangular Channels *Science* **2013**, *340*, 960-964. https://www.science.org/doi/10.1126/science.1234071.

(153) Krishna, R. Screening Metal-Organic Frameworks for Mixture Separations in Fixed-Bed Adsorbers using a Combined Selectivity/Capacity Metric. *RSC Adv.* **2017**, *7*, 35724-35737. https://doi.org/10.1039/C7RA07363A.

(154) Titze, T.; Chmelik, C.; Kärger, J.; van Baten, J. M.; Krishna, R. Uncommon Synergy Between Adsorption and Diffusion of Hexane Isomer Mixtures in MFI Zeolite Induced by Configurational Entropy Effects *J. Phys. Chem. C* **2014**, *118*, 2660-2665. https://doi.org/10.1021/jp412526t.

(155) Krishna, R.; van Baten, J. M. Screening of zeolite adsorbents for separation of hexane isomers: A molecular simulation study. *Sep. Purif. Technol.* **2007**, *55*, 246-255. https://doi.org/10.1016/j.seppur.2006.12.011.

(156) Shen, J.; He, X.; Ke, T.; Krishna, R.; van Baten, J. M.; Chen, R.; Bao, Z.; Xing, H.; Dincă, M.; Zhang, Z.; Yang, Q.; Ren, Q. Simultaneous interlayer and intralayer space control in two-dimensional metal−organic frameworks for acetylene/ethylene separation. *Nat. Commun.* **2020**, *11*, 6259. https://doi.org/10.1038/s41467-020-20101-7.

(157) Krishna, R.; van Baten, J. M. Influence of segregated adsorption on mixture diffusion in DDR zeolite. *Chem. Phys. Lett.* **2007**, *446*, 344-349. https://doi.org/10.1016/j.cplett.2007.08.060.

(158) Krishna, R.; van Baten, J. M. Onsager coefficients for binary mixture diffusion in nanopores. *Chem. Eng. Sci.* **2008**, *63*, 3120-3140.

(159) Moreton, J. C.; Krishna, R.; Van Baten, J. M.; Fylstra, N.; Chen, M.; Carr, T.; Fielder, K.; Chan, K.; Shimizu, G. K. H.; Yamamoto, S. A Thin Film Approach to Rapid, Quantitative Measurements of Mixed-Gas Adsorption Equilibrium in Nanoporous Materials. *ChemRxiv* **2024**, 1-20. https://doi.org/10.26434/chemrxiv-2024-0mhg1.

(160) Nguyen, T. T. T.; Balasubramaniam, B. M.; Fylstra, N.; Huynh, R. P. S.; Shimizu, G. K. H.; Rajendran, A. Competitive CO_2/H_2O Adsorption on CALF-20. *Ind. Eng. Chem. Res.* **2024**, *63*, 3265-3281. https://doi.org/10.1021/acs.iecr.3c04266.